HZDR-107

SYNTHETIC RADIATION DIAGNOSTICS AS A PATHWAY FOR STUDYING PLASMA DYNAMICS FROM ADVANCED ACCELERATORS TO ASTROPHYSICAL OBSERVATIONS

Richard Pausch

Wissenschaftlich Technische Berichte
HZDR-107 · ISSN ISSN 2191-8708

HZDR
HELMHOLTZ
ZENTRUM DRESDEN
ROSSENDORF

Wissenschaftlich-Technische Berichte
HZDR-107

Richard Pausch

SYNTHETIC RADIATION DIAGNOSTICS AS A PATHWAY FOR STUDYING PLASMA DYNAMICS FROM ADVANCED ACCELERATORS TO ASTROPHYSICAL OBSERVATIONS

HZDR
HELMHOLTZ
ZENTRUM DRESDEN
ROSSENDORF

Druckausgabe: ISSN 2191-8708

Elektronische Ausgabe: ISSN 2191-8716

https://www.hzdr.de/publications/Publ-29259

urn:nbn:de:bsz:d120-qucosa2-362997

Die vorliegende Arbeit wurde sowohl als Dissertation an der Fakultät Mathematik und Naturwissenschaften der Technischen Universität Dresden sowie als Wissenschaftlich-Technischer Bericht des Helmholtz-Zentrum Dresden – Rossendorf mit der Berichtsnummer **HZDR-107** veröffentlicht.

2019

Herausgegeben vom

Helmholtz-Zentrum Dresden - Rossendorf

Bautzner Landstraße 400

01328 Dresden

Germany

TECHNISCHE
UNIVERSITÄT
DRESDEN

HZDR
HELMHOLTZ
ZENTRUM DRESDEN
ROSSENDORF

Bereich Mathematik und Naturwissenschaften
Fakultät Physik, Institut für Strahlenphysik

Synthetic radiation diagnostics as a pathway for studying plasma dynamics

from advanced accelerators to astrophysical observations

Dipl.-Phys. Richard G. Pausch
Born on: 29th September 1986 in Dresden

Dissertation

to achieve the academic degree

Doctor rerum naturalium (Dr. rer. nat.)

Referees
Prof. Dr. Ulrich Schramm
Prof. Dr. Thomas E. Cowan
Prof. Dr. Mike C. Downer
Supervisor
Dr. Michael Bussmann

Submitted on: 10th December 2018
Defended on: 25th March 2019

DRESDEN
concept
Exzellenz aus
Wissenschaft
und Kultur

Abstract

In this thesis, two novel diagnostic techniques for the identification of plasma dynamics and the quantification of essential parameters of the dynamics by means of electromagnetic plasma-radiation are presented. Based on particle-in-cell simulations, both the radiation signatures of micrometer-sized laser plasma accelerators and light-year-sized plasma jets are simulated with the same highly parallel radiation simulation framework, in-situ to the plasma simulation.

The basics and limits of classical radiation calculation, as well as the theoretical and technical foundation of modern plasma simulation using the particle-in-cell method, are briefly introduced. The combination of previously independent methods in an in-situ analysis code as well as its validation and extension with newly developed algorithms for the simultaneous quantitative prediction of both coherent and incoherent radiation and the prevention of numerical artifacts is outlined in the initial chapters.

For laser wakefield acceleration, a hitherto unknown off-axis beam signature is observed, which can be used to identify the so-called blowout regime during laser defocusing. Since significant radiation is emitted only after the minimum spot size is reached, this signature is ideally suited to determine the laser focus position itself in the plasma to below $100\,\mu\mathrm{m}$ and thus to quantify the influence of relativistic self-focusing. A simple semi-analytical scattering model was developed to explain the blowout radiation signature. The spectral signature predicted by the model is verified using both a large-scale explorative simulation and a simulation parameter study, based on an experiment conducted at the HZDR. Identified by the simulations, a temporal asymmetry in the scattered laser light, which cannot be described by state of the art quasi-static models of the blowout regime, makes it possible to determine the focus position precisely by using this radiation signature.

For the so-called Kelvin-Helmholtz instability, a polarization signature is identified that allows both identifying the linear phase of the instability and quantifying its most important parameter, the growth rate. This plasma instability is suspected to occur in the shear region between plasma jets of active galactic nuclei or supernova remnants and the surrounding plasma and causes strong magnetic fields to grow along the shear surface. The measurement of the growth rate of these fields allows deducing the internal structure and dynamics of these jets and gaining an insight into previously inaccessible regions. A microscopic model of the electron dynamics was developed which describes the main radiation properties. With an unprecedentedly large and accurate simulation of the relativistic Kelvin-Helmholtz instability, the microscopic model was validated. The discovered polarization signature can be clearly identified even under arbitrary Lorentz transformations for observers on Earth and poses thus an ideal method for astronomical observations.

These very different physical scenarios clearly exemplify the possibilities of synthetic radiation diagnostics and represent the first step towards future explorative studies of plasmas and their radiation in other scenarios using simulations.

Kurzfassung

In dieser Arbeit werden zwei neuartige diagnostische Methoden vorgestellt, die auf emittierter, elektromagnetischer Strahlung basieren, um die Plasmadynamik zu identifizieren und wesentliche Parameter der Plasmaentwicklung zu quantifizieren. Die Strahlungssignaturen von mikrometergroßen Laser-Plasmabeschleunigern und von Lichtjahre großen Plasma Jets werden mit den gleichen hochparallelen Strahlungs-Simulations-Framework in-situ zur Plasmasimulation bestimmt.

Die Grundlagen und Grenzen der klassischen Strahlungsberechnung sowie die theoretischen und technischen Grundlagen der modernen Plasmasimulation mit der Particel-in-Cell-Methode werden in einem kurzen Exkurs eingeführt. Die Kombination der beiden bisher unabhängigen Methoden in einem in-situ Analysecode sowie deren Validierung und Erweiterung mit neu entwickelten Algorithmen zur gleichzeitigen quantitativen Vorhersage von kohärenter und inkohärenter Strahlung und zur Vermeidung numerischer Artefakte werden in den ersten Kapiteln skizziert.

Für die Laser-Wakefield-Beschleunigung wird eine bisher unbekannte Off-Axis-Strahlsignatur vorgestellt, mit der das sogenannte Blowout Regime bei der Laser-Defokussierung identifiziert werden kann. Da signifikante Strahlung erst nach Erreichen der minimalen Spotgröße emittiert wird, ist diese Signatur ideal geeignet, um die Laserfokusposition selbst im Plasma auf unter $100\,\mu\text{m}$ genau zu bestimmen und damit den quantitativen Einfluss der relativistischen Selbstfokussierung zu bestimmen. Ein einfaches semi-analytisches Streumodell wurde entwickelt, um die Blowout Strahlungssignatur zu erklären. Die vom Modell vorhergesagte spektrale Signatur wurde sowohl durch eine groß angelegte explorative Simulation als auch durch eine Simulationsparameterstudie, basierend auf einem am HZDR durchgeführten Experiment, verifiziert. Nur eine durch die Simulationen ermittelte zeitliche Asymmetrie, welche durch die aktuellen quasistatischen Modelle des Blowout Regimes nicht beschrieben werden kann, ermöglicht eine genaue Bestimmung der Fokusposition mit Hilfe dieser Strahlungssignatur.

Für die sogenannte Kelvin-Helmholtz-Instabilität wurde eine Polarisationssignatur entdeckt, die sowohl die Identifikation der lineare Phase der Instabilität als auch die Quantifizierung des wichtigsten Parameters, der Wachstumsrate, ermöglicht. Diese Plasmainstabilität wird im Scherbereich zwischen den Plasmastrahlen aktiver galaktischer Kerne oder Supernovaüberreste und dem umgebenden Plasma vermutet und verursacht starke Magnetfelder entlang der Scheroberfläche. Die Messung der Wachstumsrate dieser Felder erlaubt es, die innere Struktur und Dynamik dieser Jets abzuleiten und einen Einblick in bisher unzugängliche Regionen zu gewinnen. Es wurde ein mikroskopisches Modell der Elektronendynamik entwickelt, das die wichtigsten Strahlungseigenschaften abbildet. Mit Hilfe einer bislang unerreicht großen und genauen Simulation der relativistischen Kelvin-Helmholtz-Instabilität wurde das mikroskopische Modell validiert. Die dabei entdeckte Polarisationssignatur lässt sich auch bei beliebigen Lorentz-Transformationen für Beobachter auf der Erde eindeutig identifizieren und stellt somit eine ideale Methode für astronomische Beobachtungen dar.

Diese sehr unterschiedlichen physikalischen Szenarien veranschaulichen deutlich die Möglichkeiten der synthetischen Strahlendiagnostik und stellen einen ersten Schritt in Richtung zukünftiger explorativer Untersuchungen von Plasmen und ihrer Strahlung in anderen Szenarien mittels Simulationen dar.

Table of Contents

Abstract **III**

Kurzfassung **IV**

1 Synthetic radiation simulations for determining plasma dynamics - bridging spatial and temporal scales **1**
1.1 Understanding and optimizing micrometer-scale laser wakefield accelerators . . . 2
1.2 Observing plasma dynamics over astronomical distances 4
1.3 Challenges of an in-situ radiation simulation 6

2 Classical radiation emission **7**
2.1 The spectrally resolved Liénard-Wiechert potential 8
2.2 Correlation between phase space and radiation 9
2.3 Simplifying the equation: Synchrotron radiation 11
2.4 Extension to include multiple particles 12
2.5 Differences to quantum radiation 13
2.6 Summary 14

3 An introduction to simulating plasmas **15**
3.1 Fundamental aspects of the particle-in-cell algorithm 16
3.2 Enhancements to the particle-in-cell algorithm 20
  3.2.1 Particle Pusher 20
  3.2.2 Field Solver 21
  3.2.3 Current deposition schemes 22
  3.2.4 Higher order particle shapes 22
3.3 In-situ data analysis in PIConGPU 23
3.4 Summary 24

4 In situ spectral radiation calculation in PIConGPU **25**
4.1 Discrete implementation in particle-in-cell codes 25
4.2 Validating the radiation plug-in against theory 27
  4.2.1 Quasi-stationary electron in a relativistic field 27
  4.2.2 A relativistic electron in an electromagnetic wave 28
  4.2.3 Nonlinear Thomson scattering of an electron bunch 29
  4.2.4 Nonlinear Thomson scattering from a plasma 30
4.3 Coherent and incoherent radiation with form factors 32

4.4 Window functions for continuous boundary conditions . . . 34
4.5 Summary and Outlook . . . 38

5 Radiation reaction **39**
5.1 Taking radiation losses into account . . . 39
5.2 A brief derivation of the radiation reaction force . . . 40
5.3 Implementing the reduced Landau-Lifshitz equation . . . 41
5.4 Validating the radiation reaction in PIConGPU . . . 42
5.5 Summary and Outlook . . . 45

6 Radiation as diagnostics during laser wakefield acceleration **47**
6.1 Advantages of small-scale plasma accelerators and challenges in their diagnostics 47
6.2 Fundamental processes behind laser wakefield acceleration . . . 49
6.2.1 Generating plasmas with relativistic lasers . . . 49
6.2.2 The laser's ponderomotive force as the driver of a plasma wave . . . 51
6.2.3 The blowout regime . . . 54
6.2.4 How the laser evolution influences the acceleration process . . . 55
6.2.5 Getting electrons into the plasma cavity: self-injection methods . . . 58
6.3 Fundamental laser-electron scattering theory . . . 61
6.3.1 Electrons scatter laser photons . . . 61
6.3.2 The correlation between the electron drift and the scattered light . . . 63
6.3.3 Scattering in the bubble regime . . . 67
6.4 Radiation signatures for determining the laser plasma dynamics . . . 70
6.4.1 A large-scale LWFA simulation for studying the radiation . . . 70
6.4.2 Identifying several known radiation signatures . . . 74
6.4.3 Spectral broadening during the blowout regime . . . 76
6.4.4 Determining the focus position with plasma radiation . . . 80
6.4.5 Radiation signature of self-phase modulation . . . 83
6.5 A case study: Ionization injection at the DRACO laser . . . 86
6.5.1 Reaching 300pC of charge with DRACO . . . 87
6.5.2 Simulating the ionization injection . . . 90
6.6 Conclusions and Outlook . . . 97

7 Radiation signature of the Kelvin-Helmholtz instability **99**
7.1 Determination of plasma dynamics in astronomical objects through radiation . . . 99
7.2 An Introduction the the Kelvin-Helmholtz instability . . . 100
7.2.1 The electron-scale Kelvin-Helmholtz instability (ESKHI) . . . 101
7.2.2 More relativistic streams - the mushroom instability (MI) . . . 102
7.2.3 DC magnetic fields on the shear surface . . . 104
7.3 A microscopic model of the shear surface electron dynamics . . . 106
7.3.1 The electron dynamics . . . 106
7.3.2 Deriving the emitted radiation polarization . . . 109
7.3.3 Deriving the correlation between radiation and KHI growth rate . . . 111
7.4 Comparison to large scale simulations . . . 112
7.4.1 Evolution of the KHI . . . 113
7.4.2 Polarization signature . . . 117
7.4.3 Correlation between radiation power and magnetic field evolution . . . 120
7.5 Observer in the lab frame . . . 122
7.5.1 Lorentz transforming the polarization signature . . . 122
7.5.2 Consequences for an observer on Earth . . . 123

7.6 Discussion of possible observational systems 125
7.6.1 Influences of more realistic jets 125
7.6.2 Observation in jets from active galactic nuclei 127
7.6.3 Observation in lab experiments 128
7.7 Summary and Outlook 129

8 Summary **131**

9 Outlook: future applications for small- and large-scale plasmas **133**

Glossary **137**

Publications during this Ph.D. project **139**

References **143**

Acknowledgement **163**

1 Synthetic radiation simulations for determining plasma dynamics - bridging spatial and temporal scales

Plasmas occur in a wide range of parameters. Starting with micrometer-scale plasmas generated in today's laser plasma accelerators [1, 2], to millimeter- to meter-scale plasmas in inertially confined fusion, fusion reactors, and material processing in the electronic industry [3, 4], to kilometer-scale plasmas in planetary atmospheres and stars [5], to thousands of light years large intergalactic plasma jets [6]. Many of these systems show a complex plasma dynamics that cannot be probed directly.

This thesis focuses on new, indirect methods to gain insight into plasma systems using spectrally resolved electromagnetic radiation. It focuses on theoretical models, supported by simulations, that enable linking the observed spectra to the plasma dynamics and allow identifying specific phases of the plasma dynamics via distinctive spectral signatures and quantifying characteristic properties of the plasma dynamics by quantifying the emitted radiation.

Spectral methods are of great importance for the indirect detection of plasma dynamics since they make the fast- and small-scale electron dynamics in plasmas determinable by measuring radiation far away from the actual plasma dynamics. However, linking complex plasma dynamics to spectral radiation signatures is not a simple task, since both the nonlinear plasma dynamics and the complex calculation of radiation spectra are difficult to solve analytically. The modeling of plasma dynamics via ab initio simulations and the prediction of radiation by means of synthetic radiation diagnostics based on particle motion from the plasma simulation is, therefore, a valuable tool that allows directly connecting plasma dynamics with emitted radiation. This enables building simple models with predictive capabilities for the plasma dynamics and validating them using simulations. Based on these tested models, experimental measurements can determine the plasma dynamics based on the observed radiation. Providing the computational methods for these synthetic radiation simulations, developing usable models, and validating these against simulations is the main objective if this work.

This thesis covers two extreme cases: the femtosecond-nanometer-scale dynamics of a laser wakefield acceleration and the large-scale but spatially irresolvable plasma dynamics in astrophysical jets. Both scenarios are hard to resolve in space and time. This work shows that essential information on the plasma dynamics can be gained by means of measuring spectrally resolved radiation.

1.1 Understanding and optimizing micrometer-scale laser wakefield accelerators

The initial idea of using lasers to drive plasma waves in order to generate accelerating fields inside a plasma was proposed in 1979 by Tajima and Dawson [7]. Their method overcomes an intrinsic limitation of classical accelerators: since they rely on RF-cavities, they cannot provide electric fields beyond the breakdown limit of the materials used. This limits the accelerating fields to $E_{\mathrm{acc}} \sim 100\,\mathrm{MV/m}$ [8, 9]. By using plasmas to provide the accelerating electric field, field strengths of about the critical electric field of the plasma are reached [7]

$$E_{\mathrm{acc}} \sim E_{\mathrm{crit}} = \frac{m_e c \omega_{pe}}{q_e} \quad , \tag{1.1}$$

with c being the speed of light, m_e and q_e denoting the electron's mass and charge, and ω_{pe} being the plasma frequency:

$$\omega_{pe} = \sqrt{\frac{n_e q_e^2}{\varepsilon_0 m_e}} \tag{1.2}$$

with n_e denoting the electron density and ε_0 the vacuum permittivity. In laser plasma experiments, accelerating fields of $E_{\mathrm{acc}} \sim 100\,\mathrm{GV/m}$ [10, 11] have been demonstrated. This allows shrinking the size of accelerators in theory by three orders of magnitude and thus reducing cost and space for constructing an electron accelerator.

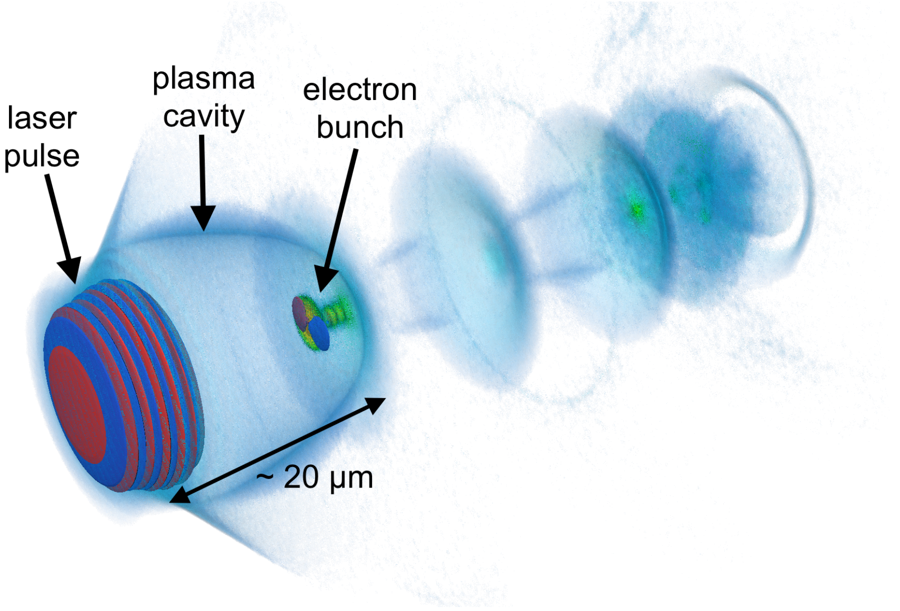

Figure 1.1: **Illustration of a laser wakefield accelerator:** A high-power laser pulse drives a plasma wave and creates a plasma cavity in which an electron bunch is accelerated. The electron density is depicted by a colored volume rendering. Densities below the initial plasma density are completely transparent for reasons of illustration. The contour plots in blue and red represent the electric field of both the laser pulse and the electron bunch. The image is a 3D visualization of a simulation performed with the particle-in-cell code PIConGPU. [R1].

In a simplified description, the laser wakefield acceleration (LWFA) is driven by a laser pulse that propagates through an *underdense*[1] plasma and pushes the plasma electrons aside due to

---

[1] An *underdense* plasma is defined as a plasma in which the plasma frequency ω_{pe} is smaller than the laser frequency ω_0. Such a laser can propagate through the plasma according to the dispersion relation. In contrast, an *overdense plasma* ($\omega_{pe} > \omega_0$) reflects and absorbs such a laser.

the laser's repulsive ponderomotive potential. Meanwhile, the ions remain almost motionless due to their high mass. This creates an electron-free space behind the laser pulse as depicted in Fig. 1.1. The attractive ion background inside this electron-free space creates a plasma cavity with contains a longitudinal electric field. By a variety of mechanisms, electrons can enter the plasma cavity and then get accelerated by the present longitudinal electric field.

A breakthrough in the quality of electron bunches was achieved in 2004 by three groups simultaneously. They generated quasi-monoenergetic electron packages with energies up to $\sim 170\,\mathrm{MeV}$ [10, 12, 13]. Today, monoenergetic bunches with energies of over $2\,\mathrm{GeV}$ and charges of a few picocoulombs can be achieved by using pre-formed plasma channels [14–16]. Even higher energies could be reached in the future by means of staging several plasma cavities consecutively [17, 18]. Using a different experimental approach, an increase in total accelerated charge was achieved, producing bunches of $0.5\,\mathrm{nC}$ with energies up to $\sim 0.5\,\mathrm{GeV}$ [R2].

These improvements were only possible due to enhanced parameter control and direct feedback from diagnostics.

> *These high-quality electron bunches were a result of a higher degree of control of the laser and plasma parameters, an* **improvement of diagnostic techniques** *, [. . .]*
>
> Eric Esarey et al. (2009) in Reviews of Modern Physics [1]

However, the diagnostics of micrometer-femtosecond scale plasma dynamics in the laser wakefield accelerator is challenging. There are various direct measurements of the plasma cavity by probing the density fluctuations or magnetic fields with a second laser or electron bunch [19–22]. These setups provide valuable insight into the plasma dynamics but come with the drawback of requiring a reasonably good synchronization between pump and probe pulse. Additionally, the performance of LWFA can fluctuate significantly from shot to shot. Without intrinsic synchronization, those fluctuations render these diagnostic methods impossible for the analysis of every individual laser shot.

On the other hand, spectral methods based on plasma self-emission avoid these synchronization limitations and indirectly infer the phase space distribution of the electrons emitting radiation. Experimentalists perform such diagnostics based on self-emission commonly by measuring the so-called betatron radiation, emitted by the electrons accelerated in the plasma cavity, to deduce the bunch parameters [23–27]. However, the spectral analysis of the self-emission of the plasma electrons is seldomly applied to study the plasma wake or laser evolution. The broadband wave-breaking signature, that is emitted during electron self-injection into the plasma cavity, is an exception to this rule [28].

The advantages of self-emission include the possibility to be measured for every laser shot without being limited by varying levels of synchronization, and the absence of a probe source and delivery system. It requires only a detector system for the radiation. Ideally, as many diagnostic procedures as possible should be combined to obtain as much information as possible about the laser plasma dynamics for reconstruction.

This thesis focuses on studying the self-emission from laser wakefield accelerators. With the discovered correlations, we can show that besides wave breaking, the laser self-focusing can be diagnosed with emissions from the plasma. This enables an experimental feedback regarding the laser focusing which is especially useful for experimental setups that strongly rely on the non-linear process of self-focusing the laser pulse.

A detailed discussion of laser wakefield acceleration, self-emission from the plasma, and an exemplary use case with focus on experiments performed at HZDR are presented in chapter 6.

1.2 Observing plasma dynamics over astronomical distances

Even though our every-day experience might fool us into believing that the solid, fluid, and gaseous state of matter are the most common forms of matter, the plasma state - sometimes called the fourth state of matter - is by far more common in the universe. In fact, by far most of the visible matter of the universe is in the plasma state [3, 5]. Determining the plasma dynamics governing extraterrestrial objects is essential in understanding the latter. Developing models or performing simulations in order to study the plasma dynamics in extraterrestrial objects is, however, just one side of gaining understanding - a verification of the suspected plasma dynamics via observations is essential.

In astrophysical observations, not the short time scales of the dynamics are the issue that makes an analysis challenging, but the vast distances between the observer on Earth to the objects of interest. These large distances prevent resolving the plasma dynamics spatially. Therefore, analyzing the spectra of the emitted radiation is an essential tool for obtaining more information on the plasma dynamics.

Even if the plasma density in interstellar space is extremely low, the relevant plasma wavelengths are still not large enough to be resolved by telescopes. This characteristic length scale can be computed according to [3]

$$\lambda_{pe} = \frac{2\pi c}{\omega_{pe}} = 2\pi c \cdot \sqrt{\frac{\varepsilon_0 m_e}{n_e q_e^2}} \tag{1.3}$$

with q_e, m_e being the electron charge and mass, and ε_0 and c being the vacuum permittivity and the speed of light. Plasma density in interstellar space can take values as low as $n_e = 10^{-5}\mathrm{cm}^{-3}$[29] but the corresponding plasma wavelength is only in the order of $\lambda_{pe} \sim 10^4\,\mathrm{km} \sim 7 \cdot 10^{-5}\,\mathrm{AU}$. For objects light years away, these spatial scales cannot be resolved, even with the best telescopes available today.

One light year away, such a plasma oscillation would be visible at an angle of

$$\tan(\alpha) = \frac{\lambda_{pe}}{1\,\mathrm{ly}} \rightarrow \alpha \approx 0.2\,\mathrm{milliarcseconds} \quad . \tag{1.4}$$

In order to resolve these scales, an array of telescopes, also called an astronomical interferometer, would require a distance between individual telescopes, the so-called baseline B, of

$$\alpha = \frac{\lambda_{\mathrm{rad}}}{B} \quad . \tag{1.5}$$

For green light of wavelength $\lambda_{\mathrm{rad}} = 500\,\mathrm{nm}$, the baseline would need to be $B \approx 0.5\,\mathrm{km}$. The best optical telescopes, the Very Large Telescope (VLT) operated by the European Southern Observatory (EOS) in Chile, has a resolution of a few milliarcseconds [30–32]. For visible light, resolving the plasma dynamics spatially would currently not be possible.

In the radio-wavelength regime, where the telescopes are distributed over the entire globe, the reachable resolution by the Very Long Baseline Array (VLBA) is $\alpha \approx 0.3\,\mathrm{milliarcseconds}$ for a wavelength of $\lambda_{\mathrm{rad}} = 1\,\mathrm{cm}$ [33–35]. This only minimal increase in resolution comes from the fact, that while the baseline of the VLBA is over $B > 8000\,\mathrm{km}$, the longer wavelength compensates this. While the size of the Earth limits the resolution of radio telescopes, optical telescope arrays are limited by the optical fiber length required for the interferometry. Therefore, there will be no significant increase in resolution any time soon. The plasma phenomena are not spatially resolvable.

However, the plasma dynamics involves the acceleration of charged particles. This causes a constant emission of radiation that is characteristic of the plasma dynamics and that allows determining the state of the plasma.

For example, the plasma dynamics inside stars determines how energy generated in the center of the star via fission is transported to the surface, where it is emitted as radiation. The broadband thermal radiation allows determining the temperature of the star, while the absorption lines enable determining the composition and age of the star [36, 37].

The plasma dynamics in Jupiter's radiation belt is strongly influenced by the planet's rotation, the moon Io's volcano eruptions, the solar wind, and many more factors. The radio emission from this plasma trapped in the planet's magnetic field, therefore, reflects these influences [38–41].

The emitted radiation spectra thus reveal a lot about the plasma dynamics, even if the actual spatial scales cannot be resolved.

An unsolved and much-discussed topic in astrophysics is the emission of high-energetic particles from plasma jets ejected from accretion disks surrounding some massive objects like black holes [42–44]. One of the more famous of these jets is in the center of the crab nebular depicted in Fig. 1.2.

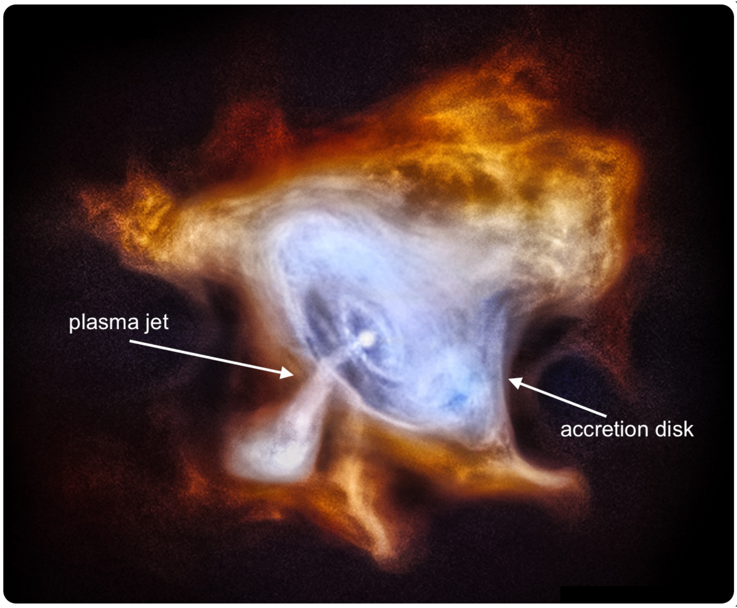

Figure 1.2: **X-ray image of the crab nebula:** This image, taken by the Chandra X-ray Observatory, of the crab nebula (also known as NGC 1952), shows clearly the plasma jet emitted by the center of the supernova remnant. The color code represents different X-ray energies: red means $0.5 - 1.2\,\mathrm{keV}$, green[2]represents $1.2 - 2.0\,\mathrm{keV}$, and blue means $2.0 - 7.0\,\mathrm{keV}$. This image was provided by NASA/CXC/SAO [45].

These jets are the origin of high-energetic particles that can be detected on Earth. Measurements have shown, that these jets contain strong magnetic fields that possibly play an important role in the jet's structure [29, 46–50]. Even though the magnetic fields are not the sole cause of the particle acceleration, they are vital in understanding the plasma dynamics of these jets which determine the environment under which these extreme accelerations occur. In order to understand the acceleration process, the jets themselves need to be understood.

There are a variety of possible plasma instabilities that can lead to the strong magnetic fields observed in these jets. For example, magnetic fields could be generated by the Weibel instability [3, 51, 52] or the Kelvin-Helmholtz instability (KHI) [53, 54]. Recent theoretical studies have shown that the KHI poses the most likely candidate for causing the magnetic fields since its

---

[2] This is an RGB color space, thus yellow in the picture is a combination of red and green while white is a combination of all three colors.

growth rate is higher than that of competing instabilities [29, 55].

Due to the high relevance of KHI in relation to astrophysical plasma jets, investigating the KHI emissions both theoretically and with simulations is a worthwhile research objective. Our research group performed a large-scale simulation of this plasma instability [R1, R3]. To this day, this is the largest simulation with the highest resolution of a KHI in the relativistic regime. In addition to the plasma dynamics, we also calculated the emitted radiation spectra for various observation directions. In parallel, a model of the KHI Vortex emissions was developed [R4]. Compared with the simulation, we could show that the model's predictions allow identifying the KHI by changes in polarization and quantifying the characteristic growth rate by measuring the change in radiation intensity over time.

Identifying the KHI in interstellar jets and determining its growth will hopefully bring more clarity to the dynamics of these giant plasma jets and perhaps pave the way to understand the acceleration mechanism behind them.

A detailed discussion of the theory behind the KHI in general, the developed emission model, the results of the large-scale simulation, and applications to both astrophysical observation as well as lab-astrophysics experiments can be found in chapter 7.

1.3 Challenges of an in-situ radiation simulation

Even if it seems easy to calculate the radiated radiation on the basis of a plasma simulation, this is an enormous challenge from a computational point of view. The two examples presented above describe a non-linear plasma dynamics in which the kinetic treatment of the particles is relevant. For such conditions, it is necessary to use particle-in-cell simulations. These codes are considered to be very computationally demanding and simulations with them are usually performed on very large computer clusters. Especially when it comes to simulating large volumes with high resolution in three dimensions, particle-in-cell simulations can only be performed on the world's largest computer clusters. By adding an in-situ radiation calculation, the computational effort is approximately increased twentyfold [R1]. Therefore, the simulations presented in this thesis took up to 10 months to be completed (the LWFA simulation from chapter 6) or days on the entire TITAN cluster, the world's largest cluster at that time (the KHI simulation from chapter 7). Consequently, the mere execution of such large-scale simulations is an immense effort - not to mention the following data analysis.

Throughout this thesis, it will be demonstrated that the unique opportunity to connect the microscopic plasma dynamics directly with the macroscopic radiation is worth this computational effort. The complex particle dynamics in the two previous examples prevent a self-contained analytical description [56, 57]. Hence, these simulations represent on the one hand an explorative approach to find connections between plasma dynamics and radiation spectra. Simple models can then be derived from these links, which necessarily neglect much of the complex dynamics. On the other hand, these models can be tested again against radiation simulations. This also allows determining the limitations of the models intrinsically, for example, the signal's contrast against background radiation. Such estimates are only possible to a limited degree in analytical models.

This makes radiation simulations a valuable tool for predicting possible spectral diagnostic methods in experiments or astrophysical observations.

2 Classical radiation emission

If a charge is accelerated due to external forces, it emits electromagnetic radiation. This can be easily illustrated. Let a point-like charge be at rest. The strength of the electric field surrounding it decreases with the inverse square of the distance in all directions. This is described by Coulomb's law $\left|\vec{E}\right| = \frac{|q_e|}{4\pi\varepsilon_0} \cdot \frac{1}{r^2}$ and illustrated on the left side of Fig. 2.1. Now, let a charge move with constant velocity. There exists a frame of reference, where the charge is at rest and where Coulomb's law holds true. The electric field in the original frame of reference is Lorentz-contracted in the direction of flight [58] and increased in magnitude by the contraction factor. This is illustrated in the center of Fig. 2.1. In either case, the field follows the motion of the particle - as if it were *attached* to the charge.

However, a field of a charge undergoing acceleration, for example, an electron following a circular path, cannot be described by such an *attached* field. At a distance of $r > c/\omega$ away from the center of the circular motion with angular velocity ω, the electric field would need to propagate faster than the speed of light (Fig. 2.1 right). This, of course, is unphysical. The field starts to detach from the charge and to propagate away. It can be shown that part of this *detached* field has a non-vanishing energy distribution infinitely far away from the charge because its strength reduces only with the inverse of the distance $\sim {}^{1}\!/_{r}$ [59]. This represents the *radiation emitted*.

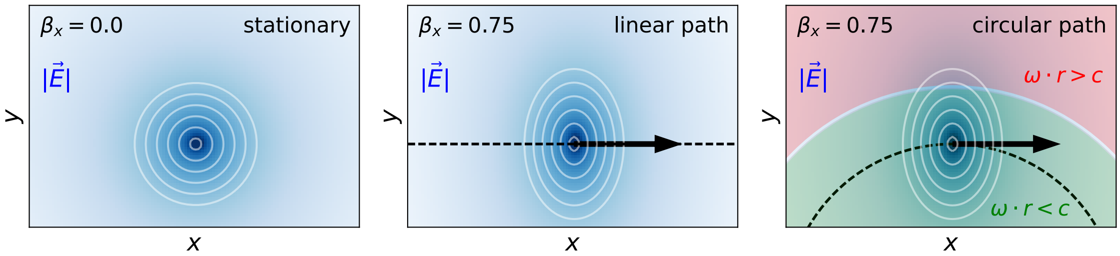

Figure 2.1: **Illustration of radiation emitted from accelerated charges:** The **left** picture illustrates a Coulomb field of a stationary charge. In the **center**, the Lorentz-contracted Coulomb field of a charge with constant velocity is shown. On the **right**, the cause for detached fields is illustrated. Starting from a charge on a circular and thus accelerated trajectory, the picture depicts a contracted Coulomb field as in the center case. The red colored patch at a radius $r > c/\omega$ marks the region where the field would need to travel faster than light. This is physically impossible and causes the fields to detach and radiate away [59].

2.1 The spectrally resolved Liénard-Wiechert potential

The electric and magnetic fields around a moving, point-like charge are described by the Liénard-Wiechert potentials [59]. In contrast to the Coulomb and Biot-Savart laws, the Liénard-Wiechert potential takes into account the relativistic retardation of the fields due to the finite speed of light. In the 3-vector notation, the Liénard-Wiechert potentials are

$$\Phi\left(\vec{r}, t\right) = \frac{1}{4\pi\varepsilon_0}\left[\frac{q}{(1-\vec{\beta}\cdot\vec{n})\,|\vec{r}-\vec{r}_e|}\right]_{\text{ret}} \tag{2.1}$$

$$\vec{A}(\vec{r}, t) = \frac{\mu_0}{4\pi}\left[\frac{q\cdot\vec{\beta}}{(1-\vec{\beta}\cdot\vec{n})\,|\vec{r}-\vec{r}_e|}\right]_{\text{ret}} \tag{2.2}$$

with $\vec{r}$ being the position in space where to evaluate the potentials, $\vec{r}_e$, q and β being the particle's position, charge and velocity normalized to the speed of light, and

$$\vec{n} = \frac{\vec{r}_e - \vec{r}}{|\vec{r}_e - \vec{r}|} \tag{2.3}$$

being the unit vector pointing from the charge towards $\vec{r}$. The bracket notation $[\ldots]_{\text{ret}}$ denotes that the included quantities are evaluated at a previous (retarded) time $t_{\text{ret}} = t - |\vec{r} - \vec{r}_e(t_{\text{ret}})|/c$ in order to take into account the finite speed of light. From this potential, the electric and magnetic fields can be derived by:

$$\vec{E} = -\vec{\nabla}\Phi - \frac{\partial\vec{A}}{\partial t} \tag{2.4}$$

$$\vec{B} = \vec{\nabla}\times\vec{A} \quad . \tag{2.5}$$

A detailed but lengthy analytical derivation of the electric and magnetic field from the Liénard-Wiechert potential can be found in [60]. Here, this detailed derivation is omitted and only the most important results are briefly summarized. The derived electric and magnetic fields comprise one part that vanishes with the inverse of the distance $\vec{E} \sim [1/|\vec{r}-\vec{r}_e|]_{\text{ret}}$ and a part that vanishes faster. The part decreasing faster with the distance is called the *velocity term* (Eq. 2.7). The contribution decreasing with $\sim r^{-1}$ is proportional to the acceleration of the charge $\vec{E} \sim \left[\dot{\vec{\beta}}\right]_{\text{ret}}$ and thus is often called the *acceleration* or *radiation term* [59]:

$$\vec{E}(\vec{r}, t) = \vec{E}^{\text{vel}}(\vec{r}, t) + \vec{E}^{\text{acc}}(\vec{r}, t) \tag{2.6}$$

$$\vec{E}^{\text{vel}} = \frac{q}{4\pi\varepsilon_0}\cdot\left[\frac{\vec{n}-\vec{\beta}}{|\vec{r}-\vec{r}_e|^2\,\gamma^2(1-\vec{\beta}\cdot\vec{n})^3}\right]_{\text{ret}} \tag{2.7}$$

$$\vec{E}^{\text{acc}} = \frac{q}{4\pi\varepsilon_0 c}\cdot\left[\frac{\vec{n}\times\left[(\vec{n}-\vec{\beta})\times\dot{\vec{\beta}}\right]}{|\vec{r}-\vec{r}_e|\,(1-\vec{\beta}\cdot\vec{n})^3}\right]_{\text{ret}} \quad . \tag{2.8}$$

By using the Poynting vector $\vec{S} = \frac{1}{\mu_0}\vec{E}\times\vec{B} = \frac{1}{\mu_0 c}E^2\vec{n}$, which describes the instantaneous energy flux in the direction $\vec{n}$, the radiation power P emitted per differential unit solid angle $\mathrm{d}\Omega$ can be described in terms of the emitted electric field [59]:

$$\frac{\mathrm{d}P}{\mathrm{d}\Omega} = \frac{1}{c\mu_0}\left|R\cdot\vec{E}\right|^2 \tag{2.9}$$

with $R = |\vec{r}-\vec{r}_e|$. Since for the above-mentioned acceleration term (Eq. 2.8), $\mathrm{d}P/\mathrm{d}\Omega$ does not depend on the distance of the observer R, its contribution to the emitted power does not vanish for an observer far away ($R \to \infty$). By integrating the power per solid angle over time, one obtains the total emitted energy. By additionally transferring the electric field into the Fourier space, one gets the spectrally-resolved emitted radiation energy per unit solid angle[3] for a single electron

$$\frac{\mathrm{d}^2 W}{\mathrm{d}\,\Omega\,\mathrm{d}\,\omega} = \frac{q^2}{16\pi^3\varepsilon_0 c} \left| \int_{-\infty}^{+\infty} \frac{\vec{n} \times \left[\left(\vec{n} - \vec{\beta} \right) \times \dot{\vec{\beta}} \right]}{\left(1 - \vec{\beta} \cdot \vec{n} \right)^2} \cdot \mathrm{e}^{\mathrm{i}\omega(t - \vec{n}\cdot\vec{r}(t)/c)}\,\mathrm{d}\,t \right|^2 \quad . \tag{2.10}$$

A step-by-step derivation of this equation can be found in [59] or [61]. For a given electron trajectory $\vec{r}_e(t)$, this equation allows computing the spectrally resolved energy for a given frequency ω and observation direction $\vec{n}$. This equation is valid for observers far away from the electron trajectory: $R \to \infty$. For practical purposes, detectors meters away from the laser plasma interaction can be considered infinitely far away from the micrometer scale electron dynamics. The same approximation holds true for observations of astronomical objects light years away.

The vector contribution inside the absolute square

$$\vec{n} \times \left[\left(\vec{n} - \vec{\beta} \right) \times \dot{\vec{\beta}} \right] \parallel \vec{E}^{\mathrm{acc}}(t) \tag{2.11}$$

is parallel to the emitted electric field. It is, therefore, proportional to the instantaneous polarization vector of the emitted radiation. If one is interested in radiation only polarized in a certain direction, defined by the unit vector $\vec{P}$, the scalar product with this unit vector should be taken before calculating the absolute square.

2.2 Correlation between phase space and radiation

A frequently used form of equation 2.10, achieved by means of partial integration, is [59]

$$\frac{\mathrm{d}^2 W}{\mathrm{d}\,\Omega\,\mathrm{d}\,\omega} = \frac{q^2\omega^2}{16\pi^3\varepsilon_0 c} \left| \int_{-\infty}^{+\infty} \vec{n} \times \left(\vec{n} \times \vec{\beta} \right) \cdot \mathrm{e}^{\mathrm{i}\omega(t - \vec{n}\cdot\vec{r}(t)/c)}\,\mathrm{d}\,t \right|^2 \quad . \tag{2.12}$$

The details of this reformulation, especially with the regard to the integration limits and the cancellation of regions with constant velocity, is given in [59]. Due to its simplicity, this equation is commonly used in analytical derivations. For numerical integrations with floating point numbers, however, this equation is more error-prone than equation 2.10 [61] since it requires a precise addition of varying velocities which mostly cancel out. Small numerical errors during the addition already lead to significant deviations. Thus equation 2.12 is not used in the implementations presented here.

For particles that move slowly compared to the speed of light $\beta \ll 1$, the influence of the position in the exponent can be neglected $t - \vec{n} \cdot \vec{r}(t)/c \to t$. Based on this assumption, Eq. 2.12 transforms into the absolute square of the Fourier transform of $\vec{n} \times (\vec{n} \times \vec{\beta})$ times the frequency squared.

$$\begin{aligned} \frac{\mathrm{d}^2 W}{\mathrm{d}\,\Omega\,\mathrm{d}\,\omega} &= \frac{q^2\omega^2}{16\pi^3\varepsilon_0 c} \left| \int_{-\infty}^{+\infty} \vec{n} \times \left(\vec{n} \times \vec{\beta} \right) \cdot \mathrm{e}^{\mathrm{i}\omega t}\,\mathrm{d}\,t \right|^2 && (2.13) \\ &= \frac{q^2\omega^2}{16\pi^3\varepsilon_0 c} \left| \mathcal{F}\left(\vec{n} \times \left(\vec{n} \times \vec{\beta} \right) \right) \right|^2 \quad . && (2.14) \end{aligned}$$

---

[3] In order to avoid confusion, this text does not follow the standard notation for energy "*I*" used in [59] but instead uses "*W*" to avoid confusion with standard symbols for intensity or electric current.

Due to the missing phase information in $\mathrm{d}^2W/\mathrm{d}\Omega\mathrm{d}\omega$, an unambiguous reconstruction of the velocity $\vec{\beta}(t)$ is in general impossible, but in practical use cases physically relevant information can still be obtained from the radiation spectra. In many diagnostic applications, the phase information is lost during intensity recording as well and yet valuable information about the emitter can be obtained. Furthermore, phase retrieval algorithms exist that are capable of reconstructing the phase [R5, 62]. For the applications presented in this thesis, however, a phase reconstruction was not needed to gain information on the plasma.

Another important question is whether the choice of observation direction will result in a loss of information that would make a reconstruction of the velocity $\vec{\beta}$ impossible. This is definitely the case for a single observation direction. For example, changes in velocity along the observation direction could not be retrieved, as no radiation is emitted in the direction of flight. But with enough observation points, a motion in any direction can be reconstructed, as will be motivated below for sub-relativistic particle motion:

Let us assume an arbitrary particle motion $\vec{\beta}(t)$ observed in directions parallel to the base vectors of the physical space $\vec{n}_i = \vec{e}_i$ with $i \in \{x, y, z\}$. Using vector identities, the radiation spectra for each observation direction can be derived:

$$\frac{\mathrm{d}^2 W}{\mathrm{d}\,\Omega\,\mathrm{d}\,\omega}(\vec{n}_i) = \frac{q^2\omega^2}{16\pi^3\varepsilon_0 c} \sum_{k\in\{x,y,z\}} (1-\delta_{ik}) \cdot |\mathcal{F}(\beta_k)|^2 \tag{2.15}$$

with δ_{ik} being the Kronecker delta and β_k being the k^{th} component of the velocity vector $\vec{\beta}$. The spectra contain information on motion perpendicular to the observation direction. With the three spectra, this allows determining the absolute square of the Fourier transform for any component.

$$|\mathcal{F}(\beta_k)|^2 = \frac{8\pi^3\varepsilon_0 c}{q^2\omega^2} \sum_{i\in\{x,y,z\}} (1-2\delta_{ik}) \cdot \frac{\mathrm{d}^2 W}{\mathrm{d}\,\Omega\,\mathrm{d}\,\omega}(\vec{n}_i) \tag{2.16}$$

The absolute square of a Fourier-transformed velocity component is proportional to the sum of the spectra perpendicular minus the spectrum parallel to this component. Although an exact velocity evolution $\vec{\beta}(t)$ cannot directly be reconstructed from the absolute squares of the Fourier transformed velocities, these "spectra" contain information about periodic motions of the particle and thus provide valuable information on the particle's dynamics. Periodic movements, in particular, are easy to identify.

In the relativistic case, the changing particle position must be taken into account within the phase of the exponential function (Eq. 2.12). This makes analysis slightly more difficult. The change in the phase leads to a shift in frequency. If the particle moves towards the observer, the retarded time passes more slowly causing an effective blue shift of the emitted radiation. Conversely, the radiation is redshifted when the particle moves away from the observer.

The frequency shift comes also with an advantage. The directional dependence of the frequency shift can be used to determine the direction of the trajectory of the particle. And, the velocity of the scattering particle can be determined based on the frequency shift of a known excitation frequency. A more detailed explanation of how to determine the velocity and direction of electrons based on scattered radiation from a known laser field can be found in section 6.3. As in the non-relativistic case, a large amount of information about particle motion can be obtained from a sufficient number of observation points. The more observation points are recorded, the more precisely the direction and speed of the particle motion can be determined. This reconstruction of electron properties is already applied today in the scattering of relativistic electrons from laser pulses and represents a promising diagnostic method [R6].

2.3 Simplifying the equation: Synchrotron radiation

Equation 2.10 is the most general form of determining the classical radiation spectra for a charged particle observed in an arbitrary direction. As long as the trajectory used during the integration describes a physically correct particle motion, the emitted radiation can be determined. This includes the scattering of radiation from an electromagnetic wave which interacts with the particle - the so-called Thomson scattering, the radiation caused by the gyration of the particle in a magnetic field - the so-called Synchrotron radiation, and a variety of other forms of emission without specific names.

However, the integration required for this general method is quite complex and laborious. A possible simplification is to assume that only instantaneous radiation is relevant and that these instantaneous spectra can be added for consecutive time steps.

For highly relativistic particles, it can be shown that the radiation under any acceleration is identical to the radiation of the particle at a constant speed on a circular path [59]. In the extreme relativistic case, instantaneous radiation is identical to synchrotron radiation. Most of the radiation is emitted in a searchlight cone of opening angle $\theta \lessapprox \gamma^{-1}$. Emitted radiation will therefore not interfere with previously emitted radiation if the pointing of the particle changes strongly compared to this opening angle. In such a case, the assumption of independent emissions becomes plausible.

Assuming that the movement of the particle is circular with a bending radius of ρ and only emissions are considered at a small angle with respect to the current velocity, a general description of synchrotron radiation can be derived [59]:

$$\frac{\mathrm{d}^2 W}{\mathrm{d}\omega \mathrm{d}\Omega}^{\text{sync}} = \frac{q^2}{12\pi^3 \varepsilon_0 c} \cdot \left(\frac{\omega\rho}{c}\right)^2 \cdot \left(\gamma^{-2} + \theta^2\right)^2 \cdot \left[K^2_{2/3}(\xi) + \frac{\theta^2}{\gamma^{-2} + \theta^2} K^2_{1/3}(\xi)\right] \tag{2.17}$$

with $K_{1/3}$ and $K_{2/3}$ being modified Bessel functions of the second kind, θ being the angle between $\vec{n}$ and $\vec{\beta}$, and

$$\xi = \frac{\omega\rho}{3c} \left(\gamma^{-2} + \theta^2\right)^{3/2} \tag{2.18}$$

being a parameter to normalize the frequency. Since the spectrum depends only on the normalized frequency ξ, the synchrotron spectrum has the same shape regardless of the particle's energy.

The shape of this spectrum depends only on the radius ρ. Assuming that there is only a magnetic field $\vec{B}$, the radius of curvature would be:

$$\rho = \frac{m \cdot \gamma \cdot \beta^2 \cdot c}{q \left|\vec{\beta} \times \vec{B}\right|} \tag{2.19}$$

with γ being the particle's Lorentz factor and m being its mass. The spectrum thus contains information about the velocity of the emitting particle and its acceleration or surrounding electromagnetic fields. Since the time integration in this model only covers an infinitely short period of time, all information about the long-term dynamics of the particle in the spectrum is lost.

The polarization of the synchrotron radiation additionally allows determining the orientation of the path curvature. From the total radiated energy, $7/8$ is emitted with a polarization parallel to the plane of the trajectory ($\vec{P} \parallel \vec{\beta} \times \vec{B}$) and only $1/8$ perpendicular to it ($\vec{P} \parallel \vec{B}$) [59].

To obtain the spectrum after a finite time, the synchrotron spectrum must be integrated over time.

$$\frac{\mathrm{d}^2 W}{\mathrm{d}\omega \mathrm{d}\Omega} = \frac{1}{t_b - t_a} \int_{t_a}^{t_b} \mathrm{d}t \frac{\mathrm{d}^2 W}{\mathrm{d}\omega \mathrm{d}\Omega}^{\text{sync}} (t) \tag{2.20}$$

As mentioned above, this approach of an averaged synchrotron spectrum cannot provide information on long-term particle dynamics, e.g., periodic motion.

The use of synchrotron radiation as a model of radiation is only applicable in exceptional cases since this approximation is only valid for high-energy particles and particle dynamics on timescales shorter than $t \lesssim \beta c / \rho$ [59]. Nevertheless, this approach significantly reduces the computing effort. Therefore it is also used in some plasma simulations [63, 64]. However, the synchrotron model's validity is limited to synchrotron-like radiation such as betatron radiation from the electron bunch in an LWFA. Scattered laser light, as produced by LWFAs and Thomson light sources, cannot be quantitatively described.

The more general Liénard-Wiechert method is a superset which also can be applied to the synchrotron case. Therefore, only this more general approach is used for the calculations presented in this thesis.

2.4 Extension to include multiple particles

Often, predicting or measuring the radiation of a single particle is not sufficient to make predictions for a system of many particles. In this case, the radiation emitted by several charges must be determined. In order to calculate the radiation of several charged particles, the phase relationship of all emitters must be taken into account. The most general approach to do this is to add all complex amplitudes for all particles before the absolute square is formed [59]:

$$\frac{\mathrm{d}^2 W}{\mathrm{d}\,\Omega\,\mathrm{d}\,\omega} = \frac{1}{16\pi^3 \varepsilon_0 c} \left| \sum_{k=1}^{N_p} \int_{-\infty}^{+\infty} q_k \cdot \frac{\vec{n} \times \left[\left(\vec{n} - \vec{\beta}_k \right) \times \dot{\vec{\beta}}_k \right]}{\left(1 - \vec{\beta}_k \cdot \vec{n} \right)^2} \cdot \mathrm{e}^{\mathrm{i}\omega (t - \vec{n} \cdot \vec{r}_k(t)/c)} \,\mathrm{d}\,t \right|^2 \tag{2.21}$$

with the index k denoting an attribute of the k^{th} particle. The consideration of the phase allows calculating both phase-matching coherent radiation and incoherent radiation with a random phase relationship between the emitters.

A common case is that the radiation is incoherent. This can be calculated with equation 2.21, but due to the more or less randomly distributed phase-relation, there are strong intensity variations in the spectrum. These fluctuations can be avoided by not considering the phase relation at all and by assuming incoherent radiation directly. For this purpose, it is no longer necessary to take the phase into account when summing over all particles and the sum can be determined after the absolute squares have been calculated.

$$\frac{\mathrm{d}^2 W}{\mathrm{d}\,\Omega\,\mathrm{d}\,\omega} = \frac{1}{16\pi^3 \varepsilon_0 c} \sum_{k=1}^{N_p} q_k^2 \cdot \left| \int_{-\infty}^{+\infty} \frac{\vec{n} \times \left[\left(\vec{n} - \vec{\beta}_k \right) \times \dot{\vec{\beta}}_k \right]}{\left(1 - \vec{\beta}_k \cdot \vec{n} \right)^2} \cdot \mathrm{e}^{\mathrm{i}\omega (t - \vec{n} \cdot \vec{r}_k(t)/c)} \,\mathrm{d}\,t \right|^2 \tag{2.22}$$

An obvious difference between the two approaches is that for particles with equal phase, equation 2.21 scales with the square of the number of all particles $\sim N_p^2$, while equation 2.22 scales only linearly with the number $\sim N_p$.

Another possibility to determine the radiation of many particles is the calculation of the radiation from mean fields. As is common in fluid mechanics and magnetohydrodynamic descriptions of plasmas, a system of particles can also be described by fields. The radiation can be calculated from the current density $\vec{J}(\vec{r})$ as follows:

$$\frac{\mathrm{d}^2 W}{\mathrm{d}\,\Omega\,\mathrm{d}\,\omega} = \frac{q^2 \omega^2}{16\pi^3 \varepsilon_0 c^3} \left| \int_{-\infty}^{+\infty} \mathrm{d}\,t \iiint \mathrm{d}^3 r \; \vec{n} \times \left(\vec{n} \times \vec{J}(\vec{r}, t) \right) \cdot \mathrm{e}^{\mathrm{i}\omega (t - \vec{n} \cdot \vec{r}/c)} \right|^2 \quad . \tag{2.23}$$

Here $\vec{r}$ denotes any position in space and not the position of a specific particle.

The obvious disadvantage of this method is that counter-propagating currents, whose total current disappears, do not radiate according to the equation. Furthermore, this fluid approach cannot predict a relativistic red or blue shift and is therefore useless in relativistic scenarios.

In all cases, the radiation from all particles is combined in the spectrum. This may mean that certain radiation signatures may no longer be distinguished from the background radiation and can therefore not be used for the reconstruction of plasma dynamics. On the other hand, only the consideration of all particles makes it possible to estimate whether radiation signatures can be clearly identified against the expected background and can be used for diagnostic purposes. Therefore, it is absolutely necessary to calculate the radiation for all particles in order to make predictions for experiments.

2.5 Differences to quantum radiation

The formalisms for radiation calculations described above are, of course, only valid in the classical range and become incorrect for very high particle energies and field strengths. A generally valid description can only be achieved by a quantum electrodynamics (QED).

The erroneous differences between QED and classical description results from the per se decoupled field and particle dynamics in classical theory which leads to divergences in the solutions for point-like particles such as electrons. Furthermore, the classical description does not take into account the quantized character of electromagnetic fields in the form of photons, nor does it reflect the statistical aspect of quantum theory.

The most obvious contradiction occurs with regard to the maximum frequency emitted. Classically, it is possible to emit radiation at a frequency for which the photon energy

$$E_{\mathrm{phot}} = \hbar\omega \tag{2.24}$$

is greater than the electron energy

$$E_{\mathrm{phot}} > E_{\mathrm{elec}} = \gamma m_e c^2 \quad . \tag{2.25}$$

On the other hand, the QED correctly predicts that the emission spectrum above this forbidden energy range is zero.

The classical and quantum field theoretical predictions agree for low particle energies and field strengths. A measure of the QED effects can be determined with the quantum non-linearity parameter which can be expressed in the rest frame of the electron as the ratio between electric field strength and the Schwinger limit

$$\chi = \frac{E}{E_{\mathrm{S}}} \tag{2.26}$$

with $\hbar$ being the Planck constant and E_{S} being the Schwinger limit [65]

$$E_{\mathrm{S}} = \frac{m_e^2 c^3}{q_e \hbar} \simeq 1.32 \times 10^{18}\,\mathrm{V/m} \quad . \tag{2.27}$$

For $\chi \ll 1$, classic and QED description agree. In today's experiments, it is not yet possible to reach $\chi \gtrsim 1$ [66] .

For moving electrons, the Lorentz contraction of the electromagnetic fields has to be taken into account. But even in head-on scattering between laser pulses with $E_{\mathrm{L}} \approx 10^{13}\,{}^{\mathrm{V}}\!/\!{}_{\mathrm{m}}$ and electrons at GeV energies ($\gamma \approx 2000$), the χ parameter is below

$$\chi \approx \frac{2\gamma E_{\mathrm{L}}}{E_{\mathrm{S}}} \approx 0.03 \ll 1 \tag{2.28}$$

and thus well within the classical limit. Only with upcoming laser facilities in the multi-petawatt range, quantum-field effects will be relevant. The only effect that is important in some present-day experiments is the energy loss due to the emitted radiation, and this can also be taken into account classically as described in chapter 5. Thus all laser-plasma experiments that are feasible today can be described in classical terms.

Nevertheless, the question arises as to why not use the more general QED description to quantitatively model radiation emission. For the prediction of radiation from systems with a high number of emitters, only the coupling of the QED models to classical particle dynamics is computationally feasible. However, this combination comes with a number of drawbacks. For example, quantum-mechanical states must be translated into momentum eigenstates in order to transfer them to the classical picture. According to the Copenhagen interpretation, this is equivalent to a measurement that destroys the quantum nature of the state. Furthermore, due to the uncertainty principle $\Delta E \cdot \Delta t \geq \hbar/2$ the temporal duration Δt, after which one switches between the classical and quantum picture, only allows predictions for photons with frequencies well above

$$\omega = \frac{E_{\mathrm{phot}}}{\hbar} \gg \frac{\Delta E}{\hbar} \geq \frac{1}{2\Delta t} \quad . \tag{2.29}$$

For typical particle-in-cell simulations, this would be only valid for x-ray radiation and would exclude the highly important infrared, optical, and ultra-violet radiation. Due to these and various other limitations, radiation is calculated classically in this thesis. An extensive discussion of approximation errors of QED radiation in plasma simulations can be found in [65].

2.6 Summary

In this chapter, the classical calculation of directionally resolved radiation spectra on the basis of partial trajectories was presented. The correlation between particle dynamics and radiation spectrum was discussed in an exemplary manner. The possibility of reconstructing particle dynamics from the emitted spectra was explained. It was shown that particle dynamics and radiation spectrum are correlated. Especially for relativistic electrons, the directional dependence of the radiation allows obtaining valuable insights into the movement of the particles.

Some simplifications of the modeling were presented and their disadvantages examined. However, to cover all cases, using a synchrotron or fluid approximation is not enough, but the superset of the more general Liénard-Wiechert method is needed. Possible extensions of the radiation calculation to systems with several particles were demonstrated. Since radiation from all parts of the plasma might contribute to and overshadow a spectral signal, radiation calculation should consider all simulated particles to make quantitative predictions and to determine the signal-to-background ratio that is essential for detecting specific signals in real experiments.

Finally, the limits of the classical description of radiation and the transition to a quantum field theoretical description were investigated and the reasonability of the classical calculation in the context of the physical scenarios presented in this thesis was explained. For current and near future experiments, the influence of quantum corrections is negligible.

3 An introduction to simulating plasmas

There are various numerical methods to model plasma dynamics using computer simulations. A methodically straightforward approach would model each charged particle individually by calculating the force, induced by the electric and magnetic fields of all other particles, acting on it and then solving the equation of motion by numerically integrating the Lorentz force.

However, this leads to a tremendous calculation effort, which scales with the square of the number of modeled particles N^2, since the calculation of the force acting on a single particle requires considering the position of $N-1$ other charged particles. In total, this leads to $N \cdot (N-1)/2$ calculations of the Lorentz force. For relativistic particles, retardation also becomes a challenge, as the previous position of the individual particles must be considered. This so-called **molecular dynamics (MD)** approach is thus limited to small, microscopic systems with only a few billion particles [67].

Another common method for simulating the dynamics of plasmas is assuming the plasma to be in a local thermal equilibrium and applying macroscopic fluid equations for solving the dynamics [56]. However, the basic assumption of thermal equilibrium intrinsic to these **magnetohydrodynamic (MHD)** simulations is limited to scenarios where the particle velocities follow a Maxwell Boltzmann distribution. This prevents simulating states of plasma which do not follow a Maxwellian velocity distribution locally [68, 69], as for example the interaction of short-pulse lasers with matter [1, 2, 56] or the thermal diffusion during the Kelvin-Helmholtz instability [53, 70].

In order to describe arbitrary velocity distributions, a particle distribution function $f(\vec{r}, \vec{v})$ can be introduced, which correlates the position and the velocity distribution of all particles. For plasma particles, such a distribution function follows the Vlasov equation [71]:

$$\frac{\partial f}{\partial t} + \vec{v} \cdot \vec{\nabla} f + \frac{q}{m}\left(\vec{E} + \vec{v} \times \vec{B}\right) \cdot \frac{\partial f}{\partial \vec{v}} = 0 \quad . \tag{3.1}$$

This equation describes the change of the particle distribution f by electromagnetic fields and by the intrinsic particle motion itself. However, solving this equation is generally numerically intractable. Simplification is therefore used. Instead of solving for the distribution function f, one samples the distribution by macroparticles and solves their equation of motion. The charge and current densities[4] associated with these macroparticles are then used to update the electric and magnetic field by numerically solving Maxwell's equation. This process is repeated for each

---

[4] Modern algorithms only require considering the current density. See section 3.2 for details.

iteration time step. The aforementioned numeric approach is called the **particle-in-cell (PIC)** method and is the technique of choice in today's laser-plasma and astro-plasma simulations. The following section gives a brief introduction to the particle-in-cell method. This thesis will focus solely on plasma simulations based on particle-in-cell simulations using PIConGPU [R1, 72].

3.1 Fundamental aspects of the particle-in-cell algorithm

Today, particle-in-cell simulations [73–75] are the method of choice for modeling laser- or beam-controlled plasma accelerators [72, 75–79]. They are also increasingly used in astrophysical simulations of plasma instabilities [53, 80, 81]. The particle-in-cell algorithm solves the plasma dynamics by discretizing the electric and magnetic field on a lattice and letting the particles propagate freely through this grid. This allows calculating the plasma-particle motion self-consistently within their intrinsic and external electromagnetic fields.

It is instructive to briefly look at the computational challenges of the particle-in-cell method using an exemplary laser wakefield acceleration (LWFA) simulation. A common small simulation volume covers $(100\,\mu\mathrm{m})^3$ at typical plasma densities of $n_e = 10^{19}\,\mathrm{cm}^{-3}$. This would require tracking trillions of electrons, which is an enormous computational challenge. Fortunately, particles that are initially located close to each other in phase space follow a similar trajectory. The motion of several particles can thus be described by that of a single macroparticle if the plasma dynamics does not become chaotic. These macroparticles discretize the distribution function of the Vlasov equation f. They describe an ensemble of real particles by treating their discrete charges as a continuous charge distribution over a finite volume. In contrast to a complete solution of the Vlasov or Fokker-Planck equation, which permits a temporal evolution of the momentum distribution, the particle-in-cell algorithm describes each macroparticle only by a single momentum value. This simplification prevents the spatial growth of the macroparticles over time. Metaphorically speaking, this stops the particle cloud, which the macroparticle represents, from flying apart. The number of real particles represented by a macroparticle is generally referred to as weighting.

Starting conditions

Based on a charged particle- and a (physically correct) electromagnetic field distribution, the particle-in-cell algorithm enables simulating the plasma evolution over time. Such an initial configuration might be a neutral gas or a plasma without electromagnetic fields, where the unlikely - but physically correct - situation occurs where every negatively charged particle is located at the same position as another positively charged particle.

Step 1: force calculation

In a first step, the particle-in-cell algorithm interpolates for each macroparticle position the electric and magnetic field, whose values were defined on a lattice, to determine the force acting on each charged macroparticle. The spatial macroparticle distribution is taken into account by a so-called assignment function, which describes how field values on the lattice affect a macroparticle with a certain charge distribution [73]. The interpolated fields are then used to calculate the forces acting on the macroparticles.

During the first iteration after initialization without electromagnetic fields, no forces act on the macroparticles. But with further iterations of the PIC cycle, electromagnetic fields are generated which then act on the plasma particles. These fields are generated either by charge separation

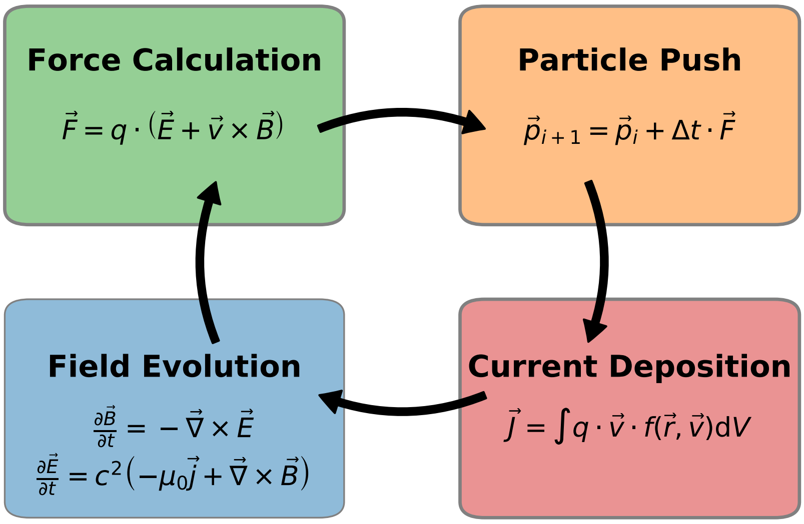

Figure 3.1: **Illustration of the particle-in-cell algorithm:** This diagram depicts the 4 steps of a particle-in-cell iteration. Starting from calculating the force acting on each macroparticle, the particles are moved according to this force. The moving charges cause a current. This current and the existing electromagnetic fields determine the evolution of the electric and magnetic field. These changed fields lead to altered forces on the particles, and the cycle recommences.

caused by the thermal movement of the simulated particles, or by the introduction of external fields such as a laser pulse.

Step 2: particle push

In a second step, the velocities and positions of the macroparticles are changed according to the acceleration caused by the Lorentz force (Eq. 3.2). A first-order scheme of such a particle push is described by the following equations.

$$\ddot{\vec{r}} = \frac{1}{m}\vec{F} = \frac{q}{m}\left(\vec{E} + \dot{\vec{r}}_i \times \vec{B}\right) \tag{3.2}$$

$$\dot{\vec{r}}_{i+1} = \dot{\vec{r}}_i + \Delta t \cdot \ddot{\vec{r}} \tag{3.3}$$

$$\vec{r}_{i+1} = \vec{r}_i + \Delta t \cdot \dot{\vec{r}}_i \tag{3.4}$$

However, this simple Euler method is rarely implemented in particle-in-cell algorithms, since its numerical error grows relatively fast with each time step. More sophisticated particle push algorithms are used, which on the one hand have a better numerical stability and on the other hand are not too expensive in their computational requirements, as they have to be performed for each macroparticle and at each time step.

This particle motion and the resulting charge separation lead to electromagnetic fields. These fields can be determined either by solving the Poisson equation or by calculating the electric current field caused by the moving charged particles and by subsequently integrating the Maxwell equation over time. Solving the Poisson equation is numerically costly. Hence it is more common in PIC codes to evaluate the current instead.

Step 3: current deposition

As with all other fields, the electric current is discretized and resolved on a grid. It is evaluated by calculating the influence of the motion of the charged particles on adjacent lattice points. The product of charge and velocity of the individual macroparticles is calculated and then aggregated to the adjacent grid points using the same assignment function as for the field interpolation. Performing this for all particles results in the discrete accumulated current density field $\vec{J}$.

Step 4: field evolution

According to the Maxwell's equation, this current density causes a change in the electric and thus magnetic fields.

$$\frac{\partial \vec{E}}{\partial t} = c^2 \left(-\mu_0 \vec{J} + \vec{\nabla} \times \vec{B}\right) \tag{3.5}$$

$$\frac{\partial \vec{B}}{\partial t} = -\vec{\nabla} \times \vec{E} \tag{3.6}$$

The numerical integration of these two equations determines the field values in the particle-in-cell subsequent iteration:

$$\vec{E}_{i+1} = \vec{E}_i + \Delta t \cdot c^2 \left(-\mu_0 \vec{J} + \vec{\nabla} \times \vec{B}_i\right) \tag{3.7}$$

$$\vec{B}_{i+1} = \vec{B}_i - \Delta t \cdot \vec{\nabla} \times \vec{E}_i \tag{3.8}$$

In these equations, the curl on the right represents the numerical spatial differentiation of the discrete field. Such a solution for the electromagnetic field is called a finite-difference-time-domain method (FDTD) and was introduced by Yee [82].

These four steps constitute a complete particle-in-cell iteration. After such a particle-in-cell cycle, the algorithm starts anew by interpolating the updated fields onto the macroparticles and determining the force acting on them, shifting these particles, determining the current, and finally calculating the field changes due to the current caused by the particle motion. A schematic of this cycle is depicted in Fig. 3.1. By repeating these particle-in-cell cycles, the plasma dynamics can be simulated over an extended time period.

Various constraints

One constraint of the particle-in-cell approach is that the finite grid resolution, inherent to the discretization of the fields, limits the minimal wavelength resolvable by the simulation. From the Nyquist-Shannon sampling theorem [83, 84], only wavelengths above $\lambda_{\text{min}} > 2 \cdot \Delta L$, with ΔL being the one-dimensional grid resolution, will be handled by the field solver algorithm. For laser-plasma interactions, there are two fundamental length scales that the grid needs to resolve: the plasma skin depth and the laser wavelength.

The plasma skin depth is the length scale on which the plasma reacts collectively to field changes. It is given by:

$$\lambda_{\text{pe}} = \frac{c}{\omega_{\text{pe}}} = \sqrt{\frac{c^2 \varepsilon_0 m_e}{n_e e^2}} \tag{3.9}$$

with ω_{pe} being the plasma frequency, n_e being the electron density and c, ε_0, e and m_e being the speed of light, permittivity of free space, the electron charge, and mass.

Similarly, the grid needs to resolve the laser wavelength. However, this requirement can be eased if the laser propagates along one grid axis. In such a case, a resolution smaller than the laser wavelength is only required in that specific grid direction. The grid points in the perpendicular directions can have a wider spacing. Their distance is limited by either the requirement of sampling the plasma skin depth or the laser transversal envelope. This of course only holds true if the laser wavelength is smaller than the plasma skin depth, which is true for so-called *underdense* plasmas. In such an underdense case, the cells are spaced at a fraction of around $1/10$ to $1/20$ of the laser wavelength along the laser propagation axis and up to an order of magnitude wider in the transversal directions. Such a non-cubic cell shape reduces the memory footprint of the lattice dramatically and is a typical approach for simulating laser wakefield acceleration, as discussed in detail in chapter 6. If the plasma skin depth is lower than the laser wavelength (so-called *over-critical* plasma densities) or if there is no laser simulated, the lattice usually consists of cubic cells. Such a plasma-only simulation is presented in chapter 7.

A limitation that relates the spatial with the temporal resolution of the field grid is the Courant-Friedrichs-Lewy (CFL) condition. This convergence criterion defines a maximal time step duration for the finite difference method as used by the FDTD field solver in the particle-in-cell algorithm [85]. For a three dimensional simulation, the CFL condition limits the time step to

$$\Delta t < \frac{1}{c} \cdot \left(\sqrt{\frac{1}{\Delta x^2} + \frac{1}{\Delta y^2} + \frac{1}{\Delta z^2}} \right)^{-1} , \tag{3.10}$$

as derived by Lam [86]. The minimum number of particle-in-cell iterations required to simulate plasma dynamics over a time duration of t_{sim} is therefore $N_{\mathrm{sim}} = \frac{t_{\mathrm{sim}}}{\Delta t}$. For laser wakefield setups, this can easily reach $100,000$ iterations, which requires long computation times. Intuitively one could assume that a reduction of the time step would improve the resolution of the plasma dynamics and lead to a better numerical convergence. But often the opposite is the case. Each iteration leads to a small numerical error in the solution due to the discrete spatial differentiation $\mathcal{O}(\Delta x)$ and the forward difference in the explicit time integration $\mathcal{O}(\Delta t)$. The error by the forward difference scales with the time step $\mathcal{O}(\Delta t) \sim \Delta t^2$ and the error by spatial differentiation scales depending on the order of the difference scheme with $\mathcal{O}(\Delta x) \sim \Delta x^p$ with $p > 2$. The total numerical error for N_{sim} iterations, therefore, scales as

$$\Delta_1^{\mathrm{total}} = N_{\mathrm{sim}} \cdot (c \cdot \mathcal{O}(\Delta t) + \mathcal{O}(\Delta x)) \ . \tag{3.11}$$

If only the time step is decreased by a factor $0 < r < 1$, the numerical error introduced by the finite time step reduces by r^2. Meanwhile, the numerical error introduced by spatial differentiation $\mathcal{O}(\Delta x)$ stays the same. Since the number of iterations required for the entire simulation increases by the inverse of r, the total numerical error for a reduced time step becomes:

$$\Delta_r^{\mathrm{total}} = \frac{N_{\mathrm{sim}}}{r} \cdot \left(r^2 \cdot c \cdot \mathcal{O}(\Delta t) + \mathcal{O}(\Delta x) \right) = N_{\mathrm{sim}} \left(r \cdot c \cdot \mathcal{O}(\Delta t) + \frac{\mathcal{O}(\Delta x)}{r} \right) . \tag{3.12}$$

This only leads to a reduction of the total error if $\mathcal{O}(\Delta x)/\mathcal{O}(\Delta t) < r < 1$, which is not necessarily fulfilled. Thus, decreasing exclusively the time step leads usually to a larger numerical error in the end. The best option is to operate close to the CFL condition. In order to reduce the total numerical error for a fixed simulation duration t_{sim}, it is necessary to reduce the error from the spatial differentiation as well.

However, if both the spatial and temporal resolutions are reduced by a factor of r, the numerical error is reduced but the computational effort increases as r^{n+1} for an n-dimensional simulation making such improvements numerically costly. Thus various numerical schemes were introduced to reduce the numerical error. A selection of these methods, relevant for the next chapters, is discussed briefly in the following section. This will not only cover improved methods for the FDTD solver but for the particle pusher and current-deposition schemes as well.

At this point, it should be noted that the maximum frequency that can be calculated with the synthetic radiation diagnostics in the particle-in-cell code PIConGPU [R1] is limited only by the duration of the time step Δt. The maximum determinable frequency of emitted radiation scales inversely with the time resolution $\omega_{\text{max}} \sim \Delta t^{-1}$. (A comprehensive discussion of the spectral resolution of the radiation calculation is presented in the section 4.1.) Decreasing Δt without reducing the spatial resolution is thus a reasonable option to increase the spectral resolution of the radiation simulations. However, the reduced accuracy of the FDTD method must be weighed against the increased spectral resolution.

3.2 Enhancements to the particle-in-cell algorithm

There is a broad variety of algorithms and optimizations that are used in particle-in-cell codes. These include fundamentally different algorithms, extensions to higher numerical orders, and implementations geared to utilize a specific hardware in an optimal manner. The purpose of this section is not to provide a thorough list of available methods but to briefly introduce algorithms used in the simulations presented in the following chapters. The focus is on a brief description of the advantages, disadvantages, and limitations of each method to provide the reader with sufficient information to follow the discussions in the subsequent chapters.

3.2.1 Particle Pusher

Boris pusher

The Boris algorithm solves the Newton-Lorentz equation of motion (Eq. 3.2) for relativistic charged particles by applying a leapfrog-like integration solver [87]. For a discretization time step Δt, position and momentum are defined $\Delta t/2$ apart. The algorithm treats the change in momentum due to the electric and magnetic field separately by applying first the electric field for half a time step, then computing the motion caused by the magnetic field for an averaged momentum, and finally applying the electric field again for another half time step. Compared to higher order schemes, this leapfrog approach has a relatively low computational footprint. It was recently proven that the Boris algorithm is not a symplectic integrator but shows a global bound on the energy error and conserves the phase space volume of the simulated particles at non-relativistic velocities [88–91]. This enables long-term plasma simulations with excellent accuracy. Both its accuracy and efficiency makes the Boris pusher a de facto standard in today's particle-in-cell simulations. However, recent studies show that with relativistic velocities the algorithm's phase space volume preservation and thus its accuracy vanishes [92].

Vay pusher

The Vay pusher is algorithmically similar to the Boris algorithm. It prevents a known issue of the Boris algorithm that causes a change of the particle velocity even for a vanishing Lorentz force $\vec{E} + \vec{v} \times \vec{B} = 0$ when the influence of the electric fields cancels the contribution of the magnetic field [93]. It does so by using an averaged velocity instead of an averaged momentum in the magnetic field calculation of the Boris algorithm. This provides more accurate results for relativistic particles and boosted-frame simulations.

Reduced Landau Lifshitz pusher

Both the Boris and the Vay algorithm are based on the Lorentz force. They do not take into account the radiation energy loss. Even though in most cases the energy loss due to radiation is much smaller than the total energy of the charged particles, $\Delta E \ll \gamma m_e c^2$, it is still important to consider these losses especially if one deals with scenarios where radiation emission is strong enough to be used as a diagnostic method. Part of this thesis was to implement the so-called reduced Landau-Lifshitz pusher developed by Maria Vranic [94] that solves the particle motion in electromagnetic fields and compensates for radiation losses. This algorithm is based on the Runge-Kutta method of 4th order and shows less long-term accuracy than the Boris algorithm. A detailed discussion of this pusher can be found in section 5.

3.2.2 Field Solver

Yee solver

The algorithm by Yee [82] is one of the most common methods to solve Maxwell's equation numerically not only for particle-in-cell codes but for a variety of problems in electrodynamics. It discretizes the electric and magnetic field on a staggered grid in such a way that the spatial derivatives introduced by the rotation (Eq. 3.5) can be calculated by the symmetric derivative quotient which is of second order and thus more precise than a simply asymmetric differentiation. The electric field components are defined to be located at the center of the grid edges while the magnetic field components are located in the center of the cell surfaces. No component is located at the same position in the cell. Additionally, the method of the symmetric derivative quotient is also applied to the time derivatives. Thus the electric and magnetic field values are defined half a time step apart. This has to be taken into account when combining the Yee solver with a particle pusher algorithm that requires the magnetic and electric field to be defined at the same time step. A required stability criterion for the Yee algorithm is the Courant-Friedrichs-Lewy (CFL) condition introduced earlier (Eq. 3.10), which limits the time step duration and thus requires a minimum number of iterations for a specific time period. Due to the discretization, the Yee algorithm results in a dispersion relation that flattens towards higher k values, causing the phase velocity to take values below the speed of light $v_\phi = \frac{\omega}{k} < c$. In combination with freely moving macroparticles, fast particles in a particle-in-cell simulation become relativistic and can overtake specific modes, and so-called *numerical Cherenkov* radiation is created [95]. In laser wakefield acceleration simulations, this causes higher beam emittance values for accelerated electron bunches [96]. This numerical dispersion relation also slightly reduces the simulated speed of (laser) light in vacuum because the group velocity is below the speed of light $v_{\text{group}} = \frac{\partial \omega}{\partial k} < c$.

Lehe solver

The issue of generating numerical Cherenkov radiation is solved by the algorithm of Lehe [96]. It alters the dispersion relation by changing the numerical differentiation introduced by the curl (Eq. 3.5) in such a way that the phase velocity is higher than the actual vacuum phase velocity $v_\phi = \frac{\omega}{k} > c$. Thus numerical Cherenkov is largely avoided in one direction. A side effect of this approach is a slightly higher velocity of (laser) light because, in contrast to the algorithm by Yee, the group velocity becomes larger than the speed of light $v_{\text{group}} = \frac{\partial \omega}{\partial k} > c$. In order to be numerically accurate, the Lehe solver has several requirements on the grid resolution which include resolving the laser wavelength well enough while not choosing a time step much smaller than $\Delta t \leq {}^{\Delta x}/_{c}$ if x is the laser propagation direction. Additionally, this solver causes numeric noise near the Nyquist frequency that causes numerical artifacts, especially when simulating large amounts of charge at relativistic velocities. These artifacts can be avoided by filtering out high-frequency contributions near the Nyquist frequency.

3.2.3 Current deposition schemes

Villasenor and Buneman current deposition scheme

Previous to the work of Morse and Nielson in 1971 [97], which was extended to non-square-like cells and 3 dimensions by Villasenor and Buneman in 1992 [98], calculating the electric and magnetic field required either a global operation on the entire simulation domain for each time step in form of a Poisson solver [73] or updating the electromagnetic fields according to the method of Yee [82] (Eq. 3.7) with a local but not charge-conserving current calculation. While the global operation of solving Poisson's equation fulfills Gauss' law $\vec{\nabla} \cdot \vec{E} = \frac{\rho}{\varepsilon_0}$, it requires taking into account the entire charge density ρ. This global data access represents the computational bottleneck of a Poisson solver, limiting efficient parallel calculation of spatially extended simulation volumes. In contrast, a local current computation requires just local charge motion and thus can easily be distributed among numerous computers, but it does not necessarily fulfill Gauss's law. Villasenor and Buneman solved this by describing the macroparticles as box-like homogeneous charge distributions and assuming a linear motion of these boxes between two time-steps. The current is discretized onto a staggered grid as proposed by Yee [82] by computing the change of this box-like charge distribution between all neighboring cells before and after the change of the macroparticle position. This is equivalent to the charge crossing at each cell boundary and rigorously ensures charge conservation.

Esirkepov current deposition scheme

A major drawback of the scheme proposed by Villasenor and Buneman is the requirement that the macroparticle charge distribution needs to be equivalent to the cell shape. This simple box shape causes numerical noise [99] that can only be reduced by using smoother, higher-order particle shapes (see the following paragraph for more details). In 2001, Esirkepov [100] extended the method of Villasenor and Buneman to arbitrary macroparticle charge distributions. This enabled reducing the numeric noise by using higher-order form factors. Today, the method developed by Esirkepov is the current deposition scheme of choice in various particle-in-cell codes. Throughout this thesis, all simulations that took currents into account were performed using this current deposition scheme.

3.2.4 Higher order particle shapes

As stated in the introduction, the particle-in-cell algorithm samples the particle distribution function of the Vlasov equation (Eq. 3.1). While the sampling in velocity space has to be a δ-distribution to avoid a diffusion of the sample particle, the macroparticle can have a spatial extent. The macroparticle's spatial extent is usually chosen such that the numeric integration in the context of the grid on which the electric and magnetic field is defined becomes easier to handle [73]. Thus typical particle shapes are point-like particles, particles with a homogeneous charge density of the same extent as the cell, called cloud-in-cell (CIC) shape, and shapes that extend to even more surrounding grid points (see [73] for a detailed derivation and discussion). Higher-order particle shapes are in general numerically more stable and reduce a numerical noise in the current deposition and consequently in the electromagnetic fields. However, they are also computationally more costly. In the context of this thesis, it is important to keep in mind that while the particle-in-cell code treats these shapes as continuous density distributions the discrete nature of the electrons actually described by these macroparticles needs to be taken into account when calculating the radiation. Otherwise, quantitative predictions cannot be derived (see section 4.3).

3.3 In-situ data analysis in PIConGPU

Simulating the plasma dynamics with a particle-in-cell code is not enough - at some point, physically meaningful data need to be extracted from the simulation. This leads to the question whether data can be stored during the simulation and analyzed afterward, the so-called post-processing approach, or if the data analysis has to be part of the simulation itself, the so-called in-situ approach.

In order to get a first idea on which kind of approach should be taken, let us have look at an exemplary laser-wakefield simulation. Let us assume the setup is moderately sized and requires $256 \times 1024 \times 256$ cells and a single macroparticle per cell to represent the plasma density. Such a setup uses 67 million cells and particles. Each cell provides a magnetic and electric vector field sample. These are in the case of PIConGPU represented by a single precision floating-point number per component. Each cell thus needs to store 6 float values of 4 bytes each resulting in a total of 1.5 Gigabyte. A macroparticle needs minimally the attributes: position, momentum, and weighting. These two vector and one scalar quantities define a minimal memory footprint of a macroparticle of 28 bytes. The ensemble of all macroparticles of this exemplary simulation requires 1.75 Gigabyte. For each iteration step, describing the simulation state requires 3.25 Gigabyte. Resolving a laser of $\lambda_0 = 800\,\mathrm{nm}$ needs a spatial resolution of approximately $\Delta x \approx {}^{\lambda_0}/_{10} = 80\,\mathrm{nm}$. The CFL condition limits the time step to be

$$\Delta t \lesssim \frac{\Delta x}{c} = 0.27\,\mathrm{fs}\ . \tag{3.13}$$

This approximation of the CFL condition assumes an asymmetric cell with a much shorter edge length Δx in laser propagation direction. For a laser moving just $L = 1\,\mathrm{mm}$ in a co-moving simulation box through the plasma, $\Delta tcdot{}^{L}/_{c} \approx 10,000$ time steps are required for simulating the laser propagation. Storing every simulation time step on disk would not only require 32 Terabyte of disk space but would also massively increase the simulation duration due to limited writing speed of the file system. Storing all available simulation data once a while is easily possible, but storing the data for all time steps is not feasible.

PIConGPU provides so-called plug-in methods that perform data analysis while the simulation is running. These plug-in methods read the simulation data in the random access memory (RAM) directly and then store only derived results, which are much smaller than the original data, on disk. This reduced memory footprint allows performing a specific data analysis at a much higher frequency than feasible with complete data output and post-processing analysis. Such plug-ins provide for example the total energy of all particles and fields, the energy distribution, or a phase space histogram of the particles.

Furthermore, the in-situ data analysis not only provides direct access to the data in the RAM of the compute units (usually CPUs or GPUs), it also allows utilizing the computing hardware for computations directly. Thus even computationally expensive data analysis, which for a post-processing analysis would require using many compute nodes, can be done directly within the running simulation with the hardware available to the simulation itself.

One extreme case of such data analysis is computing the far field radiation since this requires both accessing the entire particle data for every iteration step and performing complex computations. Performing far-field radiation calculation on the entire ensemble of macroparticles thus could so far only be accomplished with the in-situ approach[5].

A brief description of this plug-in is given in the next chapter. More details on this plug-in and its implementation can be found in [61].

3.4 Summary

In this chapter, various methods to simulate plasma dynamics were briefly introduced. With regard to this work, the functionality of the particle-in-cell algorithm was described in more detail. The four steps of the algorithms were depicted with regard to their physical representation and without many details of the technical implementation of a software algorithm. Various algorithms regarding particle motion, electromagnetic field evolution, and current computation were briefly discussed. The focus of this review was on the physical conservation laws and limitations, not on the computational performance. All plasma physics cases discussed in this thesis require using high-performance computer clusters (HPC) in order to solve the plasma dynamics. Hence using and developing efficient and parallelizable algorithms was essential for performing all the plasma simulations presented in this work.

Furthermore, the necessity of performing complex data analysis with the simulation as a so-called in-situ analysis while the simulation is running was demonstrated. The plug-in method to build various synthetic diagnostic tools in the particle-in-cell code was introduced. For the large-scale scenarios discussed in the following chapters, a post-processing data analysis is not feasible. Thus developing and utilizing in-situ synthetic diagnostics was essential in order to perform the data analysis and radiation calculations presented in this thesis.

Part of the thesis was a continuous work on the code base of the PIC-code PIConGPU. This included both new code development - a few of the added algorithms will be discussed in the following chapters - as well as validating newly added code and maintaining the code base together with a team at HZDR. As part of this development work, various large-scale simulations became possible, leading to the publications [R1–R4, R7] and theses [65, 101].

---

[5] By the best knowledge of the author, the implementation in PIConGPU is so far the only working method of such a large scale far-field computation. All other codes consider only a subset of the particles simulated.

4 In situ spectral radiation calculation in PIConGPU

The aforementioned data analysis plug-ins provide a suitable framework for embedding an in situ radiation calculation. There are various simulation codes that use spectrally resolved Liénard-Wiechert potentials (Eq. 2.10) to predict the emitted radiation of charged particles [63, 80, 102–111], but only the implementation in PIConGPU as a in-situ data analysis [61, R8] is capable of calculating the radiation of all millions to billions of macroparticles simulated in the particle-in-cell simulations for hundreds of frequencies and observation directions. This becomes possible as result of the plug-in's direct implementation into the framework of PIConGPU, the use of GPUs, and the algorithm's direct non-equidistant discrete Fourier transform that avoids many consecutive processing steps required by a Fast Fourier Transform approach. The original framework for the in situ radiation calculation was already implemented during the diploma thesis of Pausch [R8]. A brief summary of the technical implementation is presented in section 4.1. As part of this thesis, extensive many-particle tests were performed and various extensions to the original code were introduced. These are described in detail in sections 4.2 to 4.4.

4.1 Discrete implementation in particle-in-cell codes

When calculating the radiation of multiple particles numerically, Eq. 2.10 needs to be extended. In order to take the effects of coherent and incoherent radiation into account, the complex amplitudes have to be summed over all N_p particles before taking the absolute square [59]. Since macroparticles can have different charges q_p, their values need to be considered during summation as well. The integral over time becomes a sum over all sampled time steps N_t with step width Δt. Due to the commutability of linear operations, the sum over time and the sum over all particles can be interchanged. Thus the spectrally resolved Liénard-Wiechert potentials become:

$$\frac{\mathrm{d}^2 W}{\mathrm{d}\,\Omega\,\mathrm{d}\,\omega} = \frac{\Delta t}{16\pi^3 \varepsilon_0 c} \left| \sum_{k=0}^{N_t} \sum_{p=1}^{N_p} q_p \frac{\vec{n} \times \left[\left(\vec{n} - \vec{\beta}_{p,k} \right) \times \dot{\vec{\beta}}_{p,k} \right]}{\left(1 - \vec{\beta}_{p,k} \cdot \vec{n} \right)^2} \cdot \mathrm{e}^{\mathrm{i}\omega(\Delta t \cdot k - \vec{n} \cdot \vec{r}_{p,k}/c)} \right|^2 \tag{4.1}$$

with $\vec{r}_{p,k}$, $\vec{\beta}_{p,k}$ and $\dot{\vec{\beta}}_{p,k}$ being the position, normalized velocity and normalized acceleration of particle p at the time $t = \Delta t \cdot k$.

This approach not only allows treating both coherent and incoherent radiation simultaneously [R9] but also reduces the memory footprint of the simulation dramatically, since the sum over particles can be evaluated for each time step, thus avoiding the need to store entire particle trajectories for billions of particles. Details on the design of the in-situ radiation calculation in PIConGPU can be found in [61]. A computational analysis of the code's performance on the high-performance cluster TITAN at the Oak Ridge National Laboratory was published in [R1]. In the following, only the most essential features of the in-situ radiation plug-in are briefly discussed.

Equation 4.1 is a discrete Fourier transform over the retarded time $T_{\text{ret}} = t - \vec{n} \cdot \vec{r}_p(t)/c$ for each particle. The retarded time is non-equidistant and differs for each particle. According to the Nyquist-Shannon sampling theorem [83, 84], this has consequences on the highest resolvable frequency $\omega < \Omega_{\text{Nyquist}} = \frac{\pi}{\Delta t_{\text{ret}}}$. In order to demonstrate this resolution limit, let us assume a simulation with an iteration time step Δt and with two particles, one stationary $\beta_1 = 0$, the other one with a velocity of half the speed of light towards the observer $\beta_2 = 0.5$. While the retarded duration between two consecutive iteration steps of particle one is equal to the simulation time step $\Delta t_{\text{ret}\,1} = \Delta t$, the retarded time step of the second particle is only half as long $\Delta t_{\text{ret}\,2} = {}^{\Delta t}/_{2}$ thus allowing the radiation plug-in to resolve frequencies twice as high[6]. Calculating the radiation of the first particle at frequencies above $\omega > \frac{\pi}{\Delta t}$ would contain unphysical signals. Signals at these frequencies are numerically equivalent to negative frequencies and have the appearance of *reflected* signals from lower frequencies. Unfortunately, the radiation from the second particle might contain spectral signatures of interest at frequencies between $\frac{\pi}{\Delta t} < \omega < \frac{2\pi}{\Delta t}$. These would overlap with the reflected signals from the first particle. In the non-equidistant sampling case, the sampling rate needs to be above the Nyquist Shannon limit only locally [83, 112]. Thus, the Nyquist-Shannon sampling limit needs to be checked locally by introducing a so-called *Nyquist limiter* factor [61]

$$\nu(\omega, \vec{\beta}, \vec{n}) = \Theta\left(\frac{\pi}{\Delta t \cdot \left(1 - \vec{\beta} \cdot \vec{n}\right)}\omega\right) \tag{4.2}$$

with $\Theta(x) = \int\limits_{-\infty}^{x} \delta(y)\mathrm{d}y$ being the Heaviside step function. By multiplying this factor ν with the inner summand of equation 4.1, only particles that fulfill the Nyquist-Shannon limit contribute to the computed spectrum.

As part of this thesis, a restart method was implemented for the radiation plug-in. It allows storing the complex amplitudes $\vec{A}_k(\omega, \vec{n}) \in \mathbb{C}^3$ for each frequency ω and each observation direction $\vec{n}$ for various time steps k on disk before taking the absolute square and thus allows restarting from time step k without losing phase and polarization information (see Eq. 4.3). The restart files follow the OpenPMD file standard [113] and are self-describing. Only by allowing restarts during simulation runs, large-scale simulations became feasible.

Furthermore, a correct treatment of coherent and incoherent radiation from a single macroparticle itself was introduced by defining macroparticle form factors $F(q_p, \omega, \vec{n})$. These are discussed in section 4.3 and in [R9].

Additionally, window functions $\mathcal{W}(\vec{r}_p)$ were implemented to enable simulations with continuous boundary conditions as e.g., the simulation on the Kelvin-Helmholtz instability (see chapter 7). Details on these window functions are given in section 4.4.

---

[6] Please be aware that this is a retardation, not a dilatation effect.

With all these additions, Eq. 4.1 becomes:

$$\frac{\mathrm{d}^2 W}{\mathrm{d}\,\Omega\,\mathrm{d}\,\omega} = \frac{\Delta t}{16\pi^3 \varepsilon_0 c} \left| \underbrace{\sum_{k=0}^{N_t} \sum_{p=1}^{N_p} \chi_{p,k}(\omega, \vec{n}) \cdot \frac{\vec{n} \times \left[\left(\vec{n} - \vec{\beta}_{p,k} \right) \times \dot{\vec{\beta}}_{p,k} \right]}{\left(1 - \vec{\beta}_{p,k} \cdot \vec{n} \right)^2} \cdot \mathrm{e}^{\mathrm{i}\omega(\Delta t \cdot k - \vec{n} \cdot \vec{r}_{p,k}/c)}}_{\vec{A}_k(\omega, \vec{n})} \right|^2 \tag{4.3}$$

$$\text{with} \quad \chi = \nu\left(\omega, \vec{\beta}_{p,k}, \vec{n}\right) \cdot F\left(q_p, \omega, \vec{n}\right) \cdot \mathcal{W}\left(\vec{r}_{p,k}\right) \cdot q_p \quad . \tag{4.4}$$

This is the full equation currently implemented in PIConGPU to calculate the far-field radiation.

4.2 Validating the radiation plug-in against theory

Validating the results of the radiation plug-in in PIConGPU is essential for being able to make quantitative predictions. Since the main focus of PIConGPU is laser plasma physics simulations, test scenarios validating the relativistic particle energy regime, the relativistic laser intensity regimes and a combination of both are essential. Furthermore, test cases with multiple particles are necessary as well to validate scalings that are vital for quantitative predictions. In the following sections, various test simulations are discussed. The basic simulation setup is always the same: a plane wave or a Gaussian laser pulse interacts with a number of electrons. The strength of the electromagnetic wave is defined by the normalized field strength

$$a_0 = \frac{q_e \cdot E}{m_e c \omega_0} \tag{4.5}$$

with q_e and m_e being the electron charge and mass, E being the electric field amplitude, c being the speed of light, and ω_0 being the electromagnetic wave's frequency. The electrons all have the same normalized velocity β and are either initially at rest or move in the opposite direction to the propagation direction of the electromagnetic wave. In all cases, except the last one, the field created by the electrons is neglected. Computationally this is achieved by deactivating the current deposition algorithm. Only such a simplified setup allows a comparison with analytic models. The first three tests are compared to analytical predictions for nonlinear Thomson scattering in laser fields given in [114, 115].

4.2.1 Quasi-stationary electron in a relativistic field

This test scenario assumes a plane wave of normalized field strength a_0 to interact with a single electron that would be at rest without the electromagnetic wave. Due to the electromagnetic wave, the electron oscillates. At relativistic intensities, $a_0 \gtrsim 1$, the oscillating motion of the electron reaches relativistic velocities. At relativistic velocities, the magnetic field of the wave influences the electron dynamics. The one-dimensional harmonic oscillation becomes a figure-eight motion [56].

This change in electron motion also influences the emitted radiation. At non-relativistic intensities $a_0 \ll 1$, radiation is only emitted at the same wavelength as the driving wave; at relativistic intensities $a_0 \gg 1$ so-called higher harmonics are emitted as well. These are photons with frequencies at integer multiples of the incident wave frequency ω_0.

$$\omega_n = n \cdot \omega_0 \quad (n \in \mathbb{N}) \tag{4.6}$$

In order to validate the radiation plug-in, a single macroparticle with weighting $w = 1$ was used. The electromagnetic wave was fed in on one side of the simulation with a Gaussian up-ramp. The electron was given an initial velocity to compensate the push in wave propagation direction ($\vec{e}_y$) caused by the ponderomotive force. The velocity was set in such a way, that the macroparticle was, averaged over one oscillation period, at rest when reaching the plateau of the wave. With reaching the plateau, the radiation was computed for five oscillation periods for a range of observation directions $\vec{n} = (\sin\theta, \cos\theta, 0)$ in the plane of oscillation. For a normalized intensity of $a_0 = 1.0$, exemplary simulation results are confronted with theoretical predictions based on [115] in Fig. 4.1(a). The higher harmonics are clearly reproduced in the simulations. Both their frequency bandwidth and their directional structure agree with the simulation. In order to quantify the deviation of the simulation from the theoretical prediction, the following definition for a relative error was used:

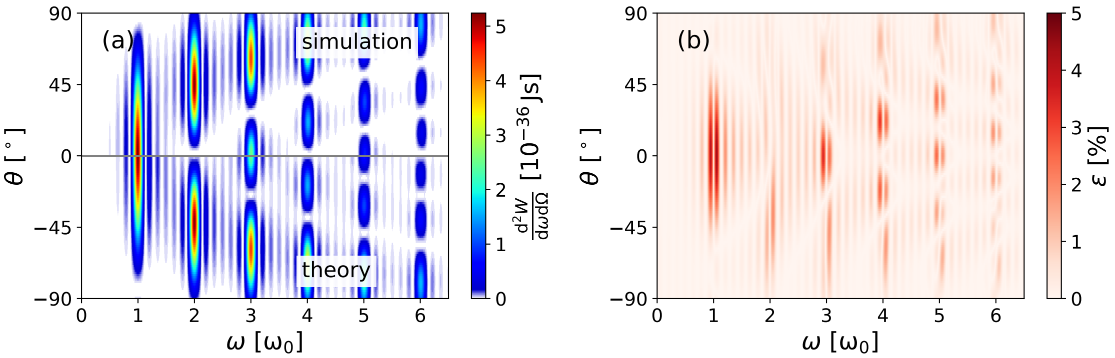

Figure 4.1: **Validation via Thomson scattering from a quasi-stationary electron: (a)** Directionally resolved spectra of a single, quasi-stationary electron in a plane wave $a_0 = 1.0$ obtained via simulation and from a theoretical model. **(b)** Relative error between theory and simulation.

$$\varepsilon = \frac{|\chi_{\text{sim}} - \chi_{\text{theo}}|}{\max(\chi_{\text{theo}})} \tag{4.7}$$

with $\chi = \frac{d^2W}{d\omega d\Omega}$ being the spectrally and directionally resolved radiation spectra from either the theory or the simulation. The deviation between theory and simulation is plotted in Fig. 4.1(b). The simulation agrees well with the theoretical predictions and the deviation is below $\varepsilon < 5\%$.

4.2.2 A relativistic electron in an electromagnetic wave

In the following test scenario, the setup was extended to include a macroparticle moving at a velocity β close to the speed of light towards the approaching electromagnetic wave. The weighting of the single macroparticle was again set to $w = 1$. Again, the wave was initialized on one side of the simulation box and propagated in $+\vec{e}_y$ direction. An initial Gaussian up-ramp was used for reaching proper starting conditions. Due to the high velocity of the macroparticle, the effect of the ponderomotive force on the electron dynamics could be neglected. The scattered light from the electron is emitted mainly in the direction of electron propagation $-\vec{e}_y$ - also called the forward direction. Due to the relativistic velocity of the electron, the wavelength of the electromagnetic wave is much shorter in its rest frame. The emitted radiation in the rest frame of the electron is thus at a higher frequency. In the lab frame, the emitted radiation in forward-direction is again blue shifted. The scattered radiation is observable at a frequency

$$\omega_n = \frac{n \cdot \omega_0 \cdot (1+\beta)^2}{(1+\beta)^2 - \frac{1}{2}(1+\cos\theta) \cdot \left(\frac{1+\frac{a_0^2}{2}}{\gamma^2} + (1+\beta)^2 \right)} \tag{4.8}$$

under an observation direction $\vec{n} = (-\cos\theta, \sin\theta, 0)$, with β and γ being the electron normalized speed and Lorentz factor [115] and n being the index of the higher harmonic. The scattered radiation is maximally blue shifted in the direction of the electron velocity. The frequency up-shift is reduced towards larger observation angles θ. The scattering frequency has a minimum in the opposite direction of the electron velocity and the laser propagation direction.

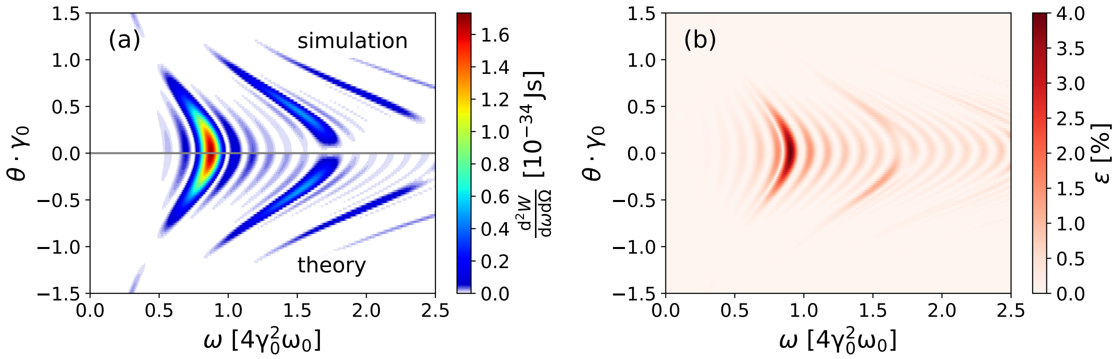

Figure 4.2: **Validation via Thomson scattering from a single relativistic electron: (a)** Directionally resolved spectra of a head-on scattering between a single electron $\gamma_0 = 5$ and a plane wave $a_0 = 0.5$ both simulated and following theoretical predictions. **(b)** The relative difference between the simulated and the theoretically predicted spectra is below 5%.

An exemplary simulation result and the corresponding theoretical predictions are illustrated in Fig. 4.2 (a). The electron had a Lorentz factor of $\gamma = 5$ and the electromagnetic wave had a normalized amplitude of $a_0 = 0.5$. The maximum deviation between simulation and theory for this test case was far below 5% (Fig. 4.2 (b)). The small remaining difference between simulation an theory results from the discretized particle trajectory in the particle-in-cell simulation. Iterations are not taken at multiples of the laser period and therefore the particle trajectory is not sampled symmetrically [R8]. The error could be reduced by decreasing the temporal step width Δt but this would increase the computational time.

More results of these single particle simulations can be found in [61].

4.2.3 Nonlinear Thomson scattering of an electron bunch

As a third benchmark scenario, a similar setup was chosen. Instead of a single macroparticle representing one electron, a macroparticle distribution representing an electron bunch of $Q = 1.9\,\mathrm{nC}$ charge was used. Again, the laser intensity and electron velocity were varied. In order to allow a comparison with the analytical theory, all macroparticles were given the same direction of flight and speed. The spatial distribution of the macroparticles followed a Gaussian distribution in all three dimensions. This test allows validating the correct addition of the phases between the individual emitters. Despite the coherent addition in equation 4.3, the total radiation should only scale incoherently, i. e. linearly with the number of electrons involved, since the spatial extent of the bunch is much larger than the wavelength of the emitted radiation $\tau \cdot c \gg \lambda_{\mathrm{rad}}$. Consequently, the theoretical spectrum for the bunch radiation is equal to the spectra for a single electron multiplied by the number of electrons in the bunch $N_e = {}^{Q}/_{q_e} \approx 1.2 \cdot 10^{10}$.

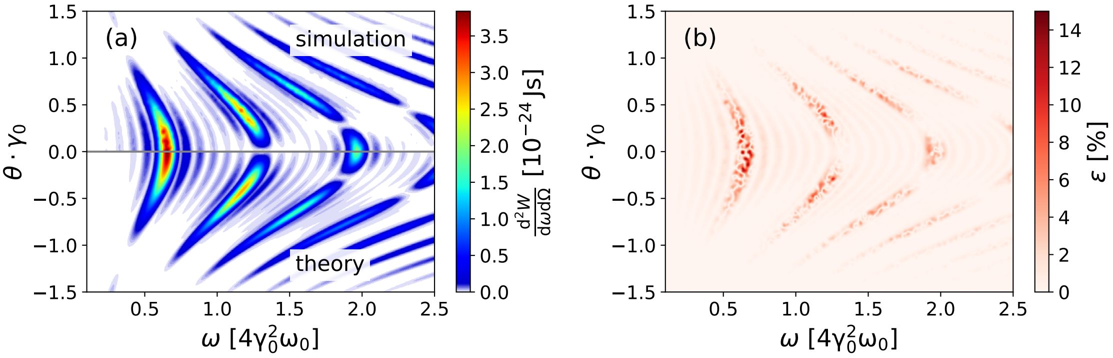

Figure 4.3: **Validation via Thomson scattering from a relativistic electron bunch: (a)** Directionally resolved spectra of a head-on scattering between an electron bunch and a plane wave both simulated and according to theory. The electron bunch has a Lorentz factor of $\gamma_0 = 5$ and a total charge of $Q = 1.9\,\mathrm{nC}$. The electromagnetic wave reaches a normalized field strength of $a_0 = 1.0$. **(b)** The relative difference between the simulated and the theoretically predicted spectra is below 15%.

An exemplary comparison between analytical prediction and simulated spectra is depicted in Fig. 4.3. The test case assumes electrons with a Lorentz-factor of $\gamma = 5$ to interact with a plane wave of normalized field strength $a_0 = 0.5$ to interact for 5 oscillation periods. The relative difference between theoretical prediction and simulation is below $\varepsilon < 15\%$.

In order to investigate this deviation further, this benchmark test was repeated for various numbers of macroparticles and resolved frequencies and directions. All physical parameters were kept constant. The discretization of the phase space via macroparticles was altered, but the charge and thus the number of real electrons represented was held constant. Similarly, the directional and frequency range was fixed and only their resolution was altered. The mean error between simulation and theory is plotted in Fig. 4.4. The deviation between theory and simulation is reduced if more macroparticles are used to represent the electron bunch in the particle-in-cell simulations. Additionally, more spectral and directional sample points also reduce the mean error. For the simple dynamics of an electron bunch in a plane wave, the difference reduces best at around $2 \cdot 10^5$ macroparticles. The slight increase in the numerical error beyond 10^6 macroparticles is caused by summation errors when using single-precision floating point numbers.

In this benchmark test, the macroparticles sample a very simple electron distribution function. For more complex phase space distributions, as in laser plasma simulations, the distribution function will be more complex. In most real cases, barely 10^5 macroparticles will show exactly the same dynamics. In order to ensure therefore a minimal error, as many macroparticles as possible should be taken into account for radiation calculations. For practical applications in PIC simulations, this means that all macroparticles should be taken into account for radiation calculations [R8]. Furthermore, correctly scaling coherent and incoherent radiation requires taking into account all macroparticles too, as will be discussed in detail in section 4.3.

4.2.4 Nonlinear Thomson scattering from a plasma

A laser pulse that interacts with an underdense plasma exhibits a much more complex electron dynamics than the benchmark cases described above. Due to the transversal and temporal envelope of the laser pulse, the electrons oscillate at different field strengths. This not only

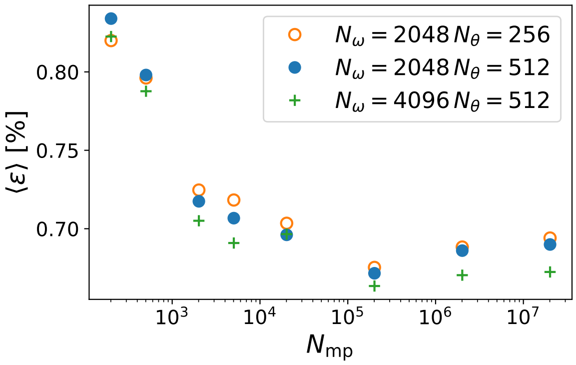

Figure 4.4: **The mean numerical error over the number of particles:** This plot depicts the reduction of the mean deviation $\langle \varepsilon \rangle$ between theory and simulation for the electron bunch Thomson scattering case over the number of macroparticles N_mp used in the simulation. By increasing the number of macroparticles which sample the bunch and with increasing the spectral (N_ω) and directional (N_θ) resolution, the mean error is reduced.

causes the higher harmonics to differ in intensity depending on the electron location but also causes the electrons to drift towards weaker field strength due to the ponderomotive force. The latter leads to density fluctuations in underdense plasma. All of this leads to a complex plasma dynamics which is highly non-trivial. Despite this complexity, there is a known radiation signature at twice the laser frequency $\omega = 2 \cdot \omega_0$ which is emitted under $\pm 45^\circ$ and $\pm 135^\circ$ to the laser propagation direction. This signature originates from the figure-8 motion of the electrons in relativistic laser intensities $a_0 > 1$. It has been observed in an experiment by Chen in 1998 [116] and since then it is a common diagnostic signature in experiments to determine if the laser intensity reached a non-linear regime. In spite of the complicated nature of the laser plasma dynamics in experiments, this is the many-particle equivalent to the first single particle benchmark. Therefore we simulated the historical experiment of Chen and used it as a benchmark.

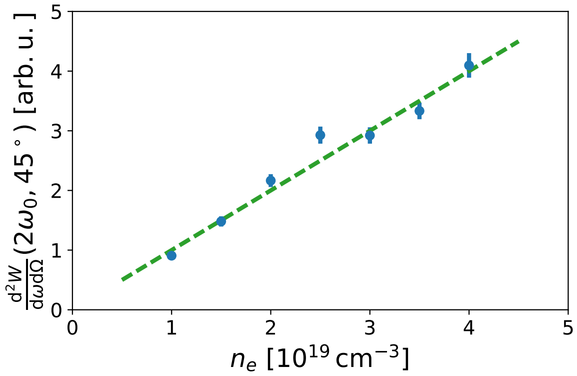

Figure 4.5: **Validation against common experimental signature at $\omega = 2 \cdot \omega_0$:** The intensity of radiation $\frac{\mathrm{d}^2 W}{\mathrm{d}\omega \mathrm{d}\Omega}$ at $2\omega_0$ under $\theta = 45^\circ$, determined with the simulation, is plotted for various plasma densities n_e (blue dots). The relation between intensity and density is linear, as expected for this incoherent radiation signature and validated via an experiment by Chen [116] (green dashed line). The simulation assumes a laser pulse of $a_0 = 1.68$, $w_0 = 7\,\mu$m and $\tau = 50$ fs with a wavelength of $\lambda_0 = 800$ nm.

This radiation pattern at $\omega = 2 \cdot \omega_0$ was observed with PIConGPU by simulating a laser of peak field strength $a_0 = 1.68$, wavelength $\lambda_0 = 800\,\mathrm{nm}$, pulse duration $\tau = 50\,\mathrm{fs}$ (FWHM intensity) and beam waist $w_0 = 7\,\mu\mathrm{m}$ propagating through a plasma of densities between $n_e = 1 \cdot 10^{19}\,\mathrm{cm}^{-3} - 4 \cdot 10^{19}\,\mathrm{cm}^{-3}$. With increasing plasma density, the intensity of the simulated $2\omega_0$ radiation increased linearly as well. The linear scaling is depicted in Fig. 4.5. This validates that the summation in Eq. 4.3 lead to an incoherent signature despite the consideration of the phase of the various emitters. The linear scaling of the radiation intensity with the plasma density was the first benchmark that provided validation against experimental results.

These four tests demonstrate that the radiation plug-in of PIConGPU is capable of quantitatively predicting the radiation emission of plasma simulations in both the relativistic and nonlinear cases even at realistic plasma densities with billions of macroparticles involved. It is further capable of quantitatively reproducing incoherent radiation signatures despite its coherent computational approach. These tests provide the basis for more detailed studies of plasma radiation as presented in this thesis.

4.3 Coherent and incoherent radiation with form factors

In the previous tests, the radiation simulation assumed either the macroparticle to represent a single real electron, or the radiation had to be scaled linearly with the particle weighting to enforce incoherent radiation. In a general scenario, however, the ensemble of electrons represented by a macroparticle can radiate both coherently and incoherently. In [61], it was already shown that taking the complex phase between macroparticles into account before computing the absolute square in Eq. 4.1 allows simulating both coherent and incoherent radiation at the same time without adjusting the equation. However, in PIC simulations, macroparticles represent an ensemble of real particles. The macroparticle just has one position; therefore, the entire ensemble would have the same phase and thus scale coherently. This is equivalent to treating macroparticles as point-like particles with charge $q_{\mathrm{mp}} = w \cdot q_e$, with w being the macroparticle weighting and q_e being the charge of a single electron. With regard to Eq. 4.1, this would increase the radiation quadratically with the weighting, independent of the emitted frequency. Using twice as many macroparticles with just half the original weighting would result in quantitatively different spectra. This weighting-dependent radiation intensity is unphysical and needs to be avoided.

If one, however, assumes that the macroparticle is a continuous charge distribution as the particle-in-cell algorithm does, the radiation of such a particle would vanish for wavelengths much smaller than the length of the macroparticle $\lambda < \Delta L$. The reason is that when integrating the phase shift over the charge distribution, the phases of different parts of the charge distributions cancel out if the charge distribution of the macroparticle is wider than the emitted wavelength. This would result in no radiation at wavelengths shorter than the macroparticle size (see Fig. 4.6). However, there is radiation as e.g., betatron radiation with a sub-nanometer wavelength which is much shorter than the typical macroparticle extent used in particle-in-cell simulations. The size of macroparticles would decrease with a finer spatial resolution of the particle-in-cell simulation, thus making the cut-off dependent on the resolution of the simulation. Again, this resolution dependency is unphysical and should be avoided.

This issue can be resolved by taking into account the discreteness of electrons represented by the macroparticle and the macroparticle extent (and thus the extent of the ensemble represented). In order to do that, let us reexamine the macroparticle in particle-in-cell codes. Macroparticles have a charge distribution but a single momentum to not be smeared out with increasing time. By extending Eq. 2.10 to many particles, one is able to include the discrete

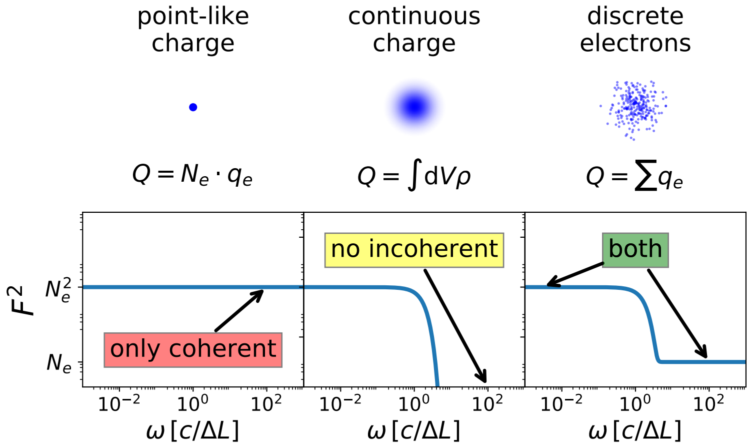

Figure 4.6: **Illustration of coherent and incoherent radiation scaling with different macroparticle representations:** On the left, a point-like macroparticle is assumed. Over the entire spectrum, the emitted radiation scales quadratically with the weighting and is therefore coherent. In the center, a macroparticle with a continuous charge distribution is illustrated. At wavelengths smaller than the macroparticle shape, no radiation is emitted and the incoherent regime cannot be reproduced. On the right, a cloud of individual electrons is considered. This discrete approach reproduces both the coherent and incoherent regime.

nature of the electrons represented by a macroparticle:

$$\frac{\mathrm{d}^2 W}{\mathrm{d}\Omega\,\mathrm{d}\omega} = \frac{1}{16\pi^3\varepsilon_0 c}\left|\int_{-\infty}^{+\infty}\sum_{k=1}^{N} q_k \frac{\vec{n}\times\left[\left(\vec{n}-\vec{\beta}_k\right)\times\dot{\vec{\beta}}_k\right]}{\left(1-\vec{\beta}_k\cdot\vec{n}\right)^2}\cdot \mathrm{e}^{\mathrm{i}\omega(t-\vec{n}\cdot\vec{r}_k(t)/c)}\,\mathrm{d}\,t\right|^2 \tag{4.9}$$

$$= \frac{q_e^2}{16\pi^3\varepsilon_0 c}\left|\int_{-\infty}^{+\infty}\frac{\vec{n}\times\left[\left(\vec{n}-\vec{\beta}\right)\times\dot{\vec{\beta}}\right]}{\left(1-\vec{\beta}\cdot\vec{n}\right)^2}\cdot \mathrm{e}^{\mathrm{i}\omega(t-\vec{n}\cdot\vec{r}(t)/c)}\cdot\sum_{k=1}^{N}\mathrm{e}^{\mathrm{i}\omega\vec{n}\cdot(\vec{r}_k(t)-\vec{r}(t))/c}\,\mathrm{d}\,t\right|^2 \tag{4.10}$$

Here, N is the number of electrons represented by a single macroparticle, $\vec{r}$ is the central position of the macroparticle, while $\vec{r}_k$ is the position of the k$^{\text{th}}$ electron represented by the macroparticle. The sum over the particles affects only the phase, but not on the vector part of the equation, since all electrons in the macroparticle ensemble are assumed to have the same momentum at all times. By separating the central position of the macroparticle from the position of the associated electrons, the equation simplifies to Eq. 4.10. The influence of the actual position of the electrons modeled is kept in the sum over all particles. This sum is the form factor of that specific electron distribution. For simplicity let us redefine this sum as:

$$F^2(\omega) = \left|\sum_{k=1}^{N}\mathrm{e}^{\mathrm{i}\omega\vec{n}\cdot\hat{\vec{r}}_k/c}\right|^2 \quad , \tag{4.11}$$

with $\hat{\vec{r}}_k = \vec{r}_k(t) - \vec{r}(t)$ being the position of the electron k relative to the center of the macroparticle. Due to the equal momentum of all particles represented by the macroparticle, this position does not change with time. This allows rewriting Eq. 4.10 as

$$\frac{\mathrm{d}^2 W}{\mathrm{d}\Omega\,\mathrm{d}\omega} = \frac{q_e^2}{16\pi^3\varepsilon_0 c}\left|\int_{-\infty}^{+\infty}\frac{\vec{n}\times\left[\left(\vec{n}-\vec{\beta}\right)\times\dot{\vec{\beta}}\right]}{\left(1-\vec{\beta}\cdot\vec{n}\right)^2}\cdot \mathrm{e}^{\mathrm{i}\omega(t-\vec{n}\cdot\vec{r}(t)/c)}\,\mathrm{d}\,t\right|^2\cdot F^2(\omega) \tag{4.12}$$

Unfortunately, we do not know the exact position of the electrons, only their distribution.

For simplicity reasons, let us assume a one-dimensional case, with x_k being the position of the electron in the frame of the macroparticle and the observation vector $\vec{n}$ becoming unity. The result can be easily extended to three dimensions. Let us assume that the electron with index k has a spatial probability distribution $\rho(x_k)$. Thus, the probability distribution of the entire ensemble of $N_{\mathrm{mp}} = w$ electrons represented by the macroparticle is the product of all single-particle density distributions.

$$\rho_N(x_1, x_2, \ldots, x_N) = \prod_{k=1}^{N} \rho(x_k) \tag{4.13}$$

This allows defining an average form factor over all possible electron distributions:

$$F^2(\omega) = \frac{\int\limits_{-\infty}^{+\infty} \cdots \int\limits_{-\infty}^{+\infty} \mathrm{d}x_1 \ldots \mathrm{d}x_N \, \rho(x_1, \ldots, x_N) \left| \sum\limits_{k=1}^{N} \mathrm{e}^{i\omega x_k} \right|^2}{\int\limits_{-\infty}^{+\infty} \cdots \int\limits_{-\infty}^{+\infty} \mathrm{d}x_1 \ldots \mathrm{d}x_N \, \rho(x_1, \ldots, x_N)} \tag{4.14}$$

Here we apply that the absolute square of complex numbers is the product of the complex number with its complex conjugated value and calculate the form factor by separating the sum. As a result, the form factor can be described by a simple equation

$$F^2(\omega) = N + \left(N^2 - N\right) \left| \int\limits_{-\infty}^{+\infty} \mathrm{d}x \rho(x) \mathrm{e}^{\mathrm{i}\omega x} \right|^2 = N + \left(N^2 - N\right) \cdot \left(\mathcal{FT}(\rho(x))\right)^2 \tag{4.15}$$

that only depends on the Fourier transform of the probability distribution $\mathcal{FT}(\rho(x))$ and the number of real particles N represented by a macroparticle. This relation was already found in 1946 by Schiff [117]. It is commonly used for modeling the coherent fields in synchrotrons and determining the bunch shape [118, 119]. This work (thesis) applies this form factor for the first time to compute simultaneously coherent and incoherent far-field radiation in particle-in-cell codes [R10].

The probability distribution is proportional to the density distribution associated with the macroparticle and thus can be calculated depending on the shape selected for simulation. Various macroparticle shapes have been implemented in the radiation plug-in of PIConGPU. However, sudden density jumps as in the CIC shape (see section 3.2) lead to oscillations in the form factor. Using a Gaussian density distribution of a size similar to that of the macroparticle avoids these side lobes. Using a Gaussian form factor is therefore much better suited for scaling the radiation intensity according to the coherent and incoherent regime and for avoiding additional spectral peaks due to oscillations in the form factor [R10].

4.4 Window functions for continuous boundary conditions

Simulating the radiation in a finite-size simulation box requires looking into influences on the radiation caused by these sharp boundaries. The retarded time in Eq. 2.10

$$t_{\mathrm{ret}} = t - \frac{\vec{n} \cdot \vec{r}(t)}{c} \tag{4.16}$$

depends on the particle position. Therefore, discontinuities in the position will lead to discontinuities in the retarded time and thus to ringing effects in the calculated radiation spectra similar to the side lobes of a sinc function $\mathrm{sinc}(\omega)$ when Fourier transforming a rectangular function $\Pi(t)$. This is a known problem in signal theory and can be avoided by introducing window functions as filters [120, 121]. In contrast to most problems from signal theory, the most dominant cause for these ringing effects is not the finite sampling time duration. The side-lobes originate from the limited retarded time of the ensemble of particles. There are no particles beyond the spatial extent of the simulation box. Thus, the range of retarded time is sharply limited by these boundaries, especially if the simulation time is short compared to the time that the light would need to propagate through the simulation box, causing ringing artifacts like side-lobes. This is illustrated by Fig. 4.7 which shows simulated spectra from a plasma under the influence of two external electric fields oscillating at different frequencies $\vec{E} = 10^{11}\,{}^{\mathrm{V}}\!/\!_{\mathrm{m}} \cdot (\sin(2.5\omega_{pe}t) + \sin(5.5\omega_{pe}))\,\vec{e}_x$. The frequencies are given in multiples of the plasma frequency ω_{pe}, and the observation angle is the angle between the x- and y-axis $\vec{n} = (\cos\theta, \sin\theta, 0)$. The simulation box has a size of $L_x = 7.12{}^{c}\!/\!_{\omega_{pe}}$, $L_y = 28.5{}^{c}\!/\!_{\omega_{pe}}$ and $L_z = 1.78{}^{c}\!/\!_{\omega_{pe}}$. The response to the external fields (marked by red dotted lines) and radiation at the plasma frequency (marked by a red dashed line) can be clearly identified (see Fig. 4.7). However, there are also side lobes overlapping the signal. These originate from the hard cut-off at the boundaries of the simulation box. Let us, for now, just consider the simulation box in the x-direction. Assuming a homogeneous density distribution, the density can be described as $\rho(x) = \rho_0 \cdot \Pi(x/L_x)$, with $\Pi(x)$ being the rectangular function

$$\Pi(x) = \begin{cases} 1 & \text{for } -0.5 \leq x \leq +0.5 \\ 0, & \text{for any other case} \end{cases} \quad . \tag{4.17}$$

By performing a Fourier transform, we get the density in reciprocal space:

$$\tilde{\rho}(k_x) = \frac{L_x}{2} \cdot \mathrm{sinc}\left(\frac{L \cdot k_x}{2}\right) \tag{4.18}$$

with $\mathrm{sinc}(y) = \frac{\sin y}{y}$. The extrema of the sinc function are at:

$$\hat{k}_x = \frac{2}{L_x} \cdot \left\{ \left(n + \frac{1}{2}\right)\pi - \frac{1}{\left(n + \frac{1}{2}\right)\pi} \right\} \quad \text{with } n \in \mathbb{N} \quad . \tag{4.19}$$

Both minima and maxima of the sinc function appear as maxima in the spectrum since Eq. 2.10 takes the absolute square of the complex Fourier transform. If one looks at the simulation box at various angles, these maxima depend on the observation angle as well:

$$\begin{aligned} \omega_{nx}(\theta) &= \frac{c k_x}{|\cos\theta|} && (4.20) \\ &= \frac{2c}{L_x \cdot |\cos\theta|} \cdot \left\{ \left(n + \frac{1}{2}\right)\pi - \frac{1}{\left(n + \frac{1}{2}\right)\pi} \right\} && (4.21) \\ \omega_{ny}(\theta) &= \frac{2c}{L_y \cdot |\sin\theta|} \cdot \left\{ \left(n + \frac{1}{2}\right)\pi - \frac{1}{\left(n + \frac{1}{2}\right)\pi} \right\} && (4.22) \end{aligned}$$

This can be generalized to all dimensions. The resulting maxima are illustrated by white dashed lines for the y boundary and white dotted lines for the x boundary in Fig. 4.7 according to Eq. 4.21 and 4.22.

In order to reduce the influence of these side lobes and in some cases to avoid them completely, the technique of window functions known from signal processing was integrated into the radiation plug-in. Window functions are applied to signals and reduce the signal strength at the start and end. This reduces the influence of the signal cut-off and reduces side lobes in the Fourier space.

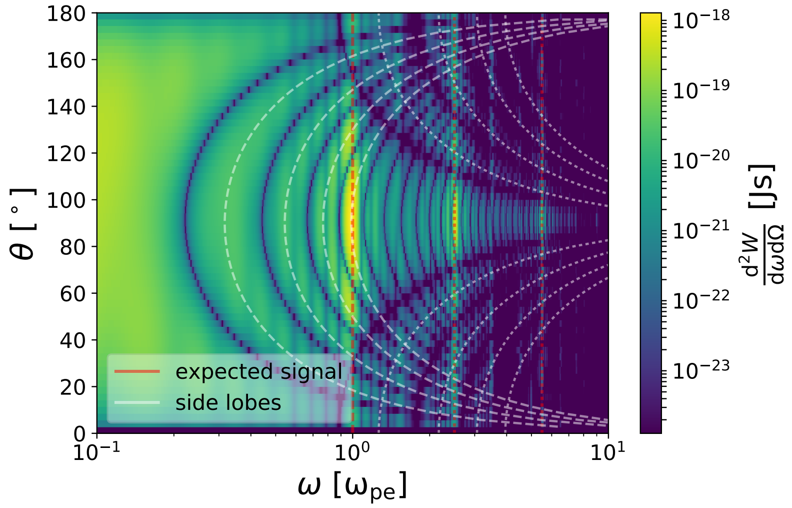

Figure 4.7: **Illustration of side lobes from simulation box boundaries:** Radiation spectra of a homogeneous plasma under the influence of an external electric field $\vec{E} = 10^{11}\,{}^{V}\!/\!{}_{\mathrm{m}} \cdot (\sin(2.5\omega_{pe} t) + \sin(5.5\omega_{pe}))\,\vec{e}_x$. The red dashed line illustrates the expected radiation signal at the plasma frequency while the red dotted lines illustrate the expected emission signal due to the external field. The white dashed and dotted lines are the side lobes caused by the finite simulation box. Due to the use of a logarithmic color scale, the influence of the side lobes is emphasized.

The development of effective filters is complicated. For example, the use of a Gaussian distribution is not a particularly good choice. However, a number of excellent filters are known from signal processing. Therefore, only their properties are briefly explained in this work. A detailed implementation can be found in [120, 121].

A list of filters included in PIConGPU and available since the beta-rc5 [122] release can be found in table 4.1. Each signal generates side lobes. It is important to be able to separate the signal from its side lobes at higher and lower frequencies. Therefore, an important attribute of filters is the so-called side lobe fall off (SLFO) [120]. It indicates how many decibels a signal has dropped at double or half the frequency.[7] The side lobe fall off (SLFO) is defined as

$$\mathrm{SLFO}\,[\mathrm{dB/Octave}] = 10 \cdot \log_{10}\left(\frac{{}^{\mathrm{d}^2W}\!/\!{}_{\mathrm{d}\omega\mathrm{d}\Omega}(2\omega_s)}{{}^{\mathrm{d}^2W}\!/\!{}_{\mathrm{d}\omega\mathrm{d}\Omega}(\omega_s)}\right) \tag{4.23}$$

with ω_s being the frequency of a signal peak. The smaller the SLFO, the better a window function suppresses side lobes caused by both the simulation box and radiation signals.

The reduced background of side lobes comes at the expense of a wider signal. While without a filter the width of a signal depends only on the sampling rate, using a filter widens a signal. This may cause a signal to swallow other weaker signals that are nearby in the spectrum. Therefore, a desirable attribute of a filter is not to cause excessive signal broadening. The signal widening is measured in the signal width at $3\,\mathrm{dB}$ in units of the sample resolution Δx and is called the 3dB-width. This corresponds to the width of a signal at $P_1/P_0 \approx 2$ which is more commonly called the full width at half maximum (FWHM) in physics. The narrower the signal remains, the better one can resolve nearby signals. Roughly speaking, two equally strong signals can be distinguished if they are more than the $3\,\mathrm{dB}$-width apart.[8] A list of all implemented window functions is given in Tab. 4.1, stating both the side lobe fall off and the 3dB-width.

In order to reduce the effect of the side lobes from the simulation box boundaries, a framework to add spatial window functions was implemented in PIConGPU as part of this thesis. The

---

[7] A decibel is a logarithmic unit that describes the signal strength of The signals P_1 to a reference signal P_0 using the

Table 4.1: A list of window functions currently implemented in PIConGPU. Values are given according to [120, 121].

Window function	**SLFO [dB/octave]**	**3dB-width** $[1/\Delta x]$	**remarks**
None [implicit rectangular]	-6	5,57	The result without a window function.
Triangle	-12	8,02	The side lobes are spaced apart with a distance twice as long as without a window function.
Hamming	-6	8,17	Even though the asymptotic SLFO is not good, the nearby side lobes are strongly reduced.
Triplet	-12	11,7	This window functions avoids any side lobes.
Gauss	-6	10,2	This is not a great window but physically reasonable.

simulation is generally confined in three dimensions, therefore a three-dimensional window function is needed. Since the spatial dimensions are independent, the window function $\mathcal{W}$ can be defined as a product of three one-dimensional filters $\mathcal{W}_1$.

$$\mathcal{W}(\vec{r}) = \mathcal{W}_1(x/L_x) \cdot \mathcal{W}_1(y/L_y) \cdot \mathcal{W}_1(z/L_z) \tag{4.24}$$

with L_x, L_y, and L_z being the extent of the simulation box in each dimension. The filter $\mathcal{W}(\vec{r})$ is applied to Eq. 2.10 according to the spatial position of each macroparticle.

$$\frac{\mathrm{d}^2 W}{\mathrm{d}\,\omega\,\mathrm{d}\,\Omega_{\mathcal{W}}}(\vec{n}, \omega) = \frac{q_e^2}{16\pi^3 \varepsilon_0 c} \cdot \left| \int_{-\infty}^{+\infty} \sum_{i=1}^{N_e} \mathcal{W}(\vec{r}_i) \cdot \frac{\vec{n} \times \left[\left(\vec{n} - \vec{\beta}_i \right) \times \dot{\vec{\beta}}_i \right]}{\left(1 - \vec{n} \cdot \vec{\beta}_i \right)^2} \cdot \mathrm{e}^{\mathrm{i}\,\omega (t - \vec{n} \cdot \vec{r}_i / c)} \,\mathrm{d}t \right|^2 . \tag{4.25}$$

Obviously, using no filter is equivalent to the following 3-dimensional rectangular filter:

$$\mathcal{W}_{\sqcap}(x, y, z) = \Pi(x/L_x) \cdot \Pi(y/L_y) \cdot \Pi(z/L_z) \tag{4.26}$$

thus causing the side lobes mentioned before. The window function attenuates the contribution of particles near the simulation boundary. By selecting a suitable window function, the strength of the side lobes in the simulation box is reduced. However, the influence of the radiation from the edge of the simulation area is also reduced and quantitative predictions may become more difficult.

Note that there is no perfect window function. The reduction of the side lobes must be weighed against a broadening of the signal. Therefore, the window function has to be chosen in view of the spectra expected. Additionally, applying a window function reduces the signal intensity and makes quantitative predictions more difficult.

In order to illustrate the effect of using a window function, Fig. 4.8 gives the spectra for the same simulation setup but using the Triangle and Triplet window function. When using the Triangle window function (Fig. 4.8 (a)), only every second side lobe overlaps the spectra. The response at the plasma frequency is clearly visible, but the response to the electric field is weaker than the signal at the plasma frequency. By using the Triplet window (Fig. 4.8 (b)), no side lobes overlap the spectra. The signals can be clearly identified. For both window functions, the overall

---

common logarithm: $L = 10 \cdot \log_{10}\left(\frac{P_1}{P_0}\right)$ dB. An octave is double (or half) the reference frequency.

[8] This is not always true. See [120] for details.

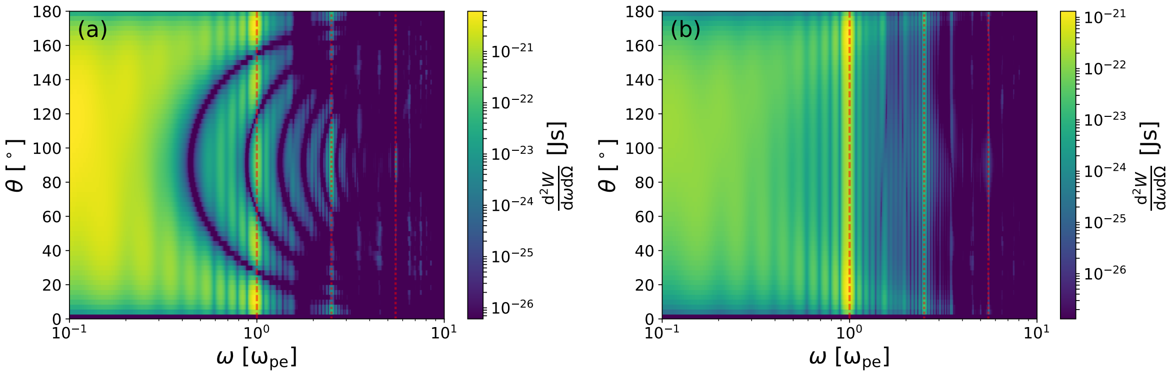

Figure 4.8: **Comparing two window functions:** Radiation spectra of the same simulation setup as in Fig. 4.7 but (a) with a Triangle window function and (b) with a Triplet window. While the Triangle window shows wider spaced side lobes as in Fig. 4.7, the Triplet window has no side lobes. The red lines mark the spectral peaks expected. The remaining side lobes arise from the finite simulation duration.

signal strength is reduced. The remaining side lobes originate from the temporal cutoff due to the finite simulation duration. These structures might contain valuable information on the duration of a signal. In PIConGPU, window functions are therefore not applied over time.

The use of filters is essential for simulations where radiation is expected at the edges of the simulation box. The Kelvin-Helmholtz instability (KHI) simulation presented in chapter 7 is such a case. In contrast, simulations in which hardly any radiation is emitted near the simulation box limits are inherently free of side lobes. For this reason, the use of window functions is not required for laser wakefield (LWFA) simulations (chapter 6).

4.5 Summary and Outlook

This chapter introduced the general methods to compute directionally resolved radiation spectra for arbitrary particle motion via Liénard-Wiechert potentials. A correct treatment of multiple particles that takes into account the phase relation between all particles was discussed. The technical implementation of the radiation diagnostics into the particle-in-cell code PIConGPU as an in-situ synthetic diagnostics was briefly reviewed. This part was kept short on purpose since it is discussed in detail in [61].

Subsequently, a number of benchmark tests were presented which validated the functionality of the in-situ plug-in. Based on the initial one-particle tests from [61], this thesis focused on the first many-particles tests and a detailed error analysis. These benchmark tests were published in [R8] and demonstrate that the radiation analysis plug-in in PIConGPU produces correct results even for many relativistic particles undergoing non-linear dynamics in highly intense laser fields.

Furthermore, two new technical methods, which were incorporated into the radiation plug-in, were presented. The form factor description of macroparticles allows a quantitatively correct prediction of coherent and non-coherent radiation. A mathematical method for deriving the form factors for arbitrary particle distributions was shown. A detailed description was published in [R10]. With this new method, quantitative predictions become possible.

The introduction of window function filters prevents side lobes in the spectrum caused by the boundary of the simulation area. Their use is essential for certain classes of PIC simulations with continuous boundary conditions to avoid interpreting misleading side lobes as real signals.

Only the extensions presented in this chapter made the work on radiation in plasmas in this thesis possible.

5 Radiation reaction

5.1 Taking radiation losses into account

In the previous sections, the emission of radiation by charged particles under acceleration and its computational modeling was discussed. Numerical issues of computing the spectrally and directionally resolved far-field radiation of test particles in a particle-in-cell simulation were examined. However, this purely diagnostic approach ignores that the charged particle loses energy due to the emitted radiation. This is an intrinsic drawback of the current radiation plug-in. However, this can be solved by including a particle pusher that takes into account the particle's energy loss due to radiation.[9] The question is whether radiation damping effects are important for laser plasma simulations. Anticipating the answer: for most scenarios currently not, but with increasing laser intensities in the labs worldwide, the radiation reaction might no longer be neglected. Following the most common *classical radiation reaction* considerations [59], the radiation damping starts playing a role when the energy loss due to emitted radiation becomes comparable with the kinetic and the potential energy of the charged particle in motion:

$$E_{\mathrm{rad}} \sim E_0 \quad . \tag{5.1}$$

The radiated energy can be approximated by the Larmor formula in the sub-relativistic approximation:

$$E_{\mathrm{rad}} = P_{\mathrm{Larmor}} \cdot \tau = \frac{q^2 a^2}{6\pi\varepsilon_0 c^3} \cdot \tau \tag{5.2}$$

with q and a being the particles charge and acceleration and τ being the characteristic time of the dynamics. In the linear acceleration case [59], this characteristic time can be approximated by

$$\tau = \frac{q^2}{6\pi\varepsilon_0 c^3 m} \tag{5.3}$$

with m being the mass of the particle. For particle motion longer than τ, radiation damping is negligible compared to the motion due to an external field. By assuming an interaction in an electromagnetic wave of frequency ω_0, the kinetic and potential energy of the particle can be approximated by $E_0 \sim m\omega_0^2 x^2$, with x being a typical amplitude of the particle motion in the

---

[9] Using the energy loss computed by the plug-in itself is not feasible. On the one hand, this calculation requires a time integration and thus would always be applied delayed. On the other hand, this time integration would have to be done for all billions of macroparticles separately which would require orders of magnitude more memory per particle than currently used. These reasons restrict this method only to extremely small test setups.

electromagnetic field. Since the acceleration is the second time derivate of the location, it can be approximated by $a \sim \omega_0^2 x$. Thus for

$$\omega_0 \tau \ll 1 \tag{5.4}$$

or equivalently for photon energies below

$$\hbar\omega_0 \ll 100\,\mathrm{MeV} \tag{5.5}$$

the radiation reaction becomes marginal for the dynamics during a single oscillation.

However, the slight energy loss still has a long-term effect on the particle dynamics. This effect highly depends on the scenario. For example, the radiation reaction becomes important for laser irradiation of a target with over-critical plasma density [123–126]. The results of these studies differ widely, ranging from no effect to a radiation damping starting already at normalized intensities above $a_0 \approx 50$. For relativistic electron bunches interacting head-on with a laser pulse, the radiation damping becomes important even earlier, for example at $a_0 = 10$ for a $150\,\mathrm{MeV}$ electron bunch [127]. These laser intensities are within reach with the DRACO laser at HZDR today [R11]. Considering radiation reaction in PIC-simulations is therefore not a purely theoretical study but of importance for upcoming experiments.

5.2 A brief derivation of the radiation reaction force

Treating the equation of motion of a charged particle that emits radiation has been investigated since the beginning of the 20th century [127]. However, for a point-like particle, like the electron, there is no completely correct, classical solution [59]. Only quantum electrodynamics is capable of handling the recoil force of an electron onto itself correctly. Such an approach, however, requires a stochastic treatment of the electron motion which itself leads to issues regarding the macroparticle sampling [128]. For instructional reasons, we will derive the radiation friction force in the sub-relativistic regime only and will provide the relativistically correct equations without deeper discussion since their derivation is lengthy and does not add to the understanding of the subject.

In the sub-relativistic case, the radiation power emitted by an electron in all directions is given by the Larmor formula:

$$\dot{E}_{\mathrm{rad}} = \frac{q^2 \dot{\beta}^2}{6\pi\varepsilon_0 c} \quad . \tag{5.6}$$

Based on this equation, Abraham and Lorentz introduced the radiation reaction force $\vec{F}_{\mathrm{rad}}$ to take into account the energy loss:

$$\Delta E_{\mathrm{rad}} = -\int_{t_1}^{t_2} \dot{E}_{\mathrm{rad}}\,\mathrm{d}\,t = -\frac{q^2}{6\pi\varepsilon_0 c}\int_{t_1}^{t_2} \dot{\beta}^2\,\mathrm{d}\,t = c \cdot \int_{t_1}^{t_2} \vec{F}_{\mathrm{rad}} \cdot \vec{\beta}\,\mathrm{d}\,t \quad . \tag{5.7}$$

It is important to notice that an electron does not only interact with its own radiation field but also with the so-called velocity field [58], an electromagnetic field caused by the particle motion, which however does not carry away energy from the electron but is reabsorbed. The interaction with the velocity field alters the electron motion, thus deriving a radiation force is only valid in a time-average description [129].

The integration of the acceleration over time can be split using integration by parts

$$\int_{t_1}^{t_2} \dot{\beta}^2\,\mathrm{d}\,t = \underbrace{\left(\vec{\beta}\cdot\dot{\vec{\beta}}\right)\Big|_{t_1}^{t_2}}_{=0} - \int_{t_1}^{t_2} \ddot{\vec{\beta}} \cdot \vec{\beta}\,\mathrm{d}\,t \tag{5.8}$$

with the boundary term being zero for small time intervals [59, 129]. Rearranging Eq. 5.7 leads to:

$$0 = \int_{t_1}^{t_2} \left(c \cdot \vec{F}_{\mathrm{rad}} - \frac{q^2}{6\pi\varepsilon_0 c} \ddot{\vec{\beta}} \right) \cdot \vec{\beta} \, \mathrm{d}\, t \quad . \tag{5.9}$$

The radiation force can thus be assumed to be:

$$\vec{F}_{\mathrm{rad}} = \frac{q^2}{6\pi\varepsilon_0 c^2} \ddot{\vec{\beta}} \quad . \tag{5.10}$$

This is the Abraham-Lorentz equation. Its relativistic generalization was accomplished by Dirac in 1938 [130]. However, these equations have unphysical "runaway" solutions. An alternative description was proposed by Landau and Lifshitz. By using the time derivative of Newton's second law $mc\ddot{\vec{\beta}} = \dot{\vec{F}}_{\mathrm{ext}}$, one can replace the second-order time derivative of the normalized speed in the Abraham-Lorentz equation:

$$\vec{F}_{\mathrm{rad}} = \frac{q^2}{6\pi\varepsilon_0 m c^3} \frac{\mathrm{d}}{\mathrm{dt}} \left(\vec{F}_{\mathrm{ext}} \right) \quad . \tag{5.11}$$

This is the sub-relativistic version of the Landau-Lifshitz equation. The full relativistic Landau-Lifshitz equation includes an additional summand scaling with q^2/m [127]:

$$\begin{aligned} \vec{F}_{\mathrm{rad}} = & \frac{q^2}{6\pi\varepsilon_0 m c^3} \left\{ \gamma q \left(\frac{\partial}{\partial t} + \vec{v} \cdot \vec{\nabla} \right) \left(\vec{E} + \vec{v} \times \vec{B} \right) \right. \\ & \left. + \frac{q^2}{mc} \left[\left[\left(\vec{\beta} \cdot \vec{E} \right) \cdot \vec{E} + c \left(\vec{E} + \vec{v} \times \vec{B} \right) \times \vec{B} \right] - \gamma^2 \vec{\beta} \cdot \left[\left(\vec{E} + \vec{v} \times \vec{B} \right)^2 - \left(\vec{\beta} \cdot \vec{E} \right)^2 \right] \right] \right\} \end{aligned} \tag{5.12}$$

Even though the Landau-Lifshitz equation is just an approximation of the Abraham-Lorentz-Dirac equation, it suffers less from runaway solutions and pre-acceleration [131]. It was shown that the critical manifold of the Abraham-Lorentz-Dirac equation, which describes stable solutions, is identical to the Landau-Lifshitz equation [132]. This, however, does not mean that the stable solution provided is physically meaningful. It still shows unphysical discontinuities in the radiation force [131].

5.3 Implementing the reduced Landau-Lifshitz equation

Implementing Eq. 5.12 into a particle-in-cell code to account for the radiation reaction is not an easy task since it depends on time derivates of the electromagnetic field. In order to include these time derivates numerically, not only the field's current value needs to be held in memory but at least a previous value as well. This doubles the required memory. It is appealing to search for simplifications of the full Landau-Lifshitz equation resembling very similar physics outcome but additionally being computationally less costly. While simplified versions of the Landau-Lifshitz equation have been implemented in particle-in-cell codes before [133], a detailed study on various simplifications has been performed only recently [94]. This study favors the following reduced version of the Landau-Lifshitz equation:

$$\vec{F}_{\mathrm{RLL}} = \frac{q^4}{6\pi\varepsilon_0 m^2 c^4} \left\{ \left[\left(\vec{\beta} \cdot \vec{E} \right) \cdot \vec{E} + c \left(\vec{E} + \vec{v} \times \vec{B} \right) \times \vec{B} \right] - \gamma^2 \vec{\beta} \cdot \left[\left(\vec{E} + \vec{v} \times \vec{B} \right)^2 - \left(\vec{\beta} \cdot \vec{E} \right)^2 \right] \right\} . \tag{5.13}$$

It simply neglects the proper time derivative $\frac{\mathrm{d}}{\mathrm{d}t} = \left(\frac{\partial}{\partial t} + \vec{v} \cdot \vec{\nabla} \right)$ in the first summand. This leads to no radiation force if the momentum is parallel to the electric field $\vec{p} \parallel \vec{E}$. However, this simplification can be made if

$$\frac{\vec{p}}{m^2 c^2} \left| \vec{F}_{\perp} \right|^2 \gg \frac{\mathrm{d}}{\mathrm{d}t} \vec{F} \tag{5.14}$$

is fulfilled [94], with $\vec{F}_\perp$ being the force perpendicular to the particle momentum. This condition is true except for very extreme fields close to the Schwinger limit. It is a useful simplification applicable to particle-in-cell codes.

As part of this thesis, the reduced Landau-Lifshitz equation was implemented in the particle-in-cell code PIConGPU. This required several changes in the framework. Using the Boris or Vay pushers (section 3.2) for integrating the particle dynamics numerically is inept since the radiation reaction force does not preserve energy and the advantage of these pushers to conserve energy becomes irrelevant. Instead, the Runge-Kutta 4th order scheme was implemented in the framework as a general differential equation solver. Then a particle-pusher was implemented that solved the following set of differential equations:

$$\dot{\vec{r}} = \frac{1}{\gamma m c} \cdot \vec{p} \tag{5.15}$$

$$\dot{\vec{p}} = q \cdot \left(\vec{E}(\vec{r}) + \frac{1}{\gamma m c} \vec{p} \times \vec{B}(\vec{r}) \right) + \frac{1}{w} \vec{F}_{\mathrm{RLL}}(\vec{r}, \vec{p}) \tag{5.16}$$

with $\vec{r}$, $\vec{p}$, q, m, γ and w being the macroparticle's position, momentum, charge, mass, relativistic Lorentz factor, and weighting respectively, using the Runge-Kutta 4th order scheme. In Eq. 5.16, the $1/w$ factor is important to notice. The change in momentum and the Lorentz force $\vec{F}_\mathrm{L}$ scale both linearly with the weighting due to their linear dependency on macroparticle mass m_mp and charge q_mp.

$$\vec{F}_\mathrm{L} \sim q_\mathrm{mp} = q_e \cdot w \tag{5.17}$$

$$\dot{\vec{p}}_\mathrm{mp} \sim m_\mathrm{mp} = m_e \cdot w \tag{5.18}$$

Therefore, the particle dynamics becomes independent of the weighting and only depends on the constant charge-to-mass ratio. This is not the case for the regular and reduced Landau-Lifshitz force (Eq. 5.12). It depends on the macroparticle charge and mass at different powers and thus scales non-linearly with the weighting. The reduced equation (Eq. 5.13) scales quadratically with the macroparticle weighting:

$$\vec{F}_\mathrm{LL} \sim \frac{q_\mathrm{mp}^4}{m_\mathrm{mp}^2} = \frac{e_e^4}{m_e^2} \cdot w^2 \quad . \tag{5.19}$$

This is, of course, unphysical, since the weighting is a purely numerical factor. This discrepancy arises from the fact that the Landau-Lifshitz equation was solely derived for electrons. The reduced Landau-Lifshitz force needs to be rescaled to a single electron in order to become independent of the weighting factor. Multiplying the force with the inverse of the macroparticle weighing (see Eq. 5.16) results in a particle dynamics independent of the macroparticle weighing. Since the Runge-Kutta method relies on sub-stepping, the field interpolation method and the particle-pusher framework in PIConGPU were extended to also support interpolation steps in between the regular particle-in-cell iteration steps. With all these implementations, the first pusher algorithm that includes radiation reaction in PIConGPU was implemented in October 2015.

5.4 Validating the radiation reaction in PIConGPU

In order to validate the correctness of the implementation and to estimate the limitations of this radiation reaction model, various tests were performed. Two of them are discussed in more detail here: an electron in a constant magnetic field and an electron interacting with a laser pulse.

In the first test case, an electron with a Lorentz factor γ_0 is propagating in a spatially homogeneous and temporally constant magnetic field B_0. Since the magnetic field performs no work on the electron, the only cause for a change in the electron's energy is the radiation reaction. Starting from the relativistic Larmor equation for circular motion [59]

$$\dot{E}_{\mathrm{rad}} = \frac{2q^2 c}{6\pi\varepsilon_0} \cdot \frac{\beta^4\gamma^4}{r^2} \tag{5.20}$$

with the time depending radius of the electron trajectory $r = \frac{m\gamma\beta c}{qB}$, the change of the electron's energy over time becomes:

$$\dot{\gamma} \cdot m \cdot c^2 = \frac{2q^4\gamma^2\beta^2}{6\pi\varepsilon_0 m^2 c} \cdot B_0^2 \quad . \tag{5.21}$$

This differential equation of form $\dot{\gamma} = \chi \cdot (\gamma^2 - 1)$ can be solved by separation of variables and has the solution [65]:

$$\gamma(t) = \frac{\gamma_0 + \tanh(\chi t)}{1 + \gamma_0 \tanh(\chi t)} \quad \text{with} \quad \chi = \frac{2q^4 B^2}{6\pi\varepsilon_0 m^3 c^3} \quad . \tag{5.22}$$

The Lorentz factor of the electron reduces from initially γ_0 to $\lim_{t\to\infty} \gamma = 1$. The rate of change is defined by χ and scales quadratically with the magnetic field.

In order to verify our implementation, simulations at various initial Lorentz factors γ_0 and magnetic field strengths B_0 were performed and compared with the analytical solution (Eq. 5.22). Exemplarily the electron trajectory and the energy evolution are illustrated in Fig. 5.1 for $\gamma_0 = 100$ and $B_0 = 10^7$ T. The evolution of the Lorentz factor matches perfectly with the prediction.

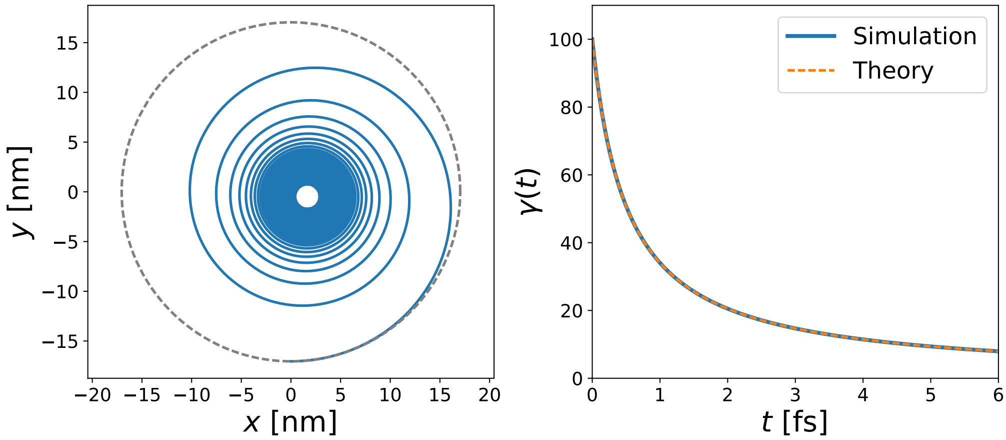

Figure 5.1: **Energy loss of an electron moving in a constant magnetic field:** Using the reduced Landau-Lifshitz (RLL) pusher to include radiation reaction, an electron with initial $\gamma_0 = 100$ was simulated in a magnetic field of strength $\vec{B}_0 = 10^7\ \mathrm{T}\ \vec{e}_z$. **Left:** The electron trajectory (blue) is contrasted to the electron trajectory without radiation damping (gray). **Right:** The energy loss is illustrated via the simulated (blue) and theoretical (orange) Lorentz factor over time.

As a second test, the head-on interaction of a relativistic electron with a laser pulse is considered. The energy loss under the influence of an electric field can be described by neglecting the first two terms in the Landau-Lifshitz equation (Eq. 5.12), since both are small compared to the third term, [123, 127] as:

$$\frac{\mathrm{d}\,\gamma}{\mathrm{d}\,t} = -\left[\frac{1}{4\pi\varepsilon_0}\frac{q^2\omega_0^2}{mc^3}\right] \cdot \gamma^2(t) \cdot a_0^2(t) \quad , \tag{5.23}$$

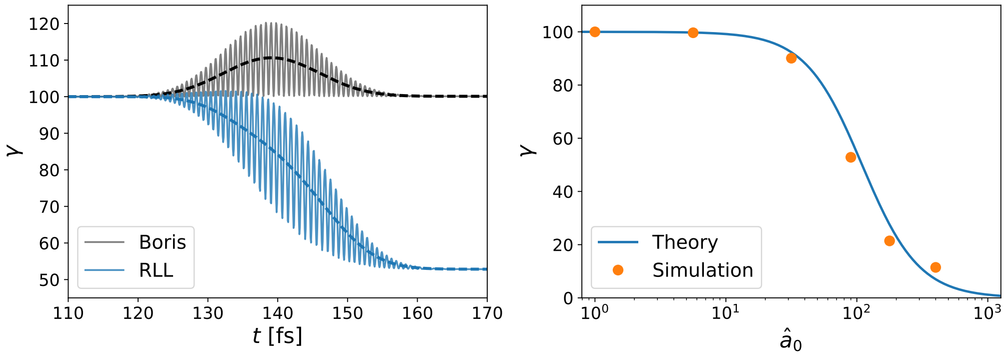

Figure 5.2: **Simulation of an electron with initial $\gamma_0 = 100$ interacting head-on with a laser pulse of FWHM pulse duration of $\tau = 30\,\mathrm{fs}$: Left:** The evolution of the relativistic Lorentz factor γ during the interaction with the laser pulse is plotted over time t for $\hat{a}_0 = 90$. In blue, the results of the reduced Landau-Lifshitz pusher (RLL) are plotted while in gray, the evolution computed using the Boris pusher is displayed. Dashed lines represent time-averaged values while the thin solid lines show the detailed evolution.**Right:** The Lorentz factor after the propagation through the laser pulse is plotted for various normalized laser field strengths $\hat{a}_0$. The simulated results are compared to theoretical predictions according to Eq. 5.24 plotted as a blue line.

with $a_0(t) = \frac{q_e E(t)}{m c \omega_0}$ being the normalized laser amplitude. For a laser amplitude of $a_0(t) = \hat{a}_0 \cdot e^{-\frac{1}{2}\left(\frac{t - x/c}{\sigma_t}\right)^2} \cdot \sin(\omega_0 t)$, with $\hat{a}_0$, σ_t and ω_0 being the peak normalized electric field strength, the laser pulse duration and laser frequency, integrating Eq. 5.23 gives the electron's Lorentz factor after passing through the laser pulse:

$$\gamma = \gamma_0 \left[1 + \frac{2\pi r_e \gamma_0 \hat{a}_0^2 \omega_0 \sigma_t \chi}{\lambda_0 + 2\pi r_e \gamma_0 \hat{a}_0^2 \omega_0 \sigma_t \chi} \right] \tag{5.24}$$

with $\lambda_0 = \frac{2\pi c}{\omega_0}$ being the laser wavelength, $r_e = \frac{1}{4\pi\varepsilon_0} \frac{e^2}{m_e c^2}$ being the classical electron radius, γ_0 being the initial Lorentz factor before the laser interaction and $\chi = \frac{\sqrt{\pi}}{2}\left(1 - e^{-\sigma_t^2 \omega_0^2}\right)$ being a factor coming from the time integration over the laser envelope[10].

In order to verify the reduced Landau-Lifshitz (RLL) pusher implementation in PIConGPU, the head-on interaction of an electron with initial Lorentz factor $\gamma_0 = 100$ interacting with a laser pulse of a full width at half maximum (FWHM) duration in intensity of $\tau = 30\,\mathrm{fs} = 2\sqrt{\ln(2)}\sigma_t$ was simulated for various intensities. An exemplary evolution of the Lorentz factor γ during the laser head-on scattering is shown in Fig. 5.2 (left). The final Lorentz factor after the electron propagated through the laser pulse is plotted for various peak intensities $\hat{a}_0$ in Fig. 5.2 (right). The reduction in energy follows the approximation in Eq. 5.24 very well. The slight deviations are caused by the limited temporal resolution of the particle-in-cell simulation and the neglecting of ponderomotive forces, which scale with $\sim a_0^2$ and become more relevant at higher a_0.

In summary, both test show excellent agreement with the theoretical predictions.

It is important to mention that this treatment of radiation losses is completely classical. In order to extend the particle-in-cell algorithm towards including quantum electrodynamic effects, scattering processes need to be included by Monte-Carlo methods [128]. By introducing photons, the energy loss during emission can be treated naturally. This approach avoids some of the

---

[10] Please note that Koga et al. [127] approximated this factor by 1. This approximation is, however, equivalent to a 63% shorter pulse compared to the pulse length definition by Koga et al.. The integration should not be neglected in quantitative comparisons.

shortcomings of the classical radiation reaction mentioned before and allows including the probabilistic nature of the emission process. However, the introduction of QED scattering processes comes at the cost of sampling issues due to the use of macroparticles in particle-in-cell codes. Recently, two QED modules, one for scattering from strong electromagnetic fields and one from the Coulomb field of the ion background, have been included in PIConGPU [65]. A comparison between the QED module and the reduced Landau-Lifshitz pusher, developed as part of this thesis, showed good agreement as long as the emitted photon energy is much smaller than the electron energy. However, the QED module is not capable of reproducing coherent radiation effects - in contrast to the classical radiation plug-in. Thus in the classical limit, only the in-situ radiation plug-in is capable of reproducing spectral features as e.g., higher harmonics at multiples of the laser frequency or during betatron radiation in the wiggler regime.

5.5 Summary and Outlook

This chapter provided a brief theoretical introduction on how to include the energy loss caused by radiation via a classical radiation-reaction force into PIConGPU. The reduced Landau-Lifshitz (RLL) pusher algorithm was discussed in detail. The focus was put on the computational effective implementation by reducing data access and the associated reduced physical accuracy of the RLL algorithm. A required rescaling of the recoil force caused by the non-linear scaling of the Landau-Lifshitz force with the macroparticle weighting was explained. Two exemplary test cases, an electron moving in a homogeneous magnetic field and an electron interacting with an intense laser pulse, were presented in detail. The simulation results agreed excellently with theoretical predictions and validated the correct implementation of the radiation recoil pusher algorithm in PIConGPU.

As part of this thesis, the framework for the pusher algorithms in PIConGPU was extended to allow sub-stepping algorithms that integrate the particle motion with smaller time steps than the PIC-cycle, thus allowing an increased numerical accuracy and a wider range of possible algorithms. With this new framework, the reduced Landau-Lifshitz pusher was implemented and tested. It now allows going beyond the limitations of previous simulations, were the radiation losses needed to be negligible [R9]. The implemented classical recoil force was also an essential test case for validating the newly developed synchrotron and bremsstrahlung modules included in PIConGPU [65]. With upcoming experiments at higher laser intensities and with longer acceleration durations due to longer gas nozzles used in laser wakefield experiments, taking radiation losses into account will become essential in future simulations.

6 Radiation as diagnostics during laser wakefield acceleration

6.1 Advantages of small-scale plasma accelerators and challenges in their diagnostics

Laser wakefield acceleration (LWFA) is a modern method for accelerating electrons that exploits the plasma response to a short, intense laser pulse.

Conventional accelerators use radio-frequency (RF) cavities to generate electric fields for accelerating charged particles. The electric fields reached in these cavities are limited to around $100\,\mathrm{MV/m}$ [8, 9]. Beyond this so-called vacuum breakdown limit, electrons are pulled out of the metal surface into the vacuum. This causes the applied electric potential and the functionality of the accelerating structure to break down. Therefore, reaching TeV electron energies requires a $10\,\mathrm{km}$ long linear accelerator when using these conventional techniques. Alternatively, a circular accelerating structure, like the synchrotron accelerator, can be utilized to reuse the accelerating structure and to reduce the size of the required construction [8]. But due to the constant transverse acceleration, radiation losses limit the compactness of these structures as well. In order to accelerate electrons to $100\,\mathrm{GeV}$, the LEP accelerator at CERN was therefore built [134] with a circumference of $27\,\mathrm{km}$ [135]. The proposed international linear collider (ILC) will have a length of $31\,\mathrm{km}$ in order to achieve a final electron energy of $0.5\,\mathrm{TeV}$ [136]. This immense size results of course from the high energies aimed for. But similar issues, regarding construction costs, size and personnel, arise with medical or industrial accelerators operating at lower particle energies. Their size is determined by the breakdown limit of the RF cavities as well.

Plasma-based accelerators such as the LWFA circumvent this limiting issue. Laser wakefield accelerators can reach electric field strengths greater than $100\,\mathrm{GeV/m}$ [137, 138], thus allowing more compact accelerator structures. By utilizing plasma structures of tens of micrometers in size, laser wakefield accelerators also provide bunch lengths of similar size. Bunch durations in the few-femtosecond range become available [21, 139] - which can hardly be reached with conventional accelerators [140]. In combination with the relatively large amount of charge accelerated, the LWFA can provide tens of kiloamperes of electric current [R2, 141, R12], while conventional accelerators can only reach a few kiloamperes [140, 142]. This higher peak current in combination with the compact accelerator structure makes LWFA ideally suited for driving small, new light sources.

Starting with the initial idea by Tajima and Dawson in 1979 [7] of using excited plasma waves to accelerate electrons, various concepts of accelerating particles by exciting plasma waves with lasers have been studied. With the developments of chirped pulse amplification by Mourou et al. [143–145], laser intensities beyond $10^{15}\,{}^{W}\!/_{\mathrm{cm}^2}$ became achievable and with today's petawatt-class lasers, intensities beyond $10^{21}\,{}^{W}\!/_{\mathrm{cm}^2}$ can be reached. These high laser intensities at short pulse durations enabled reaching higher electron energies. In 2004, the so-called blowout regime [146, 147] was experimentally realized by three groups simultaneously [10, 12, 13] reaching electron energies of $100\,\mathrm{MeV}$ with a significant charge in the order of a nanocoulomb. The crucial technical step in reaching this regime was reducing the laser pulse duration to match the plasma wavelength $\tau \cdot c \leq \lambda_{pe}$. In contrast to all other previous experiments, the charge was located in a quasi-monoenergetic electron bunch and not in a continuous energy distribution. Higher charges and energies could be reached with this method. For example, a few picocoulomb of charge were accelerated to a few GeV of energy [14, 15, 148, 149]. Most recently two orders of magnitude more charge was reached by accelerating $\sim 300\,\mathrm{pC}$ to around $300\,\mathrm{MeV}$ at HZDR [R2, R12].

By staging these LWFA accelerators and, subsequently, externally injecting the accelerated bunch into a second plasma accelerator stage [150, 151], electron energies beyond a few GeV are expected to become achievable in the future.

Most laser wakefield accelerators used today operate in a nonlinear plasma wave regime, which cannot be treated self-consistently by analytical models [1]. Gaining an understanding of the plasma dynamics thus heavily relies on particle-in-cell simulations. These simulations provide a wealth of information of the plasma and laser dynamics occurring during the laser wakefield acceleration. This ranges from time-resolved phase space distributions to a self-consistent evolution of the laser in the plasma. However, this enormous amount of information cannot be compared directly with experiments. In experiments, final electron energy distributions and laser parameters are routinely measured [10, 12, 13, R2]. In order to get some information on the electron phase space, radiation is often recorded as well. Common radiation diagnostics are wave-breaking signatures [28] or betatron radiation [23–26, 152–155] which provide information on the electron self-injection or on the accelerated electron beam in the plasma cavity. Furthermore, single shot real-time measurements of the plasma wake and the magnetic fields can be performed via shadowgraph and Faraday-rotation measurements [21]. These two methods, however, are limited to resolving only a short time period of a few femtoseconds, and cannot provide a single-shot diagnostics over the entire laser plasma dynamics. A detailed review of diagnostic methods for LWFA can be found in [156].

All these experimental measurements either provide information on the final (high-energy) electron bunch, such as the electron energy distribution measurements or the betatron radiation, or they provide information on a specific point in time, such as the shadowgraph diagnostics or the wave-breaking radiation signature. Particle-in-cell codes, on the other hand, show a wealth of plasma and laser dynamics during the laser-matter interaction, that so far cannot be observed experimentally.

Since the laser-plasma dynamics changes throughout the interaction, the electron dynamics changes as well. This electron phase space dynamics can only be continuously measured by means of radiation diagnostics where the characteristic photon emission reflects the electron distribution at a certain point in time and space. However, the correlation between the electron phase space and the emitted radiation is non-trivial during LWFA and thus requires simulating the LWFA plasma dynamics and the associated radiation. Such a synthetic radiation diagnostics is capable of linking the plasma electron dynamics to the emitted radiation since both are available in simulations and their correlation can be directly identified and quantified.

In the following, various radiation signatures are presented that allow determining different states of the laser wakefield acceleration. However, the main focus is on a newly discovered radiation signature that allows determining the spatial location of the blowout regime during laser defocusing. This spectral signature not only allows determining whether the blowout regime has been reached, but it also enables measuring the laser focus position in the plasma for every laser shot even though its focus is altered by the laser's non-linear interaction with the plasma.

In section 6.2 a brief theoretical introduction to laser wakefield acceleration is provided. It focuses on the fundamental principles, the highly nonlinear blowout regime, the laser dynamics in the plasma, and various injection methods. Subsequently, section 6.3 introduces a simple scattering model that allows describing the fundamental process behind the discovered radiation signature. Details on various characteristic radiation signatures determined via a large-scale particle-in-cell simulation are given in section 6.4. This large-scale simulation also illustrates the limitations of the quasi-static scattering model. However, these limitations are the basis for determining the focus position. The discovered radiation diagnostic method is tested against numerous simulations based on an experimental setup used at HZDR to validate whether the laser focus position can be determined by analyzing scattered radiation. The simulated spectra show that the proposed spectral method allows determining the laser focus position precisely . Finally, section 6.5 discusses this ongoing case study of a self-truncated ionization injection LWFA setup used at HZDR for accelerating quasi-monoenergetic electron bunches at an unprecedented charge. The new spectral diagnostic method, which is developed theoretically here, would allow understanding the laser plasma dynamics better in experiments and could potentially settle discrepancies between simulation and experiments. In the outlook (section 6.6), the advantages of radiation diagnostics are briefly discussed on the basis of further practical applications.

6.2 Fundamental processes behind laser wakefield acceleration

Since the initial idea of using laser pulses as drivers for plasma-based accelerators in 1979 [7] a lot of research went into this field. Not all of the developed acceleration schemes are relevant for this thesis, therefore, only the fundamental principle and the relevant concepts for understanding the following sections will be introduced in this section. Whenever possible, derivations that do not reveal fundamental principles are avoided and publications providing more information are referenced. A detailed review of the field of laser-driven plasma-based electron accelerators with a wealth of literature references can be found in [1].

6.2.1 Generating plasmas with relativistic lasers

A characteristic parameter to describe the intensity of a laser pulse is the so-called dimensionless field strength parameter:

$$\begin{aligned} a_0 &= \frac{q_e \cdot E}{m_e \cdot c \cdot \omega_0} && (6.1) \\ &= 0.85 \cdot 10^{-12} \cdot \lambda_0\,[\mathrm{nm}] \cdot \sqrt{I_0\,[\mathrm{W/cm^2}]} && (6.2) \end{aligned}$$

where q_e and m_e are the electron charge and mass, E is the electric field, c is the speed of light, ω_0 and λ_0 are the laser frequency and wavelength, and I_0 is the laser intensity. This dimensionless parameter gives the strength of the electric field relative to the resulting electron energy. For a value of $a_0 = 1$, an electron reaches a kinetic energy equal to its rest energy in half a laser period. In order to quantify the intensity of the laser pulse in an experiment or a simulation, the peak value reached in the vacuum is usually given.

The change in motion of a charged particle with charge q and mass m can be described by the Lorentz force.

$$\frac{\mathrm{d}\vec{p}}{\mathrm{d}t} = m\frac{\mathrm{d}\vec{\beta}\gamma}{\mathrm{d}t} = \vec{F} = q \cdot \left(\vec{E} + \vec{v} \times \vec{B}\right) \qquad (6.3)$$

Even for today's laser field strengths of $a_0 \sim 10$, ions with their ${}^{m_i}/_{m_e} \geq {}^{m_p}/_{m_e} = 1836$ times larger mass hardly reach relativistic velocities, so that their wiggling motion in the laser field can be neglected.

Before a laser can excite a plasma wave, the electrons need to be separated from the ions and a plasma with free-moving electrons needs to be generated. This requires energy, which is usually provided in the form of an electric field in experiments. Classically, the necessary electrical field strength needed to detach the electrons from the atomic potential can be estimated by examining the deformation of the Coulomb potential under the influence of an external electric field E_x^{ext}:

$$\Phi(x) = -\frac{Z \cdot q_e^2}{4\pi\varepsilon_0 |x|} - q_e \cdot E_x^{\text{ext}} \cdot x \tag{6.4}$$

with $\Phi(x)$ being the total potential at the position x, Z being the atomic number, and ε_0 being the electric constant (see Fig. 6.1). If the binding energy $\mathcal{E}$ is equal to the potential Φ in the maximum ${}^{\partial\Phi(x_{\text{bar}})}/_{\partial x} = 0$,

$$q_e \cdot \Phi(x_{\text{bar}}) = \mathcal{E} \quad , \tag{6.5}$$

the minimal field strength or intensity at which ionization occurs can be determined:

$$a_0 \geq \frac{\pi\varepsilon_0}{m_e c \omega_0 q_e^2} \cdot \frac{\mathcal{E}^2}{Z_{\text{eff}}} \tag{6.6}$$

$$I_0\,[\text{W/cm}^2] \geq 4.0 \cdot 10^9 \cdot \frac{\mathcal{E}_{\text{ion}}^4\,[\text{eV}]}{Z_{\text{eff}}^2} \quad . \tag{6.7}$$

Numerically this classical ionization is described by the BSI model in particle-in-cell simulation [157]. Of course, electrons can quantum-mechanically tunnel through the reduced potential wall. This lead to ionization even at lower field strengths (see Fig. 6.1). In PIC simulations this effect can be considered by the so-called ADK and Keldysh models [158].

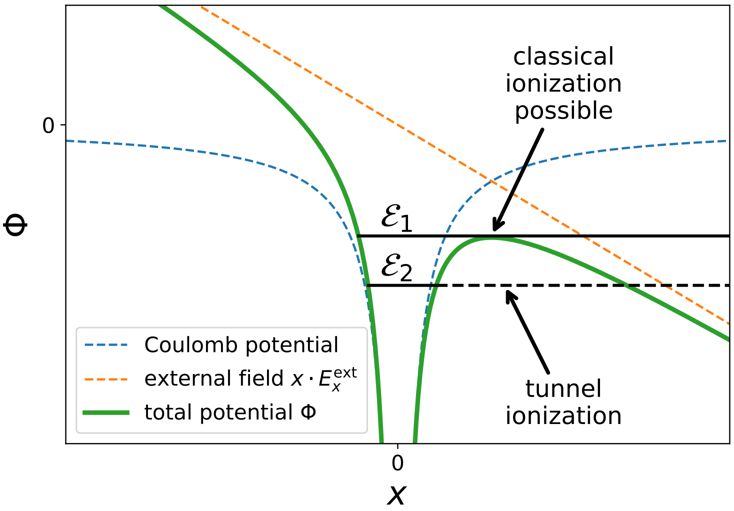

Figure 6.1: **Illustration of ionization:** This plot shows how an external electric field E changes the Coulomb potential around an atom, thus releasing electrons. Classically, the external field must reduce the total potential of Φ to the extent that the electron with binding energy $\mathcal{E}_1$ can overcome the barrier. Quantum mechanically, ionization is already possible at stronger binding energies $\mathcal{E}_2$ due to tunneling.

In order to generate a plasma in the experiment, strong electrical currents can be used, which convert neutral gas into a plasma in a so-called discharge capillary via collisional ionization.

The laser pulse can then propagate through the pre-ionized plasma. In the case of intense laser pulses, however, it is usually sufficient for the laser itself to ionize the gas via the field ionization process described above. For example, the electron of the hydrogen atom is bound with $\mathcal{E}_{\text{ion}} = 13.6\,\text{eV}$. According to equation 6.6, it can be regarded as free-moving at field strengths above $a_0 = 8 \cdot 10^{-3}$. These field strengths are reached by the laser pulse far before the pulse peak so that the laser front itself generates a plasma without losing much of its total energy or being significantly influenced in its dynamics. The only effect of this approach is an ionization-induced blueshift of the pulse front and a slight defocusing of the laser pulse. In a simulation, the assumption of pre-ionized gases is therefore justified even if no discharge capillaries were used in the experiment itself.

For the so-called ionization injection, on the other hand, pre-ionization cannot be assumed. In this scheme, the inner shell electrons separate from the ions, due to their strong binding energy, only when the laser intensity is sufficiently high. This allows a more controlled injection into the plasma cavity than with electrons from the outer shells. A detailed description of this method can be found in section 6.2.5.

6.2.2 The laser's ponderomotive force as the driver of a plasma wave

A laser pulse interacting with a plasma causes electrons to oscillate at the laser frequency. Due to the spatial (transversal) and temporal (longitudinal) laser pulse envelope, electrons experience varying field strengths during their oscillation and will undergo a drift in the direction of decreasing intensity. This so-called ponderomotive force is a time-averaged force and can be computed for non-relativistic field strengths ($a_0 \ll 1$) by:

$$\vec{F}_{\text{pond}} = -\frac{q_e^2}{4 m_e \omega_0^2} \vec{\nabla} \left(\hat{E}^2 \right) \quad , \tag{6.8}$$

with m_e, q_e being the electron mass and charge and ω_0 being the laser frequency while $\hat{E}$ is the envelope of the laser amplitude [159]. For relativistic laser intensities ($a_0 \gtrsim 1$), deriving the ponderomotive force becomes more complex and is still a field of ongoing research [159]. A valid description that still contains the slow drift momentum $\vec{p}_s$ of the electrons caused by the laser ponderomotive force is

$$F_{\text{pond}} = -m_e \cdot c^2 \vec{\nabla} \left\langle \left(1 + \frac{\vec{p}_s^{\,2}}{m^2 c^2} + \frac{a_0^2}{2} \right)^{1/2} \right\rangle \quad . \tag{6.9}$$

with $\langle \dots \rangle$ denoting the cycle-average [56]. While quantitatively resulting in a different ponderomotive force scaling, in the mildly relativistic regime the qualitative results are equivalent: electrons are pushed to the side of the laser pulse like snow by a snowplow.

Such a laser pulse propagating through a plasma will be slowed down due to the refractive index of the plasma medium. The dispersion relation of an electromagnetic wave of wave number k is

$$\omega^2 = \omega_{pe}^2 + c^2 k^2 \tag{6.10}$$

with ω_{pe} being the plasma frequency

$$\omega_{pe} = \sqrt{\frac{n_e \cdot q_e^2}{\varepsilon_0 \cdot m_e}} \tag{6.11}$$

and with n_e, q_e, m_e and ε_0 being the electron density, charge, mass and the vacuum permittivity respectively [3]. The group velocity of the laser pulse is slower than the speed of light and it can excite a plasma wave (also called plasmon or Langmuir wave) with a phase velocity v_{pe} equal to the group velocity of the laser v_g^{laser} [7]

$$v_{pe} = \frac{\omega_{pe}}{k_{pe}} = v_g^{\text{laser}} = \frac{\partial \omega}{\partial k} = c \cdot \sqrt{1 - \frac{\omega_{pe}^2}{\omega_0^2}} \tag{6.12}$$

with ω_0 being the laser frequency and k_{pe} the plasma wave number.

It can be shown, that such a plasma wave is excited most efficiently if the laser's longitudinal envelope is half as long as the plasma wavelength $\lambda_{pe} = \frac{2\pi c}{\omega_{pe}}$ [7]. Such a pulse duration ensures maximum laser energy without destroying the wakefield.

While oscillating in the laser field, the plasma electrons feel the ponderomotive force and are pushed to the front and the side of the laser pulse. This displacement causes a charge separation which attracts the electrons towards the positively charged plasma tail behind the laser after the laser has passed. The electrons start oscillating around this ion tail. At non-relativistic laser intensities ($a_0 < 1$), these electron oscillations behind the laser pulse cause a sinusoidal plasma density wave and a by $\pi/2$ shifted electric field modulation. A detailed derivation of this density fluctuation and the parallel electric field generation in the non-relativistic case can be found in [160, 161].

The influence of the laser ponderomotive force can be described by the potential Φ. In normalized units, this potential can be computed by the following second-order differential equation:

$$\Psi(\xi) = \frac{q_e \Phi(\xi)}{m_e c^2} \tag{6.13}$$

$$\frac{\partial^2 \Psi}{\partial \xi^2} = k_p^2 \gamma_p^2 \left[\beta_p \left(1 - \frac{1 + a^2(\xi)}{\gamma_p^2 (1 + \Psi(\xi))} \right)^{-1/2} - 1 \right] \tag{6.14}$$

with $\xi = z - c \cdot t$ being the co-moving position, $\beta_p = v_\phi / c \approx v_g / c$ being the normalized phase velocity, which is approximately equal to the group velocity, $\gamma_p = 1/\sqrt{1 - \beta_p^2}$, being the according Lorentz factor and $k_p = \omega_{pe}/c$ being the plasma wave number. The laser envelope $a(\xi)$ is given in units of normalized field strength a_0.

For a given laser pulse, the potential can be solved numerically. From this solution, the longitudinal electric field E_z and the density fluctuation n_e can be derived:

$$\frac{E_z}{E_0} = -\frac{c}{\omega_{pe}} \frac{\partial \Psi}{\partial \xi} \tag{6.15}$$

$$\frac{n_e}{n_0} = \gamma_p^2 \beta_p \left[\left(1 - \frac{1 + a^2(\xi)}{\gamma_p^2 (1 + \Psi(\xi))^2} \right)^{-1/2} - \beta_p \right] \tag{6.16}$$

with n_0 being the initial homogeneous electron density of the plasma and $E_0 = {}^{m_e c \omega_{pe}}/_{q_e}$ being the wave-breaking field introduced in Eq. 1.1.

Figure 6.2 depicts two exemplary cases of laser wakefield acceleration with a peak laser field strength of $a_0 = 0.5$ and $a_0 = 1.5$. The plasma density is depicted as a black solid line. Its sinusoidal modulation behind the driving laser beam can be clearly identified for the subrelativistic laser intensity $a_0 = 0.5$. A similar harmonic structure occurs for the accelerating field E_z. For the mildly relativistic case $a_0 = 1.5$, the plasma response becomes non-linear. A high electron density accumulates at the end of the plasma cavity and the accelerating field follows a sawtooth-like shape.

The electric field created by the plasma wake behind the laser has a longitudinal component that allows accelerating electrons for half of the wake's wavelength. The electrons in this field

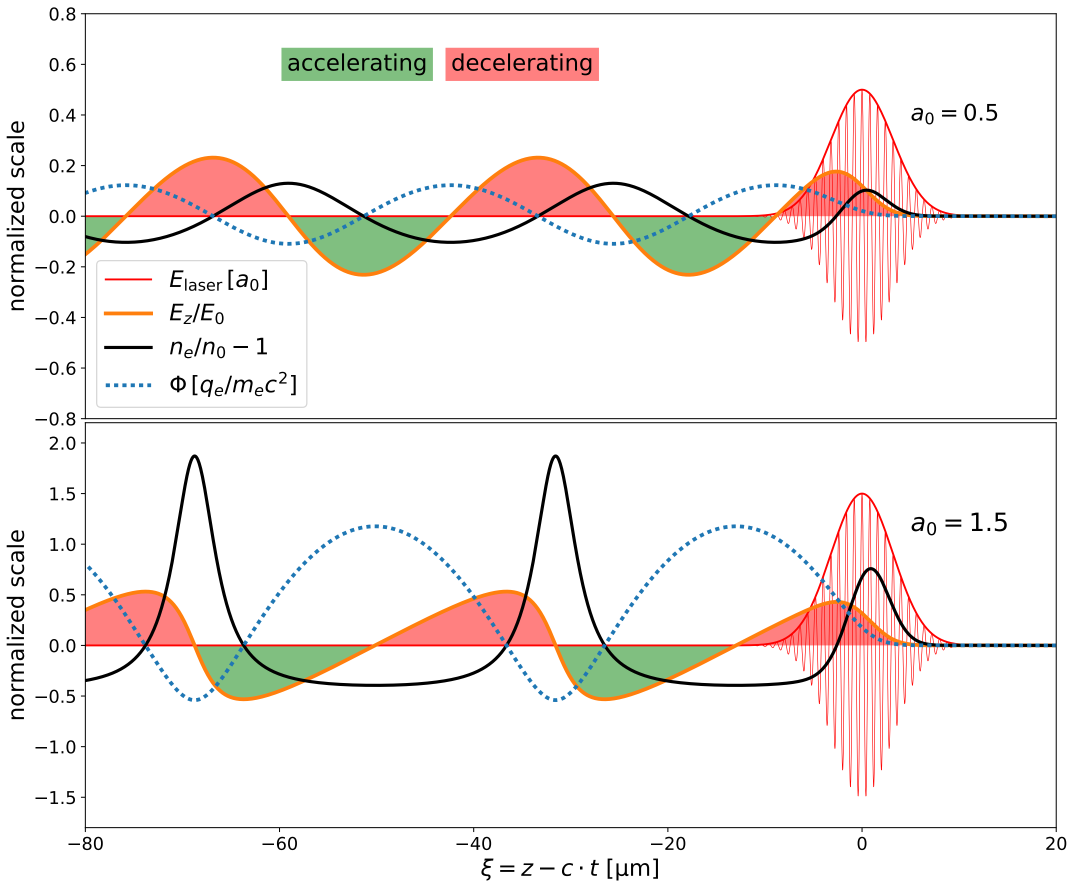

Figure 6.2: **Two plasma wakes after a short laser pulse of different intensity:** Both plots illustrate how a laser pulse generates a plasma wake. The upper plot shows a laser pulse with a normalized field strength $a_0 = 0.5$. The resulting potential, accelerating field and density have approximately a sinusoidal evolution. The lower plot shows a laser pulse in the mildly relativistic regime with $a_0 = 1.5$. The response to the pulse is nonlinear as can be clearly seen by the potential, density, and electric field. The green and red shaded background mark the accelerating and decelerating region respectively. In both cases, a laser pulse duration of $\sigma = 15\,\mathrm{fs}$ and an initial plasma density of $n_0 = 10^{18}\,\mathrm{cm}^{-3}$ was chosen. The x-axis represents the co-moving longitudinal position ξ with the laser pulse being at $\xi = 0$. The y-axis represents the following normalized quantities: the laser field E_{laser} in multiples of a_0 in red, the accelerating field E_z normalized to E_0 in orange, the density n_e normalized to the unperturbed density n_0 minus 1 in black, and the potential energy Φ in blue.

can reach relativistic velocities easily. Since after an initial acceleration the trapped electrons follow the driving laser pulse with approximately the speed of light and gain momentum mainly by the relativistic mass increase, the once trapped electrons can follow the laser pulse for quite some time $t \gg \omega_{pe}^{-1}$ and gain significant energy. The exact longitudinal field strength depends on the laser intensity and the plasma density. But by a simple dressed-photon description [7] and the critical longitudinal electric field strength of ($E_{\parallel}^{\mathrm{crit}} = m_e c \omega_{pe} q_e^{-1}$) [162], the maximum reachable Lorentz factor can be predicted as:

$$\gamma^{\max} = 2\frac{\omega_0^2}{\omega_{pe}^2} \quad . \tag{6.17}$$

In order to reach this energy, the electron propagates for $t = \Delta p / F = \gamma^{\max} m_e c / q_e E_{\parallel}^{\mathrm{crit}}$ close to the speed of light and reaches its maximum energy after [7]

$$L_\gamma = 2c\frac{\omega_0^2}{\omega_{pe}^3} \quad . \tag{6.18}$$

Exemplarily that means for a 800 nm Ti:Sapphire laser such as DRACO at HZDR [R11] and moderate electron densities of $n_e = 3 \cdot 10^{18}\,\mathrm{cm}^{-3}$, electrons can theoretically reach a maximum energy of $E^{\max} = \gamma^{\max} m_e c^2 \approx 590\,\mathrm{MeV}$ after a distance of just $L_\gamma = 3.6\,\mathrm{mm}$.

In practice, exciting these plasma waves at low laser intensities has several drawbacks ranging from lower energies than theoretically predicted, to continuous electron injection and thus broad electron energy spectra, to limitations on how to contain the laser focus for millimeter propagation distances. The issue of broad energy spectra is solved by going to the nonlinear wave-breaking regime also called the blowout regime, discussed in section 6.2.3. Limitations caused by the laser propagation are covered in section 6.2.4. Finally, various injection methods are introduced that give control over the electron injection into the plasma cavity and thus on the final energy distribution (section 6.2.5).

6.2.3 The blowout regime

With further laser improvements, the plasma wave excitation transitioned from the linear to the non-linear regime (e.g., [163]). The same was true for simulations at that time. In 2002 Pukhov and Meyer-ter-Vehn published simulation results of a laser wakefield accelerator with such high laser intensities that the ponderomotive force pushed aside all electrons, thereby creating a singular electron-free cavity directly behind the driving pulse [146]. In this cavity a quasi-monoenergetic few-fs short electron bunch was accelerated to 300 MeV. This regime was dubbed "bubble", "blowout" or "cavitation" regime [1]. It was experimentally demonstrated in 2004 by three independent groups [10, 12, 13].

This regime not only provided an extremely strong accelerating electric field but also equally strong transversal focusing fields, thus ensuring excellent electron beam quality. These transverse focusing fields cause electrons which are injected off-axis to oscillate around the center of the plasma cavity. This transverse oscillation of the accelerated electrons leads to the emission of the so-called betatron radiation at x-ray frequencies [27, 164, 165].

Since this bubble regime causes highly nonlinear plasma dynamics, there is so far no consistent 3-dimensional theory. In order to investigate it, one has to rely on simulations from which a variety of scaling laws could be derived [1].

In the ideal blowout regime, the plasma cavity takes a spherical shape with radius $R \approx \lambda_{\mathrm{pe}}$. This regime can only be reached if the laser pulse is shorter than the plasma cavity created by the laser pulse $c \cdot \tau < \lambda_{\mathrm{pe}}$. In addition, the laser spot size should correspond to the radius of the cavity $w_0 \approx R$. With this so-called matching condition, optimal self-guiding (see section 6.2.4) is automatically fulfilled as well. For an optimal bubble cavity, at least $a_0 > 4$ is required. However, almost completely electron-free plasma cavities are generated for $2 \leq a_0 \leq 4$ as well. These also show excellent acceleration properties but their shape is not yet spherical.

Under these ideal conditions, the back of the plasma cavity can reach a longitudinal electric field strength of

$$E_z^{\max} \approx \frac{m_e c \omega_{pe}}{q_e} \cdot \sqrt{a_0} = E_{\parallel}^{\mathrm{crit}} \cdot \sqrt{a_0} \tag{6.19}$$

and can, therefore, increase the acceleration gradient by a factor $\sqrt{a_0}$ compared to the linear and weakly nonlinear regime. In the co-moving coordinate frame of the bubble, the accelerating field along the laser propagation direction can be described by

$$E_z(\xi) = \frac{k_p \cdot \xi}{2} \cdot E_0 \tag{6.20}$$

with $\xi \approx z - c \cdot t$ being the co-moving position and $\xi = 0$ representing the center of the bubble. The acceleration field is independent of the radius and increases linearly with the distance to the laser pulse, thus providing ideal acceleration properties [1].

The electric and magnetic fields governing the transversal focusing inside the cavity can be described approximately by the following set of equations:

$$E_r \approx \frac{k_p \cdot r}{4} \cdot E_0 \tag{6.21}$$

$$B_\theta \approx -\frac{k_p \cdot r}{4 \cdot c} \cdot E_0 \tag{6.22}$$

with r being the radial position in the cavity and $r = 0$ being the center. These fields act as strong focusing forces on the relativistic electrons following the laser, pushing them back towards the transversal center of the cavity.

$$F_r(r) \approx q_e \cdot (E_r(r) - c \cdot B_\theta(r)) = q_e \cdot \frac{k_p \cdot r}{2} \cdot E_0 \tag{6.23}$$

Since the transversal field increase linearly with the radius r, the normalized emittance of the electron bunch is preserved during its acceleration [1]. Furthermore, these focusing fields are independent of ξ and thus do not introduce an additional energy spread to the accelerated electrons.

The plasma cavity itself is surrounded by a thin sheath of electrons which shield the outside plasma from the fields inside the cavity. A characteristic density distribution showing this dense electron sheath together with the electron-free cavity is depicted in Fig. 6.3. This figure shows a two-dimensional density distribution (gray) alongside the transversal focusing force (red and blue) and the laser field (green) in its upper half. It also shows the accelerating field (orange), density distribution (black), laser envelope (red), and potential of the wake (blue) for the central axis along the laser propagation direction in its lower half. These results have been determined via a particle-in-cell simulation. The potential was calculated by integration.

$$\Psi(\xi) = -\frac{\omega_{pe} \cdot E_0}{c} \int_{+\infty}^{\xi} E_z \mathrm{d}z \tag{6.24}$$

Characteristic for this highly non-linear regime is the massive density increase at the back of the plasma cavity. In the above case, the end of the first bubble reaches a density of more than 400 times the initial plasma density n_0. At the back of the plasma cavity, the accelerating electric field E_z shows a much steeper increase towards the laser pulse than predicted by the linear approximation (Eq. 6.20). The electric field reached right at the back of the bubble is therefore much higher than predicted by the simple linearization (Eq. 6.19 and Eq. 6.19). These extremely high field gradients are the origin of the wave-breaking injection in the bubble regime, discussed in section 6.2.5.

6.2.4 How the laser evolution influences the acceleration process

There are two main limitations regarding laser wakefield acceleration: the maximum energy an accelerated electron can reach in the plasma cavity, and the propagation length the laser driver can sustain the laser cavity before losing too much energy and depleting. There exist scaling laws for ideal laser conditions but even if these conditions are met in focus, the laser will evolve and thus the acceleration process will be sub-optimal. Thus, before covering the ideal scaling laws of electron energy gain and laser depletion, the laser evolution in a plasma will be briefly outlined.

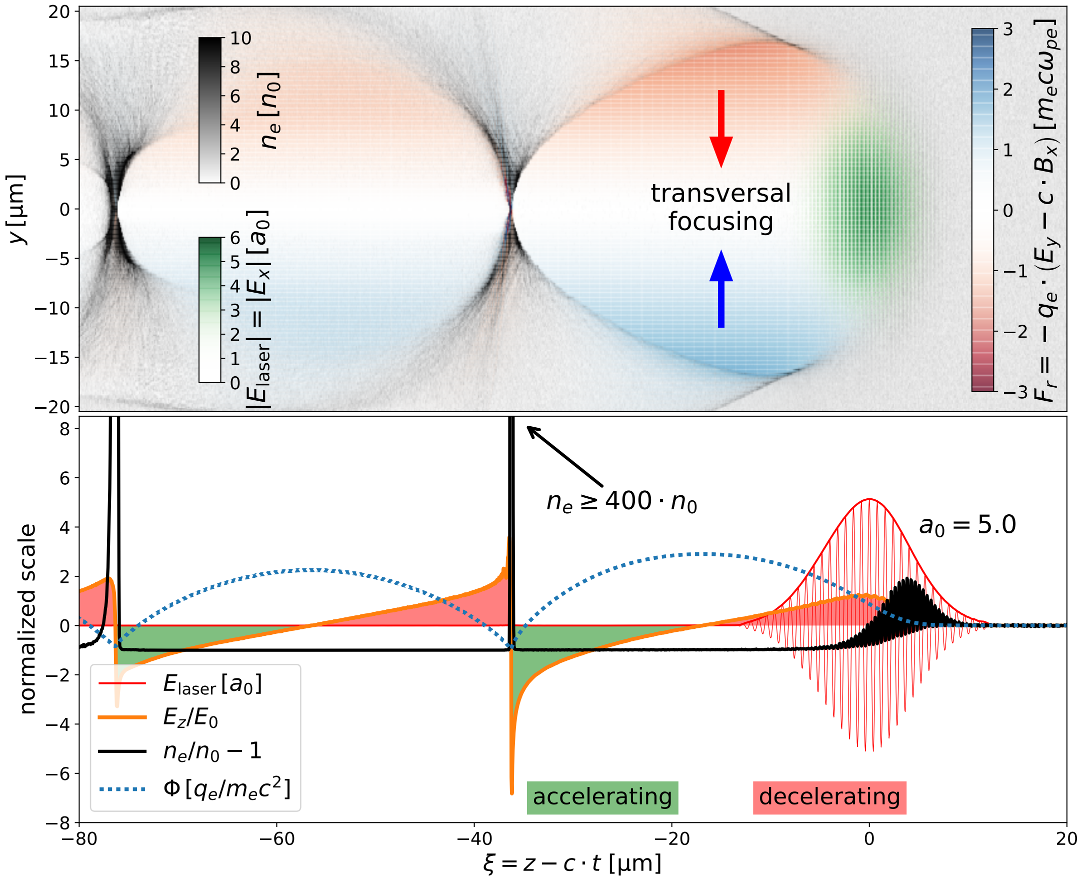

Figure 6.3: **Blowout regime:** The upper plot show the plasma density distribution (gray) of a wake created by an $a_0 = 5.0$ laser pulse with laser pulse duration of $\sigma = 15\,\text{fs}$ in an initial plasma density of $n_0 = 10^{18}\,\text{cm}^{-3}$. In addition, the transversal focusing force (red and blue) and the laser field (green) overlap the density. The lower plot shows the potential (blue), density (black), and accelerating electric field (orange) on axis, determined by a particle-in-cell simulation. The green background marks the accelerating while the red background marks the decelerating region. The axes are equivalent to Fig. 6.2.

A Gaussian laser pulse in a vacuum can be focused to a spot size of w_0 using e.g., parabolic mirrors. Without losing generality, the focus is located at the origin of the coordinate system and the laser propagates in $\vec{e}_z$ direction. The laser spot size $w(z = 0) = w_0$ is minimal in the focus. Before and after the focus the transversal profile spreads out, causing an increased spot size $w(z)$. After the so-called Rayleigh length

$$z_R = \frac{\pi \cdot w_0^2}{\lambda_0} \tag{6.25}$$

behind the focus, the beam waist has increased by $\sqrt{2}$, with λ_0 being the laser wavelength. The spot size evolves as:

$$w(z) = w_0 \sqrt{1 + \left(\frac{z}{z_R}\right)^2} \quad . \tag{6.26}$$

At a Rayleigh length from the focus, the transversal area has doubled and thus the intensity of the laser is half the magnitude compared to the focus. Thus increasing the laser pulse intensity by a tighter focus to reach the blowout regime is counterproductive, because the intensity reached is reduced faster due to diffraction thus reducing the accelerating length.

Fortunately, the plasma itself can delay the vacuum diffraction significantly thus enabling to keep high-intensity laser beam profiles for distances longer than the Rayleigh length z_R. On the one hand, the laser alters the plasma itself, changing its refractive index to cause self-focusing. On the other hand, the refractive index of the plasma can be manipulated by the experimentalist thus ensuring long propagation distances at quasi-constant laser intensity. For example, Geddes et al. [10] used a pre-formed plasma channel to maintain the bubble regime.

The refractive index η of an electromagnetic wave propagating in $\vec{e}_z$ direction in a medium is the inverse phase velocity normalized to the speed of light:

$$\eta = c \cdot \frac{k_z}{\omega} \quad . \tag{6.27}$$

In order to focus a laser pulse refractively in a plasma, the phase velocity on-axis need to be less than off-axis [1]. Thus the refractive index needs to be maximal on axis $\partial\eta/\partial r < 0$, with r being the transversal off-axis radius and k_z being the wave number for an electromagnetic wave propagating in $\vec{e}_z$ direction.

According to the dispersion relation (Eq. 6.10), the refractive index becomes

$$\eta(r) = \sqrt{1 - \frac{\omega_{pe}^2(r)}{\omega_0}^2} \quad . \tag{6.28}$$

When taking into account that the unperturbed plasma frequency $\omega_{pe,0}$ at the density n_0 is altered with changes in density and with the relativistic mass of the fast electrons in the laser focus, the local plasma frequency becomes

$$\omega_{pe}(r) = \omega_{pe,0} \cdot \sqrt{\frac{n(r)}{\gamma_e(r) n_0}} \quad . \tag{6.29}$$

For underdense plasmas with $\omega_{pe} \ll \omega_0$ this allows the approximation

$$\eta(r) \simeq 1 - \frac{\omega_{pe,0}^2}{2\omega_0^2} \frac{n(r)}{\gamma_e(r) n_0} \quad . \tag{6.30}$$

When a high-power laser interacts with a plasma, the electrons oscillate and thus can reach a relativistic Lorentz factor proportional to $\gamma \simeq \sqrt{1 + a_0^2}$. This allows approximating the refractive index by a first-order Taylor approximation:

$$\eta(r) \simeq 1 - \frac{\omega_{pe,0}^2}{2\omega_0^2} \cdot \left(1 - \frac{a_0^2(r)}{2} + \frac{\Delta n_p(r)}{n_0} + \frac{\delta n(r)}{n_0}\right) \tag{6.31}$$

where the relative density gradient from a pre-formed plasma channel $\Delta n_p / n_0$ and the density fluctuation from the plasma wave $\delta n / n_0$ have been included for completeness [1].

Since the laser intensity and thus the relativistic mass increase is always maximal on axis, the increased electron mass will always reduce the refractive index. It was shown that this relativistic self-focusing effect only compensates the Rayleigh diffraction above a critical power of $P > P_c = 17.4\,\mathrm{GW} \cdot (\omega_0/\omega_{pe,0})^2$ [166]. However, it was also demonstrated that for laser pulse lengths shorter than the plasma wavelength $\tau \cdot c < \lambda_{pe}$, the laser still strongly diffracts [167, 168] due to leading-edge erosion [169].

Additionally to the relativistic self-focusing, the expulsion of electrons due to the ponderomotive force reduces the plasma density $\delta n < 0$ on axis and thus also leads to a reduced refraction index and self-focusing. This effect is called ponderomotive self-channeling [1]. The combination of both the relativistic and the ponderomotive self-focusing was extensively studied for long pulses [170, 171]. For laser pulses shorter than the plasma wavelength there exists no coherent theoretical treatment so far. In order to understand the self-focusing of laser pulses for LWFA in the bubble regime, numerical simulations are essential to derive scaling laws [172].

Assuming that the laser can sustain its ideal conditions either by a pre-formed plasma channel or by a long Rayleigh length, compared to the experimental acceleration length, there are the limits of dephasing and depletion that prevent laser wakefield accelerators to be scaled infinitely long. First of all, electrons that are captured by LWFA cavity are accelerated in this cavity to relativistic velocities. In order to be captured, they need to propagate as fast or faster than the laser cavity in order to stay in phase. However, the cavity travels at the group velocity of the laser pulse and thus below the speed of light. Particles inside the plasma cavity can exceed this velocity easily and travel close to the speed of light. The electron will, therefore, propagate closer to the laser pulse while being further accelerated. In the middle of the plasma cavity, the longitudinal electric field changes from accelerating to decelerating the electrons. At this point, no further energy gain is possible. From Eq. 6.17 it is known that the electron can reach a maximum Lorentz factor of $\gamma^{\max} = 2\frac{\omega_0^2}{\omega_{pe}^2}$ before its phase slips and it enters the decelerating region. For non-relativistic laser intensities $a_0^2 \ll 1$, the distance traveled before reaching this maximum energy was given in Eq. 6.18. For relativistic intensities with $a_0^2 > 2$ a correction factor must be applied [R7, 172] which changes the *dephasing length* to:

$$L_d = \frac{4c}{3}\frac{\omega_0^2}{\omega_{pe}^3}\sqrt{a_0} \quad . \tag{6.32}$$

As the laser driver excites a plasma wave, its electromagnetic energy is converted into kinetic and electromagnetic energy of the plasma wave. Since the kinetic and electromagnetic energy of the plasma wave trailing the laser driver convert into each other, the energy per propagation distance transferred from the laser to the plasma can be estimated by integrating the electric field of the plasma along the propagation distance [1]. At some distance L_{dp}, the total energy of the laser is transferred to the plasma wave and the laser ceases to exist. A derivation of the non-relativistic and relativistic depletion length can be found in [173] or [172] with slightly differing scaling. The latter defines the *depletion length* for $a_0 > 2$ to be:

$$L_{dp} = \frac{\omega_0^2}{\omega_{pe}^2} \cdot c \cdot \tau \tag{6.33}$$

with τ being the laser pulse duration.

In most cases, the dephasing limit is reached before the depletion limit [1]. However, by tapering the plasma density slowly along the propagation distance, the dephasing limit can be extended and the laser depletion becomes the limiting factor [1, R7]. To overcome these limitations, transferring the accelerated electron bunch from one plasma accelerator to a second stage, driven by a fresh laser pulse, is the common method today. However, transferring the bunches from one stage to another one is difficult due to beam losses and timing issues. There is right now only one theoretical idea that could overcome both the electron dephasing and laser depletion limit: the Traveling-Wave Electron Acceleration (TWEAC) scheme [R7] derived from the original Traveling-Wave Thomson Scattering (TWTS) light source idea [174] using two of the pulse-front-tilted laser pulses required by the TWTS scheme [R13–R17].

6.2.5 Getting electrons into the plasma cavity: self-injection methods

Previously it was explained how a laser can excite a plasma wave to generate a longitudinal electric field that can potentially accelerate electrons. The question arises, under which conditions electrons are trapped by the wakefield. This is particularly interesting for the blowout regime, in which the acceleration fields are located in an (initially) electron-free plasma cavity. As with conventional accelerators, an option would be to inject electron bunches externally into the cavity. But due to the high demands on femtosecond timing in order to use the accelerating phase of the plasma wake, such an approach has not yet been a great success. Significant energy gains could be demonstrated but the overall energy spectrum was continuous [175]. So far, the best approach to inject electrons into the plasma cavity is to use electrons from the plasma itself.

In the linear and non-linear regimes, the number of electrons that can potentially be trapped and accelerated in the cavity can be estimated from the potential. A so-called separatrix defines the region in phase space which separates captured electrons from uncaptured ones [1]. Since this thesis concentrates exclusively on the acceleration in the blowout regime and the trapping of electrons either by the so-called wave-breaking injection or the self-truncated ionization injection, a description of the injection methods applicable in the linear and non-linear regime is omitted. An overview on trapping electrons in these regimes can be found in [1] and the many references therein.

The initially used injection method in the blowout regime is the so-called wave-breaking injection [10, 12, 13]. Since the electron density is extremely high and the accelerating electric field E_z has a minimum at the end of the plasma bubble, a bunch of electrons can spontaneously inject into the plasma cavity. Due to the accelerating electric field in the bubble, the injected electrons move forward relative to the bubble, enter the cavity, and are further accelerated. This spontaneous self-injection occurs for normalized laser field intensities above $a_0 > 4.3$ [176][11].

The advantage of this method is that injection occurs intrinsically and thus is technically easy to achieve. It also provides several picocoulomb of charge in quasi-monoenergetic bunches [10, 12, 13]. Its main disadvantage is that it is hard to operate in experiments reliably. Since the point of injection strongly depends on the non-linear bubble evolution, shot-to-shot fluctuations have a significant influence on the bunch quality in current experiments. For example, with the DRACO laser [R11] at HZDR, inevitable fluctuations in gas and laser quality result in optimal bunch parameters being achieved only in one out of ten shots with wave-breaking injection.

A better controllable approach to injection is the so-called down-ramp injection. By reducing the plasma density locally, the radius of the plasma bubble $r_b \sim 1/\sqrt{n_e}$ increases. The high electron density on the back of the bubble is thus encased by the spatially enlarged plasma cavity. These captured electrons immediately feel the accelerating electric field, gain enough momentum to keep up with the laser pulse, and are further accelerated in the plasma cavity. Such a density down-ramp can be achieved technically by holding a razor blade in the gas jet providing the plasma. The shock front caused by this disturbance leads to an increase in density on the downstream side where the injection occurs. Naturally, down-ramp injection also occurs at the end of the plasma at the transition to vacuum. In experiments, using a density spike for down-ramp injections leads to stable and reproducible injection. But due to the limited length of the down ramp, the injection time and thus the total injected charge is limited. This method can provide quasi-monoenergetic bunches but their charge is limited to about $100\,\mathrm{pC}$ [177].

Another method uses the strongly bond K-shell electrons from high-Z atoms. These are ionized only at relatively high laser intensities and thus in a region that most lightly-bound outer electrons cannot reach due to the ponderomotive potential of the laser. This method is called ionization injection [178–180]. It provides an electron injection with a high charge. However, the injection process can take place for the entire time that the laser intensity is high enough to ionize the K-shell electrons. The injection is therefore continuous, and the final electron bunch has a broad energy spread. Technically, this injection method is easy to implement in experiments: Only a suitable gas or gas mixture has to be used. However, the simulation of this

---

[11] This is valid for the 3D case. For 2D simulation, $a_0 > 5.36$ is needed.

injection method is more complicated since the PIC code needs to model the ionization process. PIConGPU is capable of modeling ionization based on various methods since 2015 [101].

There are three conditions that must be met to accelerate electrons with this method. First of all, the laser needs to reach a high enough intensity to ionize the strongly bound inner electrons. For example, in order to ionize the last electron from N^{6+}, which has a binding energy of $\mathcal{E}_{\text{ion}} = 667\,\text{eV}$, a normalized field strength of $a_0 = 2.75$ is needed for a Ti:Sapphire laser such as DRACO at HZDR [R11]. The required intensity can be reached by either initially focusing the laser to a sufficiently small spot size or by relying on relativistic self-focusing.

Secondly, the ionized electrons must reach a high longitudinal velocity to keep up with the velocity of the plasma cavity $v_z \geq v_\phi$ and to undergo further acceleration. A constant of motion can be derived from the Hamiltonian equation and under the assumption that the laser plasma dynamics is quasi-stationary and depends longitudinally only on $\xi = z - v_\phi \cdot t$ [181, 182]:

$$\gamma - \frac{v_\phi}{mc^2} p_z - \Psi = \text{const.} \quad . \tag{6.34}$$

Under the assumption that the just ionized electron has a velocity of zero, the constant of motion can be used to quantify a longitudinal capturing condition. Initially, the electron has no momentum $\gamma = 1$ and is ionized at a potential value of Ψ_i. When captured, the electron has reached a longitudinal velocity of $v_z = v_\phi$ and is located at a potential value greater than Ψ_f. Using the constant of motion, the following condition needs to be fulfilled in order to capture ionized electrons:

$$1 + \Psi_f - \Psi_i = 1 + \Delta\Psi \leq \frac{\gamma_f}{\gamma_\phi^2} = \frac{1}{\gamma_\phi} \tag{6.35}$$

Assuming that, as in most cases, $\gamma_\phi > 10$, equation 6.35 simplifies to [179]:

$$\Delta\Psi \lesssim -1 \quad . \tag{6.36}$$

Thirdly, when capturing the electron, there must be a focusing field to compensate for any transversal momentum gained until the capture condition $v_z = v_\phi$ is reached. This can be either a radial electric field E_r or for relativistic velocities an azimuthal magnetic field B_θ as present in the bubble regime [1]. If there are no focusing fields, the captured electron eventually leaves the accelerated region behind the laser due to its transverse drift.

In order to determine whether ionization injection can occur, the potential value at the ionization threshold Ψ_i has to be compared with the lowest potential value Ψ_f (see the exemplary wakefield in Fig. 6.4). Assuming that two bound states with an ionization threshold of $E^{\text{I}}_{\text{ion}} = 1.5\,[a_0]$ and $E^{\text{II}}_{\text{ion}} = 2.5\,[a_0]$ exist, one can see that only the second state (green) fulfills the longitudinal capturing condition. The first state (orange) cannot be captured by the wakefield since it is ionized before the potential is high enough to fulfill the capturing condition (Eq. 6.36).

Ionization injection can deliver several picocoulomb of charge but usually leads to a broadband electron spectrum since the trapping condition can be fulfilled for a long time compared to the acceleration process [179, 183]. In order to reduce the length of the injection region to a few micrometers along the transversal propagation distance of the laser, Zeng et al. suggested the so-called self-truncated ionization-injection method (STII) [184]. By not matching the transversal spot-size condition in the blowout regime, the laser pulse undergoes a self-focusing dynamics that leads to an oscillating spot size and thus more quickly changing trapping conditions. A further injection can thus be suppressed and a narrow energy bandwidth is achieved while still injecting up to $Q \sim 100\,\text{pC}$ charge [185, 186]. During this dissertation, a new charge record was reached using an STII scheme with a late focus position [R2]. A detailed discussion of this new method can be found in section 6.5.

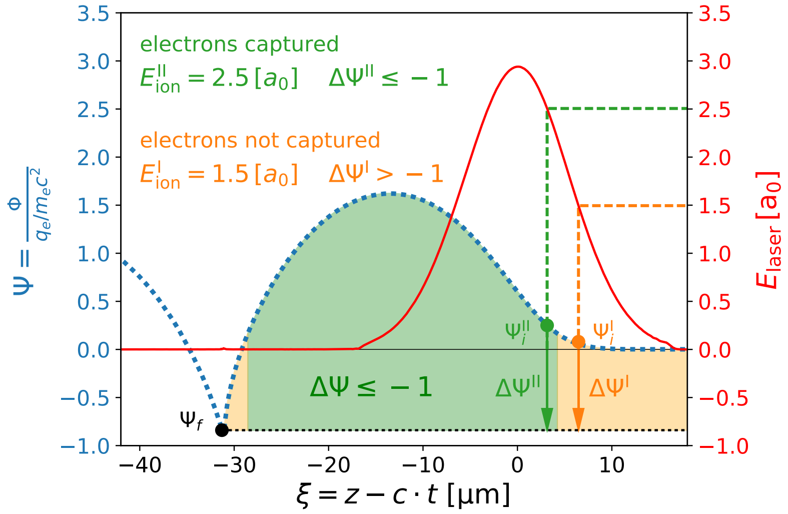

Figure 6.4: **Schematic diagram of ionization injection:** This plot illustrates the capturing condition (Eq. 6.36) for ionization injection. While the lower ionization state is ionized in a region where the maximum potential difference is not low enough and electrons from that state thus will not be captured, the higher ionization state is ionized in the capturing region. The electrons of the higher ionization state will reach a high enough longitudinal velocity to follow the plasma wake. In the wake, they will be accelerated further. The x-axis represents the co-moving position ξ. The left y-axis represents the potential Ψ (in blue) while the right y-axis shows the scale of the normalized electric field of the laser E_{laser} (in red).

6.3 Fundamental laser-electron scattering theory

In the following sections, the scattering of laser photons from the plasma electrons is discussed. In section 6.3.1, the origin of scattered radiation from the laser-plasma interaction is briefly introduced and the expected radiation dynamics is motivated. Following that, a scattering model is introduced that correlates an arbitrary electron motion in a laser field with the emitted radiation. This model forms the basis for the radiation signatures discussed. In section 6.3.3, the scattering signature of electrons in the blowout regime is examined using the simple model from the previous section. A spectral method on how to determine the existence of the blowout regime in the plasma via radiation is presented.

6.3.1 Electrons scatter laser photons

When going back to Tajima's original results [7] (see section 6.2.2), a laser pulse drives a plasma wave most efficiently when its pulse duration is approximately half as long as the plasma wavelength $\lambda_{pe} \simeq 2 \cdot \tau$. Longer pulses would interact with the plasma wake while shorter pulses, in principle, would drive the wake but would deplete much faster. For driving a solitary plasma cavity in the blowout regime, laser durations are commonly in the order of $\tau \simeq 30\,\text{fs}$ (FWHM intensity) while plasma densities vary around $n_e \simeq 5 \cdot 10^{18}\,\text{cm}^{-3}$ (e.g., [12]). Thus, the plasma wavelength is around $\lambda_{pe} = 2\pi c/\omega_{pe} \simeq 15\,\mu\text{m}$ while the laser pulse length is approximately $c \cdot \tau \simeq 9\,\mu\text{m}$. Assuming a Gaussian-shaped laser pulse, this results in a not negligible laser intensity in most of the bubble and the surrounding of the plasma cavity. This is illustrated in Fig. 6.5 where the electron density in the blowout regime is plotted together with contours of the FWHM and 5% intensity regions of the driving laser pulse. The overlap between the plasma electrons and the laser at most of the front of the plasma cavity is apparent.

The electrons in the laser field will scatter laser photons. For relativistic lasers intensities

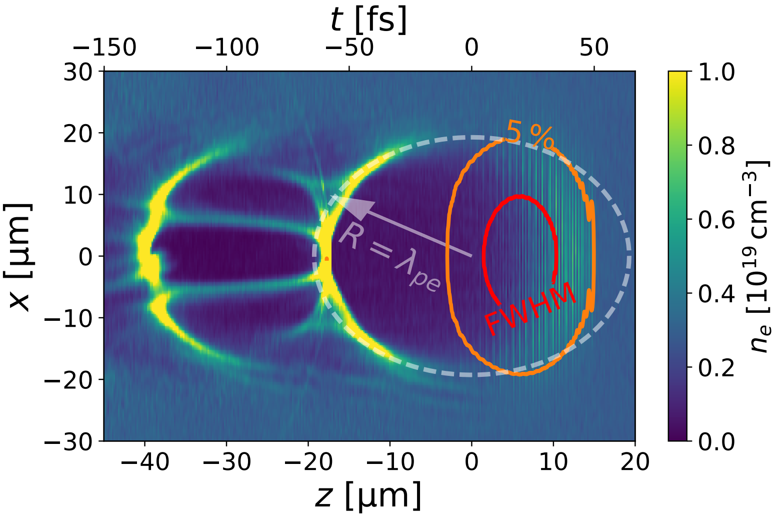

Figure 6.5: **Laser intensity around the plasma cavity:** This plasma density n_e plot of an LWFA in the blowout regime illustrates that the laser extent covers most of the front of the bubble cavity. Laser intensity contours are depicted at the FWHM and at 5% of the peak intensity. The laser with peak strength $a_0 = 5$, a spot size $w_0 = 19\,\mu$m (FWHM intensity) and pulse duration $\tau = 30$ fs propagates through a plasma of homogeneous density of $n_e = 3 \cdot 10^{18}\,\text{cm}^{-3}$. At these common parameters, the electrons creating the bubble will propagate through the laser field and thus will scatter laser light with characteristic red- and blueshift due to the electron drift velocity.

$a_0^2 \geq 1$, higher harmonics of the laser fundamental frequency will be scattered as well [115]. These higher harmonics have been observed experimentally [116]. In contrast to the theory and the experimental setup, which can assume quasi-stationary electrons that only oscillate in the laser field, in the blowout regime, the short and highly intense laser pulse will push electrons significantly due to the ponderomotive force causing a drift in addition to the fast oscillation in the laser field. This drift motion will result in a blue- and redshift of the scattered photons.

The drift motion of the electrons changes with the laser and plasma evolution. This change influences the degree of red- and blueshift.

On the very short time scale of the inverse laser frequency $\Delta t_{\text{short}} \sim \omega_0^{-1}$, the electrons oscillate in the laser field. Their drift motion does not change.

On the timescale of the inverse plasma frequency $\Delta t_{\text{mid}} \sim \omega_{pe}^{-1}$, the drift motion of the electrons changes. They are expelled from the laser focus and are pulled back behind the laser from the attractive ion potential. Assuming that the plasma density does not change quickly on that timescale, the electron trajectories are static, even though a constant flow of electrons passes the laser. Thus, the emitted radiation will not change dramatically on that timescale either. The radiation is emitted by ever-changing electrons from the flow around the laser pulse. But since their dynamics around the laser field is similar, the observable radiation is alike.

However, while propagating through the plasma, the laser dynamics changes as well on the time scale $\Delta t_{\text{long}} \sim \omega_0 \cdot \omega_{pe}^{-2} > \Delta t_{\text{mid}} > \Delta t_{\text{short}}$ due to (self)-focusing and depletion. These changes of the laser pulse's shape and amplitude will alter the plasma response and thus the drift motion of the electrons while the oscillation at the laser frequency stays relatively unaffected. Laser self-focusing will increase the ponderomotive force acting on the electrons and thus will push the electrons to higher drift velocities resulting in an increase in red- and blueshift of the scattered radiation. Furthermore, laser depletion comes at the cost of a frequency shift at the front of the laser [187, 188]. This frequency shift results in a frequency shift of the emitted photons as well, even without dramatic blue or redshift due to the electron drift motion.

6.3.2 The correlation between the electron drift and the scattered light

In the following model, the fast oscillation of electrons in the laser field is ignored, and only the drift motion is considered. This is the so-called quasi-static approximation [189, 190]. Only the drift motion of the electrons on the time scale of the inverse plasma frequency $\Delta t_{\mathrm{mid}} \sim \omega_{pe}^{-1}$ is considered. The fast oscillation, classically responsible for the radiation emission, can be neglected in this model. Instead, the model assumes mono-energetic photons (e.g., from the laser pulse) to be present. The emitted radiation is treated as the scattering of these photons from the drifting electrons. This simplification does not allow predicting nonlinear Thomson scattering with higher harmonics [115]. Higher harmonics could be included ad-hoc by additionally introducing photon sources at multiples of the laser frequency. For now, only scattering from the fundamental will be covered.

Assuming a plane wave with wave vector $\vec{k}$ oscillating at a frequency ω_0, electrons drifting with a normalized velocity $\vec{\beta} = \vec{v}/c$ will scatter photons from that plane wave in all directions. Depending on the observation direction $\vec{n}$, these photons will be blue- or red-shifted according to:

$$\omega_{sc} = \omega_0 \cdot \frac{1 - \vec{\beta}_d \cdot \vec{k}/k}{1 - \vec{\beta}_d \cdot \vec{n}} \quad . \tag{6.37}$$

The geometric relations for the three vectors is depicted in Fig. 6.6.

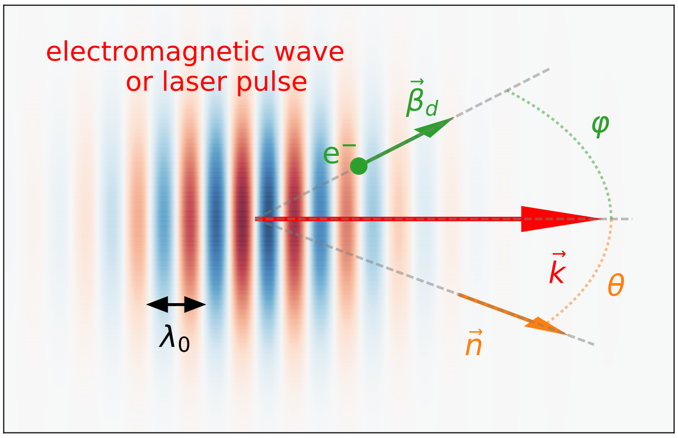

Figure 6.6: **Illustration of the geometric relations relevant for the laser scattering:** The laser wave vector $\vec{k}$, the normalized drift velocity of the electron $\vec{\beta}_d$, the unit vector pointing in observation direction $\vec{n}$ are depicted as well as the angle between the electron velocity and the laser propagation direction φ, and the angle between the observation direction and the laser propagation direction θ. A laser pulse with wavelength λ_0 was plotted but the same geometry applies to an electromagnetic plane wave.

In order to illustrate the scattering, a reduction to two dimensions is beneficial. Both the electromagnetic wave and the electron will only propagate in a plane. The angle between the wave vector $\vec{k}$ and the drift velocity $\vec{\beta}_d$ is defined as φ, while the angle between the wave vector $\vec{k}$ and the observation direction $\vec{n}$ is defined as θ. Eq. 6.37 thus simplifies to:

$$\omega_{sc} = \omega_0 \cdot \frac{1 - \beta_d \cos(\varphi)}{1 - \beta_d \cos(\varphi - \theta)} \quad . \tag{6.38}$$

The resulting scattering pattern is plotted in Fig. 6.7 for various drift velocities and directions.

From Eq. 6.38 it is obvious that independent of the electron drift, radiation emitted parallel to the propagation direction of the electromagnetic wave $\vec{k} \parallel \vec{n} \rightarrow \theta = 0$ has a frequency

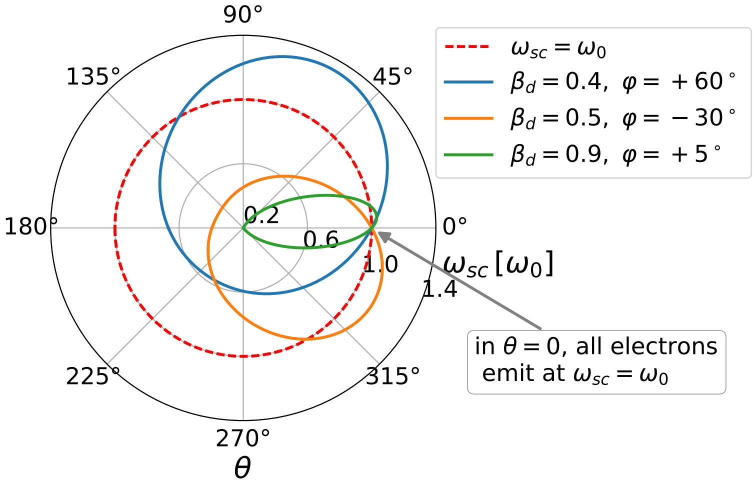

Figure 6.7: **Frequency shift of the scattered light:** The frequency shift as observed in various observation directions θ is plotted for various electron drift velocities characterized by the absolute normalized drift velocity β_d and the angle of the drift direction φ. In drift direction, the radiation is blue-shifted while opposite to the drift direction, the scattered radiation is red-shifted. In laser propagation direction $\theta = 0$, the scattered radiation is not shifted $\omega_{sc} = \omega_0$.

equaling the frequency of the electromagnetic wave $\omega_{sc} = \omega_0$. For a fixed velocity β_d, the highest scattering frequency is observed in the direction of the drift $\vec{\beta}_d \parallel \vec{n} \rightarrow \theta = \varphi$ while the lowest scattering frequency is observed in opposite direction of the electron drift $\theta = \varphi + \pi$.

The spectral width of the scattered radiation is described by the so-called resonance function $R(\omega - \omega_{sc})$ with ω being the actually scattered radiation and ω_{sc} being the mean scattered frequency in direction $\vec{n}$ by an electron with normalized velocity $\vec{\beta}$ according to Eq. 6.37. Classically, it describes the spectral bandwidth of the emitted radiation due to the finite oscillation duration. The oscillation duration might be limited by either the spatial extent of the electromagnetic wave, which the electron leaves due to its drift, or the temporally limited pulse duration, or both. For the hypothetical plane wave, the resonance function becomes a delta distribution at the scatter frequency $R(\omega) \rightarrow \delta(\omega - \omega_{sc})$ because the plane wave has neither a spatial nor a temporal end. For a finite laser pulse duration, the laser itself has a spectral bandwidth. Assuming the electron propagates through the entire laser and does not change its non-relativistic drift motion, the resonant function is:

$$R(\omega) = \left(\frac{\sin((\omega - \omega_{sc}) \cdot \tau/2)}{(\omega - \omega_{sc}) \cdot \tau/2} \right)^2 \tag{6.39}$$

with τ being the laser pulse duration [115]. For relativistically drifting electrons, the resonance function becomes more complex. The frequency bandwidth is proportional to the number of oscillations N the electron undergoes in the electromagnetic field $\Delta\omega/\omega = 1/N$. For short pulse lasers, the bandwidth of the scattered radiation for a single electron is thus approximately given by the bandwidth of the laser

$$\frac{\Delta\omega_{sc}}{\omega_{sc}} \simeq \frac{\Delta\lambda_0}{\lambda_0} \approx \frac{80\,\text{nm}}{800\,\text{nm}} = 0.1 \tag{6.40}$$

where the quantities given are based on the properties of the DRACO laser [R11, 191].

The probability of observing a photon of energy $\hbar\omega$ propagating in $\vec{n}$, scattered by an electron with normalized drift velocity $\vec{\beta}_d$, is thus given by the resonance function and is sharply peaked around the mean scattering frequency ω_{sc}. The spectrally resolved emitted energy is proportional to this probability.

$$\frac{\mathrm{d}^2W}{\mathrm{d}\omega\mathrm{d}\Omega}(\omega,\vec{n}) \sim R(\omega) \tag{6.41}$$

Furthermore, photons are not scattered uniformly in all directions but according to the differential cross section of Thomson scattering [59]. For a quasi-stationary electron, the photon distribution follows the differential Thomson scattering cross section [59] which is given for in $\vec{e}_p$ polarized electromagnetic waves by

$$\frac{\mathrm{d}\sigma}{\mathrm{d}\Omega} = \left(\frac{q_e^2}{4\pi\varepsilon_0 m_e c^2}\right)^2 \cdot \sin^2\phi \tag{6.42}$$

with ϕ denoting the angle between the polarization of the electromagnetic wave $\vec{e}_p$ and direction of photon emission $\vec{n}$. The scattering probability in 3D follows a torus-like shape, with no scattering probability in polarization direction. For drifting electrons, the probability for scattering towards the drifting direction increases while the probability for backward scattering decreases [129]. For the special case of electrons drifting parallel to the wave vector $\vec{k} \parallel \vec{\beta}_d$ the scattering probability scales as

$$\frac{\mathrm{d}\sigma}{\mathrm{d}\Omega} \sim \frac{(1-\beta\cos\phi_1)^2 - (1-\beta^2)\sin^2\phi_1\cos^2\phi_2}{(1-\beta\cos\phi_1)^5} \tag{6.43}$$

with ϕ_1 being the angle between the drift direction and the observer and ϕ_2 being the angle between the observer and the polarization. For the case of a drift parallel to the polarization direction $\vec{\beta} \parallel \vec{e}_p$, the differential cross section scales as:

$$\frac{\mathrm{d}\sigma}{\mathrm{d}\Omega} \sim \frac{\sin^2\phi}{(1-\beta\cos\phi)^5} \tag{6.44}$$

with all angles being equal $\phi = \phi_1 = \phi_2$ in this case. Even though the probability of scattering photons in the direction of polarization stays zero, the maximum of the differential cross section occurs in the highly relativistic case at $\phi_{\text{max}} = \sqrt{(1-\beta)/2}$ [129] thus leading to stronger radiation in polarization direction than in the quasi-static case. For arbitrary drift directions, an expression for the differential cross section becomes more complex. While the scattering probability changes the intensity of the scattered radiation, the frequency shift is unaffected.

For a given electron distribution $f(\vec{r},\vec{\beta})$ as in the Vlasov equation 3.1, the scattering distribution can be calculated using the resonance function and the differential cross section. For a plane wave, the position of the electron can be neglected which allows reducing the distribution function to a velocity distribution function:

$$f_v\left(\vec{\beta}\right) = \int\limits_{V_{\vec{r}}} \mathrm{d}\vec{r}\, f(\vec{r},\vec{\beta}) \quad . \tag{6.45}$$

From this velocity distribution function, a radiation distribution function can be calculated by integrating over all possible velocities:

$$F\left(\omega,\vec{n},\vec{e}_p\right) = \int\limits_{V_{\vec{r}}} \mathrm{d}\vec{\beta}\, f_v(\vec{\beta}) \cdot R\left(\omega,\omega_{sc}\left(\vec{\beta}\right)\right) \cdot \frac{\mathrm{d}\sigma}{\mathrm{d}\Omega}\left(\vec{n},\vec{\beta},\vec{e}_p\right) \tag{6.46}$$

which is not yet normalized. The radiation distribution function is proportional to the spectrally and angularly resolved radiation energy $\frac{\mathrm{d}^2W}{\mathrm{d}\omega\mathrm{d}\Omega} \sim F(\omega,\vec{n},\vec{e}_p)$. Thus any electron distribution can be translated to a scattering distribution which can be measured.

Due to the linearity of integration, Eq. 6.46 can be split apart. This enables to quantify the scattering for a particle distribution $f_t = f_1 + f_2$ by computing the radiation distribution function for $f_1 \rightarrow F_1$ and $f_2 \rightarrow F_2$ independently. The radiation distribution function of f_t equals the sum of both individual distributions $F_t = F_1 + F_2$. This allows computing the emitted radiation by sampling the electron distribution f using test particles and adding all scattering patterns for these test particles. The radiation of such combined electron distributions modeling the blowout regime in 2D is shown in the next section in Fig. 6.9. The particle velocity distribution is plotted on the left side while the associated scattering distribution is plotted on the right side. A variety of different electron ensembles are shown underneath each other. The final two plots display the combined velocity and radiation distribution of all previous ensembles. The combined radiation plot shows clearly that while at $\theta = 0$, all radiation distributions are overlapping, they can be distinguished at off-axis observation directions $\theta \neq 0$. The plots are generated by a Monte-Carlo simulation which randomly generates particles according to a given velocity distribution function. From these particle distributions, the scatter pattern is simulated by assuming a resonance function of a plane wave $R(\omega, \omega_{sc}) = \delta(\omega - \omega_{sc})$ and combining these contributions via a histogram in finite frequency bins. Furthermore, the differential cross section $\frac{\mathrm{d}\omega}{\mathrm{d}\Omega}$ has been assumed to be uniform, which is a good approch in the case of sub-relativistic velocities at observation directions perpendicular to the polarization $\vec{e}_p \cdot \vec{n} = 0$.

In order to extend Eq. 6.46 to laser pulses with a finite temporal and spatial envelope, the intensity envelope of the laser pulse needs to be taken into account because higher laser intensity will cause more scattering. Thus an additional weighting proportional to the emitted power is required similar to the classical derivation of the Thomson scattering cross section [59]. The power at a normalized laser intensity of a_0^2 is according to the Larmor equation

$$P(a_0^2) = \frac{q_e^2 \omega_0^2}{12\pi\varepsilon_0 c} \cdot \left(1 + a_0^2/2\right) \cdot a_0^2 \tag{6.47}$$

which assumes an average power over one laser period. The power is also proportional to the number of photons from which to scatter. Extending Eq. 6.46 leads to the following equation

$$\frac{\mathrm{d}^2 W}{\mathrm{d}\Omega \mathrm{d}\omega}(\omega, \vec{n}) \sim F(\omega, \vec{n}, \vec{e}_p) = \int_{V_{\vec{r}}} \mathrm{d}\vec{r} \int_{V_{\vec{\beta}}} \mathrm{d}\vec{\beta}\, f(\vec{r}, \vec{\beta}) \cdot \frac{\mathrm{d}\sigma}{\mathrm{d}\Omega} \left(\vec{n}, \vec{\beta}, \vec{e}_p\right) \cdot P(a_0(\vec{r})) \cdot R(\omega - \omega_{\mathrm{sc}}(\vec{\beta})) \tag{6.48}$$

which requires the full particle distribution function $f(\vec{r}, \vec{\beta})$ in order to incorporate the spatially varying laser intensity. In this equation, electrons scatter photons according to the local laser intensity and blue- or red-shift them with regard to their drift direction and the direction of emission.

The particle distribution function is a solution to the Vlasov equation. Since the Vlasov equation cannot be solved analytically for intense short laser pulses propagating through a plasma, the solution for the radiation distribution function either comes from simulated particle distributions or simplified model. Examples of the latter will be given in the next sections. Even with a known particle distribution, deriving an analytical expression for the scattering pattern is not trivial and requires various simplifications.

It is important to note, that typical particle-in-cell simulations cannot provide particle distributions suited for direct conversion to radiation distributions. Since particle-in-cell codes do not separate the oscillatory motion from the drift motion, the oscillation in the laser field overlaps the drift motion that is responsible for the frequency shift. Only quasi-static particle-in-cell codes, that do not resolve the oscillatory motion of the electrons and just consider the ponderomotive push of the laser pulse [77], provide drift velocities directly. However, the focus of this thesis was not to include this model in quasi-static particle-in-cell codes but to apply this model for making qualitative predictions and compare those with the full radiation simulation included in PIConGPU [R8, R9].

6.3.3 Scattering in the bubble regime

As described in section 6.2, the ponderomotive force of the laser pulse excites a plasma wave. In three dimensions, the electrons are pushed not only to the front but also to the side of the laser. This snowplow effect is especially relevant in the blowout regime, where the laser is strong enough to push all electrons in front aside.

In the linear regime and in the low-relativistic regime, where no blowout occurs, the velocity distribution of the electrons has a Gaussian shape around the forward direction. In the blowout regime, however, the electrons collectively follow a distinct path around the laser and characteristic off-axis patterns occur additionally in the velocity distribution. This can most clearly be seen by the narrow sheath which the electrons form when surrounding the bubble. In this case, a large ensemble of electrons follows the same path in phase space. The density of the sheath is much higher than the original plasma density. The electrons in the small but dense sheath volume thus originate from a much larger volume in front of the laser.

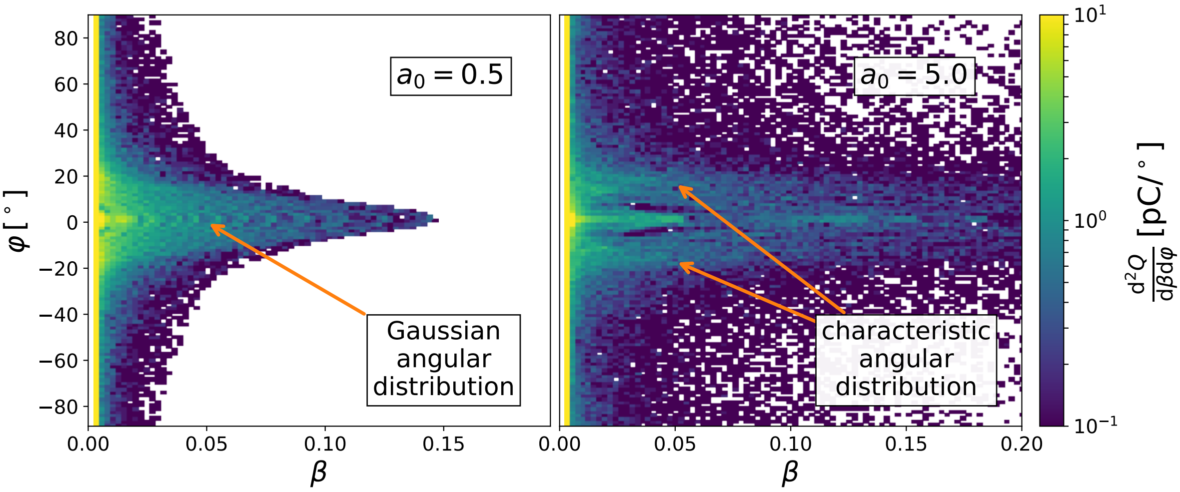

Figure 6.8: **Phase space relevant for scattering at two laser intensities:** In the linear regime $a_0 = 0.5$, the electron phase space in front of the laser shows a clear forward pattern, but no characteristic small angle pattern. In the blowout regime $a_0 = 5.0$, a characteristic angular structure emerges for a propagation direction $\phi \approx \pm 20°$.

This accumulation in phase space not only occurs in the bubble sheath behind the laser, it also occurs in front of the laser where more or less characteristic flow patterns can be identified. Figure 6.8 depicts the phase space distribution of two LWFA simulations for the electrons surrounding the laser pulse. In order to clearly draw out the signatures, only the central z-y-plane was selected, in order to avoid confusions with three-dimensional projections entirely. In accordance with the scattering theory, the phase space is given in normalized velocity $\beta = |\vec{v}|/c$ and direction of propagation φ with $\varphi = 0$ being the laser propagation direction as before. In the $a_0 = 0.5$ case no clear structures other than the peak at $\varphi = 0°$ can be identified. With relativistic laser intensities, clear patterns in the direction $\varphi \approx \pm 20°$ can be identified additionally.

As a result, the broad phase space distribution in the linear case will not result in any characteristic scattered-radiation signature other than a slight broadening of the scattered light of the laser due to the inert motion of the plasma electrons.

If one, however, takes the characteristic angular pattern of the electron motion in the blowout regime, a clear broadening of the laser spectrum at off-axis angles can be seen. This is demonstrated for a simplified model phase space distribution in Fig. 6.9. These plots depict the model phase space distribution and the according scatter pattern. A simplified distribution function was used as a basis and a random ensemble of test particles was created in a Monte Carlo simulation. The radiation emitted was modeled according to Eq. 6.48. Since the distribution $f(\beta, \varphi)$ was limited to low velocities β, the influence of the directional scattering cross section was approximated by $\frac{\mathrm{d}\sigma}{\mathrm{d}\Omega} = 1$. Furthermore, the influence of the spatial intensity distribution $P(a_0(\vec{r}))$ was also neglected. The spectral form of the scattered radiation was assumed to be a delta distribution $R(\omega - \omega_{\mathrm{sc}}) = \delta(\omega - \omega_{\mathrm{sc}})$. With these simplifications, various model photons were randomly generated based on the distribution $F(\omega, \vec{n})$ using the ensemble distribution $f(\beta, \varphi)$ (see Eq. 6.48).

The first ensemble distribution (Fig. 6.9 1(a)) models the electron background. Most of the electrons scattering laser light just interact with the base of the laser pulse at low intensities $a_0 \ll 1$. They do not gain a lot of velocity in this interaction $0 \leq \beta \ll 1$ and a good assumption is that they drift in all directions due to the plasma's temperature. Since the ensemble electrons do not have significant velocity, there is no relevant red- or blueshift of the laser frequency in any direction. The scattering pattern (Fig. 6.9 1(b)) thus shows only radiation around the laser frequency ω_0.

The second ensemble distribution (Fig. 6.9 2(a)) models the collective motion towards $\varphi = 20°$ as observed in simulations of the bubble regime (Fig. 6.8). The velocity of the electrons ranges from $\beta = 0$ to $\beta \approx 0.35$. There are fewer electrons towards higher velocities than at low velocities. This continuous velocity distribution leads to a continuous scattering pattern with the most intense radiation always at the laser frequency ω_0. If this ensemble distribution would not contain low-energetic electrons, there would be no radiation at the laser frequency at angles $\theta \neq 0$. This is illustrated by the sample particle marked in purple. Its scattering pattern (purple line Fig. 6.9 2(b)) reaches its highest frequency in the direction of flight $\theta = \varphi = 20°$. But with the addition of low energetic particles, an example marked in orange, a continuous pattern till $\omega_{\mathrm{sc}} = \omega_0$ evolves that depends on the actual velocity distribution.

The third ensemble distribution (Fig. 6.9 3(a)) models the forward push due to the laser with $\varphi = 0°$ as also observed in both the linear and bubble regime (Fig. 6.8). The scattering pattern (Fig. 6.9 3(b)) stays below to the laser frequency $\omega_{\mathrm{sc}} \leq \omega_0$. For the narrow forward observation angle selected and with the low velocities $\beta < 0.5$, the redshift is insignificant.

When combining all these ensemble distributions in order to model the entire distribution during the bubble regime (Fig. 6.9 4(a)) the scatter pattern can be added as well due to the linearity of the scattering process as mentioned previously. This allows building complex models of the scattered radiation by combining the scattering patterns of sub-ensembles of the complex total electron distribution. The model ensemble distribution, which also includes a symmetric sub-ensemble to 2(a) moving in $\varphi = -20°$ direction, has a distinct scatter pattern. At larger observation angles θ, the bandwidth of the observable radiation becomes larger. The maximum frequency is observed under $\theta = \pm 20°$. The intensity towards off-axis angles decreases with an increasing absolute angle $|\theta|$.

The actual spectral peak position of the bandwidth could be used to determine the strength of the ponderomotive push. So far, the model assumed a quasi-static laser pulse. With a laser evolving due to diffraction and relativistic self-focusing, these clear angular patterns are changing with the laser dynamics as well. They are therefore more suited for determining this evolution than to actually characterize the strength and spatial structure of the laser, which evolves more complexly during the propagation in plasma than described by the model so far. Around the focus position, the significant broadening of the scattered laser light allows determining the point of focusing in the plasma. This will be further discussed on the basis of a

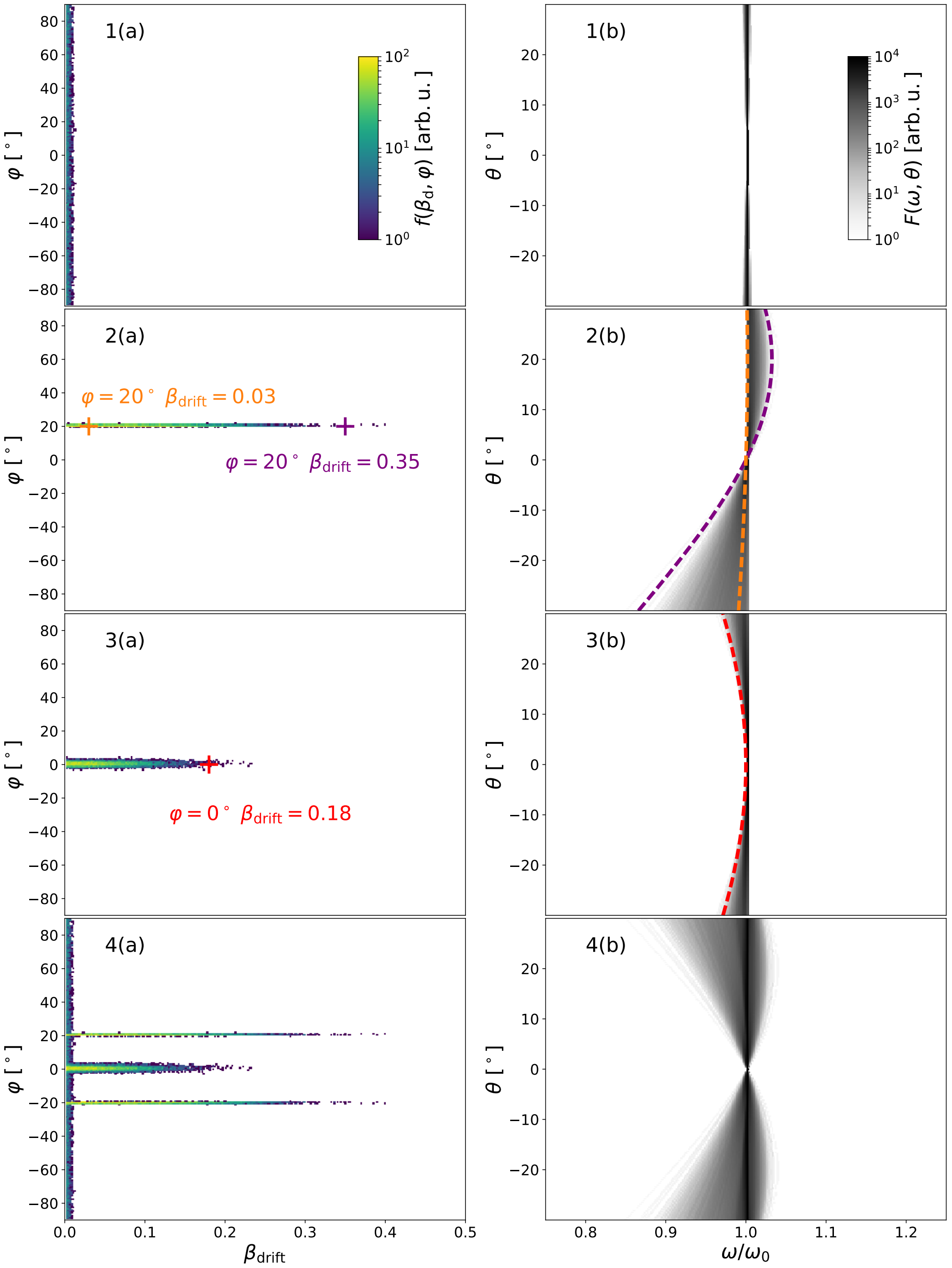

Figure 6.9: **Model phase space and corresponding scattering pattern:** These plots illustrate the way how to model the characteristic scatter pattern for the LWFA blowout regime. The assumed ensemble distribution $f(\beta, \varphi)$ is plotted on the left (**a**) while the according scatter pattern $F(\omega, \theta)$ is plotted on the right (**b**). Starting from a omnidirectional but low-energetic background of electrons (**1**), the characteristic off-axis electrons (**2**) and the forward moving electrons (**3**) all have a characteristic scattering pattern. In combination (**4**), the radiation becomes broadband at off-axis angles.

3D LWFA simulation in section 6.4.3 where a surprising asymmetry of this process is revealed which the simple quasi-static scattering model cannot explain. An exemplary case where the focus position in the plasma is of interest in an experiment will be discussed in section 6.4.4.

6.4 Radiation signatures for determining the laser plasma dynamics

For an initial study of radiation emitted during laser wakefield acceleration, a large-scale simulation was performed. The focus of this simulation was to quantitatively predict the total emitted radiation of all electrons of the plasma for all relevant observation directions for the first time. The goal of this radiation simulation was to discover new radiation signatures that might help to determine the plasma dynamics during LWFA.

6.4.1 A large-scale LWFA simulation for studying the radiation

The LWFA setup used for this explorative simulation is in the blowout regime with self-injection. Such a setup corresponds on the one hand to a multitude of nowadays experiments and on the other hand is simple enough to provide generally valid results. The parameters were kept in experimentally realizable limits: simulating a Gaussian laser pulse of maximum normalized field strength $a_0 = 3.5$ with a pulse duration of $\tau = 25\,\mathrm{fs}$ (FWHM of intensity) and a spot size of $w_0 = 10\,\mu\mathrm{m}$ (standard deviation of intensity) propagating through a pre-ionized hydrogen plasma with a maximum electron density of $n_e = 5 \cdot 10^{18}\,\mathrm{cm}^{-3}$. These are similar parameters as later used in experiments at HZDR [R2, R11] which however applied a more sophisticated self-focusing and injection scheme. On the basis of this experimentally realized setup, an extensive simulation was subsequently performed to validate the applicability of the radiation signature discovered with this simple setup (see chapter 6.4.4).

The simulation covered the radiation emitted in a half-dome of solid angle $\Omega = \pi$. The intrinsic symmetry of the LWFA leads to symmetric radiation patterns in all four quadrants that allows scanning only a single quadrant (half-dome) with $N_\Omega = 250$ virtual detectors. This half-dome alone already offers a wealth of details and reduces the computational demand significantly. The frequencies simulated ranged from infrared over optical to ultraviolet radiation $\omega \in [0.25\omega_0, 15\omega_0]$ ($\lambda \in [3.2\,\mu\mathrm{m}, 53\,\mathrm{nm}]$) with $\omega_0 = 2\pi c/\lambda_0$ being the laser frequency of the $\lambda_0 = 800\,\mathrm{nm}$ laser. A total of $N_\omega = 512$ frequencies were sampled. The initial simulation focused on this low-energy frequency range for two reasons. On the one hand, optics are more easily available for these frequencies, thus simplifying the radiation focusing and detection in an experiment. Since this low-energetic radiation is also emitted in a broad solid angle, an off-axis detector allows resolving the emission associated with the laser plasma dynamics temporally, by projecting the longitudinal position on a detector axis. On the other hand, the high-energetic radiation, like the x-ray radiation from betatron oscillation [27], is emitted in a $\Delta\theta \sim \gamma^{-1}$ cone in the electron direction of flight. This forward radiation thus arrives in a narrow spot in laser propagation direction with only a sub-femtosecond delay between the initially emitted radiation and the emission at the end of the acceleration process. Thus, the final emission overshadows the initial, weak emission and the information of the initial acceleration process is lost. The x-ray spectra are thus ideally suited to study the final electron distribution at the end of acceleration [155], but will not reveal information on the plasma dynamics during the acceleration process.

A visualization of the computed half-dome sky-map together with a visualization of the LWFA plasma density and the laser driver is given in Fig. 6.10. The plasma density shows clearly a blowout cavity behind the laser driver. In the cavity, an injection can be identified. The surrounding half dome illustrates the radiation power emitted at the moment of the snapshot ($t = 2.2\,\mathrm{ps}$). The skin depth of the half dome represents the frequency on a logarithmic frequency scale ranging from 0.25ω on the inner skin to $15\omega_0$ to the outer skin. The laser frequency, emitted

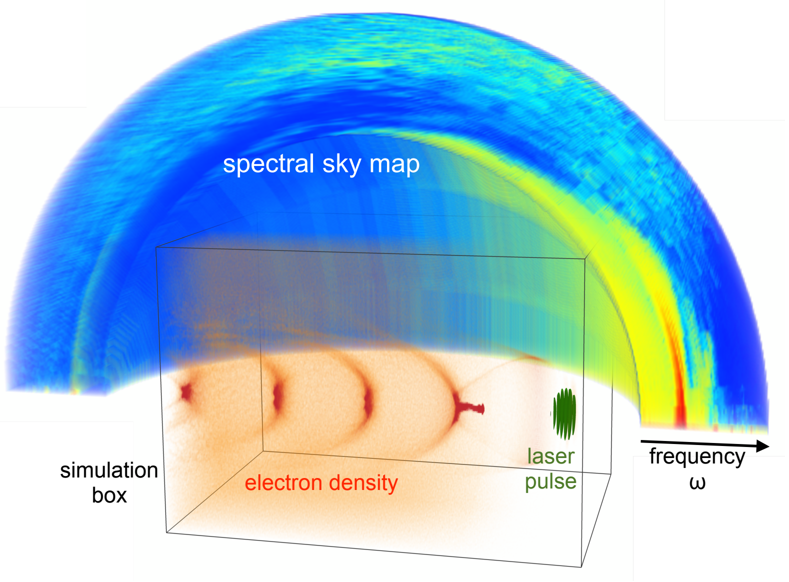

Figure 6.10: **LWFA simulation box with radiation dome:** This 3D visualization of the large-scale LWFA simulation discussed in section 6.4 illustrates the relation between the laser-plasma dynamics and the additionally computed radiation. The gray box shows the entire plasma simulation with the electron density (red) of the wakefield which has been exited by the laser pulse (green). The half dome illustrates the emitted radiation power at the current simulation time step. The position on the half dome is equivalent to the observation direction. The depth of the half dome represents the frequency, while the color equals the intensity of the radiation power with red being the strongest and blue being the lowest power.

mainly in the forward direction, can be clearly identified by the intense red color of high radiation power. The position on the sky map represents the direction of the emission. The color of the sky map is scaled non-linearly with the radiation power, red representing high and blue low power. Since both the density and the power color-maps are non-linear and geared toward an optimal visualization, color bars are not given here but will be introduced in the following sections. This graphic representation already allows exploring the simulated radiation data in order to look for interesting radiation signatures.

Such a simulation requires a lot of computing power and time. The setup was split into four simulations, each with a subset of $N_\varphi = 64$ observation directions (two of which were the same in each simulation). This was feasible because the computational demand of the particle-in-cell simulation was an order of magnitude lower than the computational demand of the radiation calculation. Therefore, performing the particle-in-cell simulation four times was a negligible extra cost. Each simulation ran on 32 k20x NVIDIA GPUs at the Taurus cluster of the Center for High-Performance Computing (ZIH) at Technische Universität Dresden. With cluster down-times and other competing simulations using the cluster, the time to finish this simulation took approximately 9 months, starting in 2014. With cluster updates at ZIH and HZDR and with GPU clusters becoming more common, this simulation could, at the time of writing this thesis, be performed in a much shorter time.

The particle-in-cell simulation used a grid of $\Delta_\perp = 177.2\,\mathrm{nm}$ transversal resolution and $\Delta_\| = 44.3\,\mathrm{nm}$ longitudinal resolution. The time step duration was set to $\Delta t = 0.08\,\mathrm{fs}$ thus trading numerical accuracy for higher frequency resolution. The electromagnetic fields were computed using the Yee solver [82] together with the Esirkepov current deposition scheme [100]. The particle motion was computed using the Boris pusher [87]. Tests with both the Vay [93] pusher and the fields solver by Lehe [96] were also performed and showed no major differences.

As discussed in section 6.2.4 the interaction between a relativistic laser pulse and a plasma leads to self-focusing effects that can be utilized to reach higher laser intensities and the blowout regime. The large-scale particle-in-cell simulation reveals just that. While the laser would reach a normalized field strength of $a_0 = 3.5$ in a vacuum, in the plasma a field strength of $a_0 \simeq 6.5$ is reached. This is depicted in Fig. 6.11. This plot shows the maximum normalized laser field strength a_0 for various simulation time steps (solid orange line). For comparison, the evolution in a vacuum is plotted as a dashed line alongside. Initially, both curves overlap. However, with increasing laser intensity and plasma density, self-focusing sets on. This is marked by the blue region. Only due to self-focusing, the laser field strength is increased by a factor of approximately 2 which enables reaching the blowout regime. The self-focusing goes hand in hand with a decrease in the laser spot size. Again, Fig. 6.11 depicts the spot size evolution in the plasma (green solid line). Alongside, the vacuum evolution is plotted as a dashed green line. Within the resolution limit of the simulation, there is no difference in focus position between the vacuum and plasma propagation. This is not necessarily the case, as will be discussed in section 6.5. However, in this scenario the vacuum focus is located close to the beginning of the plasma density plateau, thus differences caused by self-focusing are negligible. After the laser focus, the laser refracts and the spot size increases while the laser field strength decreases. Additionally, the laser undergoes self-modulation due to the energy loss caused by the generation of the plasma wave. The degree of self-modulation and its effect on radiation is discussed in section 6.4.5.

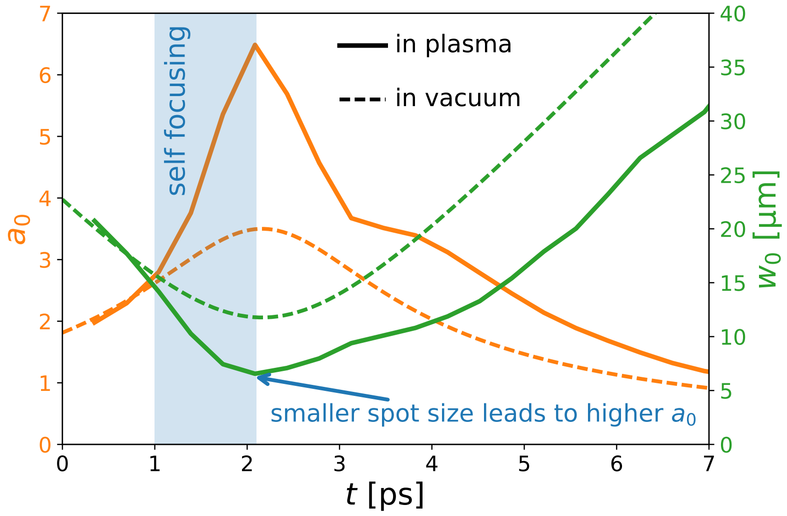

Figure 6.11: **Laser focusing under the influence of plasma:** Evolution of the laser normalized field strength a_0 and spot size w_0 (FWHM intensity) in the plasma over time compared with the theoretical laser evolution in a vacuum: Initially, both laser field strength a_0 and spot size w_0 agree with the vacuum prediction. After 1 ps, a clear deviation between plasma and vacuum evolution occurs due to the self-focusing of the laser in the plasma. This self-focusing leads to a smaller final spot size and thus to a much higher field strength a_0. The focus position is roughly the same for vacuum and plasma. After focusing, the laser diffracts, and the field strength a_0 decreases while the spot size w_0 increases again.

Numerically, both the peak field strength and the laser spot size were determined using the HDF5 data output produced every 2500th time step. A laser envelope was determined by computing the analytical function using the Hilbert transform along the laser propagation direction z for all transversal cells.

$$\vec{E}_{\text{analyt}}(z) = \vec{E}(z) + \mathcal{H}\left[\vec{E}(z)\right] \in \mathbb{C}^3 \tag{6.49}$$

with $\mathcal{H}$ being the Hilbert transform of the electric field $\vec{E}$ along the propagation direction z. This function is defined for all transversal cells and hence for the entire simulation volume as well. The absolute of the analytical function is the envelope of the laser field E_{env} along the z-axis.

$$E_{\text{env}}(z) = \left|\vec{E}_{\text{analyt}}(z)\right| \in \mathbb{R}^1 \tag{6.50}$$

By determining the maximum value from that envelope, the maximum normalized laser field strength can be computed

$$a_0(t) = \frac{q_e}{m_e \omega_0 c} \max\left[E_{\text{env}}(\vec{r}, t)\right] \tag{6.51}$$

with $\max[\dots]$ denoting the maximum value in the entire simulation volume that takes into account all envelopes along the z-axis.

Due to the fast increase of the laser intensity, the blowout regime is reached right at the start of the plasma density plateau. In this regime, electrons are injected into the cavity and are accelerated for several picoseconds. The electron energy evolution is plotted in Fig. 6.12. The first injections of electrons in the plasma cavity occur at around $1\,\text{ps} < t < 2.5\,\text{ps}$. Initially, this is a quite diffuse process, with several small-scale injections occurring quasi-simultaneously in this short time window. With ongoing acceleration in the cavity, most of these injections join. During the main acceleration phase there remain only two main electron-energy paths. Both show the same energy gain over time of approximately $\frac{\mathrm{d}E_e}{\mathrm{d}t} \approx 80\,\text{MeV/ps}$. The ribbon with the slightly higher energy contains less charge. It originates from an injection at around $t \approx 1.8\,\text{ps}$ and reaches a final energy $E_e \approx 130\,\text{MeV}$. The main ribbon arises at around $t \approx 2.2\,\text{ps}$ and reaches a final energy of around $E_e \approx 100\,\text{MeV}$. The acceleration ends at around $t \approx 4\,\text{ps}$ when the plasma density decreases rapidly and the strong accelerating field can no longer be sustained. With further propagation, the electrons lose energy since the laser is too weak to generate a plasma cavity and the bunch itself causes a plasma wakefield in the remaining, much less dense plasma which leads to an energy loss of the injected bunch.

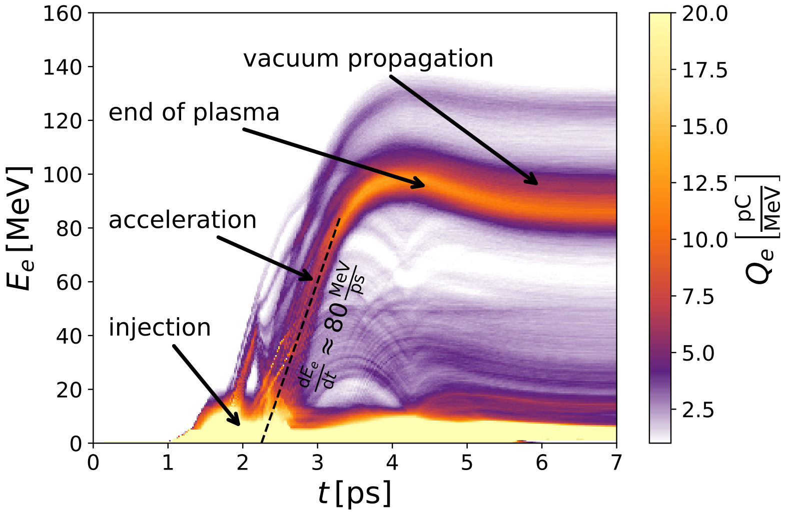

Figure 6.12: **Evolution of the electron energy distribution during the LWFA simulation:** The plot shows the electron charge Q_e distribution over energy E_e and its evolution over time t. After around $2\,\text{ps}$, the first electrons are injected into the plasma cavity and are accelerated for the next $\sim 1\,\text{ps}$ to an energy of approximately $E_e \approx 100\,\text{MeV}$ until dephasing. After the electron bunch and the laser leave the plasma and propagate through a quasi-vacuum, the electron bunch energy does not change anymore.

The data plotted in Fig. 6.12 were generated using the *energy histogram* plug-in of PIConGPU [R1]. It allows determining the electron energy distribution during the particle-in-cell simulation thus enabling more frequent data analysis steps than e.g., the analysis of the laser pulse evolution, that relied on field data output.

6.4.2 Identifying several known radiation signatures

The radiation spectra are images of the electron dynamics in Fourier space. Since the electron dynamics changes over the course of the laser wakefield acceleration, the radiation changes as well. A detector with time resolution longer than the few picoseconds of the LWFA duration measures the time-integrated radiation spectrum of all the various electron dynamics occurring during the LWFA. Such an integrated spectrum would hardly allow identifying the electron dynamics since weak radiation signals would be overlapped by stronger signals and could not be identified.

This changes if a better time resolution becomes possible. A detector with extremely fast sub-picosecond time resolution is not necessarily required for this. The plasma cavity, and thus the origin of the radiation, propagates with the speed of light. Therefore, imaging the off-axis radiation along the laser propagation direction onto a detector, e.g., a CCD camera, in addition to resolving the frequency, allows determining where and thus when a specific radiation signature occurred. The laser propagation axis is not orthogonal to the measured radiation. Imaging it along several millimeters is thus experimentally challenging but possible [192]. Therefore, the focus of this work is on off-axis radiation that allows spatial and/or temporal resolution of the plasma dynamics.

In Fig. 6.13, an exemplary time evolution of a spectrum of the LWFA simulation is plotted. The radiation depicted is emitted at an angle of $\theta = 20^\circ$ from the laser propagation axis in the plane of laser polarization. This direction was selected because the relatively large angle would allow a sub-millimeter spatial and thus a sub-picosecond temporal resolution of the plasma dynamics along the propagation direction. Furthermore, this observation direction contains a variety of radiation signatures that allow determining the plasma dynamics. Some of these radiation signatures are already known. Those are briefly discussed in this section. Two signatures, however, were discovered during this thesis and are discussed in detail in the following sections.

Figure 6.13 plots the emitted radiation energy per solid angle and frequency as a color code over six orders of magnitude. The temporal evolution is plotted along the x-axis, while the y-axis states the frequency.

A well-known characteristic radiation signature of a laser-plasma interaction is the emission of higher harmonics of the fundamental laser frequency for normalized field strength above $a_0 \gtrsim 1$ [115, 116]. It is caused by the figure-8 motion of electrons in the presence of intense electromagnetic fields where the electrons reach relativistic velocities and the influence of the magnetic field can no longer be neglected. This non-linear motion causes the emission of radiation at multiples of the laser frequency with characteristic directional structures. However, since the observation presented is off-axis, all multiples of the fundamental laser frequency ω_0 are observed. In Fig. 6.13, annotation (1) marks the second and third harmonic at $\omega = 2 \cdot \omega_0$ and $\omega = 3\omega_0$. There are even higher harmonics observable, which agrees with the theoretical work in [115] that predicts intense radiation at these higher harmonics for laser intensities around $a_0 \approx 2$, as is the case for the LWFA simulation at $t \approx 0.5\,\mathrm{ps}$ (see Fig. 6.11). However, theory predicts that the higher harmonics till the 5th harmonic are stronger than the fundamental. This is not the case in this LWFA plasma scenario due to two reasons. First of all, the theory assumes a homogeneous field strength while in an LWFA, a finite laser pulse interacts with the plasma. The field strength of $a_0 \approx 2$ is only valid in the center of the pulse. Most of the laser pulse is at much lower field strength values, thus the fundamental is more intense than the higher harmonic. Additionally, the theory assumes quasi-stationary electrons that only oscillate in the laser field but do not drift. During the LWFA, the electrons are however pushed away by the

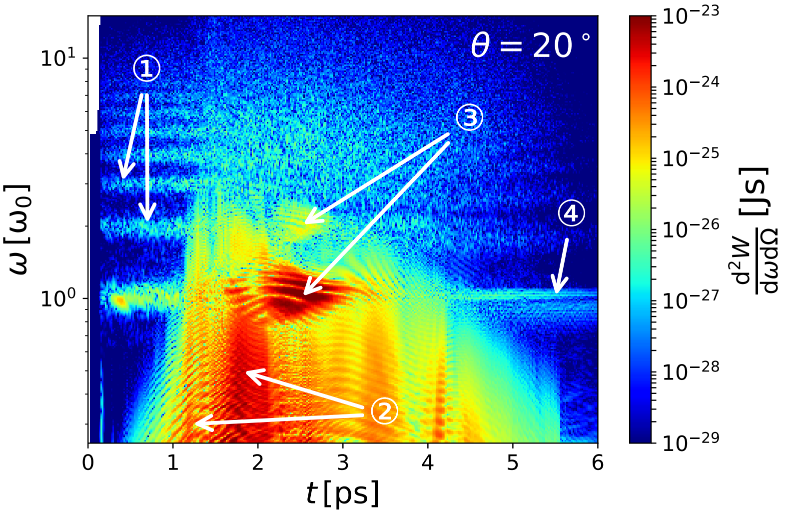

Figure 6.13: **Overview of the temporal evolution of the LWFA radiation spectrum:** Depicted is the radiation power spectra emitted under $\theta = 20^\circ$ over the entire duration of the laser wakefield acceleration. On the x-axis, the time is given. Since this spectrum is emitted off-axis, this correlates to a position along the laser propagation path which can be resolved by projecting the radiation, e.g., onto a CCD camera, thus avoiding a sub-picosecond resolution requirement. On the y-axis, the frequency of the emitted radiation is given in multiples of the laser frequency ω_0. The color code represents the energy emitted per solid angle and frequency. The annotations mark: (1) high harmonics of the laser frequency, (2) wave-breaking signature, (3) blowout signature during laser defocusing, and (4) laser self-phase modulation signature. For details, please refer to the main text.

ponderomotive force of the laser pulse like snow by a snow plow. This causes the electron to move away from the most intense part of the laser pulse, and fewer electrons actually interact with the peak field strength. This combination makes predicting the exact ratio between the higher harmonics an the fundamental for a non-linear LWFA impossible. However, over the course of time, the higher harmonics gain in intensity compared to the fundamental because of the increasing laser intensity (see Fig. 6.11).

After $t > 1.2\,\mathrm{ps}$, this higher-harmonic spectral signature is overlapped by the wave-breaking signature caused by the rapid acceleration of electrons at the dense back of the plasma cavity [28]. Between the first and second cavities of the nonlinear plasma wave, the accelerating electric field undergoes a sign change. The peak field strength is of the order of the wave-breaking field strength causing strong force gradients to the sides of the bubble sheath. Additionally, the electron density at the back of this cavity is multiple times the density of the surrounding plasma. The electrons propagating around the plasma cavity screen themselves from the ion background and the cavity fields [190]. During wave-breaking electrons suddenly change from a shielded region into the cavity with a high electric field strength. The occurring sudden acceleration force can be described by a delta distribution in time [28] causing a broadband spectral signal ranging from infrared to ultraviolet and is often accompanied by an injection of electrons. This radiation signature is particularly strong because it is emitted coherently from the very thin sheath at the end of the bubble whose thickness is similar to the emitted wavelengths [193]. This broadband signature can indicate electron injection into the plasma cavity. It is observed several times during this LWFA scenario. From Fig. 6.12 it is apparent that starting with $t > 1\,\mathrm{ps}$ there are always electrons being accelerated to energies of $E_e \sim 10\,\mathrm{MeV}$. These electrons undergo rapid acceleration and cause this broadband radiation signature, but not all of these electrons are captured and accelerated to energies of $E_e \sim 100\,\mathrm{MeV}$ in the plasma cavity. Only the most intense broadband spectral signatures, marked by annotation (2) in Fig. 6.13, correspond to two bands of electron acceleration reaching $E_e \approx 130\,\mathrm{MeV}$ and $E_e \approx 100\,\mathrm{MeV}$ (see Fig. 6.12). The still broadband but weaker radiation after $t > 2\,\mathrm{ps}$ does not correlate with a successful injection. This continuous emission makes the wave-breaking signature unsuitable for unambiguously identifying the origin of electron injection. As a side remark, the broadband radiation at $t \approx 4.1\,\mathrm{ps}$ originates from the wave-breaking when the laser pulse becomes too weak to drive a non-linear plasma wave in the blowout regime and the electron bunch starts to excite a nonlinear plasma wave itself.

The most intense radiation signature occurs between $2\,\mathrm{ps} < t < 3\,\mathrm{ps}$ and is marked by annotation point (3) in Fig. 6.13. It is caused by a distinct directional flow of electrons in front of the laser pulse during the blowout regime that interacts with the defocusing laser pulse. A detailed discussion of this signature can be found in the following section. Towards the end of the laser wakefield acceleration, the laser undergoes self-phase modulation. A second intensity peak can be observed at a slightly lower frequency than the initial laser frequency ω_0. It reflects the altered laser spectra. This self-phase modulation signature marked by (4) in Fig. 6.13 is discussed in section 6.4.5.

6.4.3 Spectral broadening during the blowout regime

From the quasi-static scattering theory derived in section 6.3.3, an off-axis scattering of laser light up to an observation angle of $\theta = 30°$ is expected in the blowout regime. This emitted light is spectrally much broader than the laser pulse itself because the electrons that scatter the light have velocities close to the speed of light and cause a significant red- and blueshift of the photons. In the blowout regime, a sub-ensemble of electrons propagates in a narrow angular direction towards $\varphi \approx \pm 20°$. Therefore, the broadest spectrum is expected under this observation angle $\theta = \varphi$.

Figure 6.13 already depicts the temporal evolution of the spectral broadening, marked by point number three. The initial broadening starts at $t \approx 2.1\,\mathrm{ps}$ right when the laser focus is reached (see Fig. 6.11) and the ponderomotive force of the laser pulse driving the plasma bubble is strongest. With further time the laser defocuses and its intensity and ponderomotive potential decreases. Along with that, the spectral broadening decreases as well. Figure 6.14 depicts four directionally resolved spectra for time steps before, during and after the blowout radiation signature.

Before the laser focus and the strongest ponderomotive force of the laser is reached, the laser light is scattered in a narrow cone in the laser forward direction $|\theta| < 10°$ (Fig. 6.14 at $t = 1.4\,\mathrm{ps}$). The scattered light is only weakly broadened. No significant radiation intensity can be detected off-axis at $\theta \approx 20°$. The corresponding electron velocity distribution is depicted in Fig. 6.15. For this analysis, macroelectrons were selected in a similar manner as in Fig. 6.8: considering only those particles that are in the central plane normal to the laser polarization and which are either in front and close around the laser pulse. At $t = 1.4\,\mathrm{ps}$, there is not yet any significant off-axis scattering structure as expected in the blowout regime. Most electrons go either in a forward direction or slightly sideways. The first signs of the side streams can already be anticipated at $\varphi \approx \pm 20°$ but these streams do not yet reach high velocities.

During the laser focus, when the laser spot size w_0 reaches its minimum and the normalized amplitude a_0 reaches its maximum (Fig. 6.11), the characteristic broadband off-axis scattering signature appears. The directionally resolved spectrum for this event at $t = 2.1\,\mathrm{ps}$ is depicted in figure 6.14. The off-axis radiation around $\omega \approx \omega_0$ reaches out to $\theta \leq 30°$. At $\theta = 20°$ it reaches an FWHM bandwidth of more than $\Delta_\lambda \approx 170\,\mathrm{nm}$ (see Fig. 6.16) and should thus be easily distinguishable against scattering of laser light from other parts within the experimental

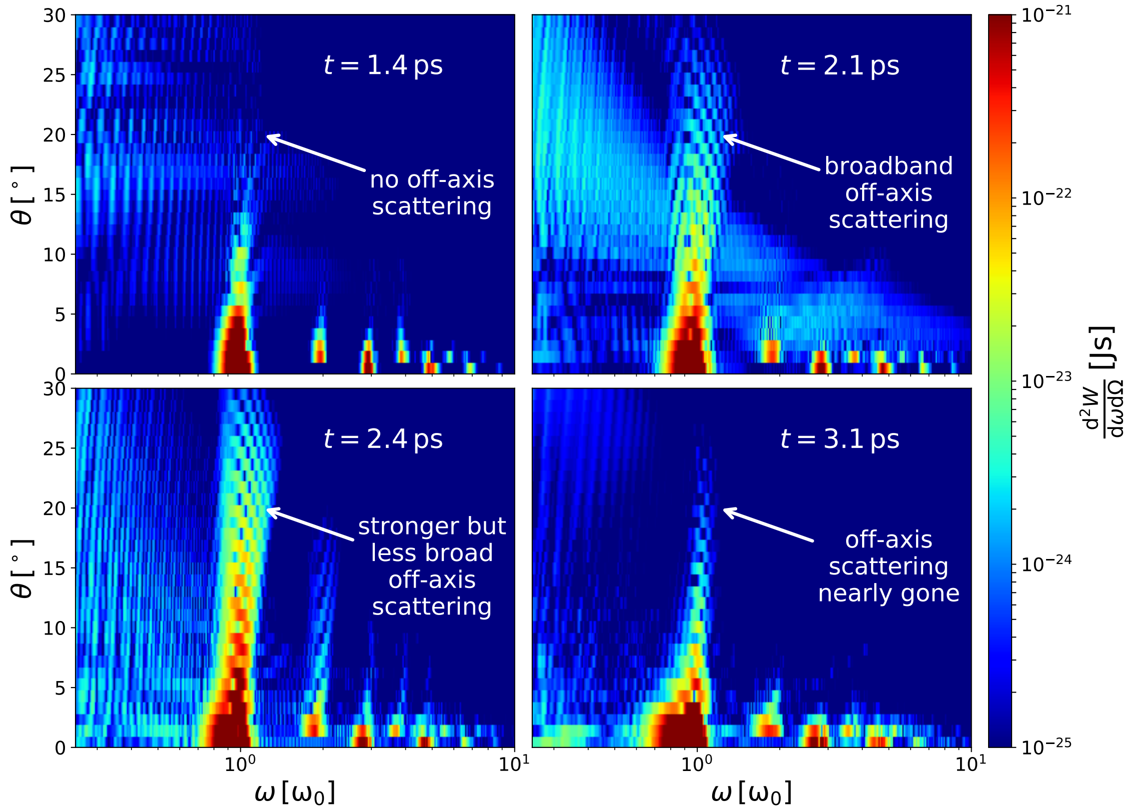

Figure 6.14: **Directionally resolved spectra for various times around the laser focus:** The four spectra show the directionally resolved radiation in the forward direction. The off-axis scattering is minimal right before the laser focus ($t = 1.4\,\mathrm{ps} < 2.0\,\mathrm{ps}$). With the onset of the defocusing of the laser, strong off-axis scattering can be observed ($t = 2.1\,\mathrm{ps}$), even at the second harmonic ($t = 2.4\,\mathrm{ps}$). The weaker, broadband, low-frequency, off-axis background radiation at $t = 2.1\,\mathrm{ps}$ originates from the initial acceleration of the injected electrons during wave-breaking. Further away from the focusing point, the off-axis scattering signature weakens again ($t = 3.1\,\mathrm{ps}$).

chamber. The velocity distribution during this phase clearly shows the characteristic lateral currents at $\varphi \approx \pm 20°$ (Fig. 6.15).

With decreasing laser peak power and a wider spot size, the characteristic off-axis radiation signature will vanish again. Before that at $t = 2.4\,\mathrm{ps}$, the spectral blowout signature becomes significantly stronger. From the purely quasi-static approximation [189], also called the frozen field approximation, which assumes that the laser evolution is negligibly slow on the time scale of the plasma response, such an asymmetry in time is not to be expected. From the quasi-static blowout model of Lu et al. which models the electron trajectories around a laser pulse, the electron path depends only on the ponderomotive potential. From the laser evolution in the simulation (Fig. 6.11), the laser is symmetric around the focus position at $t = 2.1,\mathrm{ps}$. The electron motion around the laser pulse should thus be symmetric with regard to this point in time. The radiation spectra, however, show an order of magnitude stronger off-axis radiation during defocusing ($t > 2.1\,\mathrm{s}$) than during the focusing ($t < 2.1\,\mathrm{s}$). The asymmetry with respect to the central focus position originates from the delayed response of the plasma to the laser evolution. While the typical plasma response time is of the order of $\Delta t_{\mathrm{mid}} \sim \omega_{\mathrm{pe}}^{-1}$, the laser evolution happens on time scales of $\Delta t_{\mathrm{long}} \sim \omega_0 \cdot \omega_{\mathrm{pe}}^{-2}$. For this simulation setup, the ratio

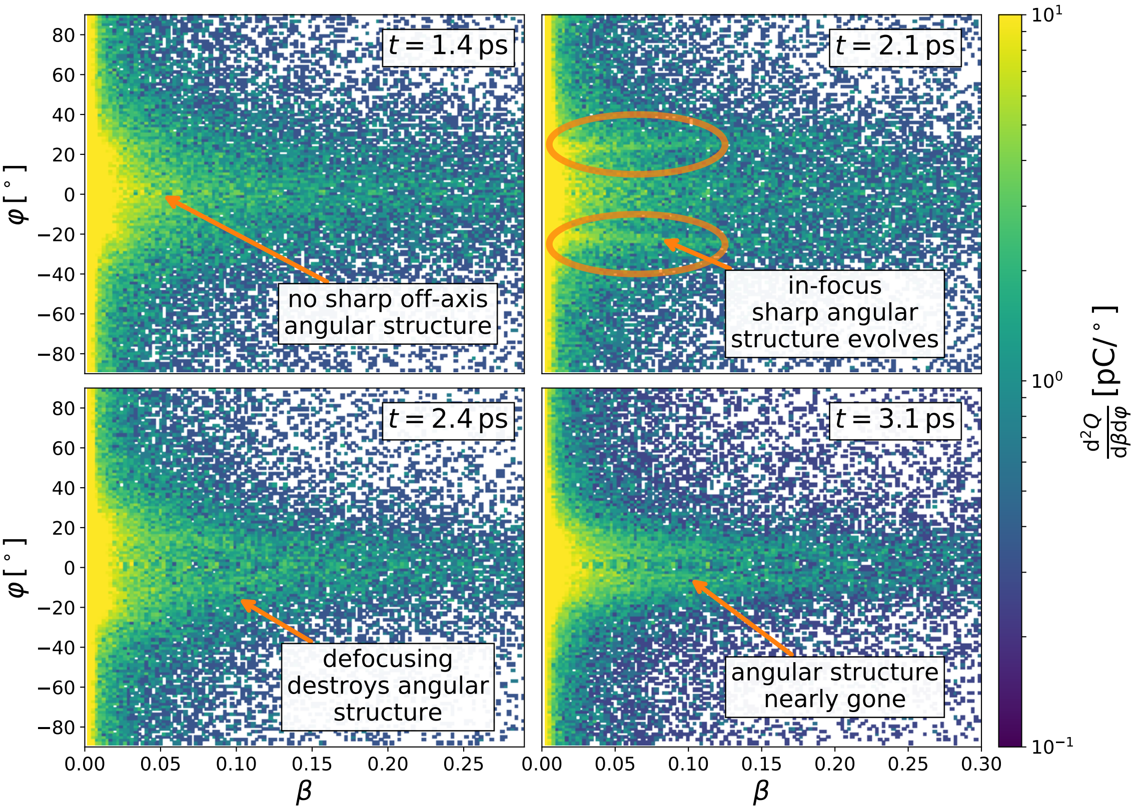

Figure 6.15: **Velocity distributions around the laser focus:** The four velocity distributions show the evolution of the distinct, directionally sharp flow of electrons around the laser pulse during defocusing. Before the defocusing, there are no sharp pattern ($t = 1.4\,\mathrm{ps} < 2.0\,\mathrm{ps}$). Right after the focus, the angularly sharp electron flows occur towards $\varphi = \pm 20^\circ$ ($t = 2.1\,\mathrm{ps}$). They rapidly break down again ($t = 2.4\,\mathrm{ps}$) and become more forward-directed $\varphi = \pm 10^\circ$ after defocusing ($t = 3.1\,\mathrm{ps}$).

between characteristic laser evolution and plasma time is

$$\frac{\Delta t_{\mathrm{long}}}{\Delta t_{\mathrm{mid}}} \approx 19 \quad . \tag{6.52}$$

The timescale Δt_{mid} on which the plasma adjusts to the laser is not significantly smaller than the laser evolution time Δt_{long}. The response time of the plasma to the evolving laser is thus not negligible.

As the laser focuses, the electrons flow around an ever-decreasing laser spot size. The electron current flows around the edge of the laser while it increases in intensity. This does not produce a strong scatter signal because the laser spot size decreases while the plasma follows.

During defocusing, on the other hand, the laser pulse, which is now widening again, eats its way into the electron current, which also narrowed down to the minimum spot size during the focusing. The interaction of the electrons with the widening laser is stronger than during focusing and a significant amount of laser light is scattered in off-axis directions. This can be clearly seen in the velocity distribution diagram Fig. 6.15 at $t = 2.4\,\mathrm{ps}$. The two characteristic currents in $\varphi = \pm 20^\circ$ become wider and less clearly recognizable due to the erosion by the laser even though the laser is strong enough to drive a bubble.

With further laser defocusing, the laser intensity becomes too low to reach the blowout regime and the characteristic off-axis velocity distribution vanishes as well as the off-axis, broadband

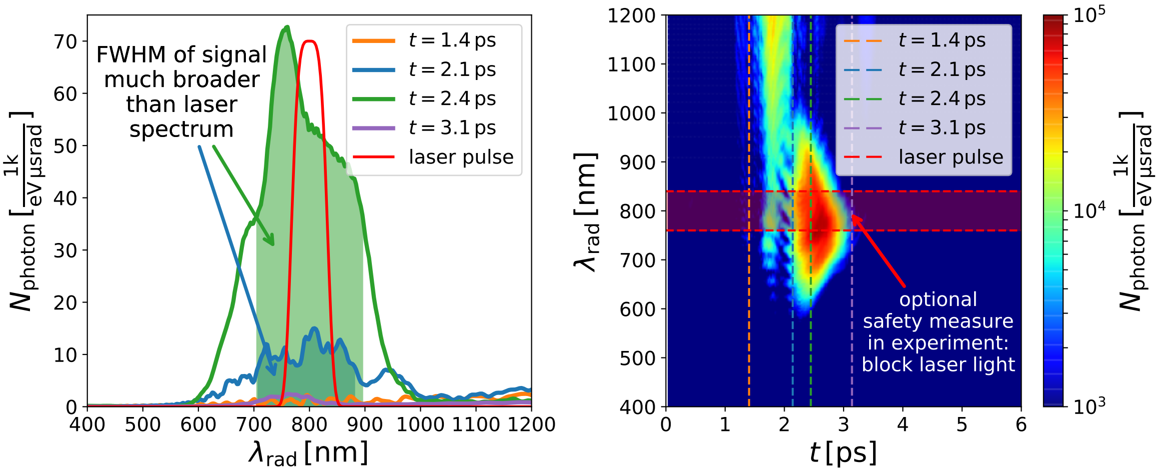

Figure 6.16: **Photon numbers of the radiation signature and possible background:** The left side depicts the radiation spectra at all characteristic times discussed before and compares is against a possible scattering from pure laser light. The off-axis radiation is much broader than the laser light and thus can be identified spectrally while blocking the laser light with a filter. The right side is an equivalent plot to Fig. 6.10 but focuses on the blowout regime signal. The dashed lines mark the characteristic times on the left side. The laser spectrum is scaled to the maximum photon number. From the plasma itself, no laser scattering should occur in this direction. The laser bandwidth is *just given for safety reasons* to not destroy any optical instruments in case of scattering other than from the plasma.

radiation signature. This is depicted in the reduced off-axis radiation at $t = 3.1$ ps in figure 6.14 and the two streams of electrons at $\varphi \pm 5^\circ$ whose direction has approached the forward direction.

An essential question is whether this broadband off-axis radiation signature for the blowout regime can be experimentally observed. There are two requirements: enough photons need to be emitted to detect the signal, and the signal needs to be spectrally broader than the laser light. The latter is *only a safety measure* to avoid destruction of the detector in case laser light from optical components is scattered inside the chamber. It could be implemented by installing a bandpass filter in front of the detector. At these large observation angles, the simulation does not predict significantly stronger scattering from the plasma at the original laser frequency. Under normal circumstances, no damage should, therefore, occur to the detectors due to direct laser irradiation.

The spectrally resolved photon number can be determined by converting the classical spectrally resolved radiation energy to a photon spectrum

$$N_{\text{photon}} = \frac{1}{\hbar\omega}\frac{\mathrm{d}^2 W}{\mathrm{d}\omega\,\mathrm{d}\Omega}\cdot\frac{\Delta E}{\hbar}\cdot\Delta\Omega \tag{6.53}$$

with ΔE being the energy width of the detector and $\Delta\Omega$ being the solid angle of observation covered by the detector. As depicted in figure 6.16, both requirements are fulfilled. The signal is broader than the laser spectrum and it reaches significant photon counts of up to $N_{\text{photons}} \approx 70,000\,\frac{\text{photons}}{\text{eV}\,\mu\text{srad}}$ which would mean more than $300,000$ photons in a spectral range of $\Delta\lambda 50$ nm on a 1 cm $\times$ 1 cm-sized detector 1 m away.

The above radiation signature not only allows determining the existence of the blowout regime but also pinpointing the focusing position and the duration of the defocusing until the laser pulse can no longer sustain the blowout regime. The accuracy with which this radiation signature can be used to determine the laser focus position in the plasma is demonstrated in the following section using a large simulation survey.

6.4.4 Determining the focus position with plasma radiation

A laser can undergo self-focusing in a plasma which leads to a different laser focus position within the plasma than when propagating in a vacuum. Similar to an experimental setup, a simulation specifies the vacuum focus position of the laser. The self-focusing in the plasma is then treated self-consistently by the particle-in-cell simulation. In experiments, the actual laser focus position in the plasma is vital for understanding and controlling the acceleration process, but it cannot be measured. (A detailed case study on how strongly the laser self-focusing influences the acceleration process during LWFA can be found in chapter 6.5.) Therefore, the input from PIC simulations is essential to quantify this self-focusing and to improve the understanding of the resulting laser plasma dynamics. As with any measured variable, the vacuum focus position is also subject to inaccuracies. In addition, higher-order laser modes strongly influence self-focusing but are difficult to quantify in experiments. As input for simulations, these inaccuracies lead to possibly faulty predictions of the plasma focus positions and thus to a wrong understanding of the laser plasma dynamics and electron acceleration. A measurement method to determine the actual laser focus position in the plasma would allow a comparison between experiment and simulations and thus a validation of the predictions of PIC simulations. However, such a diagnostic procedure has not yet been experimentally implemented. The following parameter study, therefore, provides a first essential step in validating whether the blowout radiation signature is suitable for determining the focus position in experiments. It confirms that the broadband off-axis signature discussed in the section 6.4.3 is, due to its asymmetry with respect to focusing and defocusing, ideally suited to determine the focus position of the laser in the plasma if the laser is strong enough to drive the plasma wake in the blowout regime.

Due to the vast number of simulations required for the parameter scan presented here, radiation simulations were only computationally feasible in 2D geometry. This simplification can be made since the main objective of this survey was the laser evolution which, in contrast to the plasma-bubble structure or injection, is not strongly affected by a reduction to two dimensions.

The simulations performed with PIConGPU were chosen according to an experiment performed at HZDR. In contrast to the previous simulation, the experiment applied the self-truncated ionization-injection scheme (STII - see section 6.2.5) using helium gas with a nitrogen dopant. Only nitrogen K-shell electrons are injected into the bubble and accelerated. Self-truncation is based on significant self-focusing of the laser originating from locating the vacuum focus behind the plasma. Determining the laser evolution and its actual focus position in the plasma is therefore essential for understanding the injection and acceleration. For the following discussion about the radiation parameter scan, the details of the setup are not essential. A thorough discussion of this setup, including the challenges when simulating the laser plasma evolution and resulting acceleration, can be found in chapter 6.5.

The focusing position in the plasma was varied by changing both the laser vacuum focusing position and the plasma density. In all cases, relativistic-self focusing played an essential role. The laser focus position under the influence of the plasma was determined by searching the global maximum of the laser envelope computed using the simulation data output (see Eq. 6.51).

The simulations were capable of distinguishing the radiation from the background electrons (helium K-shell and nitrogen L-shell) and the nitrogen K-shell electrons. As expected, the radiation of the nitrogen K-shell electrons did not show the blowout signature, since they are separated from the atoms in the more intense region of the laser and do not have the characteristic collective velocity distribution as the background electrons.

An exemplary evolution of the laser and the radiation spectra is depicted in figure 6.17. With the beginning of the plasma at $z = c \cdot t =\gtrsim 0.5\,\mathrm{mm}$ radiation at the laser frequency is emitted. It originates from the laser pulse which still has not yet reached enough intensity to drive a blowout regime $a_0 < 3.0$. Therefore, scattered light is not significantly blue- or red-shifted and

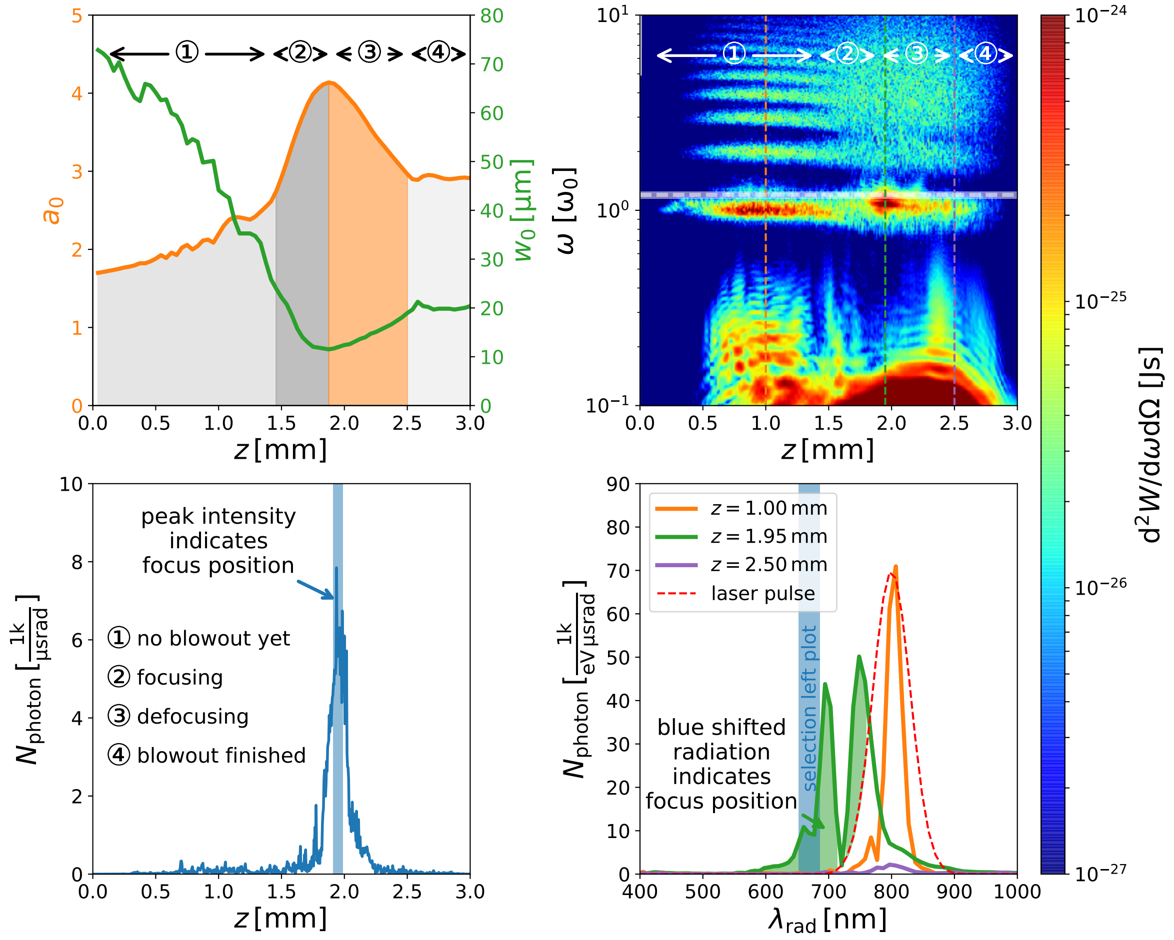

Figure 6.17: **Determining the focus position via the blowout blueshift:** The upper left plot depicts the laser pulse evolution with the normalized laser field strength a_0 (orange) and the beam waist w_0 (green) of an exemplary simulation along the laser position $z = c \cdot t$. The focus is at $z \approx 1.9$ mm. The upper right plot describes the spectral evolution with a frequency ω scale normalized to the laser frequency ω_0. Dashed lines mark the example spectra from the lower right plot in the corresponding color. The lower left plot shows the laser intensity evolution in number of photons N_{photons} at $\theta \approx 26°$. The intensity peak marks the focus position. In blue, the FWHM region of the intensity peak is marked. It was used as the uncertainty of the focus position based on the radiation. The lower right plot shows three simulated spectra for selected time steps over the wavelength λ_{rad}.

the main radiation is emitted at $\omega = \omega_0$. This early regime is marked by ①. This can also be seen in the orange-colored spectrum originating from $z = 1.00$ mm (Fig. 6.17 lower right). Its peak is centered around $\lambda \approx 800$ nm. For comparison, the spectra in the lower right corner of figure 6.17 also shows the model laser that might overshadow any scattering signal. At higher frequencies, higher harmonics can clearly be identified in this pre-blowout regime.

Between $z \approx 1.4$ and $z \approx 1.9$ the laser intensity increases. The characteristic scattering of photons at the laser frequency vanishes and the high harmonics start to blur. This is marked by ② in figure 6.17. In contrast to the previous simulation, there is no significant wave-breaking radiation, since the electrons already injected via STII reduce the field strength at the end of the plasma bubble and thus prevent self-injection via wave-breaking.

At $z = c \cdot t = 1.95$ mm, the maximum scattering intensity at $\omega = 1.2 \cdot \omega_0$ is reached. The temporal evolution of radiation intensity at this frequency is depicted on the lower left of figure 6.17. The clear rise in intensity indicates the laser focus position. As the uncertainty of the position, the FWHM of the radiation intensity is used. It is marked by the transparent blue box. The focus position according to the radiation spectrum is thus $z_{\text{focus}} = 1.95\,\text{mm} \pm 0.09\,\text{mm}$. The expected focus position according to the simulated field evolution is $z_{\text{focus}} = 1.88\,\text{mm} \pm 0.21\,\text{mm}$. The spectral method perfectly reproduced the focus position.

Since only electrons in the laser propagation and polarization plane are modeled in this two-dimensional simulation, the off-axis radiation is slightly different than in the 3D case. The missing third dimension results in a sharp selection of electrons and therefore less broadband radiation. Only the blue-shifted radiation, which is scattered by the electrons moving exactly towards the virtual detector, is reproduced correctly. In a fully three-dimensional simulation, an equivalent part of the radiation would also be scattered at the laser frequency. As the previous 3D simulation suggests, this would mean a spectrally much broader and thus more intense radiation signal in the experiment.

The defocusing region of the laser in the blowout regime is marked with a ③ in Fig. 6.17. It causes a significant off-axis radiation signature which is strongest close to the laser focus and which decreases in intensity with decreasing laser peak intensity a_0. Since this simulation assumes a slightly lower plasma density, the ratio between characteristic laser evolution time and plasma reaction time

$$\frac{\omega_0}{\omega_{\text{pe}}} \approx 25 \tag{6.54}$$

is higher than in the 3D simulation discussed in section 6.4.3. The decay of the signature thus happens faster which allows determining the focus position more accurately.

Further downstream, the off-axis radiation signature vanishes again both due to the reducing intensity when defocusing and due to the reduced number of electrons in the down ramp. This final region is marked by ④. The corresponding spectrum at $z = 2.5\,\text{mm}$ is depicted in purple in the lower right plot. In comparison to the previous emission, the number of emitted photons is strongly reduced.

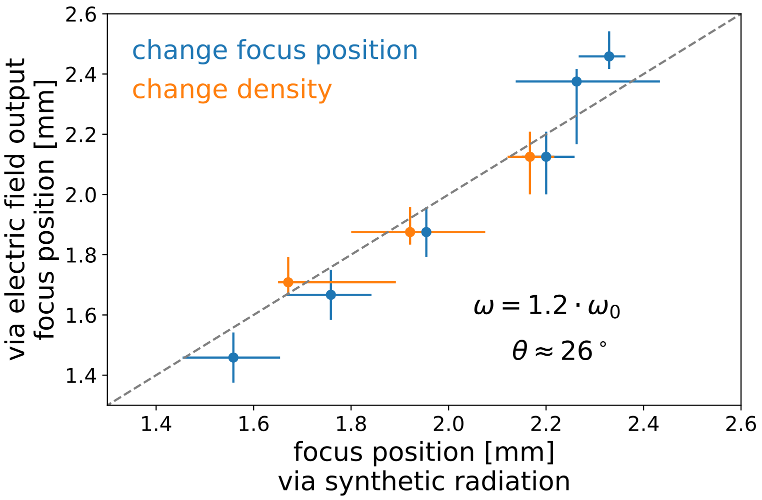

Figure 6.18: **Results of the parameter scan:** The plot illustrates the correlation between the focus position based on the simulated laser field evolution and based on the emitted blue-shifted off-axis radiation. The focus position was changed by adjusting the vacuum focus position and the plasma density. The focus position determined via synthetic radiation diagnostics is equal within the margin of errors to the focus position determined by a detailed analysis of the laser evolution in the PIC simulation.

These kinds of 2D radiation simulations were conducted for various laser vacuum focus positions and plasma densities. The vacuum focus was always set to be close to the end of the gas jet or even behind it. The relativistic self-focusing leads to an earlier laser focus in the plasma as discussed before. The laser focus was also moved forward by increasing the plasma density and thus the strength of the plasma feedback on the laser. For all simulations, the focus position was determined by analyzing the peak laser envelope value (Eq. 6.51) for each data output. The temporal uncertainty of this numerical method was assumed to be equivalent to the time between consecutive data outputs. Independent of this analysis, the position of the maximum radiation intensity at $\omega = 1.2\omega_0$ and $\theta \approx 26^\circ$ was determined. The uncertainty of this position was the FWHM of the intensity peak.

Figure 6.18 shows the correlation between both methods. The spectral method reproduces the results of the field method within the error margins. It is thus well suited for an experimental determination of the focus position.

The spectral method slightly overestimates the focus position, as expected from the temporal asymmetry of the blowout radiation signature. This is only not the case for focus positions $z_{\text{focus}} > 2.2\,\text{mm}$ where the gas density drops significantly and the spectral method predicts an earlier focus position. However, with the knowledge of the gas density distribution, the influence of these shifts can be estimated and eliminated beforehand.

The spectral method poses a new experimental technique to determine the focus position of the laser pulse in the gas. It requires only the laser to be strong enough in focus to reach the blowout regime, which is the case for most experimental LWFA setups today.

6.4.5 Radiation signature of self-phase modulation

Coming back to the original 3D explorative radiation simulation, the plasma density decreases after the density plateau. In the simulation, this is modeled by a gradual down-ramp gradient. As in reality, there is a low-density plasma remaining through which both the laser and the electron bunch need to propagate.

According to the laser evolution (Fig. 6.11), at some point in the down ramp, the laser intensity will be too weak to drive a non-linear plasma wave in the blowout regime. At that point, electrons will start to propagate through the ponderomotive potential of the laser pulse and directly interact with the bunch. The bunch, on the other hand, contains enough charge ($Q \approx 220\,\text{pC}$) that its electric field is capable of driving a non-linear plasma wave in the blowout regime. Thus, at this stage, the first electron bunch becomes the driver of a non-linear plasma wave. Such a scenario of an electron bunch driving a plasma wave is called a plasma wakefield accelerator (PWFA) [194]. Since the electron bunch drives a wakefield, it loses energy, as can be seen in Fig. 6.12. Due to the decreasing plasma density, the energy loss decreases as well. The entire electron density distribution for a slice through the center of the laser is depicted in Fig. 6.19 (left side). The blowout bubble caused by the electron bunch can be clearly identified. In the bubble itself, additional electrons are accelerated. However, due to the low plasma density, the accelerating gradient and therefore the energy gain is negligible compared to the laser-driven blowout regime.

During this PWFA stage, the laser pulse still exists and propagates in front of the electron bunch (see FWHM contour line of the laser in Fig. 6.19). It excites a weak plasma wake. Along its entire length, plasma electrons oscillate in its field as can be seen in the phase space diagram in Fig. 6.19 (right side). Thomson scattering radiation will be emitted by these oscillating electrons. Since the laser intensity is weak, the drift velocity of the electrons due to the ponderomotive potential of the laser pulse can be neglected. Thus, radiation will be scattered predominately at the laser frequency. However, due to the previous interaction of the laser with the plasma, the laser underwent self-phase modulation and thus has a broader spectrum than initially [195–197]. The exact change in frequency cannot be predicted. From the depletion length

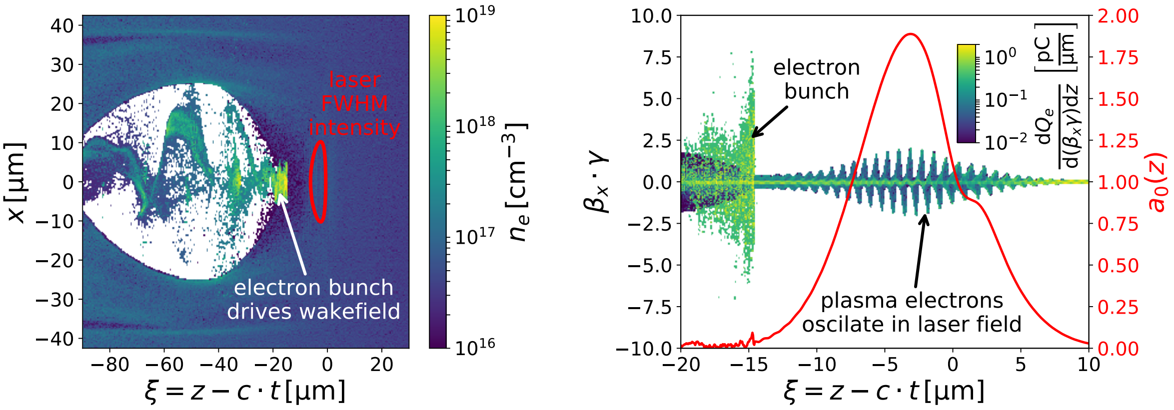

Figure 6.19: **The laser plasma dynamics after the transition from LWFA to PWFA:** The left plot shows the electron density n_e along one transversal position x and the co-propagating position $\xi = z - c \cdot t$. The right plot shows the phase space distribution of the normalized transversal momentum $\beta_x\gamma$ along the co-propagating position ξ with Q_e being the charge. The normalized field strength a_0 of the laser envelope is depicted in red. During the down ramp of the density profile, the laser becomes, due to refraction, too weak to drive the blowout regime. In contrast to that, electron bunch contains enough charge to drive a nonlinear wakefield in the blowout regime on its own. Only a few electrons in front of the bunch oscillate in the laser field. These electron scatter light from the now broader laser spectrum.

estimates introduced in section 6.2.4, one can only determine how strong the influence will be. As discussed previously, the laser peak intensity evolves due to self-focusing and refraction and thus is not constant during the plasma interaction. The same is true for the density profile. However, a rough estimate of the depletion length for a peak vacuum intensity of $a_0 = 3.5$ and a maximum density of $n_e = 5 \cdot 10^{18}\,\mathrm{cm}^{-3}$ results, according to Eq. 6.33, in a depletion length of approximately $L_{\mathrm{dp}} = 8.2\,\mathrm{mm} = c \cdot 27\,\mathrm{ps}$. From this estimate, one can expect that the laser will not vanish completely during the laser plasma interaction but since the depletion length is of the order of the propagation distance, changes in the laser pulse, like self-phase modulation, are to be expected.

In order to analyze the self-phase modulation of the laser pulse numerically, the analytic function $\vec{E}_{\mathrm{analyt}}$, introduced in section 6.4, was used again. For a spectral analysis, only the polarization component of the laser pulse needs to be considered $E_x^{\mathrm{analyt}} = \vec{e}_x \cdot \vec{E}_{\mathrm{analyt}}$. The instantaneous frequency can be determined by

$$\omega_{\mathrm{laser}}(z) = c \cdot \frac{\mathrm{d}}{\mathrm{d}z} \arg\left[E_x^{\mathrm{analyt}}(z)\right] \quad , \tag{6.55}$$

with $\arg[\ldots]$ being the argument of a complex number. Numerically, the derivative is replaced by a difference quotient.

The instantaneous frequency was computed for the entire simulation duration. It is plotted, normalized to the initial laser frequency ω_0, in Fig. 6.20. This graph shows the time evolution along the x-axis and the co-moving longitudinal position ξ relative to the initial laser center along the y-axis. The color code represents the instantaneous laser frequency, with red representing a lower frequency than the initial laser frequency (red-shifted) and blue representing a higher frequency (blue-shifted). During the interaction with the plasma, the front of the laser is red-shifted to a frequency of approximately $\omega_{\mathrm{laser}} \approx 0.8 \cdot \omega_0$. The front part also moves slowly backward with respect to the rest of the pulse. The analysis has been restricted to field strength above 20% of the maximum laser field strength at each time step ($E_x > 0.2 \max\left[E_x(z)\right]$) to avoid numerical inaccuracies in determining the instantaneous frequency at a low field strength.

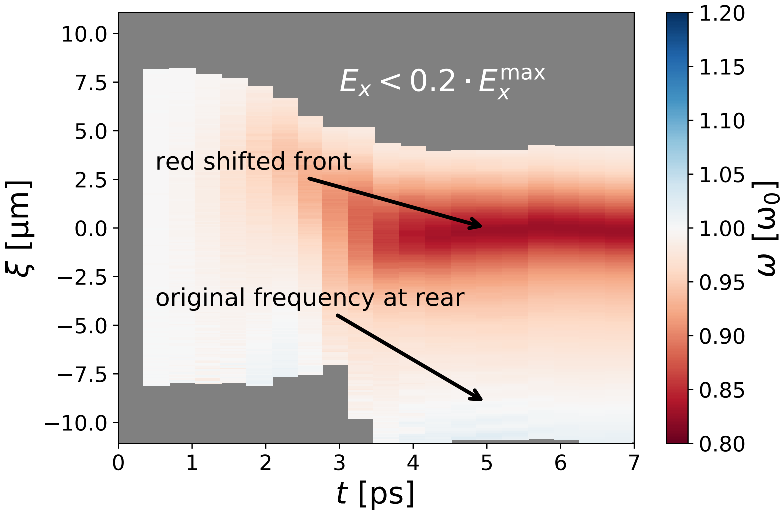

Figure 6.20: **The spectral evolution of the laser pulse:** This plot depicts the most intense frequency ω of the laser pulse along the co-propagating coordinate axis $\xi \simeq z - v_{\text{laser}} \cdot t$. The evolution of the laser spectrum is plotted over time t. The spectral contributions have been determined via a Hilbert transform. The frequency in units of the original frequency ω_0 of the laser is given as color, with blue representing a higher frequency (blueshift) while red representing a lower frequency (redshift). Initially, the laser has just one frequency with slight variations due to its finite pulse duration. With increasing propagation through the plasma, the front of the pulse is etched away and red-shifted. This shift in the driver frequency leads to a frequency shift in scattered radiation as well.

This change in laser frequency leads to a change in scattering frequency. The source frequency can no longer be assumed to be homogeneous. Since the electrons propagate through the laser pulse, they not only oscillate according to the red-shifted part of the laser at $\omega_{\text{laser}} \approx 0.8 \cdot \omega_0$ but also at the rear of the pulse at the initial laser frequency $\omega_{\text{laser}} \approx \omega_0$. Since the transition between the red-shifted part of the pulse and the unaltered part of the pulse happens on a length scale of a few micrometers, the transition between both frequencies happens fast, and thus the main scattered radiation is at $\omega \approx 0.8 \cdot \omega_0$ and $\omega \approx \omega_0$. This can be clearly seen in the line splitting after $t > 5\,\text{ps}$ in Fig. 6.13. Exemplary spectra at various time steps are plotted in Fig. 6.21. They show clearly the two peaks, one strongly red-shifted, in accordance with the laser self-modulation.

Since this radiation spectrum can be observed at an off-axis angle of $\theta = 30°$, measuring the scattered radiation in a background plasma is an alternative option for determining the laser self-phase modulation towards depletion. Current experiments need to analyze the laser pulse after the interaction by a spectrometer [198, 199]. This requires a separate diagnostics. However, the simulation shows that by measuring the side-scattered radiation from the post-LWFA region the redshift due to self-modulation can be determined equivalently. Especially in cases where the radiation is measured anyway, the costs for laser post-diagnostics can be reduced. In addition, this technique enables a non-invasive temporal resolution of the laser's spectral evolution that no other diagnostic method has been able to offer.

Furthermore, observing this double-peaked scattered radiation signature in experiments clearly shows that a rest gas is still present when the laser becomes too weak to drive a strong wakefield. It points to a PWFA regime, driven by the bunch which in turn is preceded by the laser pulse.

Determining the laser spectrum is essential in compact Thomson scattering setups where the laser pulse, after accelerating electrons via LWFA, is back-reflected onto the bunch by a plasma

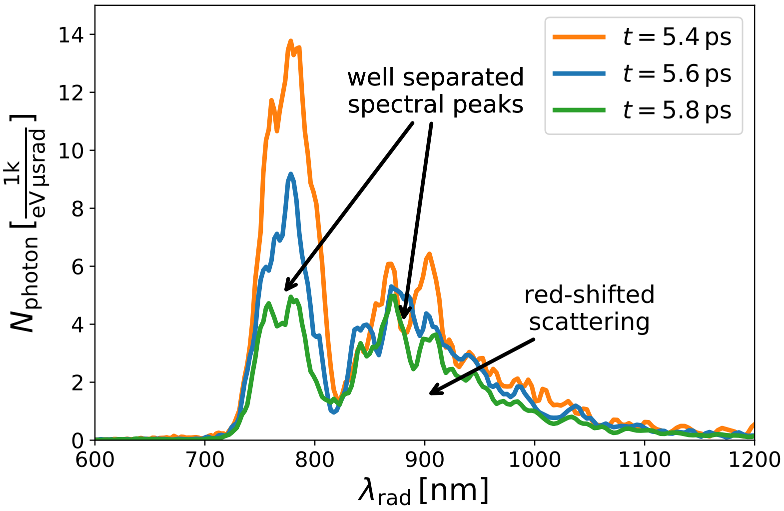

Figure 6.21: **Red-shifted second scatter peak:** The spectrum shows the number of photons N_{photons} emitted per wavelength λ_{rad} under an angle $\theta = 20°$. The figure illustrates the well separated second spectral peak caused by scattering from the red-shifted front side of the laser. This spectral line splitting is a hallmark signature of laser self-phase modulation.

wake [200, 201] or by a solid foil acting as a plasma mirror [202–206]. During the laser-bunch interaction, high-energetic radiation is scattered towards the bunch propagation direction. The spectrum of the scattered radiation depends sensitively on the laser spectrum. In order to determine the laser spectra before the laser is reflected and right after the bunch interaction in the plasma, all common methods cannot be applied since the laser spectrum measured will be further altered. Thus, only measuring the scattered radiation gives the ability to determine the quality and spectral distribution of the back-reflected laser pulse and thus the quality of the Thomson source.

6.5 A case study: Ionization injection at the DRACO laser

Recently, an experimental laser wakefield acceleration campaign based on ionization injection was conducted at HZDR. The experiment generated quasi-monoenergetic electron bunches of more than $E_e \approx 300\,\mathrm{MeV}$ peak energy with more than $Q_e \approx 300\,\mathrm{pC}$ of bunch charge [R2, R12]. The bunch generation was stable and reproducible. This not only provided an LWFA electron source with unprecedented peak current that enabled using the generated bunches as a driver for a second plasma wakefield accelerator (PWFA) stage [R18]. It also allowed performing a unique parameter survey studying the beam loading effects in an isolated environment by altering the dopant concentration without changing the plasma density significantly. As part of this thesis, simulations for this experimental setup were conducted. These allowed studying the beam loading effect qualitatively. The differences between the experimental measurements and the simulation results lead to the development of a new laser model based on Laguerre modes. Furthermore, a radiation diagnostics method was developed to quantify the remaining differences between simulation and experiment.

In section 6.5.1, the experimental setup is briefly introduced. In the following section 6.5.2, the injection and the subsequent electron acceleration, essential for quasi-mono-energetic beams, is discussed based on the simulation results. The initial discrepancies between the simulations based on a Gaussian laser pulse and the experiment are examined and improvements of using a laser model that includes the higher laser modes as in the experiment are discussed. However, even with improved laser modeling in the simulation, in-plasma focusing and thus acceleration still remains an issue that could not be satisfactorily modeled.

Therefore, the previous section 6.4.4 presented a new diagnostic method based on the scattering model introduced in section 6.3.3 that allows determining the exact laser focus position inside the plasma. It enables to pin down the remaining discrepancies between the experiment and the simulation via future experimental measurements.

6.5.1 Reaching 300pC of charge with DRACO

The LWFA experiment performed at HZDR was based on an ionization injection scheme that used helium gas with a nitrogen doping between $0.5\% < p < 3.0\%$ partial gas pressure. Both the helium K-shell ($n = 1$) electrons and the nitrogen L-shell electrons ($n = 2$) have ionization energies below a few tens of electron volts (Tab. 6.1). The nitrogen K-shell electrons, however, detach from the ion above $500\,\mathrm{eV}$ and are thus ionized at relativistic laser intensities above $a_0 > 2.2$ only. The large difference in ionization energy between the K- and L-shell makes nitrogen ideally suited and a commonly used gas for ionization injection [179]. The large concentration of helium compared to nitrogen creates the majority of plasma electrons and thus allows a stable plasma wake in which the nitrogen concentration can be altered without significantly affecting the overall plasma density. This allows changing the number of injected electrons by adjusting the nitrogen dopant concentration while keeping the dynamics of the laser-driven plasma wake unaltered.

Table 6.1: **Ionization energies of helium and nitrogen:** Listed are all ionization energies from the neutral atom state to the fully ionized state of helium and nitrogen in electron volts. Additionally, the classically required electric field for ionizing the respective state is given in units of normalized intensity with regard to a $\lambda_0 = 800\,\mathrm{nm}$ laser. The levels marked in orange are ionized by the laser pre-pulse already. The levels marked in green require much higher fields strength for ionization. The electrons from these two states are only ionized in the laser focus region and are the ones injected during the ionization injection process.

Level	**Transition**	$\mathcal{E}_{\mathrm{ion}}$ [eV]	$\lvert\vec{E}_{\mathrm{ion}}\rvert$ [a_0]
He I	$\mathrm{He} \rightarrow \mathrm{He}^{1+} + e^-$	24.6	$2.6 \cdot 10^{-2}$
He II	$\mathrm{He}^{1+} \rightarrow \mathrm{He}^{2+} + e^-$	54.4	$6.4 \cdot 10^{-2}$
N I	$\mathrm{N} \rightarrow \mathrm{N}^{1+} + e^-$	14.5	$9.1 \cdot 10^{-3}$
N II	$\mathrm{N}^{1+} \rightarrow \mathrm{N}^{2+} + e^-$	29.6	$1.9 \cdot 10^{-2}$
N III	$\mathrm{N}^{2+} \rightarrow \mathrm{N}^{3+} + e^-$	47.4	$3.3 \cdot 10^{-2}$
N IV	$\mathrm{N}^{3+} \rightarrow \mathrm{N}^{4+} + e^-$	77.5	$6.5 \cdot 10^{-2}$
N V	$\mathrm{N}^{4+} \rightarrow \mathrm{N}^{5+} + e^-$	97.9	$8.3 \cdot 10^{-2}$
N VI	$\mathrm{N}^{5+} \rightarrow \mathrm{N}^{6+} + e^-$	552.1	2.20
N VII	$\mathrm{N}^{6+} \rightarrow \mathrm{N}^{7+} + e^-$	667.0	2.75

The experiment was performed in a vacuum chamber. The plasma, in which the accelerating wakefield was generated, was produced by a Laval nozzle from which the helium-nitrogen gas mixture was released into the vacuum chamber at supersonic velocities. The gas doping was adjusted by attaching pressurized gas bottles with predefined doping ratios. Depending on the pressure at which the Laval nozzle was operated and depending on the height above the gas exit, the density of the plasma could be adjusted between $n_e = 3 \cdot 10^{18}\,\mathrm{cm}^{-3}$ and $5 \cdot 10^{18}\,\mathrm{cm}^{-3}$ (giving the density of the ionized plasma with electrons from He^{2+} and N^{5+}). Due to its better stability in the experiment, the density was mainly varied by adjusting the gas pressure. The spatially resolved gas density distribution was measured by interferometric methods [207]. The measured density profile was the basis of the simulated plasma profile. The simulated density profile was fitted according to experimental measurements and is depicted later in Fig. 6.25 when discussing simulations.

The plasma wakefield is driven by focusing the DRACO laser [R11] with an off-axis parabolic mirror (f/20) onto the rear side of the gas jet. For this experiment, the DRACO system did not operate at full power and without the last amplifier stage. It delivered pulses of $2.5\,\mathrm{J}$ total energy and a duration of approximately $\tau = 30\,\mathrm{fs}$ (FWHM intensity). With the focusing mirror, a spot size of $w_0 = 20\,\mu\mathrm{m}$ (FWHM intensity) was reached. This spot size matches a plasma density of $n_e = 2.8 \cdot 10^{18}\,\mathrm{cm}^{-3}$. The density of the experiment is slightly higher and thus the spot size is larger than according to the ideal matching condition. Since the focus was located at the end of the gas profile, self-focusing plays an essential role as is demonstrated by simulations in the next section. According to simulations, the self-focusing leads to a matching spot size and much higher laser field strength. The pulse shape modulation leads to a self-truncated ionization-injection (STII) process [184, 185, 208], that stops injection quickly and thus ensures short and quasi-monoenergetic electron bunches to be accelerated in the plasma wake [R2, R12].

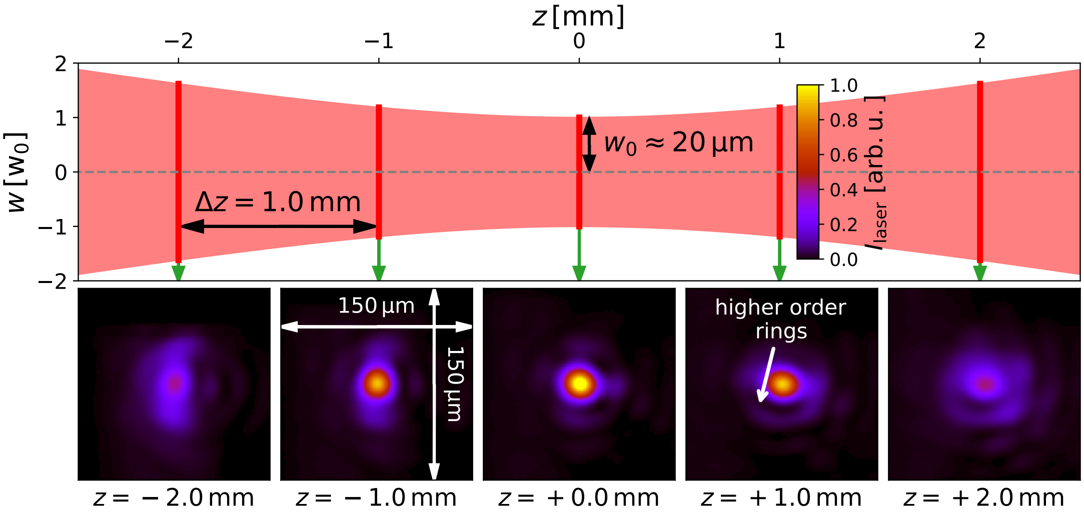

Figure 6.22: **Laser intensity profile at various positions:** These experimentally measured intensity I_{laser} profiles of the laser pulse along its propagation direction z reveal that a simple Gaussian envelope cannot describe the laser pulse but that higher order Gauss-Laguerre modes need to be considered to model the transverse structure of the laser pulse in simulations. For illustrative purposes, the theoretical evolution of the laser beam waist w relative to the beam waist at focus w_0 is plotted above the five intensity plots. Each intensity graph is an average over ten laser shots and shows the transversal laser profile.

Before the experimental campaign, the DRACO laser pulse was characterized in the vacuum. At various positions around the laser focus, the transversal profile was measured with a stationary CCD screen which was illuminated with a reduced laser intensity. The intensity was reduced by introducing partially reflective plates into the optical beam line. The various focus positions were achieved by moving the final focusing mirror. This measurement revealed that the laser not only comprised a Gauss mode but contained higher, so-called Laguerre, modes, appearing as rings around the central Gaussian pulse shape in the CCD intensity image. These rings are especially dominant a couple of millimeters away from the focus position (see Fig. 6.22). Recent simulation already suggested [209] that these higher modes have a significant influence on the performance of the acceleration process. Therefore, these higher modes were added to PIConGPU and their influence was investigated, as will be discussed in the simulation section 6.5.2. The influence of the laser profile in simulations revealed alterations in the laser plasma dynamics when including higher Gauss-Laguerre modes. Taking into account these modes is obviously essential when modeling the experiment with particle-in-cell codes.

As mentioned before, the experiment was able to produce bunch charges of $Q_e \approx 300\,\mathrm{pC}$. Most of the injected electrons reached an energy of around $E_e \approx 300\,\mathrm{MeV}$ with a narrow energy spread of $\Delta E_e \approx 50\,\mathrm{MeV}$ under optimal beam loading conditions [R2]. These electron bunch parameters were reasonably reproducible with the setup used in the experiment. Altering the group dispersion delay (GDD) of the laser further increased the stability of this setup [R12]. In Fig. 6.24, the electron energy distribution for 10 consecutive shots is plotted. Only one laser shot, labeled (j), did not produce an electron bunch with the expected parameters. This stability allowed an extensive parameter survey [R2] that could study the influence of the bunch self-charge on the acceleration process. By increasing the nitrogen doping, the trapped bunch charge could be increased. The experiment revealed that with increased bunch charge the energy spread of the bunch reduced until a point of optimal loading. During optimal loading, the accelerated field seen by all bunch electrons is equal, and thus the energy spread is reduced. By adding more charge, the bunch self-field alters the accelerating gradient further and the electron energy spread increases again. This flattening of the accelerating electric field towards the optimal loading charge could be verified by particle-in-cell simulations [R2] (see Fig. 6.23).

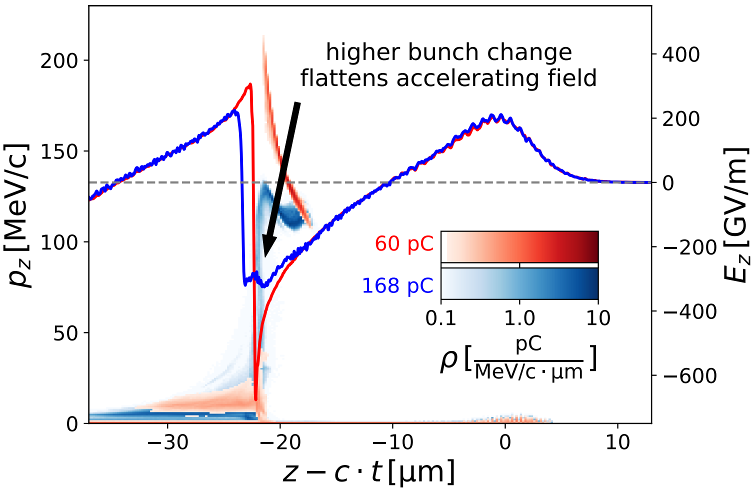

Figure 6.23: **Influence of the bunch charge on the acceleration field and the energy spread:** The solid lines display the acceleration field E_z on the right axis versus the co-moving longitudinal position $z - c \cdot t$. Additionally, the longitudinal phase space distribution is overlaid. The left axis depicted the longitudinal momentum p_z scale, with ρ being the charge density of the distribution. The color red represents a scenario with low dopant concentration and thus lower charge than the blue case with high doping. The bunch with a higher charge flattens the gradient of the acceleration field and thus leads to a lower electron energy spread.

It is important to note that although the experiment could produce thousands of shots per day, a single simulation of such a shot on more than a hundred GPUs took about 5 days. In order not to lose computing time in finding the exact experimental conditions of an optimal shot, an exact determination of the laser and plasma parameters with a shot-by-shot diagnosis would be beneficial. This could reduce the parameter space to be covered by the simulation to the (still large) range of experimental uncertainty. However, the constantly changing conditions and the limited availability and precision of shot-by-shot diagnostics in experiments prevent perfect adaptation of the simulation to the experiment. The simulation result should, therefore,

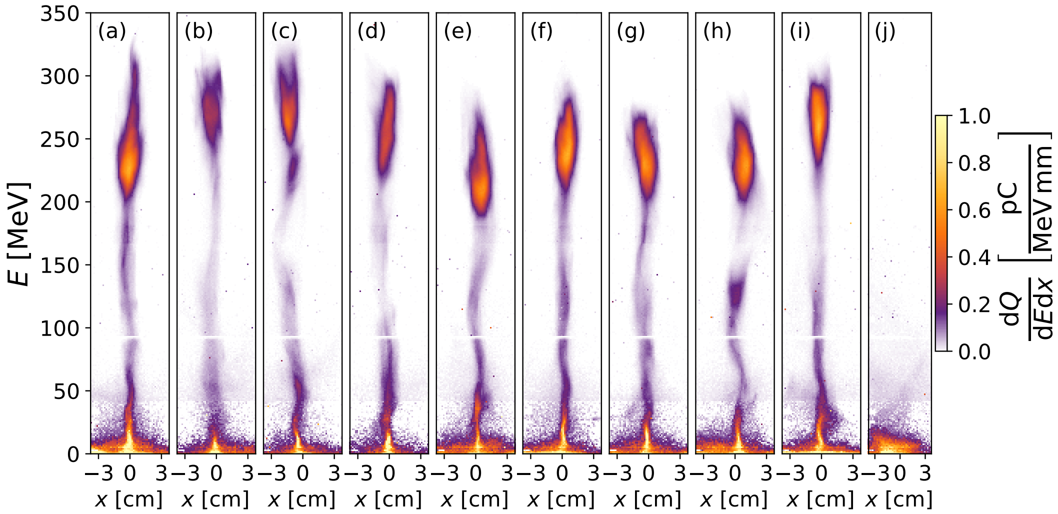

Figure 6.24: **Electron energy distribution in experiment:** The electron distribution as measured in the experiment is plotted for ten consecutive laser shots. The x-axis shows the transversal divergence of the electron beam as measured on a fluorescent LANEX screen. The y-axis represents the electron energy which was resolved using a bending magnet in the experimental setup and thus correlates to the second spatial axis on the screen. In contrast to the results published in [R2], the density is rescaled to show the distribution over the energy and not over the position. The last shot (j) in this sequence was one of the few not successful shots without a quasi-mono-energetic electron bunch produced. The white line and the denser structure around $E = 90\,\text{MeV}$ and $40\,\text{MeV}$ are caused by the LANEX screen setup in the experiment, which consists of several separated screens. More details on the experimental methods to determine the electron energy distribution can be found in [210].

be regarded as a single experimental shot with similar uncertainty as in the experiment.

6.5.2 Simulating the ionization injection

While the experiments performed at HZDR provided a wealth of data to study beam loading effects in laser wakefield acceleration, simulating the setup is essential to validate the assumption and expectations on the inner dynamics of the plasma accelerator. Therefore, an extensive simulation survey was conducted using the particle-in-cell code PIConGPU. During this study, the exact setup was refined repeatedly to better model physical effects, minimize computational time and verify hypotheses on both plasma dynamics and numerical effects. Not all simulation setups are discussed in the following, but only the most important development steps are summarized. Subsequently, the focus is on the description of the observed laser plasma dynamics.

The initial setup assumed a perfectly Gaussian laser envelope. The absence of higher order Laguerre modes allowed a transversally smaller simulation box, set to $704 \times 2352 \times 704$ cells. In order to model the helium gas with the nitrogen doping, both species were added as initially neutral atoms. In a fully ionized region, this would lead to a total of 11 macroparticles per cell. To reduce the memory consumption of this approach, one macroparticle per cell was initialized representing helium. A macroparticle representing nitrogen was only placed with a probability of $1/6$ into a cell. The weightings of both particles were adjusted accordingly to reflect various real doping ratios. This approach allowed reducing the average number of macroparticles per cell to be around 3.8, neglecting the few K-shell electrons from nitrogen. With this optimization, a lower number of graphics processing units were needed to perform the simulation.

In several improvement and optimization steps, Gauss-Laguerre modes were introduced to describe the laser. In order not to cut off these modes at the edges of the simulation box, it was necessary to simulate a larger transversal area. The simulation box was enlarged to $1056 \times 2352 \times 1056$ cells. Since both the K-shell electrons of helium and the L-shell electrons of nitrogen have very low ionization energies (see Tab. 6.1), the laser front already frees these electrons. The laser intensities present during their ionization are non-relativistic $a_0 \ll 1$ and relativistic self-focusing effects do not yet play a role. The gas can be treated as pre-ionized without strongly influencing laser propagation. This model assumption allows combing both the K-shell electrons of the helium and the L-shell electrons of the nitrogen into a single macroparticle. In addition, an N^{5+} ion is initialized in each cell. This only serves as an electron supplier in the simulation. The completely ionized helium ion can be neglected. Its influence on the laser plasma dynamics is marginal due to its high mass, therefore it does not need to be treated by the simulation. The average number of particles per cell becomes, therefore, 2 and even in the full ionization ranges only at 4. On the one hand, this optimization has the advantage that significantly less memory is required and fewer particles have to be treated, which reduces both the number of computers required and the time to solution. On the other hand, the use of nitrogen in each cell increases the sampling of the injected electrons and thus the accuracy of the modeling.

The influence of different ionization models was also tested in the simulation study. Both the classic BSI model and the ADK model [157, 158], based on quantum tunneling, showed very similar results. The total charge and the maximum energy of the accelerated electrons were approximately the same. Only the energy distribution curve was smoother with the ADK model, as it avoids hard ionization thresholds. The Keldysh model, which was also tested, did not yield any reasonable results and was therefore rejected. Since the BSI model was significantly better performing, it was used either alone or in combination with the ADK model. The combination of both models takes into account quantum mechanical tunneling ionization but immediately ionizes when the classical ionization threshold is exceeded. It is, therefore, the physically most reasonable model.

The experiment and therefore the simulation were performed at various densities as well as with different doping concentrations. The density curve used in the simulation was modeled according to experimental measurements (see Fig. 6.25). This representation is normalized to the plateau density. The profile's form has been kept the same for all simulations since the experimental measurements showed that it does not change significantly in the covered density range.

As the figure 6.25 already indicates, the simulations examined two focus positions. While the vacuum focus position of the laser was determined in the experiments to be $z_{\text{focus}} \approx 1\,\text{mm}$ behind the end of the gas down-ramp by measuring the transversal profile in $\Delta z = 300\,\mu\text{m}$ steps, simulations yielded no high energetic electrons when using this focus position at low densities. Therefore, the focus was moved towards the end of the gas density profile in simulations. The energy distribution obtained at this focus position resembles more accurately the energy distribution observed in the experiment. Up until recently the discrepancy between simulations and experiments remained a mystery. However, recent experiments showed that a filter used to reduce the laser intensity before measuring the laser profile showed defocusing effects and moved the measured focus position further out. Since the filter was removed in the actual LWFA experiment, but the focus position was stated with regard to the filter applied, a discrepancy of up to $3\,\text{mm}$ to the assumed focus position is possible. Thus, assuming a focus position inside the gas jet instead of behind the jet as already suggested by simulations seems to be correct. However, the initial mystery on the actual focus position lead to the development of focus position diagnostics that is theoretically introduced in 6.3.3 and demonstrated on the example of this experiment in 6.4.4.

In the following, only selected parameter sets will be discussed. More than 60 full-scale

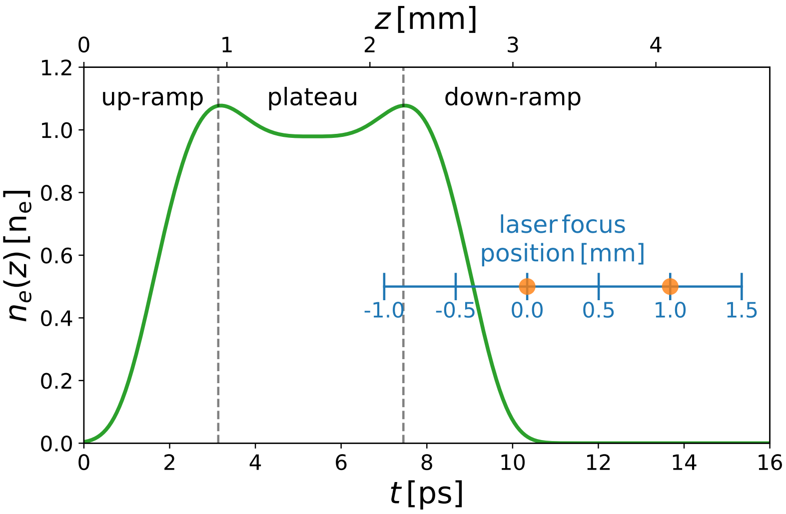

Figure 6.25: **Modeled plasma density profile:** The plot depicts the normalized density profile n_e used in simulations versus the laser propagation direction z or equivalently the propagation time $t = z/c$. It was modeled according to the experimental measurements. These also suggest that the profile is not significantly altered when operated at densities $3 \cdot 10^{18}\,\mathrm{cm}^{-3} \leq n_e \leq 5 \cdot 10^{18}\,\mathrm{cm}^{-3}$. The x-axis shows both the simulation time when the density is reached by the laser as well as the actual position in the laboratory frame. The inline axis is a reference to the focus position, with $0.0\,\mathrm{mm}$ marking the end of the gas down-ramp. Both orange dots mark focus positions used in simulations.

simulations were performed over the course of 1.5 years to explore the parameter range given by the experiment. This includes varying the doping, operating at various densities, and adjusting laser parameters as duration, spot size or focus position. However, no perfect match could be found in this initial parameter survey since the experimentally determined focus position was off by several millimeters.

Nevertheless, various aspects of the laser wakefield acceleration process relevant for this setup could be reproduced. This section concentrates on the laser plasma dynamics of only 3 distinct setups in detail.

The first setup discussed operates at a density of $n_e = 2.6 \cdot 10^{18}\,\mathrm{cm}^{-3}$. This is slightly below the lowest density used in the experiment. The reason for this slight difference comes from the definition of peak density. While in experiments, the plateau density is also called peak density, in simulations the high-density peaks at the beginning and the end of the plasma profile were defined as peak densities. This difference was quickly determined, but the initial simulations at these low densities already paved the way towards a better understanding of the fundamental laser plasma dynamics.

With a purely Gaussian laser profile and with a focus position as in the experiment at $1\,\mathrm{mm}$ behind the end of the gas jet, no electron injection and acceleration could be observed in simulations. This aroused first doubts about the late laser focusing position. However, since the laser focus position was determined to an accuracy of up to $300\,\mu\mathrm{m}$ in the experiment, the focus was moved forward by only $1\,\mathrm{mm}$ for the following test simulation. The laser evolution for this simulation is depicted in Fig. 6.26.

For the Gaussian laser profile (opaque colors), relativistic self-focusing is observable (marked in blue). The laser focuses at $z \approx 2.3\,\mathrm{mm}$ and reaches a peak electric field strength of $a_0 \approx 5.5$, much higher than the laser peak field strength in a vacuum (depicted in dashed lines). The late focus position thus leads to a regime that is governed by the non-linear self-focusing effects of a relativistic laser pulse in the underdense plasma.

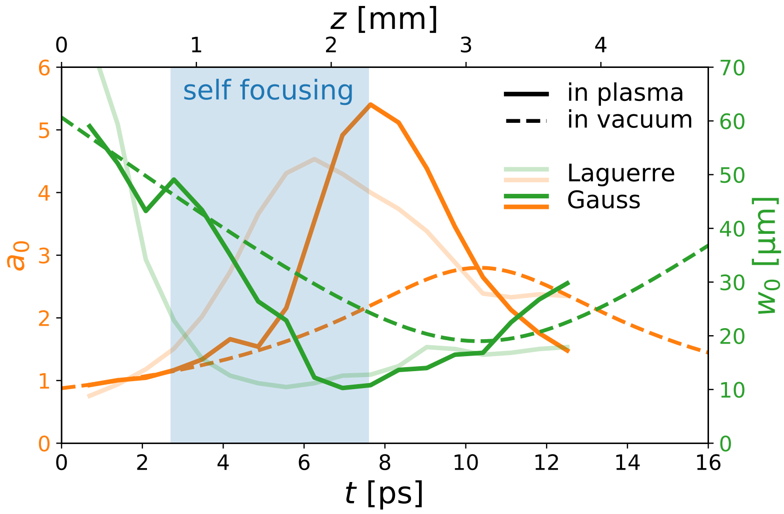

Figure 6.26: **Laser evolution for early focus and low density:** The laser evolution is depicted versus propagation time and distance. The characteristic parameters, normalized field intensity a_0 (orange) and spot size w_0 (green), are plotted as solid lines. The opaque solid lines represent a purely Gaussian laser pulse profile, while the pale solid lines represent the evolution of a laser pulse with Gauss-Laguerre modes as determined in the experiment. The dashed line represents the theoretical evolution of a Gaussian beam in vacuum. The laser vacuum focus is 0.0 mm behind the end of the density profile. The plasma density is $n_e = 2.6 \cdot 10^{18}\,\mathrm{cm}^{-3}$.

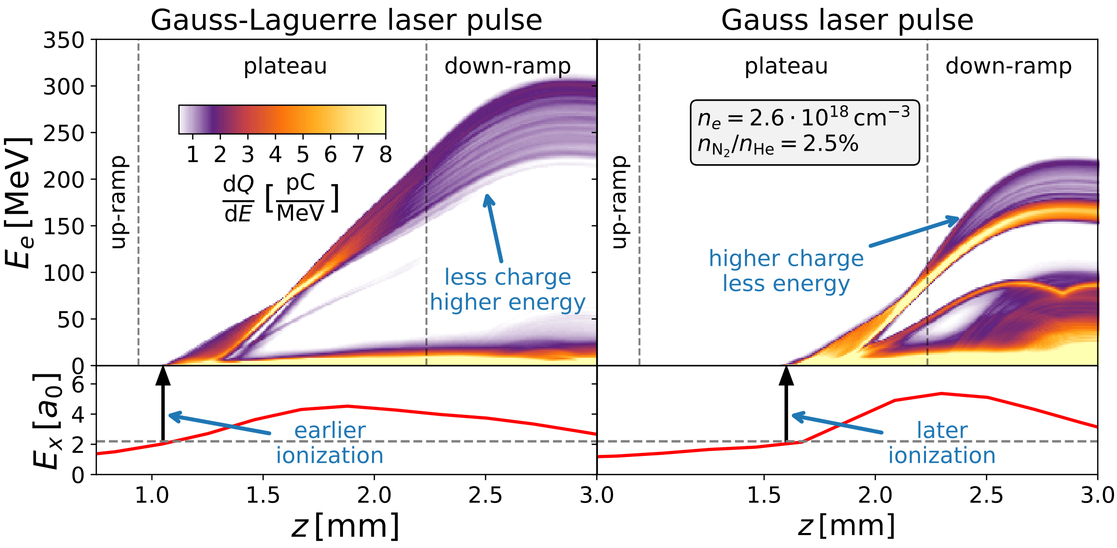

Figure 6.27: **The electron energy evolution for a Gauss-Laguerre and a Gauss-only laser profile for a low plasma density and an early focus:** The upper plots depict the electron energy E_e evolution, with the horizontal axis being the simulation time and/or position along the laser propagation direction z for both the Gauss-Laguerre (left) and Gauss-only (right) laser pulse shape. The lower plots illustrate the evolution of the peak laser field strength E_x. The threshold of the first nitrogen K-shell ionization level ($N^{5+} \rightarrow N^{6+}$) is depicted as a gray dashed line. An arrow marks the first passage of the ionization threshold. This coincides with the time of injection.

As already mentioned in the section on the experiment, the laser characterization revealed higher-order modes in the laser profile. These were modeled by the PIC code by adding Gauss-

Laguerre modes to the laser implementation. This new code was intensely tested and then used in the first production simulations for reproducing the experiments. Adding higher modes completely changes the laser-plasma dynamics as depicted in Fig. 6.26 (pale colors). With the higher modes, the laser pulse focuses much faster and its spot size becomes already smaller than that of the Gauss profile in the up-ramp of the density profile. Equivalently, this leads to a faster rising peak field strength. Even though the latter reaches only $a_0 \approx 4.5 - 5.0$, the initial threshold for ionization is reached much earlier. This allows for an earlier ionization injection and thus a much higher electron bunch energy. This difference in electron acceleration can be recognized clearly in Fig. 6.27.

Exceeding the ionization level earlier when considering the Gauss-Laguerre modes leads to an earlier injection of electrons at $z \approx 1.0\,\mathrm{mm}$. With a Gauss-only profile, the threshold is exceeded at $z \approx 1.6\,\mathrm{mm}$. Since the accelerating gradient is similar, the earlier injection leads to a higher cut-off energy. However, the Gauss-Laguerre laser pulse seems to capture fewer electrons. The total accelerated charge is much lower than with a Gauss-only profile. Even with a higher doping than used in the experiment ($p = 2.5\%$ partial pressure), charges as in the experiment could not be reached.

Therefore, the further investigation focused on the higher density regime by increasing the density to a value of $n_e = 4.4 \cdot 10^{18}\,\mathrm{cm}^{-3}$ at which the experiment observed the best results. Initially, the simulations kept the early focus position at $0.0\,\mathrm{mm}$. The resulting laser evolution is depicted in Fig. 6.28. In contrast to the previous case, the laser does not only focus due to relativistic self-focusing but also keeps its minimal beam waist for more than $1\,\mathrm{mm}$. This is true for both the Gauss-Laguerre and the Gauss-only profile. Again, the Gauss-Laguerre laser pulse shows a faster focusing but reaches a lower peak field strength than the Gauss-only profile. At $z \approx 1.0\,\mathrm{mm}$ the Gauss-Laguerre laser pulse shows a constant beam waist w_0. A bit later, at $z \approx 1.8\,\mathrm{mm}$ the Gauss laser pulse shows an equivalently small and constant beam waist. This marks the regime of self-guiding that is held until the end of the gas density profile.

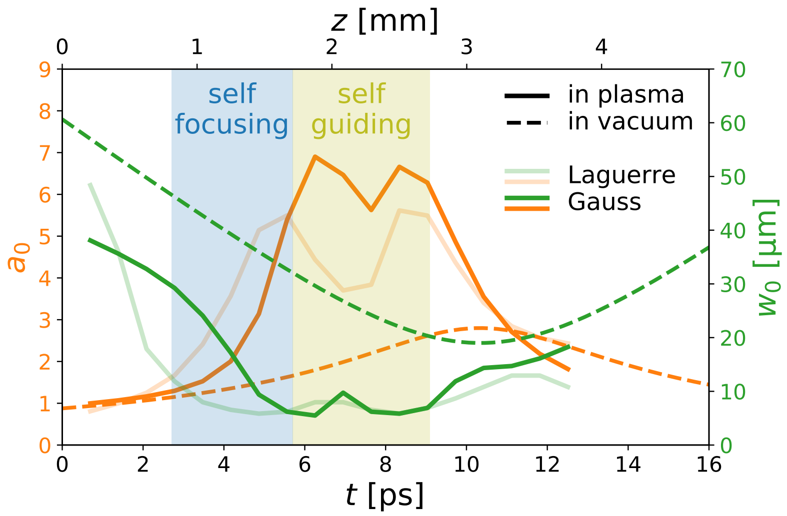

Figure 6.28: **Laser evolution for early focus and higher density:** The laser evolution is depicted versus propagation time and distance and the quantities depicted are analog to figure 6.26. The main difference is the higher plasma density ($n_e = 4.4 \cdot 10^{18}\,\mathrm{cm}^{-3}$) compared to the previous example. With this setup, a self-guiding regime (marked in yellow) is reached.

As in the low-density simulation, the faster focus of the Gauss-Laguerre laser leads to an earlier passage of the ionization threshold and thus to an earlier electron injection and a higher final electron energy (see Fig. 6.29). Due to the self-focusing regime, the excellent accelerating and focusing properties of the bubble regime are exploited in this setup and allow reaching much higher electron energies. The Gauss-Laguerre laser pulse also shows an excellent quasi-monoenergetic energy distribution, but the bunch contains again less charge than with the Gaussian profile. Both laser intensities fluctuate in the self-focusing regime. The Gauss laser, however, fluctuates at higher field strength that causes much stronger alterations in the bubble structure and thus reduces the quasi-monoenergetic properties of the injected bunch. The final energy distribution of the setup with the Gauss-profile, therefore, shows a much broader energy distribution.

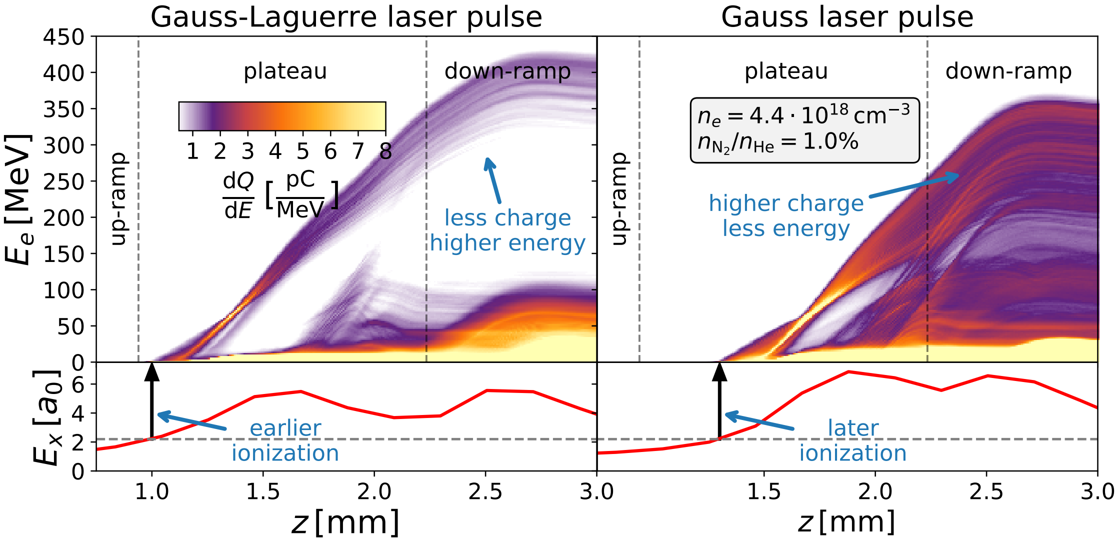

Figure 6.29: **The electron energy evolution for a Gauss-Laguerre and a Gauss-only laser profile for a higher plasma density and an early focus:** This is a plot of the electron energy evolution (upper plots) and laser fields strength (lower plots) for both a Gauss-Laguerre and a Gauss-only laser profile. The depicted quantities are equivalent to Fig. 6.27. Much higher energies are reached with this setup.

While these results looked promising with regard to the cut-off energy, the focus position was too close to the gas nozzle. Therefore, the simulation survey continued to explore the regimes with a later focus position as assumed in the experiment.

In this regime at densities of $n_e = 4.4 \cdot 10^{18}\,\mathrm{cm}^{-3}$ and a laser focus position $1\,\mathrm{mm}$ behind the end of the down-ramp, no self-guiding is reached anymore (see Fig. 6.30). Both the Gauss-Laguerre and the Gauss laser pulse show a very similar self-focusing. In the plasma plateau region, they reach similar spot size and peak field strength values. The self-focusing is cutoff by the end of the plasma. This similar evolution points to a regime of operation which is stable against fluctuations in the higher laser modes.

This is also reflected in electron energy evolution (Fig. 6.31). Due to the late focus position, the ionization threshold is surmounted at $z \approx 1.7 - 1.8\,\mathrm{mm}$ which does not leave much distance until the end of the plasma for acceleration. Surprisingly, the injection happens slightly earlier with the Gauss pulse. However, the lower charge trapped with the Gauss-Laguerre pulse does not reduce the accelerating gradient as strongly due to much smaller Coulomb field of the bunch itself. Therefore, the Gauss-Laguerre setup reaches slightly higher final electron energies.

Even though this regime appears stable against fluctuations in the transversal higher-order modes of the laser pulse, the energies reached are much lower than in experiments. The origin of this discrepancy was not clear up until very recently. Since the discrepancy in maximum

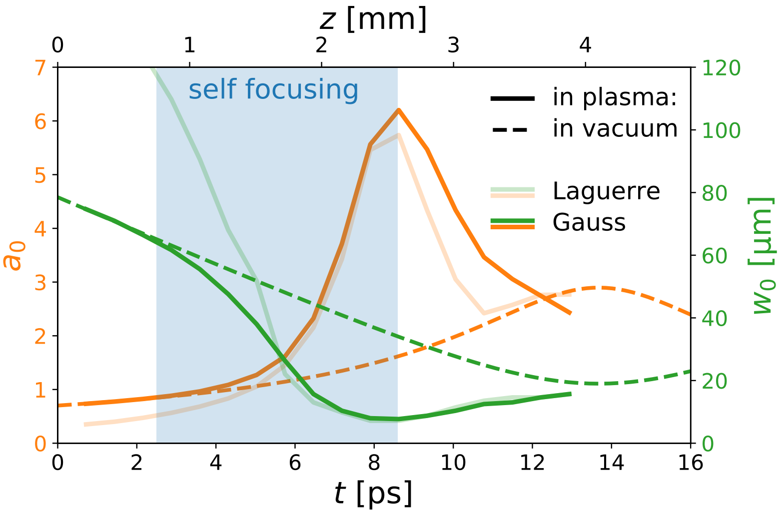

Figure 6.30: **Laser evolution for late focus and higher density:** The laser evolution is depicted versus propagation time and distance and the quantities depicted are analog to figure 6.26. The main difference is that the laser focus position is 1 mm behind the plasma down-ramp. With this setup, both the Gauss-Laguerre and the Gauss-only laser pulse show a very similar evolution.

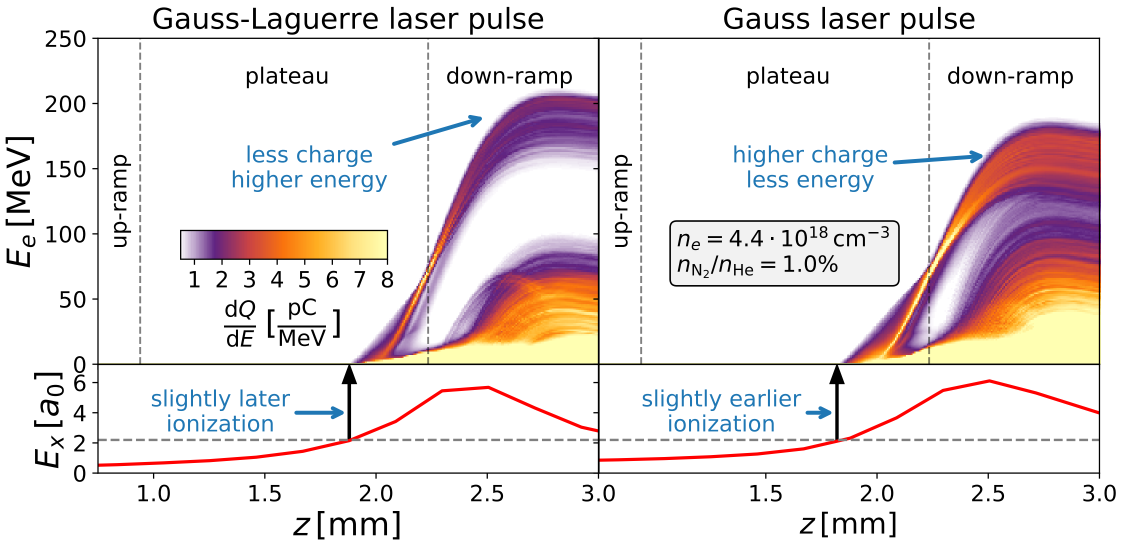

Figure 6.31: **The electron energy evolution for a Gauss-Laguerre and a Gauss-only laser profile for a higher plasma density and a later focus:** This is a plot of the electron energy evolution (upper plots) and laser fields strength (lower plots) for both a Gauss-Laguerre and a Gauss-only laser profile. The depicted quantities are equivalent to Fig. 6.27. Much lower energies are reached with this further-back focus setup but both the Gauss-Laguerre pulse and the Gauss-only pulse show a much more similar electron energy evolution.

electron energy directly relates to the laser focus in the plasma, determining a laser focus in the plasma itself while it undergoes relativistic self-focusing appeared to be the only option for testing the predictions of the PIC simulations since differences in the self-focusing might have pointed to a wrong treatment of this non-linear regime by the simulation software PIConGPU. However, there was no method to determine the focus position of a laser in a plasma for each individual laser shot. In the future, the measurement of the laser focus position in the plasma could be made possible by implementing a detector for the blowout radiation signature (see section 6.4.4).

6.6 Conclusions and Outlook

This chapter provided an introduction to Laser Wakefield acceleration. After briefly covering the sub-relativistic and mildly relativistic regime analytically, the introduction focused on the ideal acceleration and focusing properties reached in the so-called blowout regime at normalized field strength greater than $a_0 > 3$. A brief summary was given of the influence of the laser evolution in the plasma on the acceleration process, with a particular focus on self-focusing in the plasma. Various injection methods were discussed, with an emphasis on both the wave-breaking injection used in the initial simulation and the self-truncated ionization injection (STII) method which was used in experiments and the corresponding simulations.

After this brief review, a scattering theory for laser-electron interaction was derived. It is based on an arbitrary electron distribution which propagates through a laser pulse. An exact analytical description of the scattering signal was derived. However, since no analytical solution is known for the electrons' velocity distribution in the blowout regime, simplified models had to be used. As a first assumption for the electron distribution, the characteristic, off-axis electron stream was incorporated in the simplified model. The semi-analytical model predicts a broad-band, off-axis scattering during the blowout regime.

The reason for the development of this semi-analytical scattering theory was a large-scale 3D LWFA simulation, which for the first time calculated the emitted electromagnetic radiation spectrum of all simulated particles. This simulation made it possible to explore new, previously unknown scatter signals and to quantify these and other known signals against the general radiation background of all electrons in the plasma. After a short discussion of the laser-plasma dynamics based on the simulation data, the off-axis radiation development was discussed. Several known radiation signatures, such as higher harmonics and wave-breaking radiation, have been identified. Furthermore, the blowout regime radiation predicted by the semi-analytical model could also be identified clearly. A temporal asymmetry due to laser focusing and defocusing, which cannot be treated within the model, was found. Due to the delayed reaction of the plasma to the laser development, the blowout signature is only visible during defocusing. However, this allows determining the laser focus position in the plasma, which was not possible before.

A simulation series in the course of an LWFA experiment at the HZDR demonstrated the benefits of such a focus determination with the blowout radiation signature. In the experiment, the vacuum focus position was behind the plasma. Based on this setup, several simulations were performed to model the laser plasma dynamics of the experiment. However, due to a single parameter that was determined incorrectly in the experiment, the simulations could not reproduce the electron beam energies measured in the experiment. They showed that with a late focus of the laser, as in the experiment, relativistic self-focusing effects strongly influenced the laser development by pushing the focus further forward into the plasma as well as increasing the peak intensity significantly in comparison to the vacuum. Nevertheless, the acceleration gradients and lengths predicted by the simulations were not sufficiently large to reproduce the measurement. Even a slightly earlier vacuum focus could not reproduce the results of the experiment. Since the simulations also showed that higher laser modes have a significant influence on the self-focusing behavior, a diagnostic method had to be developed that allows determining the laser focus in the plasma. The previously discovered blowout signature was an ideal candidate for that. A parameter study with 2D PIC simulations showed that the blowout signature could determine the focus position with very high accuracy.

Before this new diagnostic method could be implemented experimentally, a filter was identified as the cause of an incorrect measurement of the vacuum focus in the experiment. At high laser intensities, this filter defocused the laser, apparently shifting the focus further back. Since no filter was used for the experiments, the real laser vacuum focus was probably located in the gas. First experimental estimates suggest a shift of the focus to the center of the density profile. Once the shift is accurately determined, another simulation campaign will model the laser plasma dynamics.

Recent experiments also revealed that fine-tuning the group dispersion delay (GDD) increased the electron beam quality [211]. Similar results were achieved experimentally at HZDR [R12]. However, so far, all measurements altered the GDD for optimizing the electron beam quality. In order to include these spectrally and temporally adjusted laser pulses in particle-in-cell models, a precise measurement of the spectra and temporal shape of the laser pulse is required in experiments. Currently, the DRACO team is setting up a self-referenced spectral interferometer [212–214] that allows characterizing the laser's spectra and temporal structure with an unprecedented resolution and dynamic range for each laser shot automatically. This diagnostic method is called *WizzlerHD* and will provide the parameters to improve modeling the laser pulse in simulations in the future.

The question remains whether the currently only theoretically modeled radiation diagnostics method for the determination of the focus and the blowout regime can also be implemented experimentally in the near future. An error in laser focus position measurements could thus be identified much faster. The experimental implementation of the developed method is not only useful for finding such errors, but it could also confirm, through a new and independent measurement method, that the predictions of the PIC simulations are correct.

7 Radiation signature of the Kelvin-Helmholtz instability

7.1 Determination of plasma dynamics in astronomical objects through radiation

Interstellar and intergalactic jets are of interest since they are suspected to be the origin of yet unexplained extremely high energetic particles [42–44, 215–219], but also as they provide a wealth of relativistic astro- and plasma physics [46]. The sources of these jets range from young stellar objects to massive objects like black holes or neutron stars (pulsars) associated with supernova remnants and active galactic nuclei [220] and are essential in understanding our universe. These jets are associated with strong magnetic fields [47–49, 221] and non-thermal radiation [29, 222, 223]. Since the plasma stream of the jet will shear on the surrounding plasma, the Kelvin-Helmholtz instability (KHI) is expected to occur in these astrophysical jets [29, 224]. While it can not explain the extreme particle acceleration, this plasma instability converts the kinetic energy of the jet electrons into magnetic energy and provides a mechanism behind the strong magnetic fields observed in astronomical jets. Recent theoretical studies have shown that the growth rate of the Kelvin-Helmholtz instability at density contrasts as expected in these jets will be larger than any other competing plasma instability [55], thus the KHI is very likely to occur.

While there is a comprehensive theoretical study on the plasma and particle dynamics occurring during the Kelvin-Helmholtz instability including relativistic shearing velocities and kinetic effects [53, 55, 70, 81, 225–228], these studies focus on the microscopic plasma dynamics and provide no observables for identifying and quantifying the Kelvin-Helmholtz instability in jets light years away.

There are also recent laboratory experiments that model plasma jets to improve our understanding of astrophysical jets [220] since even large-scale jet dynamics are hard to uncover in astronomical observations, with a few exceptions like the Crab nebular [36, 229]. Recently, the Kelvin-Helmholtz instability was identified by shadowgraph and schlieren methods in such laboratory experiments [230, 231]. However, these experiments only provided a snapshot of the dynamics.

As part of this thesis, a large-scale particle-in-cell simulation was performed simulating the relativistic KHI and computing the emitted radiation [R1]. The data provided by this simulation allowed developing an analytical model of the electron dynamics responsible for the primary radiation, and identifying a characteristic polarization signature that enables determining the onset and end of the linear phase of the KHI [R4]. Additionally, a correlation between the emitted power and the growth of the instability was identified that allows quantitatively studying the dynamics of the instability via radiation.

The fundamental processes driving the Kelvin-Helmholtz instability are briefly explained in section 7.2. The analytical model is discussed in section 7.3 and the large-scale simulation is presented in section 7.4. The changes that need to be considered by an observer on Earth due to Lorentz transformation are addressed in section 7.5. Possible observation scenarios and the influence of less ideal jet geometries are covered in section 7.6.

7.2 An Introduction the the Kelvin-Helmholtz instability

The Kelvin-Helmholtz instability is a shear-flow instability that was first discovered for fluids and gases where pressure fluctuations lead to turbulent mixing of the two liquids/gases along the shear surface [232]. A very similar phenomenon occurs in shearing plasma streams and was dubbed the magnetohydrodynamic Kelvin-Helmholtz instability. In plasmas, however, the interaction between the two streams arises contact-less via magnetic fields generated by current fluctuations. This plasma instability was studied using magnetohydrodynamic plasma theory and simulation codes [233]. In recent years, computers became powerful enough to study the sharing of two plasma streams with particle-in-cell codes [53]. The kinetic treatment of this shear instability revealed the existence of DC-magnetic fields on the shear surface at relativistic plasma velocities [54].

In the following section, the fundamental process driving the relativistic plasma Kelvin-Helmholtz instability will be described and a quantitative description of the plasma dynamics will be derived. Wherever possible, we will refer to the literature if derivations do not contribute essentially to the understanding of the radiation of the Kelvin-Helmholtz instability, discussed in the in proceeding section.

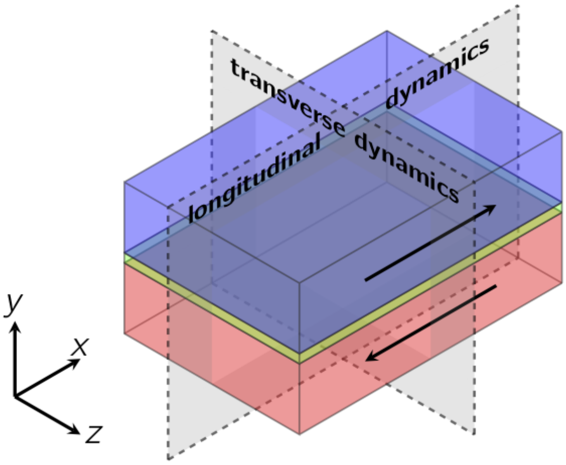

Figure 7.1: **Illustration of two shearing plasma streams in the relative velocity frame:** The two counter-propagating streams are depicted in red and blue. The shear surface is drawn in green. The planes of longitudinal (ESKHI) and transversal (MI) dynamics are depicted by gray planes.

A plasma stream shearing on another plasma stream is best described in the so-called relative velocity frame, where the mean speeds of both streams are equal and the two streams counter-propagate (see Fig. 7.1). Initially, the streams can be assumed to be charge neutral.

In the following, we will discuss instabilities which are seeded by either small fluctuations of the magnetic field or electric current on the shear surface. Due to a feedback mechanism, the current fluctuation causes a change in the magnetic field which again increases the initial current fluctuation and vice versa. This feedback between current and magnetic field leads to an exponentially growing magnetic field and to a turbulent electron motion on the shear surface.

7.2.1 The electron-scale Kelvin-Helmholtz instability (ESKHI)

First of all, let us consider the longitudinal dynamics of two relativistically shearing plasma streams. This is the so-called electron-scale Kelvin-Helmholtz instability (ESKHI) [55, 57]. In early publications, this was also referenced as just the relativistic Kelvin-Helmholtz instability [53, 225, 234]. In the two-dimensional plane of longitudinal dynamics (depicted in Fig. 7.1), we assume the density $n = n(y)$ and the velocity $\vec{v} = (v_0(y), 0, 0)$ only to vary in normal direction y, with the Cartesian coordinates being (x, y, z). Due to the two-dimensional simplification assumed, the electric field has only components in the longitudinal plane $\vec{E} = (E_x, E_y, 0)$, and the magnetic field has only a perpendicular component $\vec{B} = (0, 0, B_z)$. The plasma dynamics is governed by the continuity and conservation of momentum equations [3, 57]

$$\begin{aligned} \frac{\partial \rho}{\partial t} + \vec{\nabla} \cdot \vec{J} &= 0 & (7.1) \\ \frac{\partial \vec{p}}{\partial t} + \left(\vec{v} \cdot \vec{\nabla}\right) \vec{p} &= \vec{F} = q_e \left(\vec{E} + \vec{v} \times \vec{B}\right) & (7.2) \end{aligned}$$

with $\vec{p} = \gamma m_e \vec{v}$ being the momentum field, $\vec{v}$ being the velocity field, $\rho = q_e \cdot n$ being the charge density, q_e being the charge of an electron and $\vec{J} = \vec{v} \cdot \rho$ being the current density. The dynamics of the electric and magnetic field is described by Faraday's and Ampère's law [57, 59]

$$\begin{aligned} \vec{\nabla} \times \vec{E} &= -\frac{\partial \vec{B}}{\partial t} & (7.3) \\ c^2 \cdot \vec{\nabla} \times \vec{B} &= \frac{\partial \vec{E}}{\partial t} - \frac{1}{\varepsilon_0} \vec{J} \quad . & (7.4) \end{aligned}$$

Linearizing the field quantities Q in a constant Q_0 and fluctuation term Q_1 as

$$\begin{aligned} Q(x, y, t) &= Q_0 + Q_1(x, y, t) & (7.5) \\ Q_1(x, y, t) &= Q_1(y) \cdot \mathrm{e}^{\mathrm{i}(kx - \omega t)} & (7.6) \end{aligned}$$

allows studying the dynamics of initially small fluctuations Q_1 [55, 57, 225]. By linearizing the particle density n in the continuity equation (Eq. 7.1, as part of ρ and $\vec{J}$), the density perturbation n_1 can be solved. Similarly, by linearizing the momentum and velocity field in the conservation of momentum equation (Eq. 7.2), the perturbation of the velocity field v_{x1} and v_{y1} can be determined.

By combining these linearized equations, one obtains the linearized current density which can again be used in the linearized Maxwell's equation (Eq. 7.3 and Eq. 7.4) to derive an electromagnetic eigenmode equation of the plasma shear under small perturbations [57, 225].

$$\frac{\partial}{\partial y} \left(\chi_1 \cdot \chi_2 \cdot \frac{\partial E_{x1}}{\partial y} \right) + 2 \cdot \chi_1 \cdot \left(\frac{\partial}{\partial y} \frac{\omega_{p+}^2}{c^2} \right) \cdot \frac{\partial E_{x1}}{\partial y} + \chi_1 \cdot \chi_2^2 \cdot E_{x1} = 0 \qquad (7.7)$$

with the two parameters

$$\begin{aligned} \chi_1 &= \frac{1}{\gamma^2} \frac{\omega_{pe}^2}{(\omega - k \cdot v_0)^2} - 1 & (7.8) \\ \chi_2 &= \frac{\omega^2}{c^2} - \frac{\omega_{pe}^2}{c^2} - k^2 & (7.9) \end{aligned}$$

depending on the velocity and density field. The quantity $\omega_{p+} = \sqrt{\frac{q_e^2 n_+}{\epsilon_0 \gamma m_e}}$ is the plasma density of the upper stream and takes into account the relativistically increased mass of the electron. A detailed step-by-step derivation of the above equation can be found in P Alves et al. [55, 57].

Assuming a density jump and a sharp velocity jump at the shear surface

$$n = \begin{cases} n_+ & y > 0 \\ n_- & y < 0 \end{cases} \tag{7.10}$$

$$\vec{v} = \begin{cases} +v_0 \cdot \vec{e}_x & y > 0 \\ -v_0 \cdot \vec{e}_x & y < 0 \end{cases} \tag{7.11}$$

allows deriving a dispersion relation for the instability [53]. For equal densities $n_+ = n_- = n$, an analytical solution exists [225].

$$\Gamma = \mathrm{Im}(\omega) = \frac{\omega_{p+}}{\gamma} \sqrt{\frac{1}{2}\left(\sqrt{1 + 8 \cdot \left(\frac{\gamma k v_0}{\omega_{p+}}\right)^2} - 1 - 2\left(\frac{\gamma k v_0}{\omega_{p+}}\right)^2\right)} \tag{7.12}$$

For non-equal densities $n_+ > n_-$, the dispersion relation can only be solved numerically [57]. The dispersion relation yields an imaginary solution for ω that is zero for $k = 0$, increases towards higher k values and decreases again after

$$k_{\max} = \sqrt{\frac{3}{8}} \frac{\omega_{p+}}{\gamma \cdot v_0} \tag{7.13}$$

till $k_{\text{cut-off}} = \frac{\omega_{p+}}{\gamma \cdot v_0}$, where $\omega = 0$ again. Following the initial definition of our perturbation (Eq. 7.6), an imaginary frequency ω leads to an exponential growth. After a couple of folding times, only the fastest growing mode at $k_{\max}$ will drive the instability. Thus, the characteristic growth rate of the electron-scale Kelvin-Helmholtz instability is:

$$\Gamma = \mathrm{Im}(\omega_{\max}) = \frac{1}{\sqrt{8}} \frac{\omega_{p+}}{\gamma} \quad . \tag{7.14}$$

In a simplified picture, this means that in initial perturbation the magnetic field B_z leads to an exponential growth in time

$$B_z(t) \sim \mathrm{e}^{\Gamma \cdot t} \quad . \tag{7.15}$$

Of course, this linearized theory has its limitations and this growth will stop in the so-called saturation phase when the dynamics becomes nonlinear and the growth reduces.

7.2.2 More relativistic streams - the mushroom instability (MI)

The so-called mushroom instability (MI) occurs between two shearing plasma streams as well. As the ESKHI, it leads to an exponentially growing magnetic field on the shear surface and finally to a turbulent plasma dynamics across the shear surface. Initially, the mushroom instability was just considered the transversal part of the known Kelvin-Helmholtz instability observed in particle-in-cell simulations [53, 81, 235, 236], but with the work of Alves et al. [228], it was identified as an independent plasma instability that dominates the dynamics at high Lorentz factors of the plasma streams.

Analogous to the ESKHI, the dynamics of the mushroom instability can be studied using a linearized theory. Starting with the same set of equation (Eq. 7.1 to Eq. 7.4), we linearize the charge density, momentum, and electromagnetic fields as

$$Q(y,z,t) = Q_0 + Q_1(y,z,t) \tag{7.16}$$

$$Q_1(y,z,t) = Q_1(y) \cdot \mathrm{e}^{\mathrm{i}(kz - \omega t)} \quad . \tag{7.17}$$

Similar to the previous derivation, the dispersion relation for the mushroom instability can be derived for step-like plasma streams (Eq. 7.10 and Eq. 7.11). A detailed derivation can be found in Alves et al. [57, 228].

The resulting dispersion relation for equal densities $n_+ = n_- = n$ leads to the following exponential growth rate $\Gamma = \mathrm{Im}(\omega)$:

$$\Gamma = \frac{\omega_{pe}}{\sqrt{2}} \left(\sqrt{\frac{4k^2 v_0^2}{\gamma \omega_{pe}^2} + \chi_3^2} - \chi_3 \right)^{-1/2} \tag{7.18}$$

$$\chi_3 = \frac{1}{\gamma^3} + \frac{k^2 \cdot c^2}{\omega_{pe}^2} \tag{7.19}$$

$$\omega_{pe} = \sqrt{\frac{q_e^2 n}{\epsilon_0 m_e}} \quad . \tag{7.20}$$

Please note that the plasma frequency ω_{pe} used here is not relativistically corrected as before $\omega_{p+} = \omega_{pe} \cdot \gamma^{-1/2}$. The growth rate $\Gamma(k)$ is zero at $k = 0$ and increases monotonically. The fastest growing mode is found at $k \to \infty$ with

$$\Gamma_{\mathrm{max}} = \omega_{pe} \frac{v_0}{c\sqrt{\gamma}} \quad . \tag{7.21}$$

Comparing the growth rates of the electron-scale Kelvin-Helmholtz instability (ESKHI) and the mushroom instability (MI) for various Lorentz factors of the streams (Fig. 7.2) reveals that for non-relativistic γ the growth rate of the ESKHI is larger. However, the growth rate of the ESKHI reduces with $\gamma^{-3/2}$ and thus more rapidly than compared to the MI, which decreases with $\gamma^{-1/2}$. This causes the growth rate of the ESKHI falling below that of the MI. The MI is thus the dominant instability in the relativistic regime.

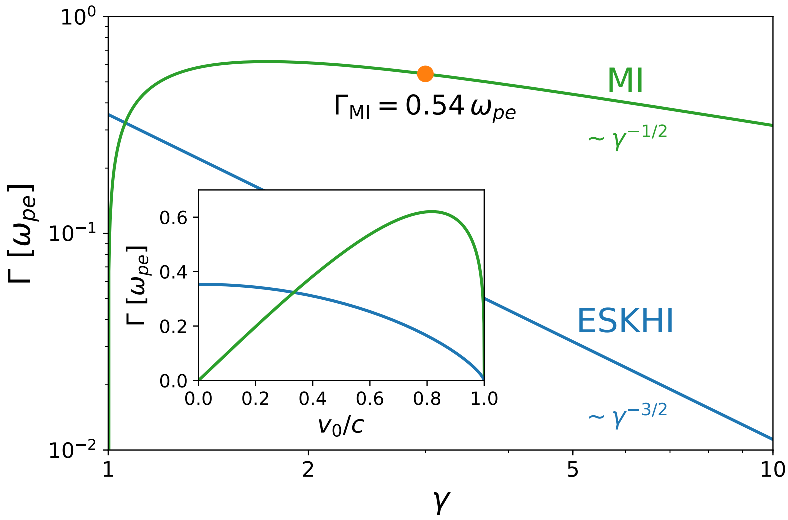

Figure 7.2: **Comparison between the maximum growth rates of the ESKHI and MI:** The maximum growth rates Γ in units of the plasma frequency ω_{pe} are plotted for both the electron-scale Kelvin-Helmholtz instability (ESKHI) and the mushroom instability (MI) as a function of the Lorentz factor γ. The inset illustrates the growth rates over normalized shear velocities $v_0/c = \beta_0$ using a linear Γ scaling. The orange dot marks the growth rate of the MI at $\gamma = 3$ as used in the simulation discussed in section 7.4.

In a three-dimensional scenario, both instabilities will mix and the fastest growing mode will dominate the dynamics. For the simulations presented in section 7.4, the Lorentz factor is

$\gamma = 3$ and the expected dynamics is mainly governed by the MI. The predicted growth rate is $\Gamma_{\text{MI}} = 0.54\,\omega_{pe}$ as marked by an orange dot in Fig. 7.2.

7.2.3 DC magnetic fields on the shear surface

When investigating the dispersion relations for both the electron-scale Kelvin-Helmholtz instability (ESKHI) (Eq. 7.12) and the mushroom instability (MI) (Eq. 7.18), the growth rate Γ for a spatially constant (DC) mode at $k = 0$ is zero. Since only modes with spatial modulation $k > 0$ grow, there should be no DC magnetic field. However, recent particle-in-cell simulations revealed a growing DC magnetic field on the shear surface [53, 54, 81, 228, 235, 237] that was demonstrated with our simulation [R1, R3] as well. The existence of these DC magnetic fields cannot be described by magneto-hydrodynamic theory and is an intrinsic kinetic effect [226].

The origin of this magnetic field is the thermal fluctuation of the electrons near the shear surface. Assuming the two streams flow with $v_x \approx \pm v_0$ in $\pm\vec{e}_x$ direction (see Fig. 7.1), the electrons and protons follow additionally to the stream velocity a Maxwellian velocity distribution since the plasma streams have a non-zero temperature $T > 0$. Due to this temperature, the particles will diffuse across the shear surface. In thermal equilibrium, the electrons will drift across the shear before the protons due to their lower mass $m_e \ll m_p$. This leads to a charge separation and to a current, which generates a magnetic field B_z. According to the Lorentz force, this magnetic field pushes more electrons across the shear surface, thus increasing the current and the magnetic field B_z. This feedback mechanism leads to an exponentially growing DC magnetic field on the shear surface.

In order to quantitatively model this kinetic effect, the Vlasov equation (Eq. 3.1) needs to be used. Since we are only interested in the particles crossing the shear, we can reduce the shear surface geometry to a one-dimensional problem, allowing particles to propagate only along y, while still allowing for three-dimensional velocities (usually abbreviated as 1D3V) [55, 226]. Initially, one can assume the shear surface region to be field free. This simplifies the equation of motion to a free streaming approximation where $y(t) = y_0 + v_{y0} \cdot t$ and $\vec{v}(t) = \vec{v}_0$. Since the entire dynamics is independent of v_z, we will neglect this velocity component, reducing the distribution function to $F(y, v_y, v_x, t) = \int_{-\infty}^{+\infty} \mathrm{d}v_z f(y, \vec{v}, t)$. A formal solution to the Vlasov equation is the initial distribution function $F(y, v_y, v_x, t) = F_0(y_0, v_{y0}, v_{x0})$, which we separate in two components, one for each stream $F_0(y) = F_0^+(y > 0) + F_0^-(y < 0)$. The current density of the electrons in the x-direction is thus:

$$J_x^{e\pm} = q_e \int\limits_{-\infty}^{+\infty} \mathrm{dv_x}\; v_x \int\limits_{-\infty}^{+\infty} \mathrm{dv_y}\; F_0(y - v_{y0} \cdot t, v_{y0}, v_{x0}) \tag{7.22}$$

where we used the free-streaming equation of motion $y_0 = y - v_{y0} \cdot t$, v_{y0} to return to the initial distribution function F_0. This initial distribution function can be described by:

$$F_0^{\pm}(y_0, v_{y0}, v_{x0}) \;=\; n_0 \cdot f_{\text{MB}}(v_{n0}) \cdot f_{MB}(v_{x0} \mp v_0) \tag{7.23}$$

$$f_{\text{MB}}(v) \;=\; \frac{1}{\sqrt{2\pi} v_{\text{T}}} \mathrm{e}^{-\frac{1}{2}\frac{v^2}{v_T^2}} \quad , \tag{7.24}$$

with f_{MB} being the Maxwell-Boltzmann distribution (for each dimension) for a thermal velocity of $v_T = \sqrt{\mathrm{k_B} T / m_e}$.

Thus, according to Eq. 7.22, the current densities are:

$$J_x^{e\pm} = \pm q_e v_0 n_0 \int\limits_{\mp y/t}^{+\infty} f_{\mathrm{MB}}(v_{y0})\, \mathrm{d}v_{y0} \tag{7.25}$$

$$= \mp \frac{e v_0 n_0}{2} \operatorname{erfc}\left(\frac{\mp y}{\sqrt{2} v_T t}\right) \quad , \tag{7.26}$$

with $e = |q_e|$ being the elementary charge and $\operatorname{erfc}(x) = 1 - \operatorname{erf}(x)$ being the complementary error function. The lower limits of the integral in Eq. 7.25 ensures that only particles from the specific stream are considered. Assuming the proton stream to be unperturbed at these time scales, the total current density is

$$J_x(y) = e v_0 n_0 \cdot \begin{cases} \operatorname{erfc}\left(\frac{y}{\sqrt{2} v_T t}\right) & y > 0 \\ \operatorname{erfc}\left(\frac{y}{\sqrt{2} v_T t}\right) - 2 & y < 0 \end{cases} \quad . \tag{7.27}$$

By integrating Ampère's equation (Eq. 7.4), the magnetic field generated by this current can be determined:

$$B_z = -\mu_0 \int \mathrm{dy}\, J_x \tag{7.28}$$

$$= -e\mu_0 v_0 n_0 \left[|y| \cdot \operatorname{erfc}\left(\frac{|y|}{\sqrt{2} v_T t}\right) - \sqrt{\frac{2}{\pi}} v_T \cdot t \cdot \mathrm{e}^{-\frac{1}{2}\left(\frac{y}{v_T t}\right)^2} \right] \quad . \tag{7.29}$$

The evolution of the current density J_x and the magnetic field B_z over time and along the shear interface is depicted in Fig. 7.3. Comparing this to the magnetic field strength in particle-in-cell simulation reveals that this theory underestimates the growth of the magnetic field strength. This is due to the free-streaming approach which fails as soon as the feedback of the generated magnetic field starts to change the electron dynamics. As mentioned before, the magnetic field starts pushing more electrons across the shear surface and increases the current and the magnetic field amplitude further.

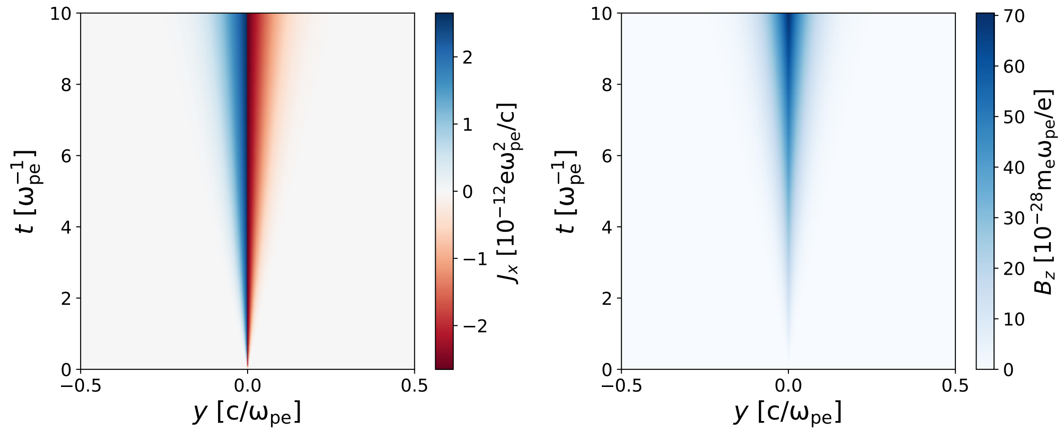

Figure 7.3: **Slices through the simulation:** Illustration of the current density $J_x(y, t)$ and magnetic field $B_z(y, t)$ evolution using exemplary parameters $\gamma = 3$ and $v_T = 0.01 v_0$ analog to the simulation performed in section 7.4. Over time the DC field becomes stronger and propagates across the shear interface. The model depicted is only valid in the initial phase where the feedback of the magnetic field onto the electrons can be neglected.

However, in case of cold plasma streams $v_T \ll v_0$, the magnetic field grows not as fast as observed in simulation, even when taking into account the feedback mechanism. The reason for this is that in the cold plasma case, a different mechanism is driving the electrons across the shear initially: the Lorentz force caused by the growing magnetic field on the shear surface due to either the ESKHI or the mushroom instability $\dot{v}_y \sim \vec{v_0} \times \vec{B} = v_0 \times B_z$. In a similar manner to the warm plasma case discussed above, the current density and magnetic field can be computed [226]. Assuming an exponentially increasing velocity $v_y \sim \mathrm{e}^{\Gamma t}$ it can be shown that the DC magnetic field at the shear interface grows equivalently to the highest mode of the ESKHI (or MI) [226], derived by magneto-hydrodynamic theory.

The maximum field strength reached by the DC magnetic field can be estimated by allowing Eq. 7.29 to reach arbitrary amplitudes. The characteristic width of the DC field is $L_{\mathrm{DC}} = \sqrt{2} t v_T \approx c\sqrt{\gamma}/\omega_{pe}$ [54]. If the magnetic field is strong enough, the Larmor radius of the electrons $r_{\mathrm{L}} = \frac{\gamma m v}{eB}$ becomes smaller than the characteristic width of the DC field. At these magnetic field amplitudes, the electrons will no longer be able to cross the shear surface and will thus not contribute to a further increase in current density. At $L_{\mathrm{DC}} \approx r_{\mathrm{L}}$ the magnetic fields stops growing. The amplitude that is reached up to saturation is:

$$\frac{eB_z^{\mathrm{sat}}}{m_e \omega_{pe}} \approx \sqrt{\gamma_0}\beta_0 \approx 1.4\sqrt{\gamma_0}\beta_0 \tag{7.30}$$

with the factor 1.4 being a result of 3D particle-in-cell simulations performed by Grismayer et al. [54] with the OSIRIS code [76, 238]

These growing DC magnetic fields are the origin of the characteristic radiation signature of the Kelvin-Helmholtz instability [R4] as we will discuss in the rest of this chapter in detail.

7.3 A microscopic model of the shear surface electron dynamics

In the linear regime, the Kelvin-Helmholtz instability is driven by the exponentially growing magnetic field on the shear surface. While the microscopic dynamics of both the electrons and the electromagnetic fields are quite complex, the mean magnetic field grows exponentially with a relatively constant growth rate since the details of the electron and field interplay average out on the scale of the shear surface (see section 7.2). Since the observable radiation is a sum of the radiation of all electrons (Eq. 4.1), the emitted radiation can be approximated by the mean motion of an electron in this exponentially growing magnetic field. By neglecting the complex interplay between plasma dynamics and electromagnetic fields and just using the global magnetic field evolution (Eq. 7.15) it becomes possible to derive a simple kinetic model that describes the mean electron dynamics and the emitted radiation. The details of this kinetic model and the resulting characteristic radiation are described in the following sections. Details on the model have been published in [R4] while the analysis of the saturation was reported on in [R1, R3].

7.3.1 The electron dynamics

As a simplification, our model only considers the most dominant magnetic field component B_z. Even though all other field components grow exponentially during the linear phase as well, their magnitude and thus their influence on the electron dynamics is orders of magnitude lower [81]. The model also neglects any effects from local field fluctuations caused e.g., by charge separation. The underlying magnetic field can be described as:

$$\vec{B}(t) = B_0 \cdot \vec{e}_z \cdot e^{\Gamma t} \tag{7.31}$$

with B_0 denoting an initial magnetic field value at time $t = 0$, $\vec{e}_z$ being the unit vector in z-direction and Γ being the exponential growth rate of the magnetic field. The model further assumes that the magnetic field amplitude is independent of the electron's position which is equivalent to a spatially homogeneous magnetic field.

Based on this magnetic field evolution (Eq. 7.31), the equation of motion can be derived using the Lorentz force:

$$\begin{aligned} \vec{F} &= \ddot{\vec{r}} \cdot \gamma \cdot m & (7.32) \\ &= q \cdot \left(\vec{E} + \vec{v} \times \vec{B} \right) & (7.33) \\ &= q \cdot B_0 \cdot e^{\Gamma t} \left(\dot{\vec{r}} \times \vec{e}_z \right) & (7.34) \end{aligned}$$

with m being the mass, $\dot{\vec{r}} = \vec{v}$ the velocity, γ the relativistic Lorentz factor and $\ddot{\vec{r}}$ the acceleration of the electron.

Obviously, there is no force and no change in motion in the z direction: $\ddot{\vec{r}} \cdot \vec{e}_z = \ddot{z} = 0$. For the other components, the Lorentz force leads to a system of coupled differential equations:

$$\begin{aligned} \ddot{\vec{r}} \cdot \vec{e}_x = \ddot{x} &= +\frac{q \cdot B_0}{\gamma \cdot m} \cdot e^{\Gamma t} \cdot \dot{y} & (7.35) \\ \ddot{\vec{r}} \cdot \vec{e}_y = \ddot{y} &= -\frac{q \cdot B_0}{\gamma \cdot m} \cdot e^{\Gamma t} \cdot \dot{x} \quad . & (7.36) \end{aligned}$$

This differential equation can be solved by the complex ansatz :

$$\dot{r}(t) = \dot{x}(t) + \mathrm{i}\dot{y}(t) = \alpha \cdot e^{\mathrm{i}\frac{\chi}{\Gamma} \cdot \left(1 - e^{\Gamma t} + \phi\right)} \ . \tag{7.37}$$

Without losing generality, one can assume an initial velocity in x direction $\dot{\vec{r}} = v_0 \cdot \vec{e}_x$. This leads to the following simplified pair of equations:

$$\begin{aligned} \dot{x}(t) = &\quad v_0 \cdot \cos\left(\tfrac{\chi}{\Gamma} \cdot \left(1 - e^{\Gamma t}\right)\right) & (7.38) \\ \dot{y}(t) = &\quad v_0 \cdot \sin\left(\tfrac{\chi}{\Gamma} \cdot \left(1 - e^{\Gamma t}\right)\right) & (7.39) \end{aligned}$$

with $\chi = \frac{q \cdot B_0}{\gamma \cdot m}$ being a time constant.

By integrating this solution over time, one finds the electron trajectory to be

$$\begin{aligned} x(t) &= x_0 - \frac{v_0}{\Gamma} \left\{ \cos\left(\frac{\chi}{\Gamma}\right) \cdot \left[\mathrm{Ci}\left(\frac{\chi}{\Gamma}\right) - \mathrm{Ci}\left(\frac{\chi}{\Gamma} e^{\Gamma t}\right) \right] + \sin\left(\frac{\chi}{\Gamma}\right) \cdot \left[\mathrm{Si}\left(\frac{\chi}{\Gamma}\right) - \mathrm{Si}\left(\frac{\chi}{\Gamma} e^{\Gamma t}\right) \right] \right\} & (7.40) \\ y(t) &= y_0 - \frac{v_0}{\Gamma} \left\{ \sin\left(\frac{\chi}{\Gamma}\right) \cdot \left[\mathrm{Ci}\left(\frac{\chi}{\Gamma}\right) - \mathrm{Ci}\left(\frac{\chi}{\Gamma} e^{\Gamma t}\right) \right] - \cos\left(\frac{\chi}{\Gamma}\right) \cdot \left[\mathrm{Si}\left(\frac{\chi}{\Gamma}\right) - \mathrm{Si}\left(\frac{\chi}{\Gamma} e^{\Gamma t}\right) \right] \right\} , & (7.41) \end{aligned}$$

with the starting conditions $x(0) = x_0$ and $y(0) = y_0$. In this equation we used the sine- $\mathrm{Si}(z)$ and cosine-integrals $\mathrm{Ci}(z)$:

$$\begin{aligned} \mathrm{Si}(z) &= \int_0^z \frac{\sin x}{x} \, \mathrm{d}x & (7.42) \\ \mathrm{Ci}(z) &= -\int_z^{+\infty} \frac{\cos x}{x} \, \mathrm{d}x \ . & (7.43) \end{aligned}$$

The electron will move on a spiral trajectory, approaching $x \to x_\infty$ and $y \to y_\infty$ for $t \to \infty$.

$$\begin{aligned} x_\infty &= x_0 - \frac{v_0}{\Gamma} \cdot \left[\cos\left(\frac{\chi}{\Gamma}\right) \cdot \mathrm{Ci}\left(\frac{\chi}{\Gamma}\right) + \sin\left(\frac{\chi}{\Gamma}\right) \cdot \mathrm{Si}\left(\frac{\chi}{\Gamma}\right) - \sin\left(\frac{\chi}{\Gamma}\right) \cdot \frac{\pi}{2} \right] & (7.44) \\ y_\infty &= y_0 - \frac{v_0}{\Gamma} \cdot \left[\sin\left(\frac{\chi}{\Gamma}\right) \cdot \mathrm{Ci}\left(\frac{\chi}{\Gamma}\right) - \cos\left(\frac{\chi}{\Gamma}\right) \cdot \mathrm{Si}\left(\frac{\chi}{\Gamma}\right) + \cos\left(\frac{\chi}{\Gamma}\right) \cdot \frac{\pi}{2} \right] . & (7.45) \end{aligned}$$

By redefining the original solution for the electron trajectory to spiral around the limes solution $(x_\infty, y_\infty) \rightarrow (0,0)$, and introducing the simplifying definitions

$$C(t) = \mathrm{Ci}\left(\frac{\chi}{\Gamma} \cdot e^{\Gamma t}\right) \tag{7.46}$$

$$S(t) = \mathrm{Si}\left(\frac{\chi}{\Gamma} \cdot e^{\Gamma t}\right) - \frac{\pi}{2} \tag{7.47}$$

$$\alpha = \frac{\chi}{\Gamma} \,. \tag{7.48}$$

one gets the simplified solution:

$$\tilde{x}(t) = x(t) - x_\infty = \frac{v_0}{\Gamma} \left[\sin\alpha \cdot S(t) + \cos\alpha \cdot C(t)\right] \tag{7.49}$$

$$\tilde{y}(t) = y(t) - y_\infty = \frac{v_0}{\Gamma} \left[\sin\alpha \cdot C(t) - \cos\alpha \cdot S(t)\right] \,. \tag{7.50}$$

This allows describing the trajectory in circular coordinates. The radius becomes:

$$r = \sqrt{\tilde{x}^2 + \tilde{y}^2} = \frac{v_0}{\Gamma} \cdot \sqrt{S^2(t) + C^2(t)} \,, \tag{7.51}$$

and the azimuth is:

$$\tan(\varphi) = \frac{\sin\alpha \cdot C(t) - \cos\alpha \cdot S(t)}{\sin\alpha \cdot S(t) + \cos\alpha \cdot C(t)} \,. \tag{7.52}$$

The solution of the equation of motion of an electron in an exponentially growing, spatially homogeneous magnetic field is a spiral trajectory. An exemplary trajectory is plotted in Fig. 7.4. The radius of the spiral decreases approximately exponentially with time. In agreement with the fact that a magnetic field does not do any work $\dot{W} = \vec{F} \cdot \dot{\vec{r}} = 0$, the absolute velocity stays constant. However, the direction of the velocity changes increasingly - equivalent to the azimuthal angle. The magnitude of the acceleration increases proportionally to the increase of the magnetic field over time.

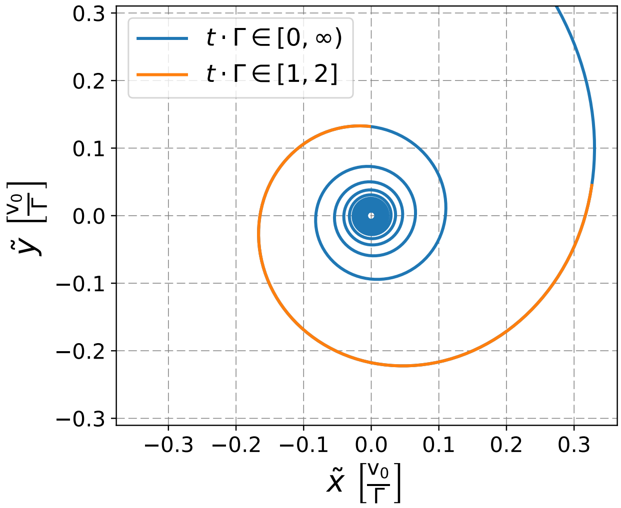

Figure 7.4: **The model electron trajectory:** The trajectory of an electron in an exponentially growing, spatially homogeneous magnetic field is plotted as assumed in the microscopic model. The entire trajectory is plotted in blue while a single duration of an inverse growth rate $\Delta t = \Gamma^{-1}$ is marked in orange.

This solution is, of course, an approximation valid in the case of negligible spatial field gradients. Since the KHI only occurs on the shear surface, this limits this solution to a small volume around the shear surface where the magnetic field undergoes a spatial extremum $\frac{\partial B_z}{\partial y} \approx 0$. This seems like a dramatic limitation, but in this region, the acceleration is also strongest and thus this region contributes dominantly to the total radiation.

In the following section 7.4, one will see that this simplification still describes the total radiation quite well. For now, one has to keep in mind that this solution is only valid on the shear surface.

7.3.2 Deriving the emitted radiation polarization

Based on the derived particle motion, the emitted radiation can be calculated using Liénard-Wiechert potentials as discussed in detail in chapter 2.1. Since the linear phase of the KHI lasts approximately $\Delta t_{\text{lin}} \approx 20\omega_{pe}^{-1}$ [R4], the electrons will perform less than

$$N_{\text{rot}} \approx \frac{\chi\left(1 - e^{\Gamma \Delta t_{\text{lin}}}\right)}{2\pi\Gamma} < 2 \tag{7.53}$$

rotations before the end of the linear phase. With an initial magnetic field of $B_0 = B_{\perp}^{\text{sat}} \cdot \mathrm{e}^{-\Gamma \Delta t_{\text{lin}}}$, no periodic motion of the electrons is expected. Thus, the radiation spectra will not feature any characteristic peaks, similar to the broadband synchrotron radiation [59]. However, in contrast to synchrotron radiation, the curvature of the trajectory will be slightly stronger. This will alter the degree of polarization compared to synchrotron radiation.

In order to compute the degree of polarization, we add a polarization filter **F** to the Liénard-Wiechert equation (Eq. 2.10).

$$\frac{\mathrm{d}^2 W}{\mathrm{d}\omega\,\mathrm{d}\Omega}(\vec{n}, \omega, \mathbf{F}) = \frac{q_e^2}{16\pi^2 \varepsilon_0 c} \cdot \left| \int_{-\infty}^{+\infty} \sum_{k=1}^{N_e} \mathbf{F} \cdot \frac{\vec{n} \times \left[\left(\vec{n} - \vec{\beta}_k\right) \times \dot{\vec{\beta}}_k\right]}{\left(1 - \vec{n} \cdot \vec{\beta}_k\right)^2} \cdot \mathrm{e}^{\mathrm{i}\omega(t - \vec{n} \cdot \vec{r}_k / c)}\,\mathrm{d}t \right|^2 \tag{7.54}$$

where the basic polarization filters are 3×3 matrices:

$$\mathbf{F}_k = \begin{bmatrix} \delta_{xk} & 0 & 0 \\ 0 & \delta_{yk} & 0 \\ 0 & 0 & \delta_{zk} \end{bmatrix} \tag{7.55}$$

for $k \in \{x, y, z\}$ and with δ_{ab} being the Kronecker delta. Any linear combination of the above is also a valid filter. Applying no filter is actually equivalent to the identity matrix and thus to a linear combination of all three filters of the Cartesian coordinate system $\mathbf{F}_1 = \mathbf{F}_x + \mathbf{F}_y + \mathbf{F}_z$.

Since our model describes the KHI in the relative velocity frame, there is no preferred direction of observation. We define the characteristic degree of polarization for a filter **F** as integral over the full solid angle 4π and all frequencies:

$$\langle\, P_{\mathbf{F}} \,\rangle = \frac{\int_0^{4\pi} \mathrm{d}\Omega \int_0^{\infty} \mathrm{d}\omega \frac{\mathrm{d}^2 W}{\mathrm{d}\omega\,\mathrm{d}\Omega}(\vec{n}, \omega, \mathbf{F})}{\int_0^{4\pi} \mathrm{d}\Omega \int_0^{\infty} \mathrm{d}\omega \frac{\mathrm{d}^2 W}{\mathrm{d}\omega\,\mathrm{d}\Omega}(\vec{n}, \omega, 1)} \,. \tag{7.56}$$

This is an averaged quantity over all observation directions $\vec{n}$, frequencies ω and particles k. We will see later in section 7.5.1 that this integrated quantity is also useful for observing the radiation on Earth.

The analytical trajectory is more complex than the synchrotron case. Therefore, solving the above equation by a numerical approach appeared to be more suitable. Due to the rotational symmetry, it is useful to define the polarization as parallel and perpendicular to the radiation, instead of relying on the Cartesian coordinates.

$$\langle\, P_{\perp} \,\rangle \quad \rightarrow \quad \mathbf{F}_{\perp} = \mathbf{F}_z \tag{7.57}$$

$$\langle\, P_{\parallel} \,\rangle \quad \rightarrow \quad \mathbf{F}_{\parallel} = \mathbf{F}_x + \mathbf{F}_y \tag{7.58}$$

In order to obtain the resulting characteristic polarization numerically, we computed the radiation by sampling 2048 directions on a half dome. The contributions from the other 3 half domes are identical for reasons of symmetry. Furthermore we calculated the radiation for 4096 frequencies in the range of $\omega \in \left[0, 10^5\Gamma\right]$. For a specific position on the trajectory, the radiation will be, due to the relativistic velocity of the electron, mainly emitted in a $1/\gamma_e$ cone in the current direction of propagation [129]. The radiation of the single electron is therefore dominated by the polarization of the radiation in the final direction of motion at the cut-off of the numeric trajectory. In order to compensate for this, the various propagation directions of electrons in the shear surface need to be considered. This can be done by taking into account an ensemble of electron trajectories with various start and final positions and averaging over their polarization. This can be interpreted both as an average over an ensemble of electrons at the same time or as a temporal average of a single electron. The first makes sense in the context of the KHI as plasma instability while the latter can only be interpreted in the single particle model.

The resulting degree of polarization is independent of the initial magnetic field value B_0 but shows a dependency both on the particle velocity v_0 and the growth rate Γ as plotted in Fig. 7.5. It shows a stronger parallel polarization for increasing initial velocity as well as for higher growth rates. However, the exact degree of polarization is relatively complex and shows local minima as well. It is important to point out that the degree of polarization differs significantly from the degree of polarization in the synchrotron case $\Gamma \to 0$. There, slight changes for sub-relativistic velocities are known [239]. The effect of the exponential growth of the magnetic field has a significant influence on the degree of polarization as well. Thus the degree of polarization allows distinguishing between this exponentially growing magnetic field regime, expected during the linear phase of the KHI, and the known characteristic polarization of synchrotron radiation.

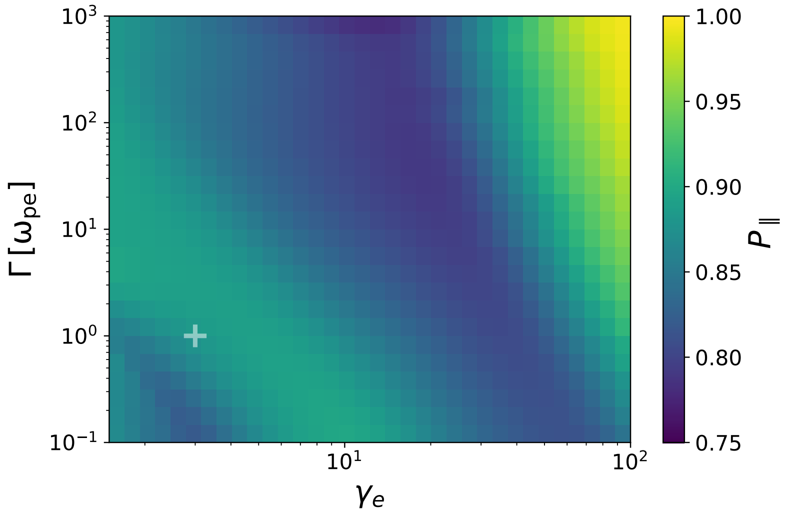

Figure 7.5: **The degree of polarization of the radiation emitted by electrons in an exponentially growing magnetic field:** The degree of polarization $P_\parallel$, describing the polarization parallel to the plane of rotation, is plotted for various Lorentz factors γ_e and growth rates Γ. A dependency on both the electron velocity and the growth rate can be seen. They differ from the degree of polarization expected for synchrotron radiation, which would be the distribution at $\Gamma \to 0$. Marked with a cross is the degree of polarization expected at the large-scale particle-in-cell simulations discussed in the following sections.

In figure 7.5, the cross already marks the degree of polarization expected for the parameters of the large-scale particle-in-cell simulation discussed in the following sections. The polarization is $\left\langle P_\parallel \right\rangle = 89.8\%$ and $\langle P_\perp \rangle = 10.2\%$.

7.3.3 Deriving the correlation between radiation and KHI growth rate

In addition to the characteristic degree of polarization, the radiated power shows a characteristic temporal evolution. The total emitted radiation power $\dot{\epsilon}_{\mathrm{rad}}$ of an electron following the spiral trajectory predicted by the model can be computed using the Larmor equation [59]

$$\dot{\epsilon}_{\mathrm{rad}}(t) = \frac{\mu_0 q_e^2 \gamma_e^6}{6\pi c}\left[(\dot{\vec{\beta}})^2 - (\vec{\beta}\times\dot{\vec{\beta}})^2\right] \tag{7.59}$$

$$= \frac{\mu_0 q_e^4 B_0^2 \gamma_e^2}{6\pi c \cdot m_e^2} \cdot \frac{v_0^2}{c^2} \cdot e^{2\Gamma t} \quad . \tag{7.60}$$

It increases exponentially

$$\dot{\epsilon}_{\mathrm{rad}} \sim e^{2\Gamma t} \equiv e^{\tilde{\Gamma}_{\mathrm{rad}} t} \quad . \tag{7.61}$$

In this equation, $\tilde{\Gamma}_{\mathrm{rad}}$ is the growth rate of the radiation power as predicted by the microscopic model.

Similarly, the total magnetic field energy evolves in the model. The component-wise total magnetic field energy, used in the following sections, is defined as:

$$\epsilon_{Bu}(t) = \int\limits_V \frac{1}{2\mu} B_u^2(\vec{r}, t)\,\mathrm{d}V \tag{7.62}$$

for the magnetic field component $\vec{B}\cdot\vec{e}_u = B_u$ with $u \in \{x, y, z\}$. For the model, which only considers the contribution of the z component, the magnetic field energy increases exponentially for a finite volume as

$$\epsilon_{Bz}(t) = \tfrac{1}{2\mu} e^{2\Gamma t} \cdot \int B_0^2(\vec{r})\,\mathrm{d}V \sim e^{2\Gamma t} \equiv e^{\tilde{\Gamma}_{Bz} t} \quad . \tag{7.63}$$

Introducing the exponential growth rate $\tilde{\Gamma}_{Bz}$ of the magnetic field energy in the model quantifies the evolution of the magnetic field energy as

$$\epsilon_{Bz}(t) \sim e^{2\Gamma t} \equiv e^{\tilde{\Gamma}_{Bz} t} \,. \tag{7.64}$$

Since the KHI is driven by the magnetic field component B_z, its development defines the evolution of the instability. Measuring $\epsilon_{Bz}(t)$ is often used in simulations to determine the growth rate Γ of the KHI using relation 7.63.

By comparing equation 7.61 with 7.63, the equivalent temporal growth of both quantities is obvious. However, these quantities can hardly be measured in experiments or during astronomical observations. Measuring the emitted radiation over time is much easier. Due to the discussed correlation between the KHI growth rate Γ, the growth rate of the magnetic field energy $\tilde{\Gamma}_{Bz}$ of the driving B_z component, and the emitted radiation power $\tilde{\Gamma}_{\mathrm{rad}}$, determining the characteristic growth rate of the KHI by measuring the radiation power is possible.

$$\frac{\mathrm{d}}{\mathrm{d}t}\frac{\dot{\epsilon}_{\mathrm{rad}}(t)}{\dot{\epsilon}_{\mathrm{rad}}(0)} = 2\Gamma\,\mathrm{e}^{2\Gamma t} = \frac{\mathrm{d}}{\mathrm{d}t}\frac{\epsilon_{Bz}(t)}{\epsilon_{Bz}(0)} \tag{7.65}$$

The previous conclusions are only valid for the microscopic model of the KHI. In case of a three-dimensional shear surface on which the KHI occurs, this finding only applies to a very small region on the shear surface, where the previously discussed limitations hold true. However, the radiation power emitted within this small region increases dramatically compared to the bulk of the streams.

In order to determine whether the radiation from the shear surface is strong enough to exceed the background radiation, a realistic three-dimensional simulation is essential.

7.4 Comparison to large scale simulations

In order to validate the kinetic model presented in the previous section, we performed a large-scale particle-in-cell simulation of the relativistic Kelvin-Helmholtz instability (KHI). By additionally simulating the emitted radiation with the in situ radiation plug-in of PIConGPU (see section 4.1), the plasma dynamics could be compared with the emitted radiation. This allowed validating the model predictions. However, particle-in-cell simulations of the KHI with relativistic shear velocities have a high computational demand.

Since the plasma dynamics happens on length scales of the plasma wavelength λ_{pe}, the simulation needs to resolve length scales smaller than:

$$\lambda_{\mathrm{pe}} = \frac{c}{\omega_{\mathrm{pe}}} = \sqrt{\frac{m_e c^2 \varepsilon_0}{n_e e^2}} \quad . \tag{7.66}$$

However, the plasma wavelength decreases with the evolution of the KHI locally, since the density increases in the vortices. Therefore, the spatial resolution must be set quite fine initially.

On the other hand, the KHI vortices in this regime are extended approximately as wide as the inverse of the KHI waves number [53]:

$$L_{\mathrm{KHI}} \approx \frac{2\pi}{k_{\mathrm{max}}} = 2\pi \cdot \lambda_{\mathrm{pe}} \cdot \sqrt{\frac{8}{3}} \cdot \beta_0 \cdot \gamma_e^{3/2} \, . \tag{7.67}$$

With a higher Lorentz factor γ_e, the vortices become larger and a larger volume needs to be simulated to cover several vortices completely.

These two requirements make simulating the KHI in the relativistic regime computationally challenging since both resolving the small-scale plasma dynamics and the macroscopic plasma vortices require many cells in particle-in-cell simulations.

Fortunately, we had the opportunity to use the largest supercomputer in the world at that time: the Titan cluster at the Oak Ridge National Laboratory. Using PIConGPU, we simulated two counter-propagating plasma streams of ionized hydrogen with Lorentz factors of $\gamma_e = 3$. This is the Mushroom Instability (MI) regime as discussed in section 7.2.2.

The two counter-propagating streams were distributed over $8000 \times 768 \times 768$ cells with each cell initially containing 8 macroprotons and 8 macroelectrons. The mass ratio between the proton and electron species was set to the relativistic value of $m_e/m_p = 1/1836$ thus avoiding a faster proton evolution. The cubic cells had an edge length of $\Delta x = 0.06 \cdot \lambda_{\mathrm{pe}}$, allowing a resolution of 16 grid points per initial plasma skin depth. Even if the vortex structure reaches a 10 times higher density than the initial density of the plasma stream, these structures would still be resolved by 5 grid points with respect to the smaller plasma skin depth at these higher densities (see Eq. 7.66). The large extent of the simulation box allowed resolving approximately 9 KHI vortices. However, such a large system required to use nearly all GPUs available on the Titan cluster. The final simulation utilized $18,432$ GPUs reaching a peak performance of $7.2\,\mathrm{PFLOP/s}$ (double precision) and $1.5\,\mathrm{PFLOP/s}$ (single precision), being the particle-in-cell simulation with the so far highest performance [R1].

The simulation went through 2000 PIC-cycle iterations at a temporal resolution of $\Delta t = 0.031\omega_{\mathrm{pe}}^{-1}$ and covered a total time of $t_{\mathrm{sim}} = 62\omega_{\mathrm{pe}}^{-1}$. This included not only the linear phase of the KHI, during which the magnetic field grows exponentially, but also the initial phase and the saturation regime.

Since the 9 vortices covered by the simulation box were smaller than a realistic shear surface extent in an astrophysical jet, continuous boundary conditions on each outer surface of the simulation box ensured that particles leaving the simulated volume would re-enter from the opposite side. The evolution of the electric and magnetic fields was simulated using the field solver by Yee [82] (see section 3.2). The reaction of both the ion and electron species to these fields and the resulting particle propagation was treated with the Boris particle pusher [87]. The resulting current was computed using the Esirkepov current deposition scheme [100] treating the macroparticles as a triangular-shaped density cloud (TSC) [73].

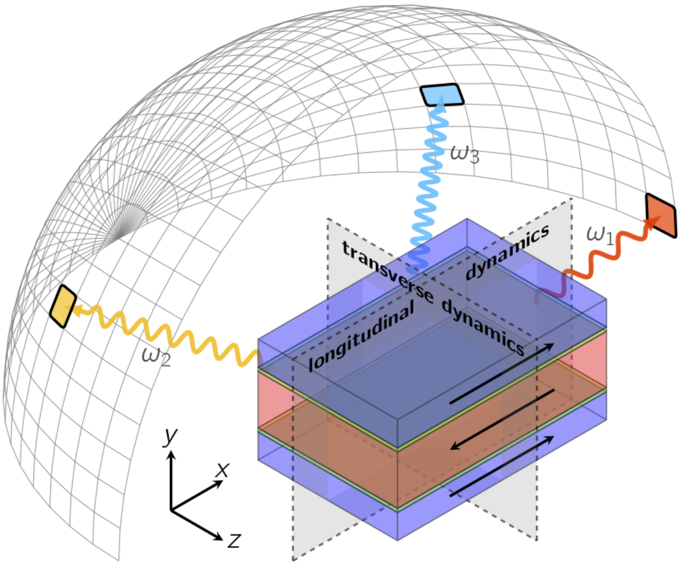

Figure 7.6: **A sketch of the KHI simulation setup:** The two counter-propagating plasma streams are shown in the center. They are surrounded by a half-dome grid. Each grid intersection represents one of the 481 observation directions $\vec{n}$ sampled for the simulation.

The radiation was calculated for frequencies between $\omega = 0.014\omega_{\text{pe}}$ and $\omega = 14\omega_{\text{pe}}$ on a logarithmic frequency scale for every second electron simulated. In order to sample the total radiation in all directions, the intrinsic symmetry of the setup was used and instead of the full $\Omega = 4\pi$ solid angle. A half dome of $\Omega = 1\pi$ was sampled using 481 observation directions $\vec{n}$. These observation directions were distributed as:

$$\vec{n} = \begin{bmatrix} \sin\theta \cdot \cos\varphi \\ \sin\theta \cdot \sin\varphi \\ \cos\theta \end{bmatrix} \tag{7.68}$$

with equidistant 32 samples along $\varphi \in [0, 2\pi]$ and 32 equidistant sampling points along $\theta \in [\pi/2, \pi]$. For $\theta = \pi$ all observation directions in φ are equal $\vec{n} = (0, 0, -1)$, thus of these only one was used for calculation.

A sketch of this setup is depicted in figure 7.6. A detailed description of the simulation and its performance can be found in [R1].

7.4.1 Evolution of the KHI

In this large-scale simulation, we expect three stages of plasma dynamics: the initial, the linear and the saturation phase. The first stage describes the onset of fields in the two plasma streams. By placing protons in the same position as electrons and setting the magnitude of the electric and magnetic fields in the entire simulation volume to zero, the simulation is initialized as charge neutral. Due to the streams' temperature, the proton and electron pairs separate, thus creating electric and magnetic fields. This initial "thermalization" is expected to cause an initial increase of magnetic and electric field energy. The particles propagate in ±x direction. They create current fluctuations in ±x direction causing strong B_y and B_y fluctuations compared to weak B_x fluctuations. Thus the total component-wise magnetic field energy ϵ_{By} and ϵ_{Bz} should initially increase (see Fig. 7.7), but we expect ϵ_{Bx} to stay relatively constant.

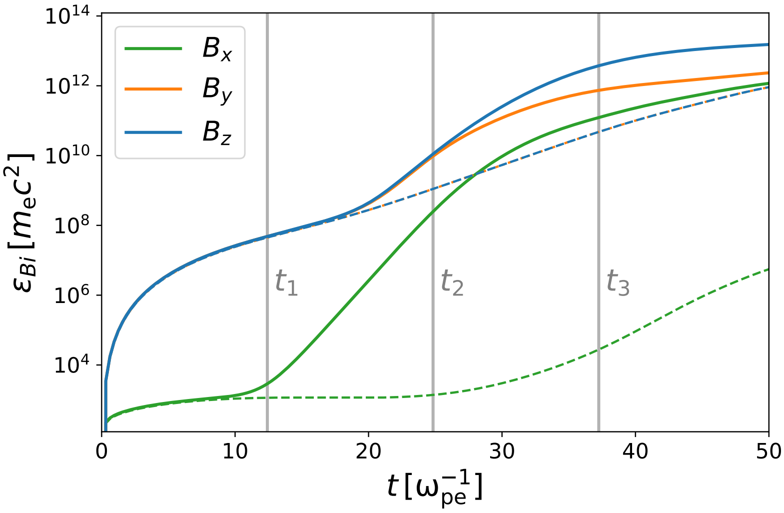

Figure 7.7: **Evolution of the magnetic field energy:** The evolution of the component-wise magnetic field energy ε_{Bi} derived from the simulation according to Eq. 7.62 is plotted versus time t. The solid lines depict values from the large-scale KHI simulation. The dashed lines represent the corresponding field energy evolution for a single plasma stream without driving a KHI. They are derived from a smaller simulation and scaled to the volume of the KHI simulation. Initially, the energy is dominated by the stream thermalization. This is followed by the linear phase of the KHI with exponential field growth. This phase can first be identified by the increase of the B_x energy. Beforehand, the B_x energy has only been weakly growing due to the stream thermalization. At $t \approx 30\omega_{pe}^{-1}$ the saturation of the KHI starts and the exponential growth reduces. The vertical gray lines mark times for which slices are plotted in Fig. 7.8.

Due to these magnetic field fluctuations, the Kelvin-Helmholtz instability is seeded on the shear surface. This leads to an exponential growth of the B_z magnetic field as discussed in section 7.2. It is called the *linear phase*. Due to this growth of the magnetic field component B_z over time, the electric field components E_x and E_y increase as well according to Maxwell's law:

$$\nabla \times \vec{E} \;=\; -\frac{\partial \vec{B}}{\partial t} \approx -\vec{e}_z \cdot \frac{\partial B_z}{\partial t} \tag{7.69}$$

$$E_x, E_y \;\sim\; \frac{\partial B_z}{\partial t} \neq 0 \quad . \tag{7.70}$$

Following Ampère's law, the temporal changes in the electric field cause the other magnetic field components to grow as well:

$$\nabla \times \vec{B} \;=\; \mu_0 \left(\vec{J} + \varepsilon_0 \frac{\partial \vec{E}}{\partial t} \right) \sim \frac{\partial^2 B_z}{\partial^2 t} \cdot (\vec{e}_x + \vec{e}_y) \tag{7.71}$$

$$B_x, B_y \;\sim\; \frac{\partial^2 B_z}{\partial^2 t} \neq 0 \quad . \tag{7.72}$$

Therefore, all magnetic field component will grow exponentially.

Initially, the exponentially growing magnetic field on the shear surface does not increase the total magnetic field energy over the entire simulation volume much. But right with the onset of the KHI, the B_x field starts growing exponentially. At some point, the field growth caused by the KHI outruns the growth due to thermalization and the B_z and B_y components increase faster. However, at this time the linear phase of the KHI is already in progress. In order to illustrate this influence of the stream thermalization, Fig. 7.7 shows the field evolution over time of a single stream, which undergoes thermalization but does not drive a KHI, as dashed lines. The separation in component-wise magnetic field energy between single stream and two stream setup can be clearly identified for the B_x component at $t \approx 10\omega_{\mathrm{pe}}^{-1}$, while the separation for the B_y and B_z component can only be identified after $t \approx 20\omega_{\mathrm{pe}}^{-1}$ due to the strong contributions of the stream thermalization at these components.

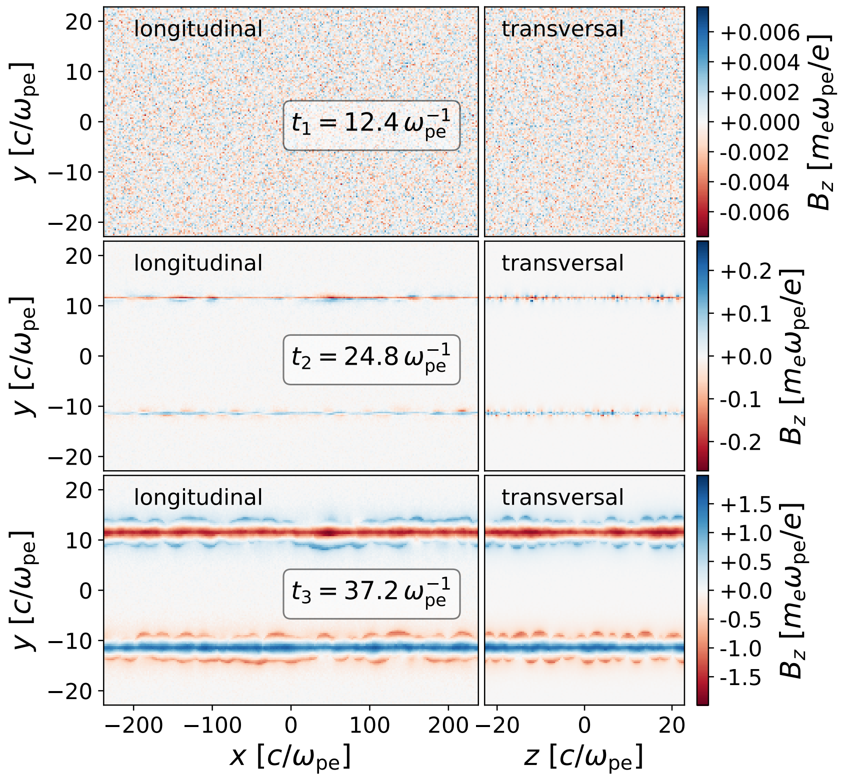

Figure 7.8: **Slices through the simulation volume for various time steps:** The magnetic field B_z evolution is depicted by slices through the simulation volume as illustrated in Fig. 7.6. Initially at t_1, the magnetic field is relatively weak and characterized by homogeneous field fluctuations. Later, at t_2, the increasing fields due to the KHI are clearly visible. Towards the end of the linear phase, at t_3, the field extends farther out and its magnitude increased further. The illustrated time steps are depicted by gray lines in Fig. 7.7.

Following this exponential growth of the magnetic field, the plasma reaches a saturation regime where the electron crossing between the two streams is reduced since the magnetic field becomes strong enough to trap electrons instead of leading to more charge separation [54]. Consequently, the increase in magnetic field energy levels off.

These three stages are depicted by slices of the magnetic field B_z along the longitudinal and transversal plane in figure 7.8.

The simulation program PIConGPU can store field distributions on the hard drive, enabling a post-processing field analysis. As discussed in section 3.3, for large simulations, like this one, storing the field distribution is limited due to bandwidth and disk storage. In our case, this allowed only data output every 200th time step. In order to analyze the field evolution with a higher temporal resolution, PIConGPU provides an in situ plug-in which integrates regularly the total component-wise field energy for the entire simulation volume. This field energy analysis plug-in reduces the electric and magnetic field data to 6 floating-point values. The reduced data can be more regularly stored on disk, allowing a finer temporal resolution. This total component-wise field energy, computed with the in-situ plug-in, is shown in figure 7.7. The spatially resolved magnetic field values for the magnetic field component B_z are exemplarily illustrated in figure 7.8. These values were obtained from the less frequent total data outputs.

This detailed discussion of the data output would not be necessary if the integration carried out by the plug-in did not cause a drawback: the initial signs of emerging KHI are drowned by the integration of the bulk magnetic field. Initially, the global field is dominated by the "thermalization" of the streams. The field evolution caused by the KHI is therefore initially hidden as discussed before. Subtracting the field energy from the field energy of the single stream simulation allows a slightly better identification of the KHI evolution. However, this subtraction has its limits, since the magnetic field grows orders of magnitude during the "thermalization".

As discussed before, the B_x component is only slightly increased due to thermalization. It is mainly driven by the KHI and thus ideally suited for identifying the evolution of the KHI in the simulation. The correlation between ϵ_{Bx} integrated over the entire volume and the magnetic field energy at the shear surface plane, derived only for discrete time steps accessible via data outputs, is demonstrated in figure 7.9. It can be clearly seen that ϵ_{Bx} follows the evolution on the shear surface.

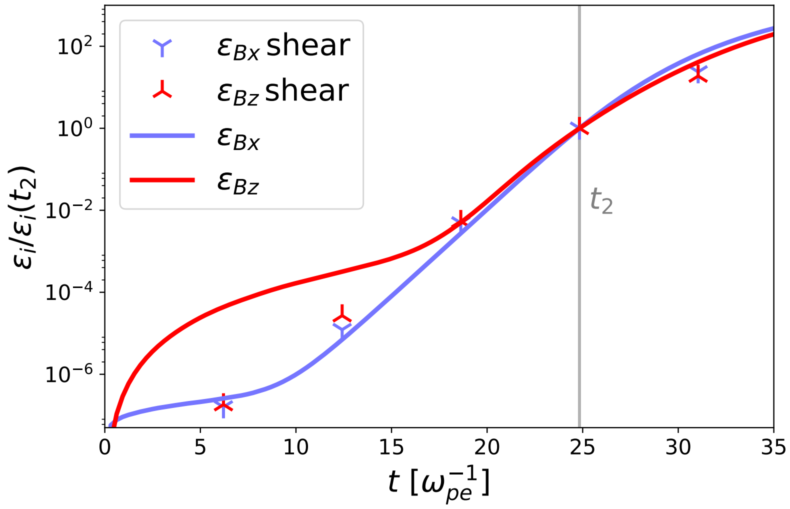

Figure 7.9: **Comparison of the global component-wise magnetic field evolution with the component-wise magnetic fields on the shear surface:** The global field energy ϵ of the B_x magnetic field component follows the same evolution as B_z on the shear surface and thus allows determining the evolution of the KHI with a better temporal resolution than achievable by field data outputs of the entire simulation volume. The energies are normalized to the time $t = 24.8\omega_{\mathrm{pe}}^{-1}$, marked by a gray line.

In conclusion: using a globally integrated B_x in contrast to B_z allows analyzing the early phase of the linear regime[12]. That is why we will use B_x for any further analysis of the KHI evolution.

From the simulated magnetic field, the exponential growth rate Γ can be determined numerically. In contrast to previous studies, we did not fit an exponential function $\mathrm{e}^{\Gamma t}$ onto the data, but resolved the temporal evolution of the growth rate by a logarithmically centered difference

---

[12] Using the integrated "global" quantities also allows avoiding errors in selecting the right region of interest.

scheme [R4]. The growth rate $\Gamma_f(t_k)$ of a quantity $f(t)$ at time $t_k = \Delta t \cdot k$ can be determined by:

$$\Gamma_f(t_k) = \frac{\log\left(\frac{f(t_{k+1})}{f(t_{k-1})}\right)}{t_{k+1} - t_{k-1}} \quad . \tag{7.73}$$

By applying this method to the magnetic field energy ϵ_{Bx} of the B_x component, as obtained from the simulation, we derive the evolution of the growth rate Γ_{Bx} over time (see Fig. 7.10). The growth rate peaks at around $\Gamma_{Bx} \approx 1\omega_{pe}$. Based on this evolution we define the duration of the linear phase of the KHI as the time, where the growth rate is larger than half of the maximum. Based on this definition, the linear phase starts at $t_1 = 9.0\omega_{pe}^{-1}$ and ends at $t_2 = 30.7\omega_{pe}^{-1}$. This time needs to be compared to the time of the linear phase determined by polarization in the next section.

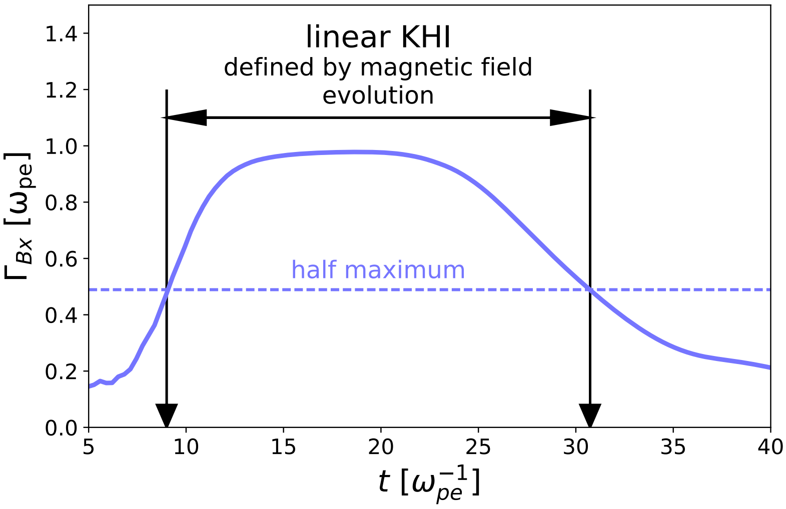

Figure 7.10: **The growth rate Γ_{Bx} of the magnetic field energy ϵ_{Bx} of the magnetic field component B_x over time t:** The plot depicts the growth rate evolution over time. The crossing of the half maximum line defines the linear phase.

7.4.2 Polarization signature

Determining the degree of polarization for every observer and every frequency is possible with PIConGPU. This allows a detailed analysis of the polarized radiation emitted during the linear phase of the KHI. In Eq. 7.54 we determined the polarization by selecting a specific vector component of the complex amplitude before calculating the radiation spectra via the spectrally resolved Liénard-Wiechert potentials. In the radiation plug-in, such a filter can be avoided since PIConGPU stores the complex amplitudes $\vec{A} \in \mathbb{C}^3$ of the computed radiation (see Eq. 4.3) [R9]. The vector components of the complex amplitude are proportional to electric field components of the emitted radiation (see section 2.1). Applying a polarization filter **F** as introduced in Eq. 7.54 is therefore possible during post-processing of the radiation data:

$$\frac{\mathrm{d}^2 W}{\mathrm{d}\,\omega\,\mathrm{d}\,\Omega}(\vec{n}, \omega, \mathbf{F}, t = \Delta t \cdot k) = \frac{\Delta t}{16\pi^2 \varepsilon_0 c} \cdot \left| \mathbf{F} \cdot \vec{A}_k(\omega, \vec{n}) \right|^2 \quad . \tag{7.74}$$

Equation 7.74 describes the total, spectrally resolved radiation emitted at frequency ω in direction $\vec{n}$ after a time of $t = k \cdot \Delta t$.

In order to resolve the evolution of the polarization over time, the finite difference method has to be applied to Eq. 7.74. The spectrally and directionally resolved power is the time derivative of the radiated energy $\frac{\mathrm{d}^2\dot{W}}{\mathrm{d}\omega\mathrm{d}\Omega} = \frac{\mathrm{d}}{\mathrm{d}t}\frac{\mathrm{d}^2 W}{\mathrm{d}\omega\mathrm{d}\Omega}$. On the one hand, the numeric integration for determining the spectra requires adding several consecutive time steps. On the other hand, it is not feasible to store the complex amplitudes for every time step. Therefore, the numeric differentiation has to be performed between complex amplitudes several time steps apart:

$$\frac{\mathrm{d}^2\dot{W}}{\mathrm{d}\omega\mathrm{d}\Omega}(\vec{n}, \omega, \mathbf{F}, t = \Delta t \cdot k) = \frac{1}{16\pi^2 \varepsilon_0 c N_A} \cdot \left| \mathbf{F} \cdot \left(\vec{A}_k(\omega, \vec{n}) - \vec{A}_{k-N_a}(\omega, \vec{n}) \right) \right|^2 \tag{7.75}$$

with N_A being the number of time steps between the two amplitudes used for the difference quotient.

Analog to the method presented in section 7.3.2, the characteristic degree of polarization is determined by integrating the radiation over the full solid angle (Eq. 7.56). Due to the symmetry of the shear interface, only the radiation on a half dome of $\Delta\Omega = \pi$ had to be simulated.

The resulting degree of polarization over time is thus numerically defined as:

$$\begin{aligned} \langle P_{\mathrm{F}} \rangle (t) &= \frac{\dot{W}(\mathbf{F}_{\{x,y,z\}}, t)}{\dot{W}(\mathbf{F}_1, t)} && (7.76) \\ \dot{W}(\mathbf{F}, t) &= 4 \cdot \sum_{\omega} \Delta\omega \sum_{\vec{n}} \Delta\Omega \frac{\mathrm{d}^2 P}{\mathrm{d}\omega\mathrm{d}\Omega}(\vec{n}, \omega, \mathbf{F}, t) && (7.77) \end{aligned}$$

with the two sums being the sum over all frequencies and observation directions simulated, $\Delta\omega$ being the frequency step width[13], and $\Delta\Omega = \Delta\theta\Delta\varphi\sin(\theta)$ being the finite solid angle of each virtual observation point (Eq. 7.68).

The resulting polarization is plotted in Fig. 7.11. The quantities simulated relate to the predictions of the microscopic model as follows:

$$\begin{aligned} &\text{simulation} && \text{model} \\ &\langle P_x \rangle = && {}^1\!/_2 \cdot P_{||} && (7.78) \\ &\langle P_y \rangle = && {}^1\!/_2 \cdot P_{||} && (7.79) \\ &\langle P_z \rangle = && P_{\perp} \quad . && (7.80) \end{aligned}$$

Initially, the radiation is predominantly polarized perpendicularly to the plasma stream $P_y, P_z \gg P_x$. The reason for this polarization is the fluctuation of the magnetic and electric field which the electrons encounter in the bulk of the plasma stream. This characteristic polarization is very similar to synchrotron radiation and has a characteristic degree of polarization of $^7\!/_{16}$ for the two components perpendicular to the stream, P_y and P_z, and $^2\!/_{16}$ parallel to the stream direction [59]. Recent studies found that radiation emitted during this jitter motion in magnetic field fluctuations differs from synchrotron radiation [240]. However, these studies focused on the spectral differences to synchrotron radiation, not on the polarization. For reasons of illustration, we thus compare the initial polarization to synchrotron radiation and find an excellent congruence.

At around $t \approx 10\,\omega_{pe}^{-1}$, the degree of polarization starts changing rapidly. We define the start of the linear phase of the KHI, according to polarization, as the point in time when the degree of polarization matches the polarization of the microscopic model of the KHI vortex dynamics better than the polarization of synchrotron radiation. This "better" match starts at $t = 9.0\,\omega_{pe}^{-1}$, which is identical to the start of the linear phase determined via the growth rate

---

[13] Due to the logarithmic frequency range, $\Delta\omega$ differs for every frequency summand.

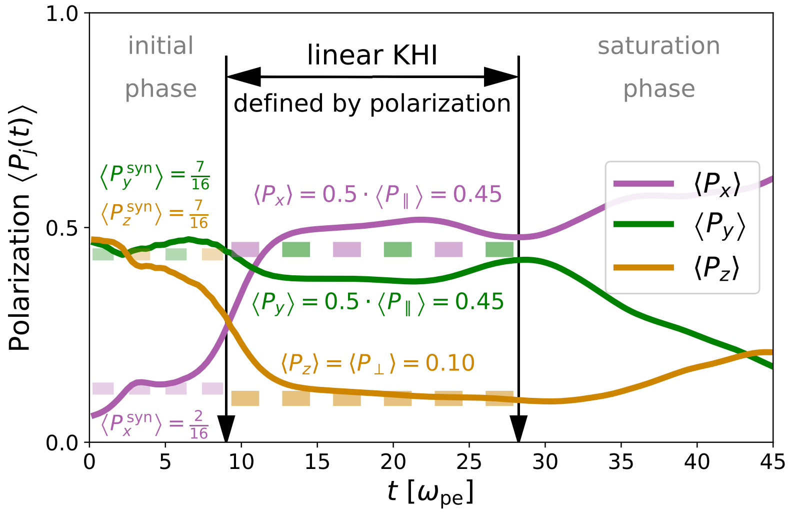

Figure 7.11: **The temporal evolution of the polarization before, during and after the linear phase of the KHI:** The linear phase can be determined by its characteristic polarization. Theoretical predictions for synchrotron and model polarization are marked by dashed lines. The expected values are stated in the color of the corresponding component. The linear phase starts when the model predictions are a better match for the polarization than the synchrotron polarization. The linear phase ends, when the anisotropy between $\langle P_x \rangle$ and $\langle P_y \rangle$ starts to grow.

of the magnetic field (see section 7.4.1). After this rapid change in polarization, the degree of polarization stabilizes and stays approximately constant till $t \approx 30\omega_{pe}^{-1}$. During this phase, the polarization of the billion particles simulated, agrees very well with the simple microscopic model, despite varying injection time and non-homogeneous magnetic field strength on the shear surface. Nonetheless, the polarization in x-direction is slightly higher than predicted by the microscopic model while the polarization in y-direction is slightly lower $\langle P_x \rangle > 0.5 \cdot \left\langle P_\parallel \right\rangle > \langle P_y \rangle$. This deviation originates from the decrease of the magnetic field strength further away from the shear surface which makes the acceleration of particles in the center of the shear stronger than at the return points further away from the interface. When crossing the shear surface, the electrons propagate perpendicularly to the shear surface $\vec{\beta} \parallel \vec{e}_y$. According to the Lorentz force, the acceleration parallel to the plasma stream is larger during the crossing than the acceleration perpendicular to the shear surface $\dot{\beta}_x \gg \dot{\beta}_y$. Therefore, radiation emitted by particles moving across the shear surface is mainly x-polarized. At the turning points, further away from the shear interface, the electrons propagate parallel to the stream $\vec{\beta} \parallel \vec{e}_x$. Again, according to the Lorentz force, the acceleration at this point is larger in y-direction than in x-direction $\dot{\beta}_x \ll \dot{\beta}_y$. Thus the emitted radiation is mostly polarized in y-direction. Since the acceleration is stronger in regions with larger magnetic fields, the radiation there is also stronger resulting in radiation being more x- than y-polarized. This anisotropy is observed in the simulation as well. Due to the inhomogeneity of the magnetic field perpendicular to the shear surface, a slight deviation from the microscopic model occurs toward a higher x-polarization providing rise to a weaker polarization.

At around $t \approx 30\,\omega_{pe}^{-1}$, the degree of polarization, after a brief approach of $\langle P_x \rangle$ and $\langle P_y \rangle$, starts to deviate from the prediction of the microscopic model. This marks the end of the linear phase of the Kelvin-Helmholtz instability and the start of the saturation phase. We define the end of the linear phase as the point, where the difference between $\langle P_x \rangle$ and $\langle P_y \rangle$ starts to grow again since there exist yet no model of the polarization of the saturation phase, to define a point in time of better matching. The end of the linear phase, according to polarization, is at

$t = 28.2\,\omega_{pe}^{-1}$. This is very close to the previously defined end of the linear phase via the growth rate Γ_{Bx}.

With the start of the saturation phase, the magnetic field becomes strong enough to trap electrons crossing the shear surface. This prevents further increase in the magnetic field and the magnetic field growth levels off [54]. According to Maxwell-Faraday's law, the increasing magnetic field B_z during the linear phase leads to an increase of the electric field E_y [55, 81]. The trapping at saturation leads to charge separation and an even stronger electric field E_y between the two shears [234]. Due to this additional electric field, the acceleration inside the shear surface is further increased compared to the radiation from the boundaries of the vortices. This leads to stronger radiation from the inside of the shear surface and thus to an increase of the anisotropy between the two parallel polarization components $\langle P_x \rangle \gg \langle P_y \rangle$.

Furthermore, the z-polarization $\langle P_z \rangle$ increases again with the onset of the saturation phase. The bunching and trapping of the electrons lead to increased electric and magnetic field fluctuations within the shear surface. The result is more acceleration in z-direction, which could be neglected during the linear phase, and an increasing $\langle P_z \rangle$ polarization.

We conclude that the polarization can be used to identify the linear phase and determine its start and end since both the initial phase and the saturation phase differ in polarization from the linear phase.

7.4.3 Correlation between radiation power and magnetic field evolution

The microscopic model predicts that the growth rate of the radiation power $\dot{\epsilon}_{\text{rad}}$ equals the growth rate of the magnetic field energy. However, the simple model could not decide whether the radiation from the shear surface is overshadowed by the radiation from the bulk of the plasma streams or the radiation from the shear surface is strong enough to measure its growth rate. Therefore we investigated the correlation in a three-dimensional particle-in-cell simulation.

The total radiation power can be computed from the spectra obtained with the radiation plug-in:

$$\dot{\epsilon}_{\text{rad}} = \frac{\mathrm{d}}{\mathrm{d}t} \int_0^{\infty} \mathrm{d}\omega \int_0^{4\pi} \mathrm{d}\Omega \frac{\mathrm{d}^2 W}{\mathrm{d}\omega \mathrm{d}\Omega} \left(\omega, \vec{n}, t\right) \quad . \tag{7.81}$$

Evaluating this integral numerically is equivalent to Eq. 7.77 with no polarization filter $\mathbf{F} = 1$. The total radiation power evolves similarly as the magnetic field energy ϵ_{Bx} (Fig. 7.9). A numerical analysis using the logarithmic finite difference method (Eq. 7.73) demonstrates the correlation between the radiation power $\dot{\epsilon}_{\text{rad}}$ and the magnetic field energy ϵ_{Bz} as depicted in Fig. 7.12. During the initial phase, the numerically determined growth rates are still strongly influenced by the initialization process, which started with no radiation power and magnetic field energy. The initially high growth of the magnetic field energy ϵ_{Bz} comes from the thermalization of the bulk of the plasma. Its value is overestimated by the simulation since the initial conditions are field free. The same is true for the radiation power growth rate. Even though the radiation of the thermalizing bulk of the stream is very weak, its initial growth is about as high as that of ϵ_{Bz}. Only ϵ_{Bx} shows nearly no increase at all since it is not directly affected by the thermalization.

With the onset of the Kelvin-Helmholtz instability, ϵ_{Bz} and, to a lesser extent, ϵ_{Bx} start growing on the shear surface (see Fig. 7.9). However, this is not directly reflected in the growth rates, since ϵ_{Bz} is still largely defined by the magnetic field in the bulk of the streams which grows much slower. Thus, only ϵ_{Bx} is a suitable quantity to define the growth of the magnetic field on the shear surface (see discussion section 7.4.1). Only when the magnetic field energy of the Kelvin-Helmholtz instability on the shear surface becomes larger than the total magnetic field energy in the bulk of the plasma streams, ϵ_{Bz} becomes a useful quantity to determine

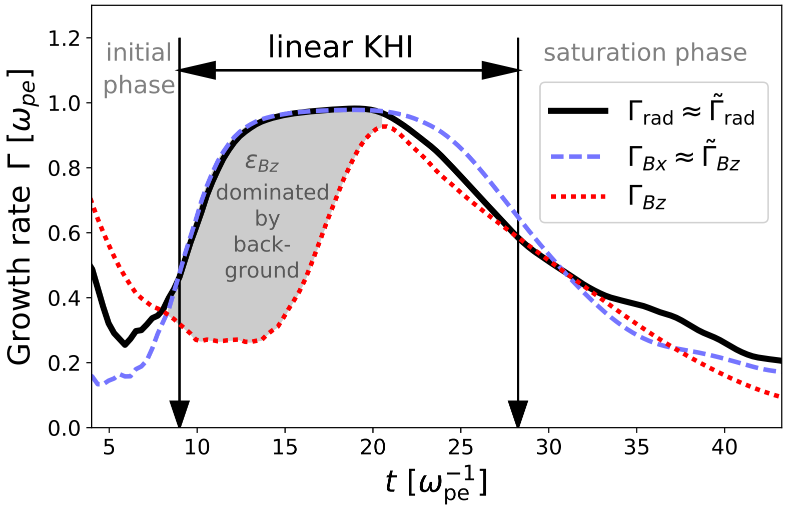

Figure 7.12: **The temporal evolution of the radiation growth rate Γ_{rad} and the growth rates (Γ_{Bx} and Γ_{Bz}) of the magnetic field components B_x and B_z:** During the linear phase, Γ_{Bx} and Γ_{rad} are equal within 11% thus demonstrating that the growth rate of the radiation allows measuring the growth the of the Kelvin-Helmholtz instability.

the growth rate of the instability. During the linear phase, the growth rate Γ_{rad} of the radiation power $\dot{\epsilon}_{\mathrm{rad}}$ equals the growth rate Γ_{Bx} of the magnetic field energy of B_x. The deviation between the two growth rates for the entire linear phase is below 11%. After the magnetic field energy of the Kelvin-Helmholtz instability becomes larger than the magnetic field energy of the entire bulk of the streams at around $t > 20\,\omega_{pe}^{-1}$, the growth rate of the B_z magnetic field energy Γ_{Bz} equals the growth rate of the radiation power Γ_{rad} as well. Both differ only be less than 9% after $t > 20\,\omega_{pe}^{-1}$.

After the linear phase, the magnetic fields start to saturate and thus all growth rates tend towards zero. The growth rate of the radiation power Γ_{rad} reduces slower than those of the magnetic fields due to the now increased electric fields caused by the charge separation that adds to the electron acceleration and thus radiation power.

The agreement between the magnetic field growth rate and the growth rate of the radiation power shows that the microscopic model is a valid approximation of the radiating process during the linear phase. Since radiation from shears in interstellar jets can directly be measured on Earth but the magnetic fields cannot, this correlation allows quantifying the growth rate of the Kelvin-Helmholtz instability by means of radiation $\Gamma = \Gamma_{\mathrm{rad}}/2 = 0.48\,\omega_{pe}$. The fact that the radiation of the Kelvin-Helmholtz instability is not initially overshadowed by the radiation from the jitter motion in the bulk of the jet is caused by the different spectrum of jitter radiation [240]. The spectral power of jitter radiation drops relatively fast for frequencies below the jitter frequency ω_{jm} while synchrotron radiation and the radiation from the shear surface reduce less toward lower frequencies. Since the analysis focused on frequencies above the plasma frequencies, only $\omega \in [1 - 14]\omega_{pe}$ were considered. At these frequencies, the jitter radiation is extremely weak. This allows measuring the growth of the radiation caused by the KHI already at the start of the linear phase. For frequencies larger than the jitter frequency, this distinction would only be possible in the later stage of the linear phase ($t > 20\,\omega_{pe}^{-1}$) similar the how the instability can be identified only delayed based on the growth rate Γ_{Bz}.

7.5 Observer in the lab frame

So far, the radiation signature of the Kelvin-Helmholtz instability was discussed in the relative velocity frame. However, except for special experimental setups where plasma jets counter-propagate with the same speed as discussed separately in section 7.6.3, this is not the frame of observation. The typical astrophysical survey will observe a jet at high-velocity shearing at the surrounding, quasi-stationary interstellar medium. Therefore, the results presented so far need to be translated to the lab frame of an observer on Earth. The following analysis assumes that the jet plasma stream propagates towards the observer since it is the most likely observation of interstellar jets and for the sake of simplicity. Jets propagating towards the observer are brighter and thus better suited for observations since their emission angle reduces to $\Delta\theta \sim \gamma^{-1}$ [59, 129, 240] due to the search-light effect of radiation from relativistic particles.

7.5.1 Lorentz transforming the polarization signature

Transferring the degree of polarization from one reference frame to another one is not trivial and requires Lorentz transforming the observation direction, the emission frequency, and the magnetic and electric fields associated with the observed radiation. Only by combining the transformations of these three quantities, the degree of polarization can be transferred to another reference frame. In the following, the Lorentz transformation of the degree of polarization is briefly sketched.

Prime symbols are introduced to mark quantities observed in the lab frame. Quantities in the relative velocity frame will have no special marks, as in the previous sections. We assume that the lab frame propagates with a relativistic Lorentz factor γ_{LT} in $-x$-direction. If the Lorentz factors of the transformation and of the stream are equal ($\gamma_{\mathrm{LT}} = \gamma_e = 3$), the lab frame observes a plasma stream of $\gamma' = 17$ shearing on a quasi-stationary plasma and approaching the observer.

The observation direction in the observer frame $\vec{n}'$ is turned in comparison to the observation direction $\vec{n}$ in the relative velocity frame towards the velocity $\vec{\beta}_{\mathrm{LT}}$ defining the Lorentz transformation:

$$\vec{n}' = \frac{\vec{n} + \vec{\beta}_{\mathrm{LT}} \cdot {}^{1}/_{\beta_{\mathrm{LT}}} \cdot \left[(\gamma_{\mathrm{LT}} - 1) \cdot (\vec{n} \cdot \vec{\beta}_{\mathrm{LT}}/\beta_{\mathrm{LT}}) - \gamma_{\mathrm{LT}} \cdot \beta_{\mathrm{LT}} \right]}{\gamma_{\mathrm{LT}} \left(1 - \vec{\beta}_{\mathrm{LT}} \cdot \vec{n} \right)} \quad . \tag{7.82}$$

Similarly, the infinitesimal solid angle $\mathrm{d}\Omega$, associated with each observer direction $\vec{n}$, changes under the Lorentz transformation

$$\mathrm{d}\Omega' = \mathrm{d}\Omega \cdot \frac{1}{\gamma_{\mathrm{LT}}^2 \cdot \left(1 - \vec{\beta}_{\mathrm{LT}} \cdot \vec{n} \right)} \tag{7.83}$$

The solid angle for an observer directly in the direction of the Lorentz transformation does not change, while the solid angle for an observer at 90° will decrease by γ^{-2}.

For transforming the frequency ω we use the Lorentz transformation of the wave vector $\vec{k} = \vec{n} \cdot \frac{\omega}{c}$. In the observer frame, the wave vector is:

$$\vec{k}' = \vec{n} + \left| \vec{k} \right| \cdot \frac{\vec{\beta}_{\mathrm{LT}}}{\beta_{\mathrm{LT}}} \cdot \left[(\gamma_{\mathrm{LT}} - 1) \cdot \left(\vec{n} \cdot \frac{\vec{\beta}_{\mathrm{LT}}}{\beta_{\mathrm{LT}}} \right) - \gamma_{\mathrm{LT}} \cdot \beta_{\mathrm{LT}} \right] \tag{7.84}$$

and the frequency is

$$\omega' = \left| \vec{k}' \right| \cdot c \quad . \tag{7.85}$$

This transformation allows computing $\mathrm{d}\omega' \approx \Delta\omega'$ for the logarithmic frequency scale, as used in the particle-in-cell radiation simulation.

In order to Lorentz-transform the degree of polarization, one can use the fact that that the vector of the complex amplitudes in Eq. 2.10 is parallel to the electric field vector of the emitted electromagnetic wave (Eq. 2.9). The component-wise magnitude of the complex amplitude Lorentz-transforms like an electric field. Under such a transformation, electric fields transform to both electric and magnetic fields and vice versa [58]. In order to take into account the contributions of the magnetic component of the electromagnetic radiation, the relation $\vec{B} \cdot c = \vec{n} \times \vec{E}$ is used, with $\vec{n}$ being the propagation direction of the electromagnetic wave and also the observation direction. The amplitudes transform as follows:

$$
\begin{aligned}
\vec{E} &\sim \vec{A} && (7.86)\\
\vec{E}' &= \vec{E}'_{\perp} + \vec{E}'_{\parallel} && (7.87)\\
\vec{E}'_{\perp} &= \gamma_{\mathrm{LT}} \cdot \left(\vec{E}_{\perp} + \vec{\beta}_{\mathrm{LT}} \times \vec{B} \cdot c\right) && (7.88)\\
\vec{E}_{\perp} &= \vec{E} - \vec{E}_{\parallel} && (7.89)\\
\vec{E}'_{\parallel} &= \vec{E}_{\parallel} = \frac{\vec{\beta}_{\mathrm{LT}}}{\beta_{\mathrm{LT}}} \cdot \left(\vec{E} \cdot \frac{\vec{\beta}_{\mathrm{LT}}}{\beta_{\mathrm{LT}}}\right) && (7.90)\\
\vec{A}' &\sim \vec{E}' && (7.91)
\end{aligned}
$$

This transformation was performed for every observation direction, every frequency, and every time step saved on hard drive. In order to determine the polarization in the lab frame, an integration over all frequencies and observation directions similar to Eq. 7.77 was performed again. For integrating the complex amplitudes in the lab frame, the differentials $\mathrm{d}\omega$ and $\mathrm{d}\Omega$ need to be Lorentz-transformed according to Eq. 7.83 and Eq. 7.85.

It appears a bit counter-intuitive to integrate the radiation over the full solid angle in the observer's frame to compute the degree of polarization if the observer is only located in front of the jet. But by examining the transformation above carefully, the radiation in jet direction dominates the polarization due to the boost of the electric field and the differentials. Thus by integrating over the full solid angle, only radiation emitted in jet direction has a significant contribution and radiation emitted close to the jet direction has a small but not-negligible contribution to the observed degree of polarization in the observer's frame. However, these small contributions need to be taken into account since astrophysical jets meander around their main flow direction [29, 36] and thus an observer on Earth will measure radiation from small angles around the idealized boost direction as well.

7.5.2 Consequences for an observer on Earth

The evolution of the polarization in the lab frame appears to be slower than in the relative velocity frame since the time of observation in the lab frame needs to be Lorentz-transformed as well:

$$t' = t \cdot \gamma_{\mathrm{LT}} \quad . \tag{7.92}$$

Furthermore, the radiation is observed at higher frequencies than in the relative velocity frame:

$$\omega' = \sqrt{\frac{1 + \beta_{\mathrm{LT}}}{1 - \beta_{\mathrm{LT}}}} \cdot \omega \quad . \tag{7.93}$$

This shift in frequency affects the radiation from the shear surface and the jitter radiation equally. Distinguishing them and identifying the radiation from the Kelvin-Helmholtz instability remains possible.

In the lab frame, the polarization parallel to the jet direction $\langle P'_x \rangle$ is imperceptible since radiation is mostly emitted in the forward direction. Only the polarizations perpendicular to the jet direction $\left\langle P'_y \right\rangle$ and $\langle P'_z \rangle$ are significant. Their ratio is plotted in Fig. 7.13 for three different Lorentz factors γ_{LT}. With the onset of the linear phase as determined previously via polarization in the relative velocity frame, an anisotropy[14] in the polarization occurs that increases the polarization parallel to the driving magnetic field $\langle P'_z \rangle$. This anisotropy reduces towards the end of the linear phase. The change in polarization is independent of the specific Lorentz boost. Thus, this anisotropy in polarization is a hallmark signature of the linear phase of the Kelvin-Helmholtz instability. It allows determining the start and end of the linear phase and gives detailed information on when to determine the growth rate of the instability via the change in radiation power observed on Earth.

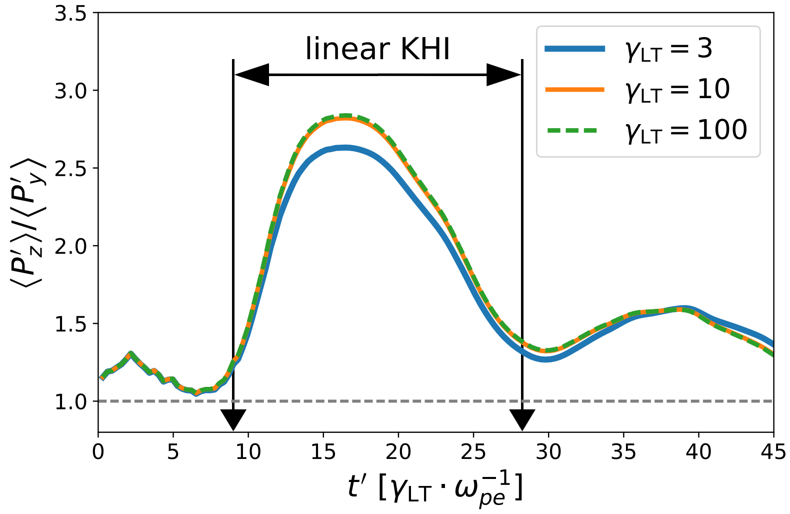

Figure 7.13: **The anisotropy of the polarization during the linear phase of the KHI:** The plot depicts the ratio between the perpendicular polarizations $\langle P'_z \rangle / \left\langle P'_y \right\rangle$, as observed in the lab frame, over time t. The polarization anisotropy ($\langle P'_z \rangle / \left\langle P'_y \right\rangle \gg 1$) during the linear phase of the Kelvin-Helmholtz instability occurs for various Lorentz factors γ_{LT} of the Lorentz transformations. Its stability against the actual velocity of the transformation makes it a hallmark signature to identify the linear phase of the instability.

When measuring the logarithmic growth rate of the radiation power in the lab frame Γ'_{rad}, the time dilatation (Eq. 7.92) needs to be taken into account as well

$$\Gamma = \frac{\Gamma'_{\mathrm{rad}} \cdot \gamma_{\mathrm{LT}}}{2} \quad . \tag{7.94}$$

By measuring the relative velocity of interstellar jets via frequency shift of known transition lines [241, 242], the Lorentz factor γ_{LT} can be measured and the growth rate Γ of the instability can be determined.

---

[14] Please note that anisotropy in this context does not mean dependent on the observation direction, but a preferred polarization direction. A spatial resolution of the plasma jet is therefore not necessary.

7.6 Discussion of possible observational systems

7.6.1 Influences of more realistic jets

So far we have discussed the results of an idealized Kelvin-Helmholtz instability, with streams of equal density and with a sharp velocity gradient in order to carve out the plasma dynamics of the instability clearly, to be able to unambiguously verify the results against analytical predictions, and to validate the correlation between radiation and plasma dynamics. However, in realistic plasma jets, both in astrophysical scenarios as well as in lab experiments, the conditions will not be as ideal. There is no comprehensive theory that incorporates these effects in the plasma dynamics yet. But there exists an extensive numerical study by P Alves et al. [55] that used numerical means of solving the dispersion relation to determine scaling laws. Here we will briefly summarize his findings as a reference for the upcoming discussion on how the radiation will be altered when considering less idealistic shears.

Influences of velocity gradients

The simulation setup assumed a sharp velocity gradient. Realistically, a smooth transfer between the two velocities is expected. When quantifying the velocity gradient as $v_{||}(y) = v_0 \cdot \tanh(y/L)$, the growth rate decreases with a smoother velocity transition caused by a larger L value. In a linear approximation for small L values, the growth rate of the ESKHI decreases with increasing L as [55]

$$\Gamma_{\max}(k_{\perp\max} \cdot L) = \Gamma_{\max}(0) \cdot \left(1 - \frac{\sqrt{3}}{8}\pi k_{\perp\max} \cdot L\right) \tag{7.95}$$

with $\Gamma_{\max}(0)$ being the maximum growth rate of the ESKHI for a sharp velocity transition (Eq. 7.14) and $k_{\perp\max}$ the wave number of the fastest growing mode. This wave number $k_{\perp\max}$ decreases slightly with increasing L, and its value can only be determined by solving the dispersion relation numerically. For estimates of small L values, it can be assumed to be constant. For larger gradients $L \gtrapprox 0.2 \frac{c}{\omega_{pe}}$ the growth rate needs to be determined by solving the dispersion relation entirely numerically. At these larger gradients, the growth rate decreases slower than predicted by the linear approximation, reaching around $0.2 \cdot \Gamma_{\max}(0)$ at $L = 1.0 \frac{c}{\omega_{pe}}$.

Similarly, the mushroom instability growth rate decreases with increasing L as well. While for $L = 0$ the fastest growing mode was at an infinitely large wave number $k \to \infty$, it has a finite value of $k_{\max} = {}^{1}/{}_{L}$ [228] for a shear gradient $L > 0$. For the same L values, the MI growth rate will always be larger than the growth rate of the ESKHI in the relativistic regime.

The maximum amplitude reachable by the DC magnetic field is also reduced by a velocity shear gradient since the decreased speed on the shear interface reduces the current and thus the magnetic field while the evolution of the Larmor radius $r_{\mathrm{L}} \sim \frac{\gamma v_0}{B}$ depends on both the reduced magnetic field and the velocity gradient. Numerical studies showed, that the magnetic field at saturation can be approximated by

$$B_{\perp}^{\mathrm{sat}}(\tilde{L}) = \frac{B_{\perp}^{\mathrm{sat}}(\tilde{L})}{1 + \chi \cdot \tilde{L}} \tag{7.96}$$

with $\tilde{L} = \frac{L \cdot \omega_{pe}}{c\sqrt{\gamma}}$ being the normalized shear gradient width and χ a numerically determined factor depending on the maximum shear velocity v_0 [55].

Influence of density gradients

If the density of the streams differs

$$n(y) = \begin{cases} n_+ & y > 0 \\ n_- & y < 0 \end{cases} \quad , \tag{7.97}$$

the growth rate of the ESKHI reduces as well. Solving the dispersion relation numerically for non-equal densities $n_+ \neq n_-$ leads to a reduced maximum growth rate, a reduction in the maximum unstable wave number, and an additional oscillating (real) term in the solution. It was found that the growth rate scales for various density ratios $r = {}^{n_+}/_{n_-} \geq 1$ as

$$\frac{\Gamma_{\mathrm{max}}(r)}{\Gamma_{\mathrm{max}}(1)} \sim \begin{cases} r^{-1/4} & r \gtrsim 1 \\ r^{-1/3} & r \gg 1 \quad \gamma \approx 1 \\ r^{-1/2} & r \gg 1 \quad \gamma \gg 1 \end{cases} \quad . \tag{7.98}$$

For the MI, there exists no conclusive study on density ratios yet. However, it was found that a vacuum gap can exist between the streams which does not prevent the MI to grow as long as the gap is smaller than $L_{\mathrm{gap}} \cdot \frac{\omega_{pe}}{c} < 2\frac{\gamma^2-1}{\sqrt{\gamma}}$. This allows the MI to grow even for extremely large gaps if the streams are highly relativistic. In this limit, the maximum growth rate is $\Gamma_{\mathrm{max}} \approx \frac{5.48 \cdot c}{L_{\mathrm{gap}}}$.

An extreme density ratio $r \gg 1$ will reduce the current created by the electron transport across the shear surface by half and thus the increase of the magnetic field. However, this effect is negligible in the cold plasma case since the growth of the DC term is equal to the growth of either the ESKHI or the MI. Thus the increased rate of the DC magnetic field is reduced similarly to the growth of the driving instability. The limiting factors for saturation still hold true, thus $B_\perp^{\mathrm{sat}}$ is not reduced by non-equal densities.

Resulting effect on polarization and radiation power growth rate

Streams of different densities and velocity gradients between the shear interface will both reduce the growth rate. This reduces the exponential growth of the radiation power equivalently, thus allowing an astronomer to deduce the density contrast and velocity gradient right at shear interface via radiation. Furthermore, since $B_\perp^{\mathrm{sat}}$ is only weakly reduced, the reduced growth rate extends the time till saturation and therefore the duration of the linear phase

$$T_{\mathrm{real}} = T_{\mathrm{ideal}} \cdot \frac{\Gamma(0,0)}{\Gamma(r,L)} \quad , \tag{7.99}$$

with $T_{\mathrm{real}}(r,L)$ being the duration of the linear phase under realistic conditions and T_{ideal} being the duration of the linear phase of the KHI under ideal conditions as simulated in section 7.4. This increase of the duration eases the requirement on astrophysical or experimental observations since the linear phase happens fast with regard to today's observation capabilities (see following sections 7.6.2 and 7.6.3). Due to a velocity gradient, the magnetic field amplitude at saturation $B_\perp^{\mathrm{sat}}$ reduces with $\sim \tilde{L}^{-1}$. Thus even velocity gradients of several plasma skin depths will lower the DC magnetic field amplitude by not more than an order of magnitude. Due to the exponential growth of the magnetic field, the reduction of the duration of the linear phase caused by the decreased magnetic field amplitude is negligible.

The Kelvin-Helmholtz instability in the ESKHI and the MI regime even with velocity gradients and density contrasts will grow faster than either the two-stream instability or the Weibel instability under the same conditions [55]. Therefore, there are no other instabilities that will destroy the characteristic radiation signature caused by the DC field of the KHI. However, the reduction in growth rate and thus the reduction in radiation power might make identifying the start of the linear phase against the background radiation from the rest of the plasma stream and other radiation sources more difficult.

According to the numeric study of the degree of polarization (Fig. 7.5), the polarization depends on both the growth rate Γ driving the magnetic field on the shear surface and the Lorentz factor of the electrons in the stream. A density contrast $r = {}^{n_+}/_{n_-}$ will change the characteristic polarization slightly due to the decreased growth rate. A velocity gradient will further alter the characteristic polarization slightly due to the growth rate as well. Additionally, the degree of polarization is altered due to the reduced Lorentz factor γ across the shear with a velocity gradient. However, the characteristic polarization is only slightly modified due to changes in Γ or γ, thus the effect is marginal and does not hinder detection.

7.6.2 Observation in jets from active galactic nuclei

Jets from active galactic nuclei (AGN) are expected to have Lorentz factors between $\gamma = 10^1 - 10^3$ [29]. The ambient medium, through which these jets propagate, have a density of approximately $n_A = 10^{-4} - 10^{-3}\,\mathrm{cm}^{-3}$ while the jets themselves vary in density between $n_J = 10^{-5} - 10^{-2}\,\mathrm{cm}^{-3}$. In the case of highly relativistic shear velocities and a significantly higher density of the environmental plasma than that of the (Lorentz contracted) jet plasma in the observation frame

$$\gamma \gg 1 \qquad \textit{and} \qquad n_a \gg \frac{n_j}{\gamma} \quad , \tag{7.100}$$

the MI growth rates is $\Gamma_{\mathrm{max}} = {}^{\omega_{pe}(n_J)}/_{\sqrt{2\gamma}}$ [228]. For nearly all possible density ratios, the presumption (Eq. 7.100) is fulfilled, and the mushroom instability will grow with the same growth rate in units of the plasma frequency. An additional shear velocity width $(\tilde{L})$ of the order of one plasma skin depth would reduce the growth rate of the ESKHI further by a factor $c_3 = 0.2$ [55]. A similar reduction is a sound assumption for the MI.

Assuming that the (normalized) duration of the linear phase is equivalent to the idealized setup of the KHI, independent of the Lorentz factor, we assume the idealized duration to be $T = 19\omega_{pe}^{-1}$ as in the simulation. This duration decreases according to Eq. 7.99 by a factor

$$T_{\mathrm{real}} = T_{\mathrm{ideal}} \cdot \frac{\Gamma_{\mathrm{ideal}}}{\Gamma_{\mathrm{real}}} = T_{\mathrm{ideal}} \cdot \frac{\beta_S \gamma_S^{-1/2}}{{}^{1}/_{\sqrt{2\gamma_J}} \cdot c_3} \tag{7.101}$$

with $\gamma_S = 3$ being the Lorentz factor of the reference simulation, β_S the according to normalized velocity and γ_J the Lorentz factor of the jet. Additionally, the observed duration T' by an observer on Earth is extended by γ_J due to time dilatation, neglecting any additional change due to relative motion between the AGN and the observer. The observation duration depends only on the jet density and its Lorentz factor. For an exemplary jet of $\gamma_J = 200$ and a jet density of $n_J = 10^{-4}\,\mathrm{cm}^{-3}$, the observed duration on Earth is $T' > 6\,\mathrm{min}$. Various observation durations are plotted in Fig. 7.14 for γ_J and n_J values expected for AGN jets.

Since today's astronomical observation networks have response times of around two minutes [50], the durations for jets with $\gamma \gtrsim 30$ are in a range, where not only a single telescope can observe the polarization but others could react and allow precise polarization and radiation power measurements.

According to Eq. 7.93, the characteristic radiation as simulated would be in the lower radio frequency range. Similar scalings are expected from other astrophysical jets both interstellar and from other galaxies, like bipolar outflow from cataclysmic variable star [243] or gamma-ray bursts [244].

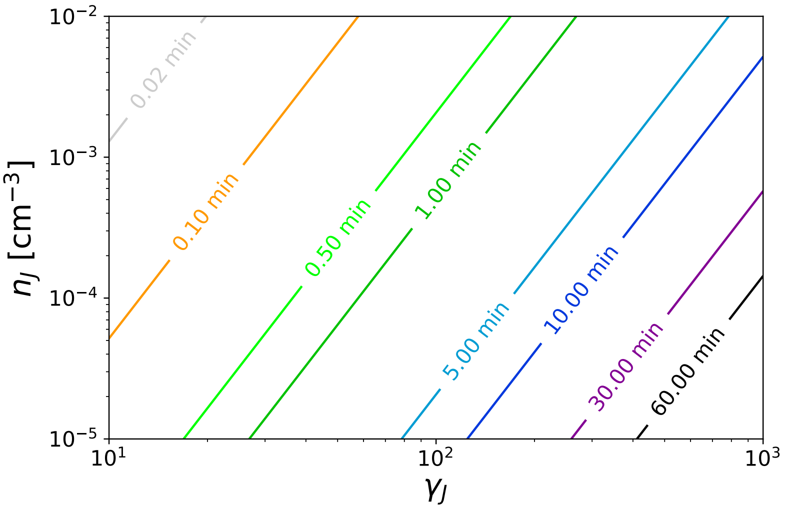

Figure 7.14: **Expected observation duration of the linear phase of the KHI (in the MI regime)** A contour plot marks various expected observation duration for various Lorentz factors γ_J of the plasma jet and densities n_J expected for AGN jets. The observed duration of the linear phase for $\gamma_J \gtrsim 30$ is well in the range of today's observation capabilities.

7.6.3 Observation in lab experiments

The Kelvin-Helmholtz instability does not only occur in astrophysical jets. Recent laser plasma experiments [230, 231] observed this instability. Their goal was to drive two plasma jets, generated by laser foil irradiation against each other, to study shearing similar to those occurring in astronomical jets. The fastest material in these experiments reaches $v_0 = 25\,\mathrm{km/s} \approx 8 \cdot 10^{-5} \cdot c$. At these low velocities, the KHI is driven by the ESKHI mechanism, with expected growth rates of $\Gamma = \frac{1}{\sqrt{8}}\omega_{pe}$. At densities around $n_e \sim 10^{17}\,\mathrm{cm}^{-3}$, this leads to an observation duration around $T' = 8.6, \mathrm{ps}$ according to Eq. 7.99. The frequency range of interest for the KHI signature is expected to be $\omega \approx 1 - 10^2\omega_{pe}$. For this non-relativistic setup, the radiation is expected to have a wavelength in the near to long-wavelength infrared with wavelengths of $\lambda \sim 1 - 10\,\mu\mathrm{m}$.

With increasing laser power, the plasma slabs generated in these experiments start reaching relativistic velocities. The observation time will increase and the observation wavelength will decrease.

Exemplarily, an experimental setup is assumed that would correspond to the simulation presented in section 7.4. When converted into the lab frame, the simulation modeled a plasma stream with Lorentz factor $\gamma' = 17$. This can be determined by the relativistic velocity summation $\beta' = \frac{2\beta}{1+\beta^2}$, with $\beta = \sqrt{1 - {}^1\!/\!{}_{\gamma^2}}$ being the shear velocity simulated. Assuming again a shear gradient on the plasma skin depth, the growth rate decreases by $c_3 = 0.2$. Including both time dilatation and the reduction due to the shear gradient, the observed duration of the linear phase becomes $T' = T \cdot \gamma' \cdot c_3^{-1} \approx 90\,\mathrm{ps}$. Lorentz transforming the frequency range according to Eq. 7.93 leads to a radiation signature at $\lambda \approx 300\mathrm{nm} - 3\mathrm{nm}$ which is in the ultraviolet to X-ray range.

Both the expected wavelength at which the KHI signature can be observed and the expected duration of the linear phase, observed in the lab, are depicted for various Lorentz factors γ of the plasma stream shearing on a quasi-stationary plasma in Fig. 7.15.

For this calculation, the maximum growth rate of either the ESKHI (Eq. 7.14) or the MI (Eq. 7.21), depending on the Lorentz factor, was used. The green range in Fig. 7.15 covers frequencies

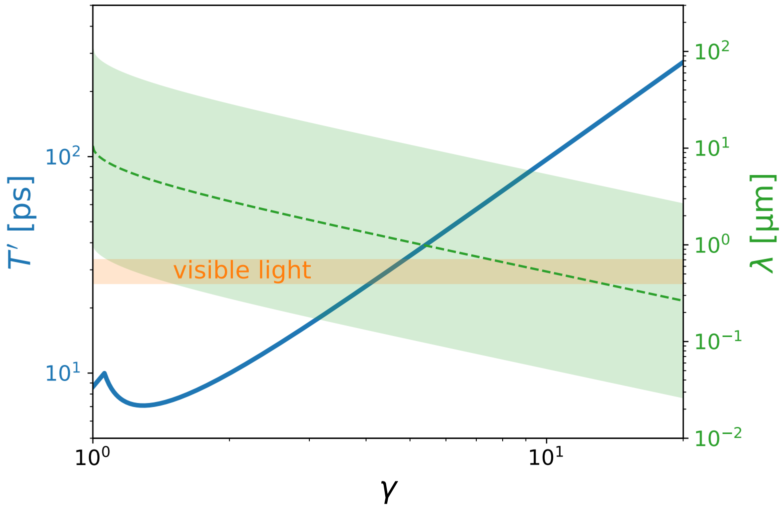

Figure 7.15: **Expected observation duration and emitted wavelength in experiments:** The expected observation duration T' of the linear phase of the KHI for Lorentz factors γ of plasma streams generated in the lab is plotted in blue. Additionally, the wavelength λ of the radiation signature is plotted. The lower wavelength limit of this radiation is a soft limit and can extend further out. At the upper wavelength limit, the radiation will not leave the plasma. The range of visible light is marked in orange.

starting from ω_{pe} to $\sim 100\omega_{pe}$. With slightly relativistic streams, the radiation signature will become observable with today's diagnostic methods [245–247], which allows not only identifying the KHI via proton radiography [230] but measuring its growth rate via radiation and thus determining plasma properties like shear and density gradients that have previously not been measurable.

7.7 Summary and Outlook

With the large-scale simulation presented [R1, R3] we were able to simulate the relativistic Kelvin-Helmholtz instability in the mushroom instability regime at unprecedented spatial and temporal resolution. In combination with computing the emitted radiation, this allowed studying the electromagnetic emission from the KHI during its linear phase for the first time [R4]. By modeling the electron dynamics in the exponentially growing DC magnetic field on the shear surface we derived an analytical model of the radiation power evolution and a semi-analytical model of the degree of polarization. This model was validated against the large-scale particle-in-cell simulation, thus verifying that the predicted polarization signature was clearly observable and not covered by jitter radiation coming from the bulk of the plasma streams. The simulation furthermore demonstrated that the radiation growth rate scales with the same growth rate as the DC magnetic field driven by the shear instability despite thermalization processes in the initially cold bulk of the plasma streams generating initially stronger magnetic fields than the Kelvin-Helmholtz instability. This is beyond the capabilities of state-of-the-art magnetic field measurements in astronomy, that rely on the Faraday rotation, which integrates the magnetic field along the line of sight from radiation sources behind the plasma jet and thus would take magnetic fields generated in the bulk of the plasma into account [48, 49]. In [R4], we demonstrated that the characteristic polarization of the KHI survives Lorentz transformation and leads to a characteristic polarization anisotropy during the linear phase. Possible scenarios of observations in both active galactic nuclei (AGN) and laboratory experiments using laser-plasma interactions were demonstrated and limits on observation duration and wavelength ranges were quantified for non-ideal shearing geometries.

Identifying the linear phase of the KHI and measuring its growth rate allows drawing conclusions on shear geometries, velocity gradients, and density contrasts. Quantifying these jet parameters via measuring the polarized radiation is vital for improving the understanding of these galactic jets. The polarization signature discovered is ideally suited for distinguishing the KHI radiation from isotropically polarized radiation background. Since the orientation under a Lorentz transformation is parallel to the magnetic field orientation ($B_\perp$), the orientation of the shear interface can be determined. With improvements in observational capabilities [34, 248, 249] even mapping complex jet-within-a-jet geometries [244] will become possible.

8 Summary

Two novel diagnostic methods for the characterization of plasma states and for the quantification of essential parameters were presented. Both methods allow determining the dynamics of the plasma which could not be detected so far. These radiation signatures based on synthetic diagnostics represent a novel approach in plasma simulation. By extending the simulation with simultaneous in-situ diagnostics, quantitative predictions for possible experimental measurements or astronomical observations are possible which allow a direct insight into the dynamics.

For laser wakefield acceleration (LWFA), occurring on micrometer scales, a spectral radiation signature was discovered that allows identifying the occurrence of the blowout regime during the laser pulse defocusing. This enables not only to decide whether and when the laser has reached the blowout regime, aspired in many experiments, but also to measure the laser focus in the plasma with an accuracy of approximately $100\,\mu\mathrm{m}$ for every laser shot.

Analogous to the study of laser wakefield acceleration, a radiation signature for the relativistic Kelvin-Helmholtz instability (KHI) was discovered. This polarization-based signature allows identifying the linear phase of the instability which is responsible for the generation of strong magnetic fields in stellar and interstellar plasma jets. Furthermore, the growth rate of the Kelvin-Helmholtz instability can be determined by measuring the increase in radiation power during the linear phase.

For both scenarios, a simple model was formulated to describe the emitted radiation. In the case of LWFA, a general scattering model was developed that only required an electron distribution around the laser pulse as input. This model can not only describe the blowout signature but is universal enough to explain other scatter signatures as well. In the case of the KHI, the driving magnetic field development was used as a basis to describe the microscopic particle dynamics on the shear surface. Based on the derived particle dynamics, the evolution of radiation and its characteristic polarization could be predicted.

At both the LWFA and the KHI, the predictions of the models were tested against a large-scale particle-in-cell simulation. While the KHI showed excellent agreement between simulation and model, the LWFA simulation showed an asymmetry in the emitted power with regard to the longitudinal focus position during the blowout regime that could not be described by the quasi-static scatter model. The predictive power of the KHI polarization signature was surprising since the radiation signature allowed the identification of the linear phase and the determination of the growth rate despite the radiation from the bulk of the jet. Thus, the simulation could provide convincing evidence that the predictions of the model remain valid even when taking into account the particles outside the shear surface, which would not have been possible with the microscopic model alone. The asymmetry of the spectral blowout signature, on the other hand, clearly showed the limits of the quasi-static model and made it evident that the usually assumed static form of the laser is only an approximation that reaches its limits in this case. The particle-in-cell simulation showed that the laser pulse evolution has an undeniable influence on the scattered radiation. The radiation intensity is significantly stronger when the laser pulse defocuses and widens the bubble than when the pulse focuses, and the bubble size decreases. Due to this influence, the spectral blowout signature starts only after the laser defocuses and thus allows a precise determination of the laser focus position in the plasma. This enables the relativistic self-focusing of the laser, which could previously only be modeled by PIC codes, to be measured experimentally. As with the KHI, the LWFA simulation showed that the predicted signature clearly differs from the background radiation.

For both the simulation of the relativistic KHI and the LWFA simulations enormous computing capacities had to be used to model the plasma dynamics with sufficiently high spatial and temporal resolution and to calculate the spectrally resolved radiation. While the LWFA radiation simulation could be carried out by continuously repeated restarts on the Taurus cluster of the Center for Information Services and High-Performance Computing (ZIH) at the Technische Universität Dresden over several months, it was not possible to run the simulation of the relativistic KHI at the ZIH due to its size. This simulation was carried out on the largest cluster in the world at that time, the Titan Cluster of Oak Ridge National Lab. Only with their 18,000 GPUs, it became possible to simulate the relativistic KHI in a resolution that has never been achieved before and to compute, for the first time, the emitted far-field radiation. Since such an unprecedented highly efficient and highly resolved simulation of the KHI had not been carried out before, this simulation was considered for the renowned Gordon Bell Prize 2013 as one of 6 finalists. Furthermore, it was awarded the HZDR Technology and Innovation Award in 2013. While plasma and radiation simulations were very computationally challenging for both the LWFA and KHI simulation, the subsequent analysis of the tremendous amounts of data produced was equivalently time-consuming.

As already mentioned, these simulations provided not only a validation of the models but also estimates on the observability of the discovered radiation signatures against influences neglected by the simple models and concurrent background radiation like additional plasma waves or thermal quivering. This consideration of other factors by simulating the radiation of all modeled particles is a crucial criterion for quantitative predictions of synthetic diagnostics for both experiments and astrophysical observations. Without consideration of all parasitic sources of radiation, it would not have been possible to make a statement as to whether the polarization signature of the linear phase of the KHI could also be differentiated by observers on Earth with regard to the signal to noise ratio. Nor would it have been possible to estimate how strongly the laser scattering from the less intense peripheries of the pulse covered the signature of the blowout regime. Conducting these simulations was thus a crucial step in testing the feasibility for future experimental and astronomical observation.

Finally, these simulations would not have been possible without the numerous improvements and extensions of the particle-in-cell code and the radiation plug-in. Without the modeling of the coherent and incoherent radiation of the macroparticles, a quantitative statement, as it is essential for the determination of observability, would not have been possible. Without the introduction of spatial filters, the influence of the simulation box would strongly influence the spectra. Within the scope of this thesis, these and many other technical improvements were incorporated into the PIC code PIConGPU, which made these comprehensive simulations possible.

9 Outlook: future applications for small- and large-scale plasmas

The use of synthetic radiation diagnostics for the identification of appropriate radiation signatures is by no means complete with this work. This work presents only two initial, at first glance very different but physically equivalently treatable scenarios in which radiation signatures were discovered for future observations. Further scenarios, especially from the laser-plasma interaction, are waiting to be studied.

These could include radiation signatures for surface instabilities generated during laser foil irradiation, which could potentially be found in the intensity variations of the reflected peaks during high harmonics generation [201, 250–252]. First preliminary simulations already showed promising results, but for a thorough investigation, more computational resources will be required and more advanced algorithms will be needed for the particle-in-cell simulation to avoid recently discovered numerical artifacts when simulating higher harmonics with finite difference time domain field solvers such as the Yee solver [253].

Recent experiments have shown that for overdense $\omega_{\mathrm{pe}} > \omega_0$ targets of limited transverse size, the passing laser imprints on the proton distribution accelerated during the laser target irradiation [R19]. This could potentially be used for proton beam manipulation and optimization as needed for medical application in cancer treatment. Due to the low rear-side plasma density with varying degree of ionization, it is difficult for a probing approach to identify the alleged electron diffusion and resulting electric field generation as the cause for the field formation responsible for the shaping. However, the plasma electrons' radiation could potentially self-indicate the origin of the imprint process. Modeling the radiation and identifying a signature could be possible in a similar manner using the in-situ radiation diagnostics presented here.

Another field in which the use of synthetic radiation diagnostics has already been successfully demonstrated but where extensive studies would still be of interest is the nonlinear Thomson scattering of electron bunches on laser pulses [R6]. The cited simulations carried out by the author during this thesis have revealed discrepancies in the experimental assumptions on electron beam dynamics that could be attributed to the Earth's magnetic fields. As in the case of the LWFA, synthetic radiation diagnostics has been able to enhance the understanding of the experiment.

Moreover, it is essential to further expand the already established close collaboration between experiment and simulation within the scope of laser wakefield acceleration. This cross-fertilizing collaboration not only allows identifying errors in the experimental setup quickly and deepening the understanding of laser plasma dynamics, but it also enables a unique validation of the simulation based on real experiments which provides confidence in the simulation even in other fields. Thanks to the synthetic radiation diagnostics presented here, a quantitative comparison comes into reach.

The same intensification of cooperation is also necessary when modeling experiments with simulations. While in most simulations today laser pulses are assumed to be Gaussian, the studies presented in this thesis have already shown that realistic modeling has a significant influence on the results of the simulation. But a real laser pulse is not yet fully described by higher Laguerre modes. The laser spectrum, chirp, and other effects will probably also have a significant impact on the plasma dynamics [R12] and should, therefore, be modeled in future simulations. Close cooperation with the experiment is necessary to determine the experimental parameters precisely enough that they can be used in simulations since scanning a poorly determined experimental parameter over its range of uncertainty is a very time-consuming process for simulations. Currently, an experimental setup is being developed at the HZDR which, by using the Wizzler diagnostic method [212–214], automatically determines the laser spectrum and temporal profile for each shot and which will provide precise input parameters for simulations.

Furthermore, with increasing laser power, experiments will reach a regime where radiation reaction will be important when modeling the laser-plasma interaction. With the now included radiation reaction pusher algorithm, radiation signatures that reveal these radiation losses are of particular interest. Simulation studies that combine both the synthetic radiation diagnostics and the radiation damping will become more and more relevant in the near future.

By extending synthetic radiation diagnostics to electron oscillations on time scales shorter than the iteration period of the PIC algorithm by externally emulating theses fast oscillations, the photon scattering of X-ray probe lasers could be modeled as well [254–257]. This would enable predicting scatter images as they will be measured during upcoming experiments at the XFEL for temporally resolving the plasma dynamics during laser foil irradiation. In contrast to all previous methods of computing these scattering images, this approach would be based on Liénard-Wiechert potentials and thus automatically include spectral shifts due to electron dynamics. Therefore, this method extends current predictions which are based on static electron distributions. Thereby the limitation of the predictive capabilities of the scattering method due to spectral broadening become obvious, but at the same time, providing estimates about the electron dynamics based on this spectral broadening becomes possible. The physically more correct approach used in PIConGPU would thus enable better quantitative predictions for XFEL experiments than the previously used static-scattering models.

A number of plasma instabilities of relevance for astrophysics would also be of interest for further investigations. For example, for the Weibel instability spectra have already been calculated for individual electron trajectories [52, 103, 104, 106, 109, 258, 259], but there has been no comprehensive study of the background radiation yet. Such a thorough investigation of the radiation of Weibel instability would be possible with the radiation plug-in.

Another current application of synthetic radiation calculation can be found in the development of modern compact radiation sources such as the Traveling Wave Thomson Scattering (TWTS) [174, R13–R17, R20, 260]. This scheme achieves a significantly more effective laser electron bunch overlap by pulse-front tilting the laser. Thus, it is capable of significantly increasing the power of the emitted radiation through coherent superposition. Extensive simulations are currently running to study this so far purely theoretical concept with simulations before experiments are assembled.

The established feedback loop between experiment and simulation will stimulate both sides in the long run and increase the confidence in the theoretical prediction capabilities of particle-in-cell simulations and at the same time increase the in-depth comprehension of experiments simulated with these codes. The synthetic radiation diagnostics poses an essential step to realize these cross-checks between simulation and experiments. The experience from studying synthetic radiation provides the basis for extending the predictive capabilities of PIConGPU to other fields such as laboratory astrophysics or plasma based light sources in the near future.

A worthwhile longer-term goal would be developing reconstruction methods that solve the inverse problem and enable reconstructing the particle dynamics from radiation directly. Such a task would require the development of reliable phase-retrieval algorithms beyond what is technically feasible right now. The in-situ radiation calculation, presented in this thesis, could provide synthetic data for both estimating the capabilities and limits of such algorithms, similar to reconstruction algorithms for coherent transition radiation already developed today [R5], and providing training data for machine learning algorithms.

Glossary

ADK	tunnel ionization model developed by Ammosov, Delone, and Krainov
AGN	active galactic nuclei
BSI	barrier suppression ionization model
CCD	charge-coupled device
CERN	European Organization for Nuclear Research
CFL	Courant–Friedrichs–Lewy condition
CIC	cloud-in-cell macroparticle shape
CPU	central processing unit
DC	direct current - in the context of KHI: not oscillating
DRACO	Dresden laser acceleration source
EOS	European Southern Observatory
ESKHI	electron-scale Kelvin-Helmholtz instability
FDTD	finite-difference-time-domain method
FWHM	full width at half maximum
GDD	group dispersion delay
GPU	graphics processing unit
HDF5	a hierarchical data format
HPC	high-performance computing
HZDR	Helmholtz-Zentrum Dresden - Rossendorf
ILC	international linear collider
KHI	Kelvin-Helmholtz instability
LEP	Large Electron-Positron Collider

LWFA	laser wakefield acceleration
MD	molecular dynamics
MHD	magnetohydrodynamic
MI	mushroom instability
NGC	new general catalogue of nebulae and clusters of stars
NVIDIA	a company specialized in developing and producing GPUs
PIC	particle-in-cell
PIConGPU	particle-in-cell code developed at HZDR
PWFA	plasma wakefield acceleration
QED	quantum electrodynamics
RAM	random-access memory
RF	radio-frequency
RGB	Red Green Blue color space
RLL	reduced Landau Lifshitz particle pusher
SLFO	side lobe fall off
STII	self-truncated ionization-injection
TSC	triangular-shaped macroparticle shape
TWEAC	Traveling-Wave Electron Acceleration
TWTS	Traveling-Wave Thomson Scattering
VLBA	Very Long Baseline Array
VLT	Very Large Telescope
XFEL	European X-Ray Free-Electron Laser Facility
ZIH	center for information service and high-performance computing of the TU Dresden

Publications during this Ph.D. project

[R1] M Bussmann, H Burau, TE Cowan, A Debus, A Huebl, G Juckeland, T Kluge, WE Nagel, **R Pausch**, F Schmitt, U Schramm, J Schuchart, and R Widera. „Radiative signatures of the relativistic Kelvin-Helmholtz instability“. In: *SC '13 Proceedings of the International Conference for High Performance Computing, Networking, Storage and Analysis*. 2013, pp. 5–1 – 5–12. ISBN: 978-1-4503-2378-9. DOI: `10.1145/2503210.2504564` (cit. on pp. 2, 6, 16, 20, 24, 26, 73, 99, 104, 106, 112, 113, 129).

[R2] JP Couperus, **R Pausch**, A Köhler, O Zarini, JM Krämer, M Garten, A Huebl, R Gebhardt, U Helbig, S Bock, K Zeil, A Debus, M Bussmann, U Schramm, and A Irman. „Demonstration of a beam loaded nanocoulomb-class laser wakefield accelerator“. In: *Nature Communications* 8 (2017), p. 487. ISSN: 2041-1723. DOI: `10.1038/s41467-017-00592-7` (cit. on pp. 3, 24, 47, 48, 60, 70, 86, 88–90).

[R3] A Huebl, D Pugmire, F Schmitt, **R Pausch**, and M Bussmann. „Visualizing the Radiation of the Kelvin-Helmholtz Instability“. In: *IEEE Transactions on Plasma Science* 42.10 (2014), pp. 2638–2639. ISSN: 0093-3813. DOI: `10.1109/TPS.2014.2327392`. arXiv: `1404.2507` (cit. on pp. 6, 24, 104, 106, 129).

[R4] **R Pausch**, M Bussmann, A Huebl, U Schramm, K Steiniger, R Widera, and A Debus. „Identifying the linear phase of the relativistic Kelvin-Helmholtz instability and measuring its growth rate via radiation“. In: *Physical Review E* 96.1 (2017), p. 013316. ISSN: 2470-0045. DOI: `10.1103/PhysRevE.96.013316` (cit. on pp. 6, 24, 100, 106, 109, 117, 129).

[R5] O Zarini, A Köhler, J Couperus, **R Pausch**, T Kurz, S Schöbel, H Meißner, M Bussmann, U Schramm, A Irman, and A Debus. „Advanced methods for temporal reconstruction of modulated electron bunches“. In: *2018 IEEE Advanced Accelerator Concepts Workshop, ACC 2018 - Proceedings* (2018), pp. 1–5. DOI: `10.1109/AAC.2018.8659388` (cit. on pp. 10, 135).

[R6] JM Krämer, A Jochmann, M Budde, M Bussmann, JP Couperus, TE Cowan, A Debus, A Köhler, M Kuntzsch, A Laso García, U Lehnert, P Michel, **R Pausch**, O Zarini, U Schramm, and A Irman. „Making spectral shape measurements in inverse Compton scattering a tool for advanced diagnostic applications“. In: *Scientific Reports* 8.1 (2018), p. 1398. ISSN: 2045-2322. DOI: `10.1038/s41598-018-19546-0` (cit. on pp. 10, 133).

[R7] A Debus, **R Pausch**, A Huebl, K Steiniger, R Widera, TE Cowan, U Schramm, and M Bussmann. „Circumventing the Dephasing and Depletion Limits of Laser-Wakefield Acceleration“. In: *Physical Review X* 9.3 (2019), p. 031044. ISSN: 2160-3308. DOI: `10.1103/PhysRevX.9.031044` (cit. on pp. 24, 58).

[R8] **R Pausch**, A Debus, R Widera, K Steiniger, A Huebl, H Burau, M Bussmann, and U Schramm. „How to test and verify radiation diagnostics simulations within particle-in-cell frameworks“. In: *Nuclear Instruments and Methods in Physics Research, Section A: Accelerators, Spectrometers, Detectors and Associated Equipment* 740 (2014), pp. 250–256. ISSN: 0168-9002. DOI: 10.1016/j.nima.2013.10.073 (cit. on pp. 25, 29, 30, 38, 67).

[R9] **R Pausch**, H Burau, M Bussmann, JP Couperus, TE Cowan, A Debus, A Huebl, A Irman, A Köhler, U Schramm, K Steiniger, and R Widera. „Computing angularly-resolved far field emission spectra in particle-in-cell codes using GPUs“. In: *Proceeding of IPAC2014*. Vol. MOPRI069. 2014, pp. 761–764. ISBN: 978-3-95450-132-8. DOI: 10.18429/JACoW-IPAC2014-MOPRI069 (cit. on pp. 26, 45, 67, 117).

[R10] **R Pausch**, A Debus, A Huebl, U Schramm, K Steiniger, R Widera, and M Bussmann. „Quantitatively consistent computation of coherent and incoherent radiation in particle-in-cell codes - A general form factor formalism for macro-particles“. In: *Nuclear Instruments and Methods in Physics Research Section A: Accelerators, Spectrometers, Detectors and Associated Equipment* 909 (2018), pp. 419–422. ISSN: 0168-9002. DOI: 10.1016/j.nima.2018.02.020. arXiv: 1802.03972 (cit. on pp. 34, 38).

[R11] U Schramm, M Bussmann, A Irman, M Siebold, K Zeil, D Albach, C Bernert, S Bock, F Brack, J Branco, JP Couperus, TE Cowan, A Debus, C Eisenmann, M Garten, R Gebhardt, S Grams, U Helbig, A Huebl, T Kluge, A Köhler, JM Krämer, S Kraft, F Kroll, M Kuntzsch, U Lehnert, M Loeser, J Metzkes, P Michel, L Obst, **R Pausch**, M Rehwald, R Sauerbrey, HP Schlenvoigt, K Steiniger, and O Zarini. „First results with the novel petawatt laser acceleration facility in Dresden“. In: *Journal of Physics: Conference Series - Proceedings of IPAC2017*. Vol. 874. 1. 2017, pp. 48–52. DOI: 10.1088/1742-6596/874/1/012028 (cit. on pp. 40, 54, 59, 60, 64, 70, 88).

[R12] A Irman, JP Couperus, A Debus, A Köhler, JM Krämer, **R Pausch**, O Zarini, and U Schramm. „Improved performance of laser wakefield acceleration by tailored self-truncated ionization injection“. In: *Plasma Physics and Controlled Fusion* 60.4 (2018), p. 044015. ISSN: 0741-3335. DOI: 10.1088/1361-6587/aaaef1 (cit. on pp. 47, 48, 86, 88, 89, 98, 134).

[R13] K Steiniger, R Widera, **R Pausch**, A Debus, M Bussmann, and U Schramm. „Wave optical description of the Traveling-Wave Thomson-Scattering optical undulator field and its application to the TWTS-FEL“. In: *Nuclear Instruments and Methods in Physics Research, Section A: Accelerators, Spectrometers, Detectors and Associated Equipment* 740 (2014), pp. 147–152. ISSN: 0168-9002. DOI: 10.1016/j.nima.2013.10.091 (cit. on pp. 58, 134).

[R14] K Steiniger, A Debus, A Irman, A Jochmann, **R Pausch**, U Schramm, TE Cowan, and M Bussmann. „All-optical Free Electron Lasers using Travelling-wave Thomson Scattering“. In: *Proceeding of IPAC2014*. Vol. WEPRO053. 2014, pp. 2065–2068. ISBN: 978-3-95450-132-8. DOI: 10.18429/JACoW-IPAC2014-WEPRO053 (cit. on pp. 58, 134).

[R15] K Steiniger, M Bussmann, **R Pausch**, TE Cowan, A Irman, A Jochmann, R Sauerbrey, U Schramm, and A Debus. „Optical free-electron lasers with Traveling-Wave Thomson-Scattering“. In: *Journal of Physics B: Atomic, Molecular and Optical Physics* 47.23 (2014), p. 234011. ISSN: 0953-4075. DOI: 10.1088/0953-4075/47/23/234011 (cit. on pp. 58, 134).

[R16] K Steiniger, A Debus, A Irman, A Jochmann, **R Pausch**, U Schramm, and M Bussmann. „Brilliant and efficient optical free-electron lasers with traveling-wave Thomson-Scattering“. In: *AIP Conference Proceedings*. Vol. 1777. 2016, p. 080016. ISBN: 978-0-73541-439-6. DOI: 10.1063/1.4965673 (cit. on pp. 58, 134).

[R17] K Steiniger, D Albach, M Bussmann, M Loeser, **R Pausch**, F Röser, U Schramm, M Siebold, and A Debus. „Building an Optical Free-Electron Laser in the Traveling-Wave Thomson-Scattering Geometry“. In: *Frontiers in Physics* 6 (2019), p. 155. ISSN: 2296-424X. DOI: `10.3389/fphy.2018.00155` (cit. on pp. 58, 134).

[R18] A Martinez de la Ossa, RW Assmann, M Bussmann, S Corde, JP Couperus Cabadağ, A Debus, A Döpp, A Ferran Pousa, MF Gilljohann, T Heinemann, B Hidding, A Irman, S Karsch, O Kononenko, T Kurz, J Osterhoff, **R Pausch**, S Schöbel, and U Schramm. „Hybrid LWFA–PWFA staging as a beam energy and brightness transformer: conceptual design and simulations“. In: *Philosophical Transactions of the Royal Society A: Mathematical, Physical and Engineering Sciences* 377.2151 (2019), p. 20180175. ISSN: 1364-503X. DOI: `10.1098/rsta.2018.0175` (cit. on p. 86).

[R19] L Obst-Huebl, T Ziegler, FE Brack, J Branco, M Bussmann, TE Cowan, CB Curry, F Fiuza, M Garten, M Gauthier, S Göde, SH Glenzer, A Huebl, A Irman, JB Kim, T Kluge, SD Kraft, F Kroll, J Metzkes-Ng, **R Pausch**, I Prencipe, M Rehwald, C Roedel, HP Schlenvoigt, U Schramm, and K Zeil. „All-optical structuring of laser-driven proton beam profiles“. In: *Nature Communications* 9 (2018), p. 5292. ISSN: 2041-1723. DOI: `10.1038/s41467-018-07756-z` (cit. on p. 133).

[R20] U Schramm, M Bussmann, JP Couperus, TE Cowan, A Debus, A Irman, A Jochmann, **R Pausch**, R Sauerbrey, and K Steiniger. „Bright X-ray Pulse Generation by Laser Thomson-Backscattering and Traveling Wave Optical Undulators“. In: *Frontiers in Optics 2014*. Optical Society of America, 2014, FTu4G.2. ISBN: 1-55752-286-3. DOI: `10.1364/FIO.2014.FTu4G.2` (cit. on p. 134).

References

[1] E Esarey, CB Schroeder, and WP Leemans. „Physics of laser-driven plasma-based electron accelerators“. In: *Reviews of Modern Physics* 81.3 (2009), pp. 1229–1285. ISSN: 0034-6861. DOI: `10.1103/RevModPhys.81.1229` (cit. on pp. 1, 3, 15, 48, 49, 54, 55, 57–60).

[2] A Macchi, M Borghesi, and M Passoni. „Ion acceleration by superintense laser-plasma interaction“. In: *Reviews of Modern Physics* 85.2 (2013), p. 751. ISSN: 0034-6861. DOI: `10.1103/RevModPhys.85.751`. arXiv: `1302.1775` (cit. on pp. 1, 15).

[3] FF Chen. *Introduction to plasma physics*. 2nd. New York: Plenum Pr., 2006. ISBN: 0-306-41332-9 (cit. on pp. 1, 4, 5, 51, 101).

[4] MA Lieberman and AJ Lichtenberg. *Principles of plasma discharges and materials processing*. New York: John Wiley and Sons, Inc., 1994. ISBN: 0-471-00577-0 (cit. on p. 1).

[5] A Piel. *Plasma Physics - An Introduction to Laboratory, Space, and Fusion Plasmas*. Berlin Heidelberg: Springer-Verlag Berlin Heidelberg, 2010. ISBN: 978-3-642-43631-4. DOI: `10.1007/978-3-642-10491-6` (cit. on pp. 1, 4).

[6] VERITAS Collaboration, VLBA 43 GHz M87 Monitoring Team, H.E.S.S. Collaboration, and MAGIC Collaboration. „Radio Imaging of the Very-High-Energy γ-Ray Emission Region in the Central Engine of a Radio Galaxy“. In: *Science* 325.5939 (2009), pp. 444–448. ISSN: 0036-8075. DOI: `10.1126/science.1175406` (cit. on p. 1).

[7] T Tajima and JM Dawson. „Laser Electron Accelerator“. In: *Physical Review Letters* 43.4 (1979), pp. 267–270. ISSN: 0031-9007. DOI: `10.1103/PhysRevLett.43.267` (cit. on pp. 2, 47, 49, 52–54, 61).

[8] H Wiedemann. *Particle Accelerator Physics I*. Berlin, Heidelberg: Springer Berlin Heidelberg, 1999. ISBN: 978-3-662-03829-1. DOI: `10.1007/978-3-662-03827-7` (cit. on pp. 2, 47).

[9] A Grudiev, S Calatroni, and W Wuensch. „New local field quantity describing the high gradient limit of accelerating structures“. In: *Physical Review Special Topics - Accelerators and Beams* 12.10 (2009), p. 102001. ISSN: 1098-4402. DOI: `10.1103/PhysRevSTAB.12.102001` (cit. on pp. 2, 47).

[10] CGR Geddes, C Toth, J van Tilborg, E Esarey, CB Schroeder, D Bruhwiler, C Nieter, J Cary, and WP Leemans. „High-quality electron beams from a laser wakefield accelerator using plasma-channel guiding“. In: *Nature* 431.7008 (2004), pp. 538–541. ISSN: 0028-0836. DOI: `10.1038/nature02900` (cit. on pp. 2, 3, 48, 54, 57, 59).

[11] J Faure, C Rechatin, A Norlin, A Lifschitz, Y Glinec, and V Malka. „Controlled injection and acceleration of electrons in plasma wakefields by colliding laser pulses“. In: *Nature* 444.7120 (2006), pp. 737–739. ISSN: 0028-0836. DOI: `10.1038/nature05393` (cit. on p. 2).

[12] J Faure, Y Glinec, A Pukhov, S Kiselev, S Gordienko, E Lefebvre, JP Rousseau, F Burgy, and V Malka. „A laser-plasma accelerator producing monoenergetic electron beams“. In: *Nature* 431.7008 (2004), pp. 541–544. ISSN: 0028-0836. DOI: `10.1038/nature02963` (cit. on pp. 3, 48, 54, 59, 61).

[13] SPD Mangles et al. „Monoenergetic beams of relativistic electrons from intense laser-plasma interactions“. In: *Nature* 431.7008 (2004), pp. 535–538. ISSN: 0028-0836. DOI: `10.1038/nature02939` (cit. on pp. 3, 48, 54, 59).

[14] X Wang et al. „Quasi-monoenergetic laser-plasma acceleration of electrons to 2 GeV“. In: *Nature Communications* 4 (2013), p. 1988. ISSN: 2041-1723. DOI: `10.1038/ncomms2988` (cit. on pp. 3, 48).

[15] WP Leemans et al. „Multi-GeV Electron Beams from Capillary-Discharge-Guided Subpetawatt Laser Pulses in the Self-Trapping Regime“. In: *Physical Review Letters* 113.24 (2014), p. 245002. ISSN: 0031-9007. DOI: `10.1103/PhysRevLett.113.245002` (cit. on pp. 3, 48).

[16] AJ Gonsalves et al. „Generation and pointing stabilization of multi-GeV electron beams from a laser plasma accelerator driven in a pre-formed plasma waveguidea)“. In: *Physics of Plasmas* 22.5 (2015), p. 056703. ISSN: 1070-664X. DOI: `10.1063/1.4919278` (cit. on p. 3).

[17] CB Schroeder, E Esarey, CGR Geddes, C Benedetti, and WP Leemans. „Physics considerations for laser-plasma linear colliders“. In: *Physical Review Special Topics - Accelerators and Beams* 13.10 (2010), p. 101301. ISSN: 1098-4402. DOI: `10.1103/PhysRevSTAB.13.101301` (cit. on p. 3).

[18] S Steinke, J van Tilborg, C Benedetti, CGR Geddes, J Daniels, KK Swanson, AJ Gonsalves, K Nakamura, BH Shaw, CB Schroeder, E Esarey, and WP Leemans. „Staging of independent laser plasma accelerators“. In: *AIP Conference Proceedings*. Vol. 1812. 1. 2017, p. 020003. ISBN: 978-0-73541-480-8. DOI: `10.1063/1.4975839` (cit. on p. 3).

[19] JR Marquès, JP Geindre, F Amiranoff, P Audebert, JC Gauthier, A Antonetti, and G Grillon. „Temporal and Spatial Measurements of the Electron Density Perturbation Produced in the Wake of an Ultrashort Laser Pulse“. In: *Physical Review Letters* 76.19 (1996), pp. 3566–3569. ISSN: 0031-9007. DOI: `10.1103/PhysRevLett.76.3566` (cit. on p. 3).

[20] NH Matlis, S Reed, SS Bulanov, V Chvykov, G Kalintchenko, T Matsuoka, P Rousseau, V Yanovsky, A Maksimchuk, S Kalmykov, G Shvets, and MC Downer. „Snapshots of laser wakefields“. In: *Nature Physics* 2.11 (2006), pp. 749–753. ISSN: 1745-2473. DOI: `10.1038/nphys442` (cit. on p. 3).

[21] A Buck, M Nicolai, K Schmid, CMS Sears, A Sävert, JM Mikhailova, F Krausz, MC Kaluza, and L Veisz. „Real-time observation of laser-driven electron acceleration“. In: *Nature Physics* 7.7 (2011), pp. 543–548. ISSN: 1745-2473. DOI: `10.1038/nphys1942` (cit. on pp. 3, 47, 48).

[22] CJ Zhang, JF Hua, XL Xu, F Li, CH Pai, Y Wan, YP Wu, YQ Gu, WB Mori, C Joshi, and W Lu. „Capturing relativistic wakefield structures in plasmas using ultrashort high-energy electrons as a probe“. In: *Scientific Reports* 6 (2016), p. 29485. ISSN: 2045-2322. DOI: `10.1038/srep29485` (cit. on p. 3).

[23] S Corde et al. „Mapping the X-Ray Emission Region in a Laser-Plasma Accelerator“. In: *Physical Review Letters* 107.21 (2011), p. 215004. ISSN: 0031-9007. DOI: `10.1103/PhysRevLett.107.215004`. arXiv: `1104.2451` (cit. on pp. 3, 48).

[24] M Schnell et al. „Deducing the Electron-Beam Diameter in a Laser-Plasma Accelerator Using X-Ray Betatron Radiation“. In: *Physical Review Letters* 108.7 (2012), p. 075001. ISSN: 0031-9007. DOI: `10.1103/PhysRevLett.108.075001` (cit. on pp. 3, 48).

[25] CGR Geddes et al. „Low-emittance electron bunches from a laser-plasma accelerator measured using single-shot X-ray spectroscopy“. In: *AIP Conference Proceedings*. Vol. 1507. 1. 2013, pp. 278–283. ISBN: 978-0-73541-125-8. DOI: `10.1063/1.4773707` (cit. on pp. 3, 48).

[26] S Corde, C Thaury, KT Phuoc, A Lifschitz, G Lambert, O Lundh, P Brijesh, L Arantchuk, S Sebban, A Rousse, J Faure, and V Malka. „Betatron emission as a diagnostic for injection and acceleration mechanisms in laser plasma accelerators“. In: *Plasma Physics and Controlled Fusion* 54.12 (2012), p. 124023. ISSN: 0741-3335. DOI: `10.1088/0741-3335/54/12/124023`. arXiv: `1211.5365` (cit. on pp. 3, 48).

[27] S Corde, K Ta Phuoc, G Lambert, R Fitour, V Malka, A Rousse, A Beck, and E Lefebvre. „Femtosecond x rays from laser-plasma accelerators“. In: *Reviews of Modern Physics* 85.1 (2013), pp. 1–48. ISSN: 0034-6861. DOI: `10.1103/RevModPhys.85.1` (cit. on pp. 3, 54, 70).

[28] AGR Thomas, SPD Mangles, Z Najmudin, MC Kaluza, CD Murphy, and K Krushelnick. „Measurements of Wave-Breaking Radiation from a Laser-Wakefield Accelerator“. In: *Physical Review Letters* 98.5 (2007), p. 054802. ISSN: 0031-9007. DOI: `10.1103/PhysRevLett.98.054802` (cit. on pp. 3, 48, 75).

[29] A Ferrari. „Modeling Extragalactic Jets“. In: *Annual Review of Astronomy and Astrophysics* 36.1 (1998), pp. 539–598. ISSN: 0066-4146. DOI: `10.1146/annurev.astro.36.1.539` (cit. on pp. 4–6, 99, 123, 127).

[30] RAMJ Wijers et al. „Detection of Polarization in the Afterglow of GRB 990510 with the ESO Very Large Telescope“. In: *The Astrophysical Journal Letters* 523.1 (1999), pp. L33–L36. ISSN: 0004-637X. DOI: `10.1086/312262`. arXiv: `astro-ph/9906346 [astro-ph]` (cit. on p. 4).

[31] A Boccaletti, P Riaud, P Baudoz, J Baudrand, D Rouan, D Gratadour, F Lacombe, and AM Lagrange. „The Four-Quadrant Phase Mask Coronagraph. IV. First Light at the Very Large Telescope“. In: *Publications of the Astronomical Society of the Pacific* 116.825 (2004), pp. 1061–1071. ISSN: 0004-6280. DOI: `10.1086/425735` (cit. on p. 4).

[32] ESO. *Very Large Telescope*. `http://www.eso.org/public/unitedkingdom/teles-instr/paranal-observatory/vlt/`. Accessed: 2018-10-16 (cit. on p. 4).

[33] P Napier, D Bagri, B Clark, A Rogers, J Romney, A Thompson, and R Walker. „The Very Long Baseline Array“. In: *Proceedings of the IEEE*. Vol. 82. 5. 1994, pp. 658–672. DOI: `10.1109/5.284733` (cit. on p. 4).

[34] RB Wayth, WF Brisken, AT Deller, WA Majid, DR Thompson, SJ Tingay, and KL Wagstaff. „V-FASTR: the VLBA Fast Radio Transients Experiment“. In: *The Astrophysical Journal* 735.2 (2011), p. 97. ISSN: 0004-637X. DOI: `10.1088/0004-637X/735/2/97`. arXiv: `1104.4908` (cit. on pp. 4, 130).

[35] LBO. *Very Long Baseline Array*. `https://science.lbo.us/facilities/vlba`. Accessed: 2018-10-16 (cit. on p. 4).

[36] MC Weisskopf, JJ Hester, AF Tennant, RF Elsner, NS Schulz, HL Marshall, M Karovska, JS Nichols, Da Swartz, JJ Kolodziejczak, and SL O’Dell. „Discovery of Spatial and Spectral Structure in the X-Ray Emission from the Crab Nebula“. In: *The Astrophysical Journal Letters* 536.2 (2000), pp. L81–L84. ISSN: 0004-637X. DOI: `10.1086/312733` (cit. on pp. 5, 99, 123).

[37] GF Bignami, PA Caraveo, AD Luca, and S Mereghetti. „The magnetic field of an isolated neutron star from X-ray cyclotron absorption lines“. In: *Nature* 423.6941 (2003), pp. 725–727. ISSN: 0028-0836. DOI: `10.1038/nature01703` (cit. on p. 5).

[38] GRA Ellis. „Physical Sciences: Fine Structure of the Jupiter Radio Bursts“. In: *Nature* 241.5389 (1973), pp. 387–389. ISSN: 0028-0836. DOI: `10.1038/241387a0` (cit. on p. 5).

[39] GRA Ellis. „Spectra of the Jupiter radio bursts“. In: *Nature* 253.5491 (1975), pp. 415–417. ISSN: 0028-0836. DOI: `10.1038/253415a0` (cit. on p. 5).

[40] GA Dulk, Y Leblanc, and A Lecacheux. „The complete polarization state of Io-related radio storms from Jupiter: A statistical study“. In: *Astronomy and Astrophysics* 286.2 (1994), pp. 683–700. ISSN: 0004-6361 (cit. on p. 5).

[41] SJ Bolton et al. „Ultra-relativistic electrons in Jupiter's radiation belts“. In: *Nature* 415.6875 (2002), pp. 987–991. ISSN: 0028-0836. DOI: `10.1038/415987a` (cit. on p. 5).

[42] M Tavani et al. „Extreme particle acceleration in the microquasar Cygnus X-3.“ In: *Nature* 462.7273 (2009), pp. 620–623. ISSN: 0028-0836. DOI: `10.1038/nature08578`. arXiv: `0910.5344` (cit. on pp. 5, 99).

[43] JA Gaidos et al. „Extremely rapid bursts of TeV photons from the active galaxy Markarian 421“. In: *Nature* 383.6598 (1996), pp. 319–320. ISSN: 0028-0836. DOI: `10.1038/383319a0` (cit. on pp. 5, 99).

[44] Y Uchiyama, CM Urry, CC Cheung, S Jester, J Van Duyne, P Coppi, RM Sambruna, T Takahashi, F Tavecchio, and L Maraschi. „Shedding New Light on the 3C 273 Jet with the Spitzer Space Telescope“. In: *The Astrophysical Journal* 648.2 (2006), pp. 910–921. ISSN: 0004-637X. DOI: `10.1086/505964`. arXiv: `astro-ph/0605530 [astro-ph]` (cit. on pp. 5, 99).

[45] NASA/CXC/SAO. *Four Supernova Remnants: NASA's Chandra X-ray Observatory Celebrates 15th Anniversary - Crab Nebula*. `http://chandra.harvard.edu/photo/2014/15year/`. Accessed: 2018-10-16 (cit. on p. 5).

[46] M Birkinshaw. „Instabilities in astrophysical jets“. In: *Astrophysics and Space Science* 242.1-2 (1996), pp. 17–91. ISSN: 0004-640X. DOI: `10.1007/BF00645111` (cit. on pp. 5, 99).

[47] T Piran. „Magnetic Fields in Gamma-Ray Bursts: A Short Overview“. In: *AIP Conference Proceedings*. Vol. 784. AIP, 2005, pp. 164–174. ISBN: 0-73-540273-6. DOI: `10.1063/1.2077181` (cit. on pp. 5, 99).

[48] RT Zavala and GB Taylor. „Faraday Rotation Measure Gradients from a Helical Magnetic Field in 3C 273“. In: *The Astrophysical Journal Letters* 626.2 (2005), pp. L73–L76. ISSN: 0004-637X. DOI: `10.1086/431901`. arXiv: `astro-ph/0505357 [astro-ph]` (cit. on pp. 5, 99, 129).

[49] JL Gómez, M Roca-Sogorb, I Agudo, AP Marscher, and SG Jorstad. „Faraday rotation in jets of AGN: the case of 3C 120“. In: *Journal of Physics: Conference Series*. Vol. 355. 1. 2012, p. 012022. DOI: `10.1088/1742-6596/355/1/012022` (cit. on pp. 5, 99, 129).

[50] E Troja et al. „Significant and variable linear polarization during the prompt optical flash of GRB 160625B“. In: *Nature* 547.7664 (2017), pp. 425–427. ISSN: 0028-0836. DOI: `10.1038/nature23289` (cit. on pp. 5, 127).

[51] K Nishikawa, P Hardee, G Richardson, R Preece, H Sol, and GJ Fishman. „Particle Acceleration in Relativistic Jets Due to Weibel Instability“. In: *The Astrophysical Journal* 595.1 (2003), pp. 555–563. ISSN: 0004-637X. DOI: `10.1086/377260`. arXiv: `astro-ph/0305091 [astro-ph]` (cit. on p. 5).

[52] KI Nishikawa et al. „Radiation from relativistic shocks in turbulent magnetic fields“. In: *Advances in Space Research* 47.8 (2011), pp. 1434–1440. ISSN: 0273-1177. DOI: `10.1016/j.asr.2011.01.032`. arXiv: `arXiv:0906.5018v1` (cit. on pp. 5, 134).

[53] EP Alves, T Grismayer, SF Martins, F Fiúza, Ra Fonseca, and LO Silva. „Large-Scale Magnetic Field Generation Via the Kinetic Kelvin-Helmholtz Instability in Unmagnetized Scenarios“. In: *The Astrophysical Journal Letters* 746.2 (2012), p. L14. ISSN: 2041-8205. DOI: `10.1088/2041-8205/746/2/L14` (cit. on pp. 5, 15, 16, 99–102, 104, 112).

[54] T Grismayer, EP Alves, Ra Fonseca, and LO Silva. „dc-Magnetic-Field Generation in Unmagnetized Shear Flows“. In: *Physical Review Letters* 111.1 (2013), p. 015005. ISSN: 0031-9007. DOI: `10.1103/PhysRevLett.111.015005` (cit. on pp. 5, 100, 104, 106, 115, 120).

[55] E P Alves, T Grismayer, R A Fonseca, and L O Silva. „Electron-scale shear instabilities: magnetic field generation and particle acceleration in astrophysical jets“. In: *New Journal of Physics* 16.3 (2014), p. 035007. ISSN: 1367-2630. DOI: `10.1088/1367-2630/16/3/035007`. arXiv: `1404.0555` (cit. on pp. 6, 99, 101, 102, 104, 120, 125–127).

[56] P Gibbon. *Short Pulse Laser Interactions with Matter*. London: Imperial College Press, 2005. ISBN: 978-1-86094-135-1. DOI: `10.1142/p116` (cit. on pp. 6, 15, 27, 51).

[57] EP Alves. „Microphysical plasma processes: in silico studies and a route to the required laser intensities for laboratory exploration“. PhD thesis. Universidade de Lisboa, 2015 (cit. on pp. 6, 101–103).

[58] RP Feynman, RB Leighton, and M Sands. *The Feynman Lectures on Physics Vol. II*. 6th. Reading, MA: Addison-Wesley Publishing Company, 1964. ISBN: 0-201-02117-X (cit. on pp. 7, 40, 123).

[59] JD Jackson. *Classical Electrodynamics*. Third. New York: John Wiley and Sons, Inc., 1998. ISBN: 0-471-30932-X (cit. on pp. 7–9, 11, 12, 25, 39–41, 43, 65, 66, 101, 109, 111, 118, 122).

[60] K Wille. *Synchrotron Radiation*. `https://indico.cern.ch/event/218284/contributions/1520454/attachments/352184/490697/JUAS2013_Synchrotron_Radiation_1.pdf`. 2008 (cit. on p. 8).

[61] R Pausch. „Electromagnetic Radiation from Relativistic Electrons as Characteristic Signature of their Dynamics“. Diploma thesis. Technische Universität Dresden, 2012. DOI: `10.5281/zenodo.843510` (cit. on pp. 9, 24–26, 29, 32, 38).

[62] M Zacharias. „Model-driven parameter reconstructions from small angle X-ray scattering images“. Master thesis. Technische Universität Dresden, 2017. DOI: `10.5281/zenodo.1208410` (cit. on p. 10).

[63] KT Phuoc, F Burgy, JP Rousseau, V Malka, A Rousse, R Shah, D Umstadter, A Pukhov, and S Kiselev. „Laser based synchrotron radiation“. In: *Physics of Plasmas* 12.2 (2005), p. 023101. ISSN: 1070-664X. DOI: `10.1063/1.1842755` (cit. on pp. 12, 25).

[64] TP Yu, A Pukhov, ZM Sheng, F Liu, and G Shvets. „Bright Betatronlike X Rays from Radiation Pressure Acceleration of a Mass-Limited Foil Target“. In: *Physical Review Letters* 110.4 (2013), p. 045001. ISSN: 0031-9007. DOI: `10.1103/PhysRevLett.110.045001` (cit. on p. 12).

[65] H Burau. „Entwicklung und Überprüfung eines Photonenmodells für die Abstrahlung durch hochenergetische Elektronen“. Diploma thesis. Technische Universität Dresden, 2016, p. 105. DOI: `10.5281/zenodo.192116` (cit. on pp. 13, 14, 24, 43, 45).

[66] A Di Piazza, C Müller, KZ Hatsagortsyan, and CH Keitel. „Extremely high-intensity laser interactions with fundamental quantum systems". In: *Reviews of Modern Physics* 84.3 (2012), pp. 1177–1228. ISSN: 0034-6861. DOI: `10.1103/RevModPhys.84.1177`. arXiv: `1111.3886` (cit. on p. 13).

[67] DF Richards, JN Glosli, B Chan, MR Dorr, EW Draeger, JL Fattebert, WD Krauss, T Spelce, FH Streitz, MP Surh, and JA Gunnels. „Beyond homogeneous decomposition: scaling long-range forces on Massively Parallel Systems". In: *Proceedings of the Conference on High Performance Computing Networking, Storage and Analysis - SC '09*. New York, USA: ACM Press, 2009, 60:1–60:12. ISBN: 978-1-60558-744-8. DOI: `10.1145/1654059.1654121` (cit. on p. 15).

[68] J Ameres. „Stochastic and Spectral Particle Methods for Plasma Physics". PhD thesis. Technischen Universität München and Max-Planck-Institut für Plasmaphysik Garchingen, 2018. DOI: `10.17617/2.2599157` (cit. on p. 15).

[69] P McKenna, D Neely, R Bingham, and D Jaroszynski, eds. *Laser-Plasma Interactions and Applications*. Heidelberg: Springer International Publishing, 2013. ISBN: 978-3-319-00037-4. DOI: `10.1007/978-3-319-00038-1` (cit. on p. 15).

[70] P Henri et al. „Nonlinear evolution of the magnetized Kelvin-Helmholtz instability: From fluid to kinetic modeling". In: *Physics of Plasmas* 20.10 (2013), p. 102118. ISSN: 1070-664X. DOI: `10.1063/1.4826214`. arXiv: `1310.7707` (cit. on pp. 15, 99).

[71] R Dendy. *Plasma Physics: An Introductory Course*. Cambridge: Cambridge University Press, 1993. ISBN: 0-521-43309-6 (cit. on p. 15).

[72] H Burau, R Widera, W Hönig, G Juckeland, A Debus, T Kluge, U Schramm, TE Cowan, R Sauerbrey, and M Bussmann. „PIConGPU: A fully relativistic particle-in-cell code for a GPU cluster". In: *IEEE Transactions on Plasma Science* 38.10 PART 2 (2010), pp. 2831–2839. ISSN: 0093-3813. DOI: `10.1109/TPS.2010.2064310` (cit. on p. 16).

[73] RW Hockney and JW Eastwood. *Computer simulation using particles*. Bristol and New York: Adam Hilger - IOP Publishing Ltd, 1988. ISBN: 0-85274-392-0 (cit. on pp. 16, 22, 113).

[74] CK Birdsall and AB Langdon. *Plasma physics via computer simulation*. Bristol, Philadelphia and New York: Adam Hilger, 1991. ISBN: 0-07-005371-5 (cit. on p. 16).

[75] BB Godfrey. „Review and recent advances in PIC modeling of relativistic beams and plasmas". In: *AIP Conference Proceedings*. Vol. 1777. 2016, p. 020004. ISBN: 978-0-73541-439-6. DOI: `10.1063/1.4965593`. arXiv: `1408.1146` (cit. on p. 16).

[76] RA Fonseca, LO Silva, FS Tsung, VK Decyk, W Lu, C Ren, WB Mori, S Deng, S Lee, T Katsouleas, and JC Adam. „OSIRIS: A Three-Dimensional, Fully Relativistic Particle in Cell Code for Modeling Plasma Based Accelerators". In: *Computational Science - ICCS 2002: International Conference Amsterdam - Proceedings Part III*. 2002, pp. 342–351. ISBN: 978-3-540-43594-5. DOI: `10.1007/3-540-47789-6_36` (cit. on pp. 16, 106).

[77] C Huang, VK Decyk, C Ren, M Zhou, W Lu, WB Mori, JH Cooley, TM Antonsen, and T Katsouleas. „QUICKPIC: A highly efficient particle-in-cell code for modeling wakefield acceleration in plasmas". In: *Journal of Computational Physics* 217.2 (2006), pp. 658–679. ISSN: 0021-9991. DOI: `10.1016/j.jcp.2006.01.039` (cit. on pp. 16, 66).

[78] JL Vay, DP Grote, RH Cohen, and A Friedman. „Novel methods in the Particle-In-Cell accelerator Code-Framework Warp". In: *Computational Science & Discovery* 5.1 (2012), p. 014019. ISSN: 1749-4699. DOI: `10.1088/1749-4699/5/1/014019` (cit. on p. 16).

[79] T Mehrling, C Benedetti, CB Schroeder, and J Osterhoff. „HiPACE: a quasi-static particle-in-cell code“. In: *Plasma Physics and Controlled Fusion* 56.8 (2014), p. 084012. ISSN: 0741-3335. DOI: `10.1088/0741-3335/56/8/084012` (cit. on p. 16).

[80] T Haugbølle, JT Frederiksen, and Å Nordlund. „Photon-Plasma: A modern high-order particle-in-cell code“. In: *Physics of Plasmas* 20.6 (2013), p. 062904. ISSN: 1070-664X. DOI: `10.1063/1.4811384`. arXiv: `arXiv:1211.4575v3` (cit. on pp. 16, 25).

[81] KI Nishikawa, PE Hardee, I Duţan, J Niemiec, M Medvedev, Y Mizuno, A Meli, H Sol, B Zhang, M Pohl, and DH Hartmann. „Magnetic Field Generation in Core-Sheath Jets via the Kinetic Kelvin-Helmholtz Instability“. In: *The Astrophysical Journal* 793.1 (2014), p. 60. ISSN: 1538-4357. DOI: `10.1088/0004-637X/793/1/60`. arXiv: `1405.5247` (cit. on pp. 16, 99, 102, 104, 106, 120).

[82] KS Yee. „Numerical solution of initial boundary value problems involving Maxwell's equations in isotropic media“. In: *IEEE Transactions on Antennas and Propagation* 14.3 (1966), pp. 302–307. ISSN: 0018-926X. DOI: `10.1109/TAP.1966.1138693` (cit. on pp. 18, 21, 22, 71, 113).

[83] CE Shannon. „Communication In The Presence Of Noise“. In: *Proceedings of the IEEE*. Vol. 86. 2. 1998, pp. 447–457. DOI: `10.1109/JPROC.1998.659497` (cit. on pp. 18, 26).

[84] A Jerri. „The Shannon sampling theorem—Its various extensions and applications: A tutorial review“. In: *Proceedings of the IEEE* 65.11 (1977), pp. 1565–1596. ISSN: 0018-9219. DOI: `10.1109/PROC.1977.10771` (cit. on pp. 18, 26).

[85] R Courant, K Friedrichs, and H Lewy. „Über die partiellen Differenzengleichungen der mathematischen Physik“. In: *Mathematische Annalen* 100.1 (1928), pp. 32–74. ISSN: 0025-5831. DOI: `10.1007/BF01448839` (cit. on p. 19).

[86] DH Lam. *Finite Difference Methods for Electromagnetic Scattering Problems*. `http://ece-research.unm.edu/summa/notes/In/0044.pdf`. Accessed: 2018-10-16. 1969 (cit. on p. 19).

[87] JP Boris. „Relativistic Plasma Simulation - Optimization of a Hybrid Code“. In: *Proc. 4th Conf. on Num. Sim. of Plasmas*. ADA023511. Naval Research Laboratory, Washington, D.C., `http://www.dtic.mil/docs/citations/ADA023511/`: Defense Technical Information Center, 1970, pp. 3–67 (cit. on pp. 20, 71, 113).

[88] H Qin, S Zhang, J Xiao, J Liu, Y Sun, and WM Tang. „Why is Boris algorithm so good?“ In: *Physics of Plasmas* 20.8 (2013), p. 084503. ISSN: 1070-664X. DOI: `10.1063/1.4818428` (cit. on p. 20).

[89] SD Webb. „Symplectic integration of magnetic systems“. In: *Journal of Computational Physics* 270 (2014), pp. 570–576. ISSN: 1090-2716. DOI: `10.1016/j.jcp.2014.03.049`. arXiv: `arXiv:1309.3723v1` (cit. on p. 20).

[90] S Zhang, Y Jia, and Q Sun. „Comment on "Symplectic integration of magnetic systems" by Stephen D. Webb [J. Comput. Phys. 270 (2014) 570-576]“. In: *Journal of Computational Physics* 282 (2015), pp. 43–46. ISSN: 1090-2716. DOI: `10.1016/j.jcp.2014.10.062` (cit. on p. 20).

[91] CL Ellison, JW Burby, and H Qin. „Comment on "Symplectic integration of magnetic systems": A proof that the Boris algorithm is not variational“. In: *Journal of Computational Physics* 301 (2015), pp. 489–493. ISSN: 1090-2716. DOI: `10.1016/j.jcp.2015.09.007`. arXiv: `1509.02863` (cit. on p. 20).

[92] R Zhang, J Liu, H Qin, Y Wang, Y He, and Y Sun. „Volume-preserving algorithm for secular relativistic dynamics of charged particles“. In: *Physics of Plasmas* 22.4 (2015), p. 044501. ISSN: 1070-664X. DOI: `10.1063/1.4916570` (cit. on p. 20).

[93] JL Vay. „Simulation of beams or plasmas crossing at relativistic velocity“. In: *Physics of Plasmas* 15.5 (2008), p. 056701. ISSN: 1070-664X. DOI: `10.1063/1.2837054` (cit. on pp. 20, 71).

[94] M Vranic, JL Martins, RA Fonseca, and LO Silva. „Classical radiation reaction in particle-in-cell simulations“. In: *Computer Physics Communications* 204 (2016), pp. 141–151. ISSN: 00104655. DOI: `10.1016/j.cpc.2016.04.002`. arXiv: `1502.02432` (cit. on pp. 21, 41, 42).

[95] BB Godfrey. „Numerical Cherenkov instabilities in electromagnetic particle codes“. In: *Journal of Computational Physics* 15.4 (1974), pp. 504–521. ISSN: 1090-2716. DOI: `10.1016/0021-9991(74)90076-X` (cit. on p. 21).

[96] R Lehe, A Lifschitz, C Thaury, V Malka, and X Davoine. „Numerical growth of emittance in simulations of laser-wakefield acceleration“. In: *Physical Review Special Topics - Accelerators and Beams* 16.2 (2013), p. 021301. ISSN: 1098-4402. DOI: `10.1103/PhysRevSTAB.16.021301` (cit. on pp. 21, 71).

[97] RL Morse and CW Nielson. „Numerical Simulation of the Weibel Instability in One and Two Dimensions“. In: *Physics of Fluids* 14.4 (1971), p. 830. ISSN: 0031-9171. DOI: `10.1063/1.1693518` (cit. on p. 22).

[98] J Villasenor and O Buneman. „Rigorous charge conservation for local electromagnetic field solvers“. In: *Computer Physics Communications* 69.2-3 (1992), pp. 306–316. ISSN: 0010-4655. DOI: `10.1016/0010-4655(92)90169-Y` (cit. on p. 22).

[99] AB Langdon. „Some Electromagnetic Plasma Simulation Methods and Their Noise Properties“. In: *Physics of Fluids* 15.6 (1972), p. 1149. ISSN: 0031-9171. DOI: `10.1063/1.1694042` (cit. on p. 22).

[100] TZ Esirkepov. „Exact charge conservation scheme for Particle-in-Cell simulation with an arbitrary form-factor“. In: *Computer Physics Communications* 135.2 (2001), pp. 144–153. ISSN: 0010-4655. DOI: `10.1016/S0010-4655(00)00228-9`. arXiv: `physics/9901047 [physics]` (cit. on pp. 22, 71, 113).

[101] M Garten. „Modellierung und Validierung von Feldionisation in parallelen Particle-in-Cell-Codes“. Master thesis. Technische Universität Dresden, 2015. DOI: `10.5281/zenodo.202500` (cit. on pp. 24, 60).

[102] CB Hededal and Å Nordlund. „Gamma-Ray Burst Synthetic Spectra from Collisionless Shock PIC Simulations“. In: *arXiv* (2005). arXiv: `astro-ph/0511662 [astro-ph]` (cit. on p. 25).

[103] KI Nishikawa, Y Mizuno, P Hardee, H Sol, M Medvedev, B Zhang, Å Nordlund, JT Frederiksen, GJ Fishman, and R Preece. „Radiation from relativistic jets“. In: *Proceedings of Science - Workshop on Blazar Variability across the Electromagnetic Spectrum*. 2008. DOI: `10.22323/1.063.0053`. arXiv: `0808.3781` (cit. on pp. 25, 134).

[104] L Sironi and A Spitkovsky. „Synthetic Spectra From Particle-in-Cell Simulations of Relativistic Collisionless Shocks“. In: *The Astrophysical Journal Letters* 707.1 (2009), pp. L92–L96. ISSN: 0004-637X. DOI: `10.1088/0004-637X/707/1/L92` (cit. on pp. 25, 134).

[105] JL Martins, SF Martins, RA Fonseca, and LO Silva. „Radiation post-processing in PIC codes“. In: *Proceedings of SPIE Optics + Optoelectronics*. Vol. 7359. 2009, pp. 73590V–1–73590V–8. DOI: `10.1117/12.820736` (cit. on p. 25).

[106] KI Nishikawa et al. „Radiation from relativistic jets in turbulent magnetic fields“. In: *AIP Conference Proceedings*. Vol. 1133. AIP, 2009, pp. 235–237. ISBN: 978-0-73540-670-4. DOI: `10.1063/1.3155889` (cit. on pp. 25, 134).

[107] AGR Thomas. „Algorithm for calculating spectral intensity due to charged particles in arbitrary motion“. In: *Physical Review Special Topics - Accelerators and Beams* 13.2 (2010), p. 020702. ISSN: 1098-4402. DOI: `10.1103/PhysRevSTAB.13.020702`. arXiv: `0906.0758` (cit. on p. 25).

[108] JT Frederiksen, T Haugbølle, MV Medvedev, and Å Nordlund. „Radiation Spectral Synthesis of Relativistic Filamentation“. In: *The Astrophysical Journal Letters* 722.1 (2010), pp. L114–L119. ISSN: 2041-8205. DOI: `10.1088/2041-8205/722/1/L114` (cit. on p. 25).

[109] MV Medvedev, JT Frederiksen, T Haugbølle, and Å Nordlund. „Radiation Signatures of Sub-Larmor Scale Magnetic Fields“. In: *The Astrophysical Journal* 737.2 (2011), p. 55. ISSN: 0004-637X. DOI: `10.1088/0004-637X/737/2/55` (cit. on pp. 25, 134).

[110] SG Rykovanov, M Chen, CGR Geddes, CB Schroeder, E Esarey, and WP Leemans. „Virtual detector of synchrotron radiation (VDSR) - A C++ parallel code for particle tracking and radiation calculation“. In: *AIP Conference Proceedings: 15th Advanced Accelerator Concepts Workshop*. Vol. 1507. 2012, pp. 399–403. ISBN: 978-0-73541-125-8. DOI: `10.1063/1.4773729` (cit. on p. 25).

[111] M Chen, E Esarey, CGR Geddes, CB Schroeder, GR Plateau, SS Bulanov, S Rykovanov, and WP Leemans. „Modeling classical and quantum radiation from laser-plasma accelerators“. In: *Physical Review Special Topics - Accelerators and Beams* 16.3 (2013), p. 030701. ISSN: 1098-4402. DOI: `10.1103/PhysRevSTAB.16.030701` (cit. on p. 25).

[112] F Marvasti, ed. *Nonuniform Sampling*. Information Technology: Transmission, Processing, and Storage. Boston, MA: Springer US, 2001. ISBN: 978-1-4613-5451-2. DOI: `10.1007/978-1-4615-1229-5` (cit. on p. 26).

[113] A Huebl and R Lehe. *OpenPMD*. `http://www.openpmd.org`. Accessed: 2018-10-16 (cit. on p. 26).

[114] ES Sarachik and GT Schappert. „Classical Theory of the Scattering of Intense Laser Radiation by Free Electrons“. In: *Physical Review D* 1.10 (1970), pp. 2738–2753. ISSN: 0556-2821. DOI: `10.1103/PhysRevD.1.2738` (cit. on p. 27).

[115] E Esarey, SK Ride, and P Sprangle. „Nonlinear Thomson scattering of intense laser pulses from beams and plasmas“. In: *Physical Review E* 48.4 (1993), pp. 3003–3021. ISSN: 1063-651X. DOI: `10.1103/PhysRevE.48.3003` (cit. on pp. 27–29, 62–64, 74).

[116] Sy Chen, A Maksimchuk, and D Umstadter. „Experimental observation of relativistic nonlinear Thomson scattering“. In: *Nature* 396.6712 (1998), pp. 653–655. ISSN: 0028-0836. DOI: `10.1038/25303`. arXiv: `physics/9810036 [physics]` (cit. on pp. 31, 62, 74).

[117] LI Schiff. „Production of particle energies beyond 200 Mev“. In: *Review of Scientific Instruments* 17.1 (1946), pp. 6–14. ISSN: 0034-6748. DOI: `10.1063/1.1770395` (cit. on p. 34).

[118] JS Nodvick and DS Saxon. „Suppression of Coherent Radiation by Electrons in a Synchrotron“. In: *Physical Review* 96.1 (1954), pp. 180–184. ISSN: 0031-899X. DOI: `10.1103/PhysRev.96.180` (cit. on p. 34).

[119] CJ Hirschmugl, M Sagurton, and GP Williams. „Multiparticle coherence calculations for synchrotron-radiation emission“. In: *Physical Review A* 44.2 (1991), pp. 1316–1320. ISSN: 1050-2947. DOI: `10.1103/PhysRevA.44.1316` (cit. on p. 34).

[120] FJ Harris. „On the use of windows for harmonic analysis with the discrete Fourier transform“. In: *Proceedings of the IEEE* 66.1 (1978), pp. 51–83. ISSN: 0018-9219. DOI: `10.1109/PROC.1978.10837` (cit. on pp. 35–37).

[121] T Butz. *Fouriertransformation für Fußgänger*. 7th. Wiesbaden: Vieweg+Teubner Verlag | Springer Fachmedien Wiesbaden GmbH, 2011. ISBN: 978-3-8348-0946-9. DOI: `10.1007/978-3-8348-8295-0` (cit. on pp. 35–37).

[122] A Huebl, R Widera, F Schmitt, R Pausch, H Burau, C Schumann, C Eckert, and M Bussmann. *PIConGPU beta-rc5*. 2014. DOI: `10.5281/zenodo.10305` (cit. on p. 36).

[123] A Zhidkov, J Koga, A Sasaki, and M Uesaka. „Radiation Damping Effects on the Interaction of Ultraintense Laser Pulses with an Overdense Plasma“. In: *Physical Review Letters* 88.18 (2002), p. 185002. ISSN: 0031-9007. DOI: `10.1103/PhysRevLett.88.185002` (cit. on pp. 40, 43).

[124] N Naumova, T Schlegel, VT Tikhonchuk, C Labaune, IV Sokolov, and G Mourou. „Hole Boring in a DT Pellet and Fast-Ion Ignition with Ultraintense Laser Pulses“. In: *Physical Review Letters* 102.2 (2009), p. 025002. ISSN: 0031-9007. DOI: `10.1103/PhysRevLett.102.025002`. arXiv: `0903.3718` (cit. on p. 40).

[125] M Chen, A Pukhov, TP Yu, and ZM Sheng. „Radiation reaction effects on ion acceleration in laser foil interaction“. In: *Plasma Physics and Controlled Fusion* 53.1 (2011), p. 014004. ISSN: 0741-3335. DOI: `10.1088/0741-3335/53/1/014004`. arXiv: `0909.5144` (cit. on p. 40).

[126] IV Sokolov, NM Naumova, JA Nees, GA Mourou, and VP Yanovsky. „Dynamics of emitting electrons in strong laser fields“. In: *Physics of Plasmas* 16.9 (2009), p. 093115. ISSN: 1070-664X. DOI: `10.1063/1.3236748`. arXiv: `0904.0405` (cit. on p. 40).

[127] J Koga, TZ Esirkepov, and SV Bulanov. „Nonlinear Thomson scattering in the strong radiation damping regime“. In: *Physics of Plasmas* 12.9 (2005), p. 093106. ISSN: 1070-664X. DOI: `10.1063/1.2013067` (cit. on pp. 40, 41, 43, 44).

[128] A Gonoskov, S Bastrakov, E Efimenko, A Ilderton, M Marklund, I Meyerov, A Muraviev, A Sergeev, I Surmin, and E Wallin. „Extended particle-in-cell schemes for physics in ultrastrong laser fields: Review and developments“. In: *Physical Review E* 92.2 (2015), p. 023305. ISSN: 1539-3755. DOI: `10.1103/PhysRevE.92.023305` (cit. on pp. 40, 44).

[129] DJ Griffiths. *Introduction to Electrodynamics*. 3rd. Upper Saddle River, New Jersey: Prentice Hall, 1999. ISBN: 0-13-805326-X (cit. on pp. 40, 41, 65, 110, 122).

[130] PAM Dirac. „Classical Theory of Radiating Electrons“. In: *Proceedings of the Royal Society A: Mathematical, Physical and Engineering Sciences*. Vol. 167. 929. 1938, pp. 148–169. DOI: `10.1098/rspa.1938.0124` (cit. on p. 41).

[131] DJ Griffiths, TC Proctor, and DF Schroeter. „Abraham-Lorentz versus Landau-Lifshitz“. In: *American Journal of Physics* 78.4 (2010), pp. 391–402. ISSN: 0002-9505. DOI: `10.1119/1.3269900` (cit. on p. 41).

[132] H Spohn. „The critical manifold of the Lorentz-Dirac equation“. In: *EPL (Europhysics Letters)* 50.3 (2000), pp. 287–292. ISSN: 0295-5075. DOI: `10.1209/epl/i2000-00268-x`. arXiv: `physics/9911027 [physics]` (cit. on p. 41).

[133] M Tamburini, F Pegoraro, A Di Piazza, CH Keitel, and A Macchi. „Radiation reaction effects on radiation pressure acceleration“. In: *New Journal of Physics* 12.12 (2010), p. 123005. ISSN: 1367-2630. DOI: `10.1088/1367-2630/12/12/123005`. arXiv: `1008.1685` (cit. on p. 41).

[134] OPAL Collaboration. „Tests of the standard model and constraints on new physics from measurements of fermion-pair production at 189-209 GeV at LEP“. In: *European Physical Journal C* 33.2 (2004), pp. 173–212. ISSN: 1434-6044. DOI: `10.1140/epjc/s2004-01595-9` (cit. on p. 47).

[135] L Arnaudon et al. „Effects of terrestrial tides on the LEP beam energy“. In: *Nuclear Instruments and Methods in Physics Research Section A: Accelerators, Spectrometers, Detectors and Associated Equipment* 357.2-3 (1995), pp. 249–252. ISSN: 0168-9002. DOI: `10.1016/0168-9002(94)01526-0` (cit. on p. 47).

[136] T Behnke, JE Brau, B Foster, J Fuster, M Harrison, JM Paterson, M Peskin, M Stanitzki, N Walker, and H Yamamoto. *The International Linear Collider Technical Design Report | Volume 1 : Executive Summary*. Tech. rep. 2013. arXiv: `1306.6327` (cit. on p. 47).

[137] A Modena et al. „Electron acceleration from the breaking of relativistic plasma waves“. In: *Nature* 377.6550 (1995), pp. 606–608. ISSN: 0028-0836. DOI: `10.1038/377606a0` (cit. on p. 47).

[138] D Umstadter, SY Chen, A Maksimchuk, G Mourou, and R Wagner. „Nonlinear Optics in Relativistic Plasmas and Laser Wake Field Acceleration of Electrons“. In: *Science* 273.5274 (1996), pp. 472–475. ISSN: 0036-8075. DOI: `10.1126/science.273.5274.472` (cit. on p. 47).

[139] O Lundh, J Lim, C Rechatin, L Ammoura, A Ben-Ismaïl, X Davoine, G Gallot, JP Goddet, E Lefebvre, V Malka, and J Faure. „Few femtosecond, few kiloampere electron bunch produced by a laser-plasma accelerator“. In: *Nature Physics* 7 (2011), pp. 219–222. ISSN: 1745-2473. DOI: `10.1038/nphys1872` (cit. on p. 47).

[140] Y Ding et al. „Measurements and Simulations of Ultralow Emittance and Ultrashort Electron Beams in the Linac Coherent Light Source“. In: *Physical Review Letters* 102.25 (2009), p. 254801. ISSN: 0031-9007. DOI: `10.1103/PhysRevLett.102.254801` (cit. on p. 47).

[141] YF Li et al. „Generation of 20 kA electron beam from a laser wakefield accelerator“. In: *Physics of Plasmas* 24.2 (2017), p. 023108. ISSN: 1070-664X. DOI: `10.1063/1.4975613` (cit. on p. 47).

[142] EA Schneidmiller and MV Yurkov. „Baseline Parameters of the European XFEL“. In: *38th International Free Electron Laser Conference*. 2017, pp. 109–112. ISBN: 978-3-95450-179-3. DOI: `10.18429/JACoW-FEL2017-MOP033` (cit. on p. 47).

[143] D Strickland and G Mourou. „Compression of amplified chirped optical pulses“. In: *Optics Communications* 56.3 (1985), pp. 219–221. ISSN: 0030-4018. DOI: `10.1016/0030-4018(85)90120-8` (cit. on p. 48).

[144] G Mourou and D Umstadter. „Development and applications of compact high-intensity lasers“. In: *Physics of Fluids B: Plasma Physics* 4.7 (1992), pp. 2315–2325. ISSN: 0899-8221. DOI: `10.1063/1.860202` (cit. on p. 48).

[145] MD Perry and G Mourou. „Terawatt to Petawatt Subpicosecond Lasers“. In: *Science* 264.5161 (1994), pp. 917–924. ISSN: 0036-8075. DOI: `10.1126/science.264.5161.917` (cit. on p. 48).

[146] A Pukhov and J Meyer-ter-Vehn. „Laser wake field acceleration: The highly non-linear broken-wave regime“. In: *Applied Physics B: Lasers and Optics* 74.4-5 (2002), pp. 355–361. ISSN: 0946-2171. DOI: `10.1007/s003400200795` (cit. on pp. 48, 54).

[147] W Lu, C Huang, M Zhou, WB Mori, and T Katsouleas. „Nonlinear Theory for Relativistic Plasma Wakefields in the Blowout Regime“. In: *Physical Review Letters* 96.16 (2006), p. 165002. ISSN: 0031-9007. DOI: `10.1103/PhysRevLett.96.165002` (cit. on p. 48).

[148] WP Leemans, B Nagler, AJ Gonsalves, C Tóth, K Nakamura, CGR Geddes, E Esarey, CB Schroeder, and SM Hooker. „GeV electron beams from a centimetre-scale accelerator“. In: *Nature Physics* 2 (2006), pp. 696–699. ISSN: 1745-2473. DOI: `10.1038/nphys418` (cit. on p. 48).

[149] CE Clayton et al. „Self-Guided Laser Wakefield Acceleration beyond 1 GeV Using Ionization-Induced Injection“. In: *Physical Review Letters* 105.10 (2010), p. 105003. ISSN: 0031-9007. DOI: `10.1103/PhysRevLett.105.105003` (cit. on p. 48).

[150] HT Kim, KH Pae, HJ Cha, IJ Kim, TJ Yu, JH Sung, SK Lee, TM Jeong, and J Lee. „Enhancement of Electron Energy to the Multi-GeV Regime by a Dual-Stage Laser-Wakefield Accelerator Pumped by Petawatt Laser Pulses“. In: *Physical Review Letters* 111.16 (2013), p. 165002. ISSN: 0031-9007. DOI: `10.1103/PhysRevLett.111.165002`. arXiv: `1307.4159` (cit. on p. 48).

[151] S Steinke et al. „Multistage coupling of independent laser-plasma accelerators“. In: *Nature* 530.7589 (2016), pp. 190–193. ISSN: 0028-0836. DOI: `10.1038/nature16525` (cit. on p. 48).

[152] F Albert, BB Pollock, JL Shaw, KA Marsh, JE Ralph, YH Chen, D Alessi, A Pak, CE Clayton, SH Glenzer, and C Joshi. „Angular Dependence of Betatron X-Ray Spectra from a Laser-Wakefield Accelerator“. In: *Physical Review Letters* 111.23 (2013), p. 235004. ISSN: 0031-9007. DOI: `10.1103/PhysRevLett.111.235004` (cit. on p. 48).

[153] Y Ma, LM Chen, NAM Hafz, DZ Li, K Huang, WC Yan, J Dunn, ZM Sheng, and J Zhang. „Diagnosis of bubble evolution in laser-wakefield acceleration via angular distributions of betatron x-rays“. In: *Applied Physics Letters* 105.16 (2014), p. 161110. ISSN: 0003-6951. DOI: `10.1063/1.4900412` (cit. on p. 48).

[154] V Horný, J Nejdl, M Kozlová, M Krůs, K Boháček, V Petržílka, and O Klimo. „Temporal profile of betatron radiation from laser-driven electron accelerators“. In: *Physics of Plasmas* 24.6 (2017), p. 063107. ISSN: 1070-664X. DOI: `10.1063/1.4985687` (cit. on p. 48).

[155] A Curcio, M Anania, F Bisesto, E Chiadroni, A Cianchi, M Ferrario, F Filippi, D Giulietti, A Marocchino, M Petrarca, V Shpakov, and A Zigler. „Trace-space reconstruction of low-emittance electron beams through betatron radiation in laser-plasma accelerators“. In: *Physical Review Accelerators and Beams* 20.1 (2017), p. 012801. ISSN: 2469-9888. DOI: `10.1103/PhysRevAccelBeams.20.012801` (cit. on pp. 48, 70).

[156] MC Downer, R Zgadzaj, A Debus, U Schramm, and MC Kaluza. „Diagnostics for plasma-based electron accelerators“. In: *Reviews of Modern Physics* 90.3 (2018), p. 035002. ISSN: 0034-6861. DOI: `10.1103/RevModPhys.90.035002` (cit. on p. 48).

[157] D Bauer and P Mulser. „Exact field ionization rates in the barrier-suppression regime from numerical time-dependent Schrödinger-equation calculations“. In: *Physical Review A* 59.1 (1999), pp. 569–577. ISSN: 1050-2947. DOI: `10.1103/PhysRevA.59.569`. arXiv: `physics/9802042 [physics]` (cit. on pp. 50, 91).

[158] LV Keldysh. „Ionization in the field of a strong electromagnetic wave“. In: *Soviet Physics JETP* 20.5 (1965), pp. 1307–1314. ISSN: 0038-5646 (cit. on pp. 50, 91).

[159] A Macchi. *A Superintense Laser-Plasma Interaction Theory Primer*. SpringerBriefs in Physics. Dordrecht: Springer Netherlands, 2013. ISBN: 978-94-007-6124-7. DOI: `10.1007/978-94-007-6125-4` (cit. on p. 51).

[160] L Gorbunov and V Kirsanov. „Excitation of plasma waves by an electromagnetic wave packet“. In: *Soviet Physics JETP* 66.2 (1987), pp. 290–294. ISSN: 0038-5646 (cit. on p. 52).

[161] P Sprangle, E Esarey, A Ting, and G Joyce. „Laser wakefield acceleration and relativistic optical guiding“. In: *Applied Physics Letters* 53.22 (1988), pp. 2146–2148. ISSN: 0003-6951. DOI: `10.1063/1.100300` (cit. on p. 52).

[162] E Esarey, P Sprangle, J Krall, and A Ting. „Overview of plasma-based accelerator concepts“. In: *IEEE Transactions on Plasma Science* 24.2 (1996), pp. 252–288. ISSN: 0093-3813. DOI: `10.1109/27.509991` (cit. on p. 53).

[163] V Malka et al. „Electron Acceleration by a Wake Field Forced by an Intense Ultrashort Laser Pulse“. In: *Science* 298.5598 (2002), pp. 1596–1600. ISSN: 0036-8075. DOI: `10.1126/science.1076782` (cit. on p. 54).

[164] S Kiselev, A Pukhov, and I Kostyukov. „X-ray Generation in Strongly Nonlinear Plasma Waves“. In: *Physical Review Letters* 93.13 (2004), p. 135004. ISSN: 0031-9007. DOI: `10.1103/PhysRevLett.93.135004` (cit. on p. 54).

[165] A Rousse, KT Phuoc, R Shah, A Pukhov, E Lefebvre, V Malka, S Kiselev, F Burgy, JP Rousseau, D Umstadter, and D Hulin. „Production of a keV X-Ray Beam from Synchrotron Radiation in Relativistic Laser-Plasma Interaction“. In: *Physical Review Letters* 93.13 (2004), p. 135005. ISSN: 0031-9007. DOI: `10.1103/PhysRevLett.93.135005` (cit. on p. 54).

[166] P Sprangle, CM Tang, and E Esarey. „Relativistic self-focusing of short-pulse radiation beams in plasmas“. In: *IEEE Transactions on Plasma Science* 15.2 (1987), pp. 145–153. ISSN: 1939-9375. DOI: `10.1109/TPS.1987.4316677` (cit. on p. 57).

[167] P Sprangle, E Esarey, and A Ting. „Nonlinear interaction of intense laser pulses in plasmas“. In: *Physical Review A* 41.8 (1990), pp. 4463–4469. ISSN: 1050-2947. DOI: `10.1103/PhysRevA.41.4463` (cit. on p. 57).

[168] P Sprangle and E Esarey. „Interaction of ultrahigh laser fields with beams and plasmas“. In: *Physics of Fluids B: Plasma Physics* 4.7 (1992), pp. 2241–2248. ISSN: 0899-8221. DOI: `10.1063/1.860192` (cit. on p. 57).

[169] CD Decker, WB Mori, KC Tzeng, and T Katsouleas. „The evolution of ultra-intense, short-pulse lasers in underdense plasmas“. In: *Physics of Plasmas* 3.5 (1996), pp. 2047–2056. ISSN: 1070-664X. DOI: `10.1063/1.872001` (cit. on p. 57).

[170] GZ Sun, E Ott, YC Lee, and P Guzdar. „Self-focusing of short intense pulses in plasmas“. In: *Physics of Fluids* 30.2 (1987), p. 526. ISSN: 0031-9171. DOI: `10.1063/1.866349` (cit. on p. 58).

[171] B Hafizi, A Ting, P Sprangle, and RF Hubbard. „Relativistic focusing and ponderomotive channeling of intense laser beams“. In: *Physical Review E* 62.3 (2000), pp. 4120–4125. ISSN: 1063-651X. DOI: `10.1103/PhysRevE.62.4120` (cit. on p. 58).

[172] W Lu, M Tzoufras, C Joshi, FS Tsung, WB Mori, J Vieira, RA Fonseca, and LO Silva. „Generating multi-GeV electron bunches using single stage laser wakefield acceleration in a 3D nonlinear regime“. In: *Physical Review Special Topics - Accelerators and Beams* 10.6 (2007), p. 061301. ISSN: 1098-4402. DOI: `10.1103/PhysRevSTAB.10.061301`. arXiv: `physics/0612227 [physics]` (cit. on p. 58).

[173] BA Shadwick, CB Schroeder, and E Esarey. „Nonlinear laser energy depletion in laser-plasma accelerators“. In: *Physics of Plasmas* 16.5 (2009), p. 056704. ISSN: 1070-664X. DOI: `10.1063/1.3124185` (cit. on p. 58).

[174] AD Debus, M Bussmann, M Siebold, A Jochmann, U Schramm, TE Cowan, and R Sauerbrey. „Traveling-wave Thomson scattering and optical undulators for high-yield EUV and X-ray sources“. In: *Applied Physics B: Lasers and Optics* 100.1 (2010), pp. 61–76. ISSN: 0946-2171. DOI: `10.1007/s00340-010-3990-1` (cit. on pp. 58, 134).

[175] M Everett, A Lal, D Gordon, CE Clayton, KA Marsh, and C Joshi. „Trapped electron acceleration by a laser-driven relativistic plasma wave“. In: *Nature* 368.6471 (1994), pp. 527–529. ISSN: 0028-0836. DOI: `10.1038/368527a0` (cit. on p. 59).

[176] FS Tsung, R Narang, WB Mori, C Joshi, RA Fonseca, and LO Silva. „Near-GeV-Energy Laser-Wakefield Acceleration of Self-Injected Electrons in a Centimeter-Scale Plasma Channel“. In: *Physical Review Letters* 93.18 (2004), p. 185002. ISSN: 0031-9007. DOI: `10.1103/PhysRevLett.93.185002` (cit. on p. 59).

[177] A Buck, J Wenz, J Xu, K Khrennikov, K Schmid, M Heigoldt, JM Mikhailova, M Geissler, B Shen, F Krausz, S Karsch, and L Veisz. „Shock-Front Injector for High-Quality Laser-Plasma Acceleration“. In: *Physical Review Letters* 110.18 (2013), p. 185006. ISSN: 0031-9007. DOI: `10.1103/PhysRevLett.110.185006` (cit. on p. 59).

[178] M Chen, E Esarey, CB Schroeder, CGR Geddes, and WP Leemans. „Theory of ionization-induced trapping in laser-plasma accelerators“. In: *Physics of Plasmas* 19.3 (2012), p. 033101. ISSN: 1070-664X. DOI: `10.1063/1.3689922` (cit. on p. 59).

[179] A Pak, KA Marsh, SF Martins, W Lu, WB Mori, and C Joshi. „Injection and Trapping of Tunnel-Ionized Electrons into Laser-Produced Wakes“. In: *Physical Review Letters* 104.2 (2010), p. 025003. ISSN: 0031-9007. DOI: `10.1103/PhysRevLett.104.025003` (cit. on pp. 59, 60, 87).

[180] C McGuffey et al. „Ionization Induced Trapping in a Laser Wakefield Accelerator“. In: *Physical Review Letters* 104.2 (2010), p. 025004. ISSN: 0031-9007. DOI: `10.1103/PhysRevLett.104.025004` (cit. on p. 59).

[181] P Mora and TM Antonsen, Jr. „Kinetic modeling of intense, short laser pulses propagating in tenuous plasmas“. In: *Physics of Plasmas* 4.1 (1997), pp. 217–229. ISSN: 1070-664X. DOI: `10.1063/1.872134` (cit. on p. 60).

[182] E Oz et al. „Ionization-Induced Electron Trapping in Ultrarelativistic Plasma Wakes“. In: *Physical Review Letters* 98.8 (2007), p. 084801. ISSN: 0031-9007. DOI: `10.1103/PhysRevLett.98.084801` (cit. on p. 60).

[183] TL Audet et al. „Investigation of ionization-induced electron injection in a wakefield driven by laser inside a gas cell“. In: *Physics of Plasmas* 23.2 (2016), p. 023110. ISSN: 1070-664X. DOI: `10.1063/1.4942033` (cit. on p. 60).

[184] M Zeng, M Chen, ZM Sheng, WB Mori, and J Zhang. „Self-truncated ionization injection and consequent monoenergetic electron bunches in laser wakefield acceleration“. In: *Physics of Plasmas* 21.3 (2014), p. 030701. ISSN: 1070-664X. DOI: `10.1063/1.4868404`. arXiv: `1312.5825` (cit. on pp. 60, 88).

[185] M Mirzaie et al. „Demonstration of self-truncated ionization injection for GeV electron beams“. In: *Scientific Reports* 5 (2015), p. 14659. ISSN: 2045-2322. DOI: `10.1038/srep14659` (cit. on pp. 60, 88).

[186] NA Hafz, S Li, G Li, M Mirzaie, M Zeng, and J Zhang. „Generation of high-quality electron beams by ionization injection in a single acceleration stage“. In: *High Power Laser Science and Engineering* 4.E24 (2016), pp. 1–7. ISSN: 2052-3289. DOI: `10.1017/hpl.2016.25` (cit. on p. 60).

[187] J Faure, Y Glinec, G Gallot, and V Malka. „Ultrashort laser pulses and ultrashort electron bunches generated in relativistic laser-plasma interaction“. In: *Physics of Plasmas* 13.5 (2006), p. 056706. ISSN: 1070-664X. DOI: `10.1063/1.2180727` (cit. on p. 62).

[188] CD Murphy et al. „Evidence of photon acceleration by laser wake fields“. In: *Physics of Plasmas* 13.3 (2006), p. 033108. ISSN: 1070-664X. DOI: `10.1063/1.2178650` (cit. on p. 62).

[189] P Sprangle, E Esarey, and A Ting. „Nonlinear theory of intense laser-plasma interactions“. In: *Physical Review Letters* 64.17 (1990), pp. 2011–2014. ISSN: 0031-9007. DOI: `10.1103/PhysRevLett.64.2011` (cit. on pp. 63, 77).

[190] W Lu, C Huang, M Zhou, M Tzoufras, FS Tsung, WB Mori, and T Katsouleas. „A nonlinear theory for multidimensional relativistic plasma wave wakefields“. In: *Physics of Plasmas* 13.5 (2006), p. 056709. ISSN: 1070-664X. DOI: `10.1063/1.2203364` (cit. on pp. 63, 75, 77).

[191] K Zeil, SD Kraft, S Bock, M Bussmann, TE Cowan, T Kluge, J Metzkes, T Richter, R Sauerbrey, and U Schramm. „The scaling of proton energies in ultrashort pulse laser plasma acceleration“. In: *New Journal of Physics* 12 (2010). ISSN: 1367-2630. DOI: `10.1088/1367-2630/12/4/045015` (cit. on p. 64).

[192] T Li, S Ota, J Kim, ZJ Wong, Y Wang, X Yin, and X Zhang. „Axial Plane Optical Microscopy“. In: *Scientific Reports* 4 (2014), p. 7253. ISSN: 2045-2322. DOI: `10.1038/srep07253` (cit. on p. 74).

[193] DF Gordon, B Hafizi, D Kaganovich, and A Ting. „Electro-Optic Shocks from Ultraintense Laser-Plasma Interactions“. In: *Physical Review Letters* 101.4 (2008), p. 045004. ISSN: 0031-9007. DOI: `10.1103/PhysRevLett.101.045004` (cit. on p. 75).

[194] JB Rosenzweig, DB Cline, B Cole, H Figueroa, W Gai, R Konecny, J Norem, P Schoessow, and J Simpson. „Experimental Observation of Plasma Wake-Field Acceleration“. In: *Physical Review Letters* 61.1 (1988), pp. 98–101. ISSN: 0031-9007. DOI: `10.1103/PhysRevLett.61.98` (cit. on p. 83).

[195] CE Max, J Arons, and AB Langdon. „Self-Modulation and Self-Focusing of Electromagnetic Waves in Plasmas“. In: *Physical Review Letters* 33.4 (1974), pp. 209–212. ISSN: 0031-9007. DOI: `10.1103/PhysRevLett.33.209` (cit. on p. 83).

[196] DF Gordon, B Hafizi, RF Hubbard, JR Peñano, P Sprangle, and A Ting. „Asymmetric Self-Phase Modulation and Compression of Short Laser Pulses in Plasma Channels“. In: *Physical Review Letters* 90.21 (2003), p. 215001. ISSN: 0031-9007. DOI: `10.1103/PhysRevLett.90.215001` (cit. on p. 83).

[197] J Faure, Y Glinec, JJ Santos, F Ewald, JP Rousseau, S Kiselev, A Pukhov, T Hosokai, and V Malka. „Observation of Laser-Pulse Shortening in Nonlinear Plasma Waves“. In: *Physical Review Letters* 95.20 (2005), p. 205003. ISSN: 0031-9007. DOI: `10.1103/PhysRevLett.95.205003` (cit. on p. 83).

[198] J Schreiber, C Bellei, SPD Mangles, C Kamperidis, S Kneip, SR Nagel, CAJ Palmer, PP Rajeev, MJV Streeter, and Z Najmudin. „Complete Temporal Characterization of Asymmetric Pulse Compression in a Laser Wakefield“. In: *Physical Review Letters* 105.23 (2010), p. 235003. ISSN: 0031-9007. DOI: `10.1103/PhysRevLett.105.235003`. arXiv: `arXiv:1010.3694v1` (cit. on p. 85).

[199] S Shiraishi, C Benedetti, aJ Gonsalves, K Nakamura, BH Shaw, T Sokollik, J van Tilborg, CGR Geddes, CB Schroeder, C Tóth, E Esarey, and WP Leemans. „Laser red shifting based characterization of wakefield excitation in a laser-plasma accelerator“. In: *Physics of Plasmas* 20.6 (2013), p. 063103. ISSN: 1070-664X. DOI: `10.1063/1.4810802` (cit. on p. 85).

[200] SV Bulanov, T Esirkepov, and T Tajima. „Light Intensification towards the Schwinger Limit“. In: *Physical Review Letters* 91.8 (2003), p. 085001. ISSN: 0031-9007. DOI: `10.1103/PhysRevLett.91.085001` (cit. on p. 86).

[201] AS Pirozhkov et al. „Frequency multiplication of light back-reflected from a relativistic wake wave“. In: *Physics of Plasmas* 14.12 (2007), p. 123106. ISSN: 1070-664X. DOI: `10.1063/1.2816443` (cit. on pp. 86, 133).

[202] K Ta Phuoc, S Corde, C Thaury, V Malka, A Tafzi, JP Goddet, RC Shah, S Sebban, and A Rousse. „All-optical Compton gamma-ray source“. In: *Nature Photonics* 6 (2012), pp. 308–311. ISSN: 1749-4885. DOI: `10.1038/nphoton.2012.82`. arXiv: `1301.3973` (cit. on p. 86).

[203] HE Tsai, X Wang, J Shaw, AV Arefiev, Z Li, X Zhang, R Zgadzaj, W Henderson, V Khudik, G Shvets, and MC Downer. „Compact tunable Compton x-ray source from laser wakefield accelerator and plasma mirror“. In: *AIP Conference Proceedings: 16th Advanced Accelerator Concepts Workshop*. Vol. 1777. 2016, p. 080006. ISBN: 978-0-73541-439-6. DOI: `10.1063/1.4965663`. arXiv: `1411.2134` (cit. on p. 86).

[204] C Yu et al. „Ultrahigh brilliance quasi-monochromatic MeV γ-rays based on self-synchronized all-optical Compton scattering“. In: *Scientific Reports* 6 (2016), p. 29518. ISSN: 2045-2322. DOI: `10.1038/srep29518` (cit. on p. 86).

[205] HE Tsai, AV Arefiev, JM Shaw, DJ Stark, X Wang, R Zgadzaj, and MC Downer. „Self-aligning concave relativistic plasma mirror with adjustable focus“. In: *Physics of Plasmas* 24.1 (2017), p. 013106. ISSN: 1070-664X. DOI: `10.1063/1.4973432`. arXiv: `1610.02007` (cit. on p. 86).

[206] JM Shaw et al. „Bright 5 - 85 MeV Compton gamma-ray pulses from GeV laser-plasma accelerator and plasma mirror“. In: *arXiv* (2017). arXiv: `1705.08637` (cit. on p. 86).

[207] JP Couperus, A Köhler, TAW Wolterink, A Jochmann, O Zarini, HMJ Bastiaens, KJ Boller, A Irman, and U Schramm. „Tomographic characterisation of gas-jet targets for laser wakefield acceleration“. In: *Nuclear Instruments and Methods in Physics Research, Section A: Accelerators, Spectrometers, Detectors and Associated Equipment* 830 (2016), pp. 504–509. ISSN: 0168-9002. DOI: `10.1016/j.nima.2016.02.099` (cit. on p. 87).

[208] S Li, NAM Hafz, M Mirzaie, T Sokollik, M Zeng, M Chen, Z Sheng, and J Zhang. „Enhanced single-stage laser-driven electron acceleration by self-controlled ionization injection“. In: *Optics Express* 22.24 (2014), p. 29578. ISSN: 1094-4087. DOI: `10.1364/OE.22.029578` (cit. on p. 88).

[209] J Vieira, SF Martins, F Fiúza, CK Huang, WB Mori, SPD Mangles, S Kneip, S Nagel, Z Najmudin, and LO Silva. „Influence of realistic parameters on state-of-the-art laser wakefield accelerator experiments“. In: *Plasma Physics and Controlled Fusion* 54.5 (2012), p. 055010. ISSN: 0741-3335. DOI: `10.1088/0741-3335/54/5/055010`. arXiv: `arXiv:1204.1170v1` (cit. on p. 88).

[210] JP Couperus. „Optimal beam loading in a nanocoulomb-class laser wakefield accelerator“. PhD thesis. Technische Universität Dresden, 2018. DOI: `10.5281/zenodo.1463710` (cit. on p. 90).

[211] HT Kim et al. „Stable multi-GeV electron accelerator driven by waveform-controlled PW laser pulses“. In: *Scientific Reports* 7 (2017), pp. 1–8. ISSN: 2045-2322. DOI: `10.1038/s41598-017-09267-1` (cit. on p. 98).

[212] T Oksenhendler, S Coudreau, N Forget, V Crozatier, S Grabielle, R Herzog, O Gobert, and D Kaplan. „Self-referenced spectral interferometry“. In: *Applied Physics B: Lasers and Optics* 99.1-2 (2010), pp. 7–12. ISSN: 0946-2171. DOI: `10.1007/s00340-010-3916-y` (cit. on pp. 98, 134).

[213] T Oksenhendler. „Self-referenced spectral interferometry theory“. In: *arXiv* (2012). arXiv: `1204.4949` (cit. on pp. 98, 134).

[214] T Oksenhendler, P Bizouard, O Albert, S Bock, and U Schramm. „High dynamic, high resolution and wide range single shot temporal pulse contrast measurement“. In: *Optics Express* 25.11 (2017), p. 12588. DOI: `10.1364/OE.25.012588` (cit. on pp. 98, 134).

[215] M Punch et al. „Detection of TeV photons from the active galaxy Markarian 421“. In: *Nature* 358.6386 (1992), pp. 477–478. ISSN: 0028-0836. DOI: `10.1038/358477a0` (cit. on p. 99).

[216] S Jester, DE Harris, HL Marshall, and K Meisenheimer. „New Chandra Observations of the Jet in 3C 273. I. Softer X-Ray than Radio Spectra and the X-Ray Emission Mechanism“. In: *The Astrophysical Journal* 648.2 (2006), pp. 900–909. ISSN: 0004-637X. DOI: `10.1086/505962`. arXiv: `astro-ph/0605529 [astro-ph]` (cit. on p. 99).

[217] S Collin. „Are AGN the Best Factories for High Energy Particles and Photons?“ In: *arXiv* (2008). arXiv: `0811.1731` (cit. on p. 99).

[218] RU Abbasi et al. „Indications of Intermediate-Scale Anisotropy of Cosmic Rays with Energy Greater than 57 EeV in the Northern Sky Measured with the Surface Detector of the Telescope Array Experiment“. In: *The Astrophysical Journal Letters* 790.2 (2014), p. L21. ISSN: 2041-8205. DOI: `10.1088/2041-8205/790/2/L21`. arXiv: `1404.5890` (cit. on p. 99).

[219] Pierre Auger Collaboration. „Observation of a large-scale anisotropy in the arrival directions of cosmic rays above 8×10^{18} eV“. In: *Science* 357.6357 (2017), pp. 1266–1270. ISSN: 0036-8075. DOI: `10.1126/science.aan4338`. arXiv: `arXiv:1709.07321v1` (cit. on p. 99).

[220] PM Bellan. „Miniconference on astrophysical jets“. In: *Physics of Plasmas* 12.5 (2005), p. 058301. ISSN: 1070-664X. DOI: `10.1063/1.1900563` (cit. on p. 99).

[221] DS de Young. „Turbulent generation of magnetic fields in extended extragalactic radio sources“. In: *The Astrophysical Journal* 241 (1980), p. 81. ISSN: 0004-637X. DOI: `10.1086/158320` (cit. on p. 99).

[222] G Benford. „Collective emission from rapidly variable quasars“. In: *The Astrophysical Journal Letters* 391 (1992), p. L59. ISSN: 0004-637X. DOI: `10.1086/186398` (cit. on p. 99).

[223] D Guetta, T Piran, and E Waxman. „The Luminosity and Angular Distributions of Long-Duration Gamma-Ray Bursts“. In: *The Astrophysical Journal* 619.1 (2005), pp. 412–419. ISSN: 0004-637X. DOI: `10.1086/423125` (cit. on p. 99).

[224] M Birkinshaw. „The Kelvin-Helmholtz instability for relativistic particle beams - II. Flows bounded by a simple shear layer“. In: *Monthly Notices of the Royal Astronomical Society* 252.4 (1991), pp. 505–527. ISSN: 0035-8711. DOI: `10.1093/mnras/252.4.505` (cit. on p. 99).

[225] A Gruzinov. „GRB: magnetic fields, cosmic rays, and emission from first principles?“ In: *arXiv* (2008). arXiv: `0803.1182` (cit. on pp. 99, 101, 102).

[226] T Grismayer, EP Alves, RA Fonseca, and LO Silva. „Theory of multidimensional electron-scale instabilities in unmagnetized shear flows“. In: *Plasma Physics and Controlled Fusion* 55.12 (2013), p. 124031. ISSN: 0741-3335. DOI: `10.1088/0741-3335/55/12/124031` (cit. on pp. 99, 104, 106).

[227] KI Nishikawa et al. „Evolution of global relativistic jets: collimations and expansion with kKHI and the Weibel instability“. In: *The Astrophysical Journal* 820.2 (2016), p. 94. ISSN: 1538-4357. DOI: `10.3847/0004-637X/820/2/94`. arXiv: `1511.03581` (cit. on p. 99).

[228] EP Alves, T Grismayer, RA Fonseca, and LO Silva. „Transverse electron-scale instability in relativistic shear flows“. In: *Physical Review E* 92.2 (2015), 021101(R). ISSN: 1539-3755. DOI: `10.1103/PhysRevE.92.021101`. arXiv: `1505.06016` (cit. on pp. 99, 102–104, 125, 127).

[229] JJ Hester. „The Crab Nebula: An Astrophysical Chimera“. In: *Annual Review of Astronomy and Astrophysics* 46.1 (2008), pp. 127–155. ISSN: 0066-4146. DOI: `10.1146/annurev.astro.45.051806.110608` (cit. on p. 99).

[230] Y Kuramitsu et al. „Kelvin-Helmholtz Turbulence Associated with Collisionless Shocks in Laser Produced Plasmas“. In: *Physical Review Letters* 108.19 (2012), p. 195004. ISSN: 0031-9007. DOI: `10.1103/PhysRevLett.108.195004` (cit. on pp. 99, 128, 129).

[231] J Meinecke et al. „Developed turbulence and nonlinear amplification of magnetic fields in laboratory and astrophysical plasmas“. In: *PNAS* 112.27 (2015), pp. 8211–8215. ISSN: 0027-8424. DOI: `10.1073/pnas.1502079112` (cit. on pp. 99, 128).

[232] W Thomson. „XLVI. Hydrokinetic solutions and observations“. In: *The London, Edinburgh, and Dublin Philosophical Magazine and Journal of Science* 42.281 (1871), pp. 362–377. ISSN: 1941-5982. DOI: `10.1080/14786447108640585` (cit. on p. 100).

[233] AK Sen. „Stability of Hydromagnetic Kelvin-Helmholtz Discontinuity“. In: *Physics of Fluids* 6.8 (1963), p. 1154. ISSN: 0031-9171. DOI: `10.1063/1.1706875` (cit. on p. 100).

[234] EP Alves. „Magnetic field generation via the Kelvin-Helmholtz instability“. Master thesis. Universidade de Lisboa, 2010 (cit. on pp. 101, 120).

[235] E Liang, M Boettcher, and I Smith. „Magnetic Field Generation and Particle Energization at Relativistic Shear Boundaries in Collisionless Electron-Positron Plasmas“. In: *The Astrophysical Journal Letters* 766.2 (2013), p. L19. ISSN: 2041-8205. DOI: `10.1088/2041-8205/766/2/L19` (cit. on pp. 102, 104).

[236] E Liang, W Fu, M Boettcher, I Smith, and P Roustazadeh. „Relativistic Positron-Electron-Ion Shear Flows and Application to Gamma-Ray Bursts“. In: *The Astrophysical Journal Letters* 779.2 (2013), p. L27. ISSN: 2041-8205. DOI: `10.1088/2041-8205/779/2/L27` (cit. on p. 102).

[237] M Böttcher, EP Liang, IA Smith, and P Roustazadeh. „Magnetic-field generation and particle acceleration in relativistic shear layers“. In: *AIP Conference Proceedings*. Vol. 1505. 2012, pp. 618–621. ISBN: 978-0-73541-123-4. DOI: `10.1063/1.4772336` (cit. on p. 104).

[238] RA Fonseca, SF Martins, LO Silva, JW Tonge, FS Tsung, and WB Mori. „One-to-one direct modeling of experiments and astrophysical scenarios: pushing the envelope on kinetic plasma simulations“. In: *Plasma Physics and Controlled Fusion* 50.12 (2008), p. 124034. ISSN: 0741-3335. DOI: `10.1088/0741-3335/50/12/124034`. arXiv: `0810.2460` (cit. on p. 106).

[239] JA Clarke. *The Science and Technology of Undulators and Wigglers*. 4th. Oxford: Oxford University Press, 2004. ISBN: 978-0-19850-855-7. DOI: `10.1093/acprof:oso/9780198508557.001.0001` (cit. on p. 110).

[240] MV Medvedev. „Theory of "Jitter" Radiation from Small-Scale Random Magnetic Fields and Prompt Emission from Gamma-Ray Burst Shocks“. In: *The Astrophysical Journal* 540.2 (2000), pp. 704–714. ISSN: 0004-637X. DOI: `10.1086/309374`. arXiv: `astro-ph/0001314v2 [astro-ph]` (cit. on pp. 118, 121, 122).

[241] R Salvaterra et al. „GRB 090423 at a redshift of z $\approx$ 8.1“. In: *Nature* 461.7268 (2009), pp. 1258–1260. ISSN: 0028-0836. DOI: `10.1038/nature08445`. arXiv: `0906.1578` (cit. on p. 124).

[242] NR Tanvir et al. „A γ-ray burst at a redshift of z $\approx$ 8.2“. In: *Nature* 461.7268 (2009), pp. 1254–1257. ISSN: 0028-0836. DOI: `10.1038/nature08459`. arXiv: `0906.1577 [astro-ph.CO]` (cit. on p. 124).

[243] MV Torbett. „Hydrodynamic ejection of bipolar flows from objects undergoing disk accretion - T Tauri stars, massive pre-main-sequence objects, and cataclysmic variables“. In: *The Astrophysical Journal* 278 (1984), pp. 318–325. ISSN: 0004-637X. DOI: `10.1086/161796` (cit. on p. 127).

[244] T Piran. „The physics of gamma-ray bursts“. In: *Reviews of Modern Physics* 76.4 (2005), p. 1143. ISSN: 0034-6861. DOI: `10.1103/RevModPhys.76.1143`. arXiv: `astro-ph/0405503 [astro-ph]` (cit. on pp. 127, 130).

[245] Z Chang, A Rundquist, J Zhou, MM Murnane, HC Kapteyn, X Liu, B Shan, J Liu, L Niu, M Gong, and X Zhang. „Demonstration of a sub-picosecond x-ray streak camera“. In: *Applied Physics Letters* 69.1 (1996), pp. 133–135. ISSN: 0003-6951. DOI: `10.1063/1.118099` (cit. on p. 129).

[246] M Drabbels, GM Lankhuijzen, and LD Noordam. „Demonstration of a far-infrared streak camera“. In: *IEEE Journal of Quantum Electronics* 34.11 (1998), pp. 2138–2144. ISSN: 0018-9197. DOI: `10.1109/3.726606` (cit. on p. 129).

[247] CH Sarantos and JE Heebner. „Solid-state ultrafast all-optical streak camera enabling high-dynamic-range picosecond recording.“ In: *Optics Letters* 35.9 (2010), pp. 1389–1391. ISSN: 0146-9592. DOI: `10.1364/OL.35.001389` (cit. on p. 129).

[248] K Hada, A Doi, M Kino, H Nagai, Y Hagiwara, and N Kawaguchi. „An origin of the radio jet in M87 at the location of the central black hole“. In: *Nature* 477.7363 (2011), pp. 185–187. ISSN: 0028-0836. DOI: `10.1038/nature10387` (cit. on p. 130).

[249] TP Krichbaum. „Millimiter VLBI observations: Black Hole Physics and the Origin of Jets“. In: *Proceedings of 12th European VLBI Network Symposium and Users Meeting — PoS(EVN 2014)*. Vol. 230. SESSION 2 - Powerful AGN, jets and gamma-ray emission. Cagliari, Italy, 2015, pp. 013–1 – 013–6. DOI: `10.22323/1.230.0013` (cit. on p. 130).

[250] A Tarasevitch, K Lobov, C Wünsche, and D von der Linde. „Transition to the Relativistic Regime in High Order Harmonic Generation“. In: *Physical Review Letters* 98.10 (2007), p. 103902. ISSN: 0031-9007. DOI: `10.1103/PhysRevLett.98.103902` (cit. on p. 133).

[251] C Rödel, M Heyer, M Behmke, M Kübel, O Jäckel, W Ziegler, D Ehrt, MC Kaluza, and GG Paulus. „High repetition rate plasma mirror for temporal contrast enhancement of terawatt femtosecond laser pulses by three orders of magnitude“. In: *Applied Physics B: Lasers and Optics* 103.2 (2011), pp. 295–302. ISSN: 0946-2171. DOI: `10.1007/s00340-010-4329-7` (cit. on p. 133).

[252] J Bierbach et al. „Generation of 10μW relativistic surface high-harmonic radiation at a repetition rate of 10 Hz“. In: *New Journal of Physics* 14 (2012). ISSN: 1367-2630. DOI: `10.1088/1367-2630/14/6/065005` (cit. on p. 133).

[253] G Blaclard, H Vincenti, R Lehe, and JL Vay. „Pseudospectral Maxwell solvers for an accurate modeling of Doppler harmonic generation on plasma mirrors with particle-in-cell codes“. In: *Physical Review E* 96.3 (2017), p. 033305. ISSN: 2470-0045. DOI: `10.1103/PhysRevE.96.033305`. arXiv: `1608.05739` (cit. on p. 133).

[254] T Kluge, C Gutt, LG Huang, J Metzkes, U Schramm, M Bussmann, and TE Cowan. „Using X-ray free-electron lasers for probing of complex interaction dynamics of ultra-intense lasers with solid matter“. In: *Physics of Plasmas* 21.3 (2014), p. 033110. ISSN: 1070-664X. DOI: `10.1063/1.4869331`. arXiv: `1306.0420` (cit. on p. 134).

[255] T Kluge, M Bussmann, HK Chung, C Gutt, LG Huang, M Zacharias, U Schramm, and TE Cowan. „Nanoscale femtosecond imaging of transient hot solid density plasmas with elemental and charge state sensitivity using resonant coherent diffraction“. In: *Physics of Plasmas* 23.3 (2016), p. 033103. ISSN: 1070-664X. DOI: `10.1063/1.4942786`. arXiv: `1508.03988` (cit. on p. 134).

[256] T Kluge et al. „Nanometer-scale characterization of laser-driven compression, shocks, and phase transitions, by x-ray scattering using free electron lasers“. In: *Physics of Plasmas* 24.10 (2017), p. 102709. ISSN: 1070-664X. DOI: `10.1063/1.5008289` (cit. on p. 134).

[257] T Kluge et al. „Observation of Ultrafast Solid-Density Plasma Dynamics Using Femtosecond X-Ray Pulses from a Free-Electron Laser“. In: *Physical Review X* 8.3 (2018), p. 031068. ISSN: 2160-3308. DOI: `10.1103/PhysRevX.8.031068`. arXiv: `1801.08404` (cit. on p. 134).

[258] KI Nishikawa, J Niemiec, B Zhang, M Medvedev, P Hardee, Y Mizuno, Å Nordlund, J Frederiksen, H Sol, M Pohl, DH Hartmann, and GJ Fishman. „Simulation of Relativistic Jets and Associated Self-Consistent Radiation“. In: *International Journal of Modern Physics: Conference Series*. Vol. 08. 2012, pp. 259–264. DOI: `10.1142/S2010194512004680` (cit. on p. 134).

[259] KI Nishikawa et al. „Radiation from Particles Accelerated in Relativistic Jet Shocks and Shear-flows“. In: *5th Fermi Symposium*. Nagoya, Japan, 2014. arXiv: `arXiv:1412.7064v1` (cit. on p. 134).

[260] K Steiniger. „High-Yield Optical Undulators Scalable to Optical Free-Electron Laser Operation by Traveling-Wave Thomson-Scattering“. PhD thesis. Technische Universität Dresden, 2017. DOI: `10.5281/zenodo.439523` (cit. on p. 134).

Einen herzlichen Dank ...

Es war ein langer, teils steiniger Weg bis zur Vollendung dieser Arbeit. Rückblickend war es eine Erfahrung, die ich keinesfalls missen möchte. Danke, dass mir das Vertrauen geschenkt wurde selbstständig in einem faszinierenden Forschungsfeld arbeiten zu dürfen. Auf diesem Weg wurde ich von vielen Menschen unterstützt, gefördert und gefordert. Ohne euch wäre ich nicht so weit gekommen. Vielen Dank.

Ich danke Prof. Ulrich Schramm und Dr. Michael Bussmann dafür, dass sie mir nach meiner Diplomarbeit eine Promotion ermöglicht haben und mich meine begonnene Arbeit auf große und realistische Probleme der Astrophysik und Laser Plasma Beschleunigung haben anwenden lassen.

Michael, deine Fähigkeit immer das große Ganze und damit die Verknüpfungen zwischen scheinbar verschiedenen Gebieten zu sehen haben mich über meinen Tellerrand hinaussehen lassen. Auch wenn dein unnachgiebiges Streben nach Perfektion mich manchmal hat verzweifeln lassen, so war das Ergebnis durch deinen Input am Ende immer deutlich besser. Alexander Debus, deine fast schon überschäumende Faszination für Physik ist beflügelnd. Deine Bereitschaft jederzeit Probleme und Fragen meinerseits auch in großem Detail zu diskutieren hat mich ein aufs andere Mal vorangebracht. Danke Klaus, dass du immer da warst, wenn ich jemanden zum Diskutieren brauchte. Deine besonnene und gründliche Art hat mir oft die Augen geöffnet, mir immer den richtigen Einblick ermöglicht und mich Sorgen überwinden lassen. Ohne das überwältigende technische Verständnis von René wäre ich sicherlich häufiger verzweifelt. Danke, dass du immer ein offenes Ohr für meine Fragen hattest und mich an deinem Wissen über Programmabläufe und Fehlermeldungen hast teilhaben lassen. Danke für deine Geduld. Axel, viel Dank, dass du mir die Welt von offener Software näher gebracht hast, die du in allem was du tust vorlebst. Danke für die vielen Diskussionen über Physik und Programmierung. Marco, danke das du mein häufiges Fluchen ertragen hast, wenn etwas mal nicht klappte. Der Austausch mit dir, nicht nur zur Arbeit, hat mich bereichert. Ich danke auch dem Rest des Theorieteams, insbesondere Alexander Matthes, Thomas Kluge, Jan, Joao und Ilja für viele tolle Diskussionen.

Danke Uli, dass deine Bürotür für Fragen und Anliegen aller Art immer offen stand. Vielen Dank, dass du es ermöglicht hast meine Arbeit auf so vielen internationalen Konferenzen vorstellen zu können und selbst bei meinem Abstecher in die Astrophysik mir mit gutem Rat zur Seite standest. „How many holy atoms are in a glass of water?” – Asking us students such Fermi problems changed how I approach physics questions. Thank you, Tom, for pushing us to trust in our own assumptions and models.

I am grateful for the exciting collaboration with the entire electron team. I will always remember the daily discussions with Arie und Jurjen. Thank you for letting me ask you all the silly questions only a theoretician could ask without making me feel stupid. Your answers helped me a lot in modeling the experiment. Ich bedanke mich auch für die vielen Gespräche mit Alexander Köhler und Omid. Die enge Zusammenarbeit mit euch hat mir die Grenzen unserer aktuellen Modellierungen gezeigt aber auch viel über experimentelle Fragestellungen gelehrt. Jakob, auch wenn die Ergebnisse unserer Zusammenarbeit nur am Rande dieser Dissertation eingeflossen sind, so habe ich im Zuge dessen viel gelernt, was ich später anwenden konnte. Vielen Dank. Special thanks also go to Professor Mike Downer and his team: Rafal, Andrea, and Max. Thank you for all the insightful discussions.

Dank gebührt auch Karl und Lotti für die Diskussionen im Rahmen des „proton shaping“. Die Erkenntnis, dass die Parameter eines echten Hochleistungslasers viel schwieriger zu bestimmen sind, als ich es mir je vorgestellt habe verdanke ich Stefan Bock. Danke, dass du mir nicht nur die Parameter von DRACO näher gebracht hast, sondern mich auch in die WizzerHD Entwicklung involviert hast.

I also thank Sergey Rykovanov for his warm welcome in Jena, for sharing his expertise on high harmonic generation with me, and for letting me build his mini-GPU cluster to run PIConGPU. I am grateful to Maria Vranic for sharing her knowledge of the RLL pusher with me. I also thank Theresa Brümmer for being one of the few brave Clara2 users.

Ich bedanke mich bei all meinen Kollegen, die regelmäßig mit mir bouldern waren. Danke für die tolle Zeit.

Ein wunderbarer Ausgleich zur Thesis waren die vielen Abende, das Bouldern und die Urlaube zusammen mit Johannes und Johanna. Das Gleiche gilt für die regelmäßigen Kinobesuche, die langen Abende mit den neusten Folgen einer Serie oder den lagen Spieleabende mit Tim. Philipp, vielen Dank für die vielen schönen Abende und für deine Einblicke in das Leben nach der Promotion.

Ein großer Dank gebührt meinen Eltern. Ohne euren bindungslosen Rückhalt und eure umfassende Unterstützung wäre ich jetzt nicht an diesem Punkt. Danke, dass ihr in den letzten Jahren immer wieder Verständnis für mich aufgebracht habt, wenn ich der Arbeit Vorrang gab. Danke, für die unzählige Hilfe, die ihr mir immer wieder gewährt habt. Vielen Dank auch an meinen Bruder Johannes für die unzähligen Diskussionen über Gott und die Welt, aber insbesondere über Physik, besonders auf langen Wanderungen weit abseits der Zivilisation.

Leo, danke für dein Verständnis, wenn ich abends wieder lange arbeiten musste und du mich nicht zu Gesicht bekommen hast. Danke, dass du immer für den größten Quatsch zu haben bist und das du mit mir Lego baust. Du bist der beste Ziehsohn der Welt. Danke Jördis, dass du mit mir die Hochs und Tiefs der Dissertation durchgemacht hast. Du verstehst mich manchmal besser als ich mich selbst und deine Einblicke waren, wenn auch nicht immer leichter, sehr guter Rat. Danke für dein Verständnis, wenn ich wieder lange auf Arbeit bleiben musste oder auf Dienstreise war und dass du die viel zu lange andauernde Schreibphase ertragen hast. Es gibt so viel, wofür ich dir dankbar bin, daher hier einfach nur: Danke!

Erklärungen

Hiermit versichere ich, dass ich die vorliegende Arbeit ohne unzulässige Hilfe Dritter und ohne Benutzung anderer als der angegebenen Hilfsmittel angefertigt habe; die aus fremden Quellen direkt oder indirekt Übernommenen Gedanken sind als solche kenntlich gemacht. Die Arbeit wurde bisher weder im Inland noch im Ausland in gleicher oder ähnlicher Form einer anderen Prüfungsbehörde vorgelegt.

Die Dissertation wurde unter der wissenschaftlichen Betreuung von Prof. Dr. Ulrich Schramm, Dr. Michael Bussmann und Dr. Alexander Debus am Helmholtz-Zentrum Dresden – Rossendorf angefertigt.

Die Promotionsordnung der Fakultät Mathematik und Naturwissenschaften an der Technischen Universität Dresden vom 23. Februar 2011 mit letzten Änderungen vom 18. Juni 2014 erkenne ich an.

Dresden, 10. Dezember 2018

Richard Pausch

HZDR

HELMHOLTZ
ZENTRUM DRESDEN
ROSSENDORF

Tel. +49 351 260-3547
Fax +49 351 260-13547
r.pausch@hzdr.de
http://www.hzdr.de